



Development of ultra-high quality mechanical oscillators

Høj, Dennis

Publication date:
2021

Document Version
Publisher's PDF, also known as Version of record

[Link back to DTU Orbit](#)

Citation (APA):
Høj, D. (2021). *Development of ultra-high quality mechanical oscillators*. Department of Physics, Technical University of Denmark.

General rights

Copyright and moral rights for the publications made accessible in the public portal are retained by the authors and/or other copyright owners and it is a condition of accessing publications that users recognise and abide by the legal requirements associated with these rights.

- Users may download and print one copy of any publication from the public portal for the purpose of private study or research.
- You may not further distribute the material or use it for any profit-making activity or commercial gain
- You may freely distribute the URL identifying the publication in the public portal

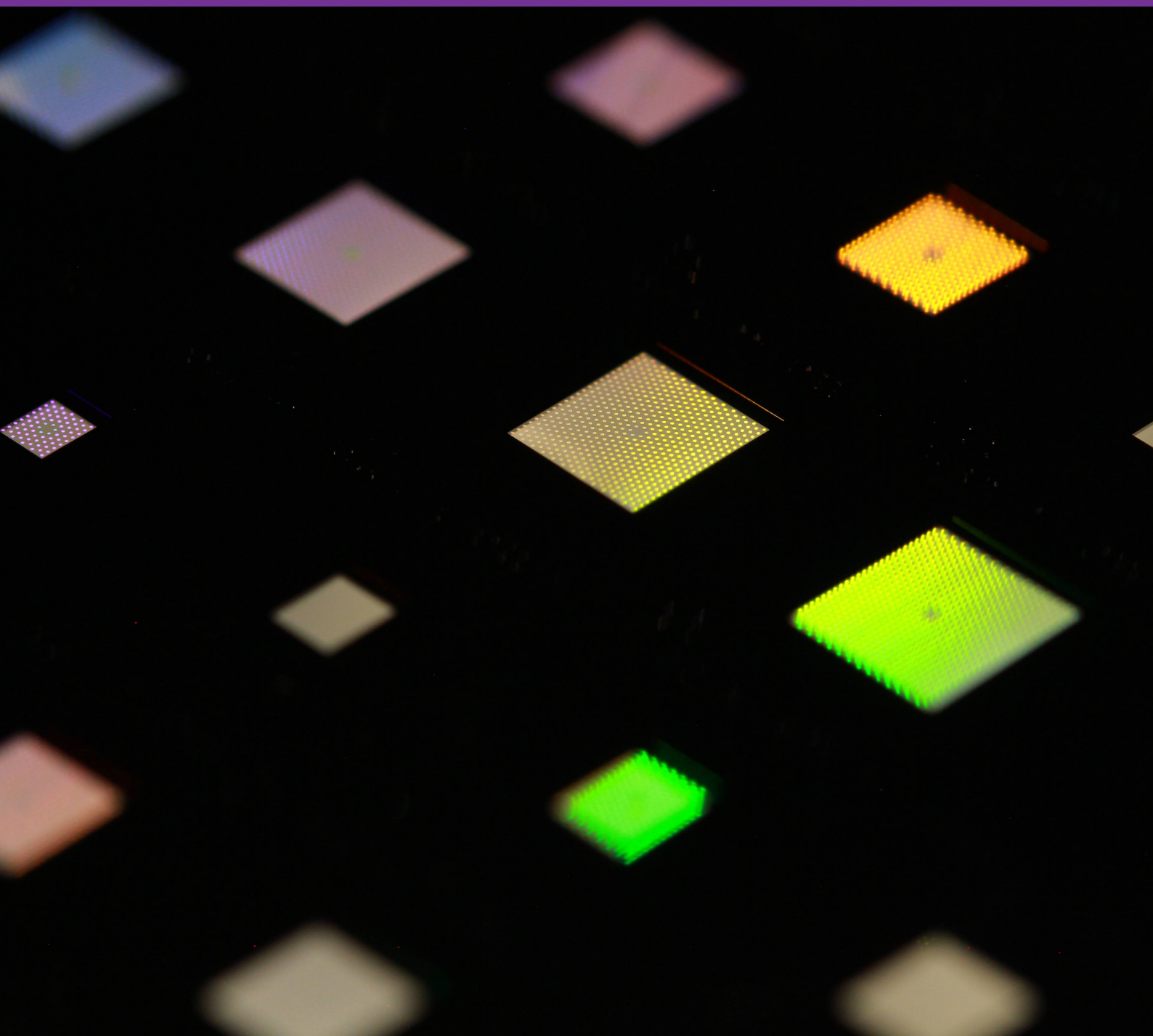
If you believe that this document breaches copyright please contact us providing details, and we will remove access to the work immediately and investigate your claim.

Development of ultra-high quality mechanical oscillators

Dennis Høj
January, 2021

Supervisor: Ulrik Lund Andersen
Co-supervisor: Ole Sigmund

PhD Thesis



Development of ultra-high quality mechanical oscillators

PhD Thesis
January, 2021

By
Dennis Høj

Supervisor
Ulrik Lund Andersen

Co-supervisor
Ole Sigmund

Copyright: Reproduction of this publication in whole or in part must include the customary bibliographic citation, including author attribution, report title, etc.

Cover photo: Ulrich Busk Hoff, 2021

Published by: DTU, Department of Physics, Fysikvej, Building 307, 2800 Kgs. Lyngby Denmark
www.fysik.dtu.dk

*To the love of my life,
for whom my heart will forever oscillate*

Approval

This thesis has been prepared over the course of three years and three months at the Center for Macroscopic Quantum States (bigQ), Department of Physics, at the Technical University of Denmark, DTU, in partial fulfillment of the requirements for acquiring a Doctor of Philosophy degree in Physics.

It is assumed that the reader has basic knowledge in the areas of mechanics and micro-fabrication.

Dennis Høj

.....
Signature

.....
Date

Abstract

In this thesis, ultra-coherent micro mechanical oscillators based on thin-film stoichiometric silicon nitride were developed and experimentally tested. This work gathers on all existing literature in the field. This includes theory work where a stochastic model was developed for predicting how vibrations from sub-MHz oscillators couple to the surrounding substrate and are subsequently lost. While this model hasn't been systematically tested experimentally yet, early results look promising and succeeds in predicting at least part of the high spread in results.

Two design approaches were developed and tested in an effort to fabricate the most coherent device possible. The first approach uses *topology optimization* to enhance the coherence of the fundamental mode of a resonator, which is to be used in quantum optomechanics. Numerical evaluations showed a Qf product enhancement above a factor of two compared to a reference design. Experimental results showed the best devices for each design are limited by intrinsic losses. However, the large spread in the results indicated most of them were heavily affected by phonon tunneling losses, which highlighted flaws in the topology optimization implementation. The best results matched the numerical predictions making them the best fundamental mode resonators in existence with $Qf = 2.8 \times 10^{13}$.

The second design approach developed called *density phononics* is based on phononic crystals defined by modulating the effective density of a material. This novel membrane design was achieved by fabricating microscopic pillars. Early results showed fabrication is non-trivial, but it is expected this can be optimized greatly by changing the process steps. Nonetheless, the design approach was validated and the early batch resulted in 1.4 MHz resonators with $Qf = 8 \times 10^{14}$ at room temperature, which is a new record for this type of device. Furthermore, models predict quality factors above 10^9 should be possible with continued refinement of fabrication.

Finally, two designs for both reducing and enhancing the tensile stress of two-dimensional membranes was proposed. Numerical evaluations showed the former can reduce the tensile stress by multiple orders of magnitude. This has applications in enhancing the sensitivity of thermal sensing and derived sensing schemes. The second design used for stress enhancement results in enhancements up to a factor of three. When combined with density phononics, it is expected that room temperature resonators with Qf products above 10^{16} should be possible.

Resumé

I denne afhandling er ultrakohærente mikromekaniske oscillatorer baseret på tyndfilm støkiometrisk siliciumnitrid udviklet og eksperimentelt afprøvet. Arbejdet samler på al eksisterende litteratur inden for feltet. Det teoretiske arbejde inkluderer bl.a. udviklingen af en stokastisk model til at estimere hvordan vibrationerne fra en sub-MHz oscillator kobler til den omkringliggende substrat og er efterfølgende tabt. Systematisk test af modellen er ikke blevet udført eksperimentelt endnu. Tidlige resultater viser dog gode resultater og modellen formår delvist at beskrive spredningen observeret i resultaterne.

To fremgangsmåder til at designe oscillatorerne blev udviklet og eksperimentelt afprøvet for at opnå den mest kohærente enhed muligt. I den første blev *topologioptimering* brugt til at generere en struktur der maksimerer kohærensens for den fundamentale vibrationstilstand til brug i kvanteoptomekanik. Numeriske beregninger viste at Qf produktet blev forbedret med over en faktor to sammenlignet med en reference. Eksperimentelle resultater viste de bedste prøver var begrænset af intrinsiske tab. Til gengæld indikerede den store spredning i resultaterne at fonon-tunnelerings-tab var betydelig. Dette fremhævede brister i modellen brugt til topologioptimering. Baseret på de bedste prøver blev den samme forbedring observeret. Dermed er disse de bedste eksisterende oscillatorer for fundamentale vibrationstilstand med $Qf = 2.8 \times 10^{13}$.

Den anden fremgangsmåde kaldet *densitetsfononik* er baseret på fononiske krystaller, som er defineret af en modulering af materialets effektive densitet. Denne nye type membran blev realiseret ved at fabrikere mikroskopiske søjler. Fabrikationen viste sig ikke at være trivial, men det forventes dette kan optimeres ved at ændre på fabrikationsprocesserne. Ikke desto mindre kunne fremgangsmåden valideres eksperimentelt og foreløbige resultater førte til 1.4 MHz oscillatorer med $Qf = 8 \times 10^{14}$, hvilket er en ny rekord for membraner. Endvidere, ud fra numeriske beregninger forventes det at kvalitetsfaktorer over 10^9 burde være muligt såfremt fabrikationen optimeres.

Endeligt blev to strukturer udviklet til henholdsvis at sænke og hæve den elastiske spænding i todimensionelle membraner. Numeriske beregninger viste at førstnævnte kan reducere den elastiske spændingen med flere størrelsesordner. Dette har anvendelse inden for maksimering af følsomheden for termiske og afledte sensorer. Den anden struktur viste en elastisk spændingsforøgelse med op til en faktor 3. Når dette kombineres med densitetsfononiske membraner er forventningen at oscillatorer med Qf produkter over 10^{16} ved stuetemperatur vil være mulige.

Acknowledgments

First of all, I am grateful for my supervisor Ulrik Lund Andersen giving me the opportunity to be part of his exciting group. Under his guidance, I have learned a lot and advanced greatly as a researcher.

I would like to thank my co-supervisor Ole Sigmund for introducing me to the wonders of topology optimization. His algorithms are like magic to me and I am always amazed by the capabilities of his work.

Special thanks goes to my team leader Ulrich Busk Hoff. A very knowledgeable person who is always eager to help. His cheerfulness and wacky humor is an inspiration to us all.

I would like to thank Kristian Hagsted Rasmussen. You were my cleanroom guru from the very start. I appreciate all the help you gave me and I cherish the discussions we've had along the way.

I am grateful for all the members of the optomech team. You are all fantastic individuals whom I've enjoyed every moment spend together. Joost van der Heijden, you always have an unbreakable optimism and I love the discussions we've had over the years. Jan Bilek, you are my first "customer" and all your feedback was highly valuable. Iman Moaddel Haghighi, you were always full of ideas. Your drive and creativity was an inspiration for the whole team. Sissel Bay Nielsen, your shining positive energy always lights up the room. Angelo Manetta, I am grateful for all the Italian mafia tricks you've taught me. These will be put to good use. Frederik Werner Isaksen, I thank you for your continuous feedback and your expertise in statistics has helped me a lot.

I would like to specially thank Fengwen Wang and Wenjun Gao. Their hard work in implementing topology optimization was crucial for obtaining the great results.

I am grateful for working with Silvan Schmid and his inspiring team at Vienna University of Technology. I would like to thank Silvan for his motivational guidance which has helped me ever since. Special thanks goes to: Niklas Luhman, a fantastic individual living life to the fullest. And, Robert G. West for all our political, philosophical and wacky discussions in the office.

I would like to thank the great people working at DTU Nanolab. Special thanks goes to: Conny Hjort. Your help in the cleanroom throughout my work is invaluable. Karen Birkelund. Your continuous feedback and suggestions is what helped me fine-tune my processes. Thomas Aarøe Anhøj for always being ready for my lithography problems. Berit Herstrøm for helping me understand and optimize the dry processes. And, the rest of the DTU Nanolab staff for their continuous help and expertise.

I have enjoyed my time in the office with colleagues which came and went over the years. Mikkel Vilsbøll Larsen helped me getting settled at DTU, Sepehr Ahmadi ensured a constant supply of exotic teas, and Olivier Gobron for in office sparring of all kinds of problems in work and in life.

Special thanks goes to Tine Hougaard Klitmøller. In times of need you were always ready to assist in all bureaucratic matters. This PhD wouldn't be possible without your help.

Finally, my deepest gratitude for the love of my life. Your constant love and support helped me get through all these years. You have endured much in the finale year. I can only hope to make up for the lost time in years to come.

The work presented in this thesis is funded by the Villum Foundation and the Danish National Research Foundation.

Declaration

Peer-reviewed journal articles

- Niklas Luhmann, Dennis Høj, Markus Piller, Hendrik Kähler, Miao Hsuan Chien, Robert G. West, Ulrik Lund Andersen, and Silvan Schmid. “Ultrathin 2 nm gold as impedance-matched absorber for infrared light”. In: *Nature Communications* 11.1 (2020). ISSN: 20411723. DOI: 10.1038/s41467-020-15762-3. arXiv: 1911.13126

Conferences

- Dennis Høj, Wenjun Gao, Fengwen Wang, Ole Sigmund, Ulrich Busk Hoff, and Ulrik Lund Andersen. “Ultra-coherent fundamental mode mechanical resonators designed using topology optimization”. In: *The 3rd International Forum on Quantum Metrology and Sensing*. Kyoto, 2020

Contents

1	Introduction	1
Part I	Fundamentals of High-Q Micromechanical Resonators	3
2	Overview	5
3	Differential equations of motion	7
3.1	1D system	7
3.2	2D system	9
4	Mechanical damping mechanisms	11
4.1	Gas damping	11
4.2	Intrinsic damping	13
4.2.1	Friction losses	13
4.2.2	Thin-film loss model	15
4.2.3	Fundamental losses	15
4.2.4	Quality factor from intrinsic losses	17
4.2.5	Damping dilution using high tensile stress	18
4.2.6	Intrinsic losses on typical resonators	18
4.2.7	Concluding remarks on intrinsic losses	22
4.3	Phonon tunneling loss	22
4.3.1	Infinite sized substrates	23
4.3.2	Finite sized substrates	29
4.3.3	Substrates with phononic shields	33
4.3.4	Concluding remarks on phonon tunneling losses	35
4.4	Conclusion on damping mechanisms	36
5	Nonlinear analysis	39
5.1	Source of nonlinearity: String elongation	39
5.2	Modeling damping	41
5.2.1	Nondimensionalization	42
5.3	Multiple scales analysis	42
5.4	Conclusion on nonlinear analysis	44
6	Phononic crystal patterned membranes and soft-clamping	45
6.1	Phononic crystal theory	45
6.2	Implementations of one & two dimensional crystals	47
6.3	Soft-clamping of the fundamental mode: Fractals	49
6.4	Conclusion on soft-clamped resonators	50
7	Ringdown experiment	53
7.1	Displacement measurement using homodyne detection	53
7.2	The optical setup and measurement	55
7.2.1	Vacuum system	56
7.2.2	Quality factor estimation	57
7.3	Noise and perturbation during measurement	57

7.3.1 Thermal drift	57
7.3.2 Nonlinear mechanical effects	58
7.3.3 External vibrations	59
7.3.4 Other effects	60
7.4 Conclusion	60
Part II Topology Optimized Trampolines	61
8 Overview	63
9 Topology optimization	65
9.1 Basic theory and implementation	65
9.2 Topology optimized designs	67
9.2.1 Numerical evaluation of the designs	68
9.2.2 Discussion on results	70
9.3 Conclusion on topology optimization	72
10 Fabrication	73
10.1 Initial wafer and low-pressure chemical vapor deposition	73
10.2 Resonator design transfer	75
10.3 Protective layer deposition	76
10.4 KOH etch window design transfer	77
10.5 Membrane release	78
10.6 Post process cleaning, drying and dicing	80
10.7 Collapsing and buckling structures	81
10.8 Concluding on fabrication	82
11 Experimental results and discussion	85
12 Conclusion and outlook	91
Part III Density Phononic Membranes	93
13 Overview	95
14 Theory and design development	97
14.1 One-dimensional density enhanced string	97
14.2 Two-dimensional density enhanced membrane	98
14.3 Optimizing the density phononic crystal	101
14.4 Phononic membrane designs	102
14.5 Density distribution to pillar layout conversion	105
15 Fabrication	109
15.1 Etch and release of pillars and membrane	111
15.2 Resulting membranes	112
16 Experimental results and discussion	115
17 Conclusion and outlook	119

Part IV Two-dimensional strain engineering	121
18 Overview	123
19 Stress reduced design	125
19.1 Design	125
19.2 Proposed fabrication	126
20 Stress enhanced design	129
20.1 Design principle	129
20.2 Design optimization	130
20.3 Discussion	132
21 Overall conclusion and outlook	135
Bibliography	137
A Material parameters	143
B Derivation of basic properties for typical resonators	144
B.1 String	144
B.2 Trampoline	144
B.3 Circular membrane	145
B.4 Rectangular membrane	146
C Process flows	148

1 | Introduction

The study of ultra-coherent micromechanical resonators is a study of the very fundamentals of mechanics. The overarching question of the thesis is: How can one design the ultimate coherent micromechanical resonator? Answering this question is of great value in a multitude of fields. Being part of the *Center for Macroscopic Quantum States (bigQ)*, the immediate application is quantum optomechanics, where ultra-coherent resonators is key for realizing a number of great experiments and devices [3]. Examples of this include fundamental tests of quantum mechanics, gravitational wave detection and solid-state quantum memory. Beyond the scope of quantum mechanics, the exceptionally low mechanical noise may enable the development of sensors with groundbreaking sensitivities.

There exists a large range of different mechanical oscillators. This is true even when one only considers micromechanical devices, which even includes oscillations of individual atoms [4]. To limit the scope of this project the focus is on thin-film resonators [5] with an emphasis on stoichiometric silicon nitride. In more than a decade this type of resonator have demonstrated impressive results with iterative improvements over the years. However, their full potential haven't been reached yet. This leaves room for pushing the coherence of these devices to even higher levels. This work strives to achieve just that.

The thesis consists of four parts. Part I combines all the relevant theory of the field. Basic concepts of thin-film membranes are introduced. An overview of all important damping mechanisms is given, which includes theoretical work to cover aspects not already covered by literature. State-of-the-art resonators are presented and discussed. Moreover, the experimental setup used to characterize all devices is described. The part is used as a foundation for the whole thesis and important results therein will continually be referenced to. Part II is the first of the major projects and the original motivation for the this work. *Topology optimization* is used to generate the best possible design for a fundamental mode resonator. Experimental results show world-record performance for this type of resonator. Part III introduces an alternative approach for implementing phononic crystals based on *modulating the effective material density* of a membrane. These are used as platform for demonstrating resonators with unprecedented coherence for membranes not matched anywhere else in the field. Finally, Part IV presents theoretical work on applying strain engineering for both reducing and enhancing the tensile stress on *two-dimensional* membranes.

Throughout the thesis some material parameters are used constantly in many of the calculations and simulations. The values of these are found in appendix A unless otherwise stated. All finite element simulations were performed using COMSOL Multiphysics.

Part I

Fundamentals of High-Q Micromechanical Resonators

2 | Overview

The aim of the first part of the thesis is to provide an overview of all the important theory and concepts in the field of ultra-coherent micromechanical resonators. Many of the results here will be used in the following parts. Therefore, the first part acts as a foundation for the rest of the thesis. Since a lot has already been done in this field, the first part is partly a literature study while some novelty has been added where discrepancies or a lack of knowledge was encountered.

What is considered important? Firstly, the focus is on micromechanical resonators based on very thin (200 nm and below) silicon nitride layers kept under high tensile stress. These devices have interesting properties which set them apart from the more common thicker and relaxed counterparts. To gain a proper understanding of their behavior the differential equations governing their solutions will be studied in chapter 3.

In the quest for maximizing the coherence of a resonator a key challenge is to reduce *all* loss contributions which limit their performance. Understanding which damping mechanisms affect these resonators and how each of them can be minimized is of great importance. Chapter 4 introduces all the relevant mechanisms. This includes a deeper study into phonon tunneling losses, i.e. vibrations of the resonator which couple to the surrounding environment. It was found the latter is poorly understood in case of resonators operating at relatively low frequencies. This lead to an extensive study into how this can be modeled correctly.

One of the key properties of resonators with ultra-high quality factors and low mass is that they can easily be excited to high amplitudes. This makes them prone to nonlinear effects which perturb their response and behavior. These are briefly discussed in chapter 5, where both the effects on resonance frequency and damping are investigated.

One of the recent innovations in the field which has pushed the quality factor \times frequency (Qf) products by at least an order of magnitude is the use of patterns, or phononic crystals, to localize a mode of vibrations to a defect. This isolation of the mode has great advantages and is right now the design of choice for ultra-coherent resonators. The theory of phononic crystals is briefly presented in chapter 6 and examples of its implementation in literature is discussed.

Finally, the resonators fabricated during this work need to be characterized. The extremely high quality factors and small dimensions creates a number of criteria which needs to be fulfilled for a successful characterization. A setup was built based on the mechanical ringdown method and is described in chapter 7.

It is expected that after the reader has studied the first part of the thesis, he or she will know the basics and important aspects in designing ultra-coherent resonators. The reader will be well equipped to understand and hopefully motivated to see how this knowledge has been utilized to push the coherence to new extreme heights in the field of ultra-coherent resonators.

3 | Differential equations of motion

To obtain a good understanding on the fundamentals of micromechanical resonators, studying the differential equations which govern their motion is a good starting-point. In literature there are countless examples on how to derive the wave equation dominated by bending stiffness of strings and plates [6] as well as approximate solutions for corresponding tensile stress dominated strings and membranes [7]. As will be seen in this chapter, even though the dynamics at high tensile stress can be described purely by the tensile stress induced stiffness, the bending stiffness still plays a vital role in order to obtain a full understanding of how the systems behave and how to predict key properties like damping.

This chapter is divided into two sections. First, a one-dimensional string is studied. This simple case is easy derive, yet it gives, in principle, all the insight needed to understand all key effects in play. In the following section, the solution is briefly extended to a two-dimensional membrane.

3.1 1D system

The partial differential equation of a beam under tensile stress can be derived by studying a small beam segment shown on Figure 3.1. At first, the movement along the x-direction is considered. Using Newton's second law, the total force on the x-axis must equal the beam element's mass times its acceleration, i.e.

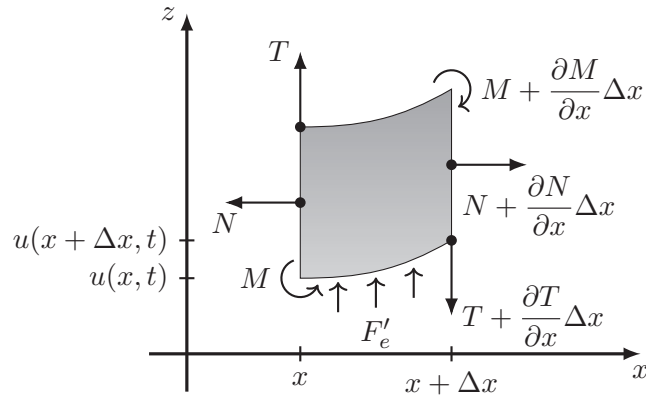


Figure 3.1: A differential beam segment with length Δx and with the in-plane force N , transversal force T , bending moment M and external force distribution F'_e illustrated.

$$T - \left(T + \frac{\partial T}{\partial x} \Delta x \right) = m' \frac{\partial^2 \xi}{\partial t^2} \Delta x, \quad (3.1)$$

where T is the beam tension in units of force, $m' = \rho A$ is the mass per unit length where ρ and A are the beam's material density and cross-sectional area, respectively, and ξ is the longitudinal beam displacement. When a transversal displacement is present the total beam length experiences an elongation which creates a coupling between the transversal and longitudinal displacements. However, in section 5.1 it will be shown this relation is nonlinear. For small transversal displacements the induced longitudinal displacement is

negligible and will henceforth be ignored, i.e. $\partial^2 \xi / \partial t^2 \rightarrow 0$. Solving Eq. (3.1) then leads to

$$T(x) \rightarrow T = \sigma A \quad (3.2)$$

where σ is the tensile stress in the string and A its cross-sectional area. The transversal force balance can be written as

$$F - \left(F + \frac{\partial F}{\partial x} \Delta x \right) + F'_e = m' \Delta x \frac{\partial^2 u}{\partial t^2} \Rightarrow \frac{\partial F}{\partial x} = F'_e - m' \frac{\partial^2 u}{\partial t^2}, \quad (3.3)$$

where F is the total force, and F'_e the external force distribution. F can be related to the bending moment M by looking at the moment balance

$$M - \left(M + \frac{\partial M}{\partial x} \Delta x \right) - F \Delta x - \frac{\partial u}{\partial x} \Delta x T - \frac{F'_e}{2} \Delta x^2 \approx 0 \quad (3.4)$$

$$F \rightarrow \lim_{\Delta x \rightarrow 0} F = -\frac{\partial u}{\partial x} T - \frac{\partial M}{\partial x}, \quad (3.5)$$

where the element's rotational inertia is ignored, since the wavelength is assumed much longer than the beam thickness. M can be derived by considering the bending induced strains inside the beam element illustrated on Figure 3.1

$$\begin{aligned} M(x, t) &= \int_A (\sigma + \Delta \sigma(x, z, t)) z \, dA \\ &= \int_A \sigma z \, dA + \int_A \Delta \sigma(x, z, t) z \, dA \\ &= \int_A E \Delta \sigma(x, z, t) z \, dA \\ &= E \int_A \left(-\frac{\partial^2 u}{\partial x^2} z \right) z \, dA \\ &= -B \frac{\partial^2 u}{\partial x^2}, \end{aligned} \quad (3.6)$$

where $\Delta \sigma(z, t)$ and $\Delta \varepsilon(z, t)$ are the bending induced changes in longitudinal stress and strain, respectively. Note the σz term cancels out in the integration. $B = EI$ is the beam stiffness, where E is the material Young's modulus and $I = \int_A z^2 \, dA$ is the area moment of inertia. For rectangular beams it is defined as $I = wh^3/12$, where h and b are the beam's thickness and width, respectively. Substituting Eq. (3.5) and (3.6) into (3.3) finally yields the one-dimensional wave equation

$$\frac{\partial^2}{\partial x^2} \left(B \frac{\partial^2 u}{\partial x^2} \right) - T \frac{\partial^2 u}{\partial x^2} + m' \frac{\partial^2 u}{\partial t^2} = F'_e, \quad (3.7)$$

which is a fourth order partial differential equation (PDE). For a uniform beam, i.e. $\partial B / \partial x = 0$, the above simplifies to

$$B \frac{\partial^4 u}{\partial x^4} - T \frac{\partial^2 u}{\partial x^2} + m' \frac{\partial^2 u}{\partial t^2} = F'_e. \quad (3.8)$$

An interesting case is when the tensile stress is high. Here, the stiffness from the stress will dominate the total stiffness everywhere except at regions with sharp modeshape features. The latter is typically present near the boundaries of a domain. When far away from any boundaries the PDE reduces to

$$-c_\sigma^2 \frac{\partial^2 u}{\partial x^2} + \frac{\partial^2 u}{\partial t^2} = F'_e, \quad (3.9)$$

which is a typical inhomogeneous wave equation where $c_\sigma = \sqrt{\sigma/\rho}$ is the propagation velocity of a wave traveling in a tensile stress dominated beam. From the homogeneous part of Eq. (3.8) the dispersion relation of a uniform beam can be derived by assuming a harmonic wave of the form $u(x, t) = e^{i(kx - \omega t)}$ leading to

$$B\tilde{k}^4 - T\tilde{k}^2 - m'\omega^2 = 0. \quad (3.10)$$

The wavenumber \tilde{k} has 4 solutions

$$\tilde{k} = \begin{cases} \pm k \\ \pm ik_e \end{cases}, \quad (3.11)$$

where

$$k = \frac{\sqrt{2BT \left(\sqrt{4Bm'\omega^2/T + 1} - 1 \right)}}{2B}, \quad k_e = \frac{\sqrt{2BT \left(\sqrt{4Bm'\omega^2/T + 1} + 1 \right)}}{2B}. \quad (3.12)$$

When in the high stress regime, i.e. $T^2 \gg 4Bm'\omega^2$ and assuming a rectangular beam this can be simplified to

$$k \approx \omega \sqrt{\frac{\rho}{\sigma}}, \quad k_e \approx \sqrt{\frac{12\sigma}{Eh^2}}. \quad (3.13)$$

When on the other hand no tensile stress is present i.e. $T = 0$, Eq. (3.12) can be reduced to

$$k = k_e = \left(\omega^2 \frac{m'}{B} \right)^{1/4} = \left(\omega^2 \frac{12\rho}{Eh^2} \right)^{1/4} \quad (3.14)$$

The general solution for a beam at a given frequency is

$$u(x) = a_1 e^{ikx} + a_2 e^{-ikx} + b_1 e^{k_e x} + b_2 e^{-k_e x}. \quad (3.15)$$

suitable for traveling waves. It is clear from Eq. (3.15) that the first two terms are traveling waves whereas the last two terms are evanescent waves with a characteristic length of $1/k_e \approx \sqrt{Eh^2/12\sigma}$. For a typical silicon nitride beam with $h = 50$ nm and $\sigma = 1$ GPa the characteristic length is $\lambda_e \approx 200$ nm. It can be seen that high tensile stress may lead to very short but extremely sharp bending at domain boundaries. This effect can lead to enhanced damping along a boundary as described in section 4.2.6. Finally, for standing waves a more suitable form of Eq. (3.15) is

$$u(x) = A_1 \cos kx + A_2 \sin kx + B_1 \cosh k_e x + B_2 \sinh k_e x. \quad (3.16)$$

3.2 2D system

Deriving the PDE for a two-dimensional system can be done in a similar manner, and will therefore simply be stated. It is worth noting that during the derivation extra care must be taken to ensure that all relevant cross coupling between forces in x and y directions are included. The two-dimensional wave equation for a tensile stressed embedded plate is given by

$$B'\nabla^4 u - T'_x \frac{\partial^2 u}{\partial x^2} - T'_y \frac{\partial^2 u}{\partial y^2} + m'' \frac{\partial^2 u}{\partial t^2} = p_e, \quad (3.17)$$

and if $T'_x = T'_y = T'$, it simplifies to

$$B'\nabla^4 u - T'\nabla^2 u + m'' \frac{\partial^2 u}{\partial t^2} = p_e, \quad (3.18)$$

where $\nabla^2 = \partial^2/\partial x^2 + \partial^2/\partial y^2$ and $\nabla^4 = \nabla^2 \nabla^2$. $T_i = h\sigma_i$ with $i = \{x, y\}$ are the tensile stress per unit length in both in-plane directions, $B' = Eh^3/[12(1 - \nu^2)]$ is the bending stiffness per unit length and $m'' = \rho h$ is the mass per unit area. The shear force per unit length are given by

$$F'_x = -T'_y \frac{\partial u}{\partial y} - \frac{\partial M'_{xy}}{\partial y} - \frac{\partial M'_{xx}}{\partial x}, \quad F'_y = -T'_x \frac{\partial u}{\partial x} - \frac{\partial M'_{yx}}{\partial x} - \frac{\partial M'_{yy}}{\partial y}, \quad (3.19)$$

where F_x is the force per unit length along the x -direction. The bending moments M_{ij} are given by

$$M'_{xy} = -B' \left(\frac{\partial^2 u}{\partial y^2} + \nu \frac{\partial^2 u}{\partial x^2} \right), \quad M'_{yx} = -B' \left(\frac{\partial^2 u}{\partial x^2} + \nu \frac{\partial^2 u}{\partial y^2} \right). \quad (3.20)$$

while the bending contribution from in-plane shearing is given by

$$M_{xx} = -M_{yy} = \int_A \Delta \tau_{xy} z \, dA = -B'(1 - \nu) \frac{\partial^2 u}{\partial x \partial y}. \quad (3.21)$$

From the homogeneous part of Eq. (3.17) the dispersion relation can be derived by assuming a harmonic wave of the form $u(x, y, t) = e^{i(\tilde{k}_x x + \tilde{k}_y y - \omega t)}$. When there is a non-uniformity in the stress, i.e. $T'_x \neq T'_y$ this is non-trivial to solve. For a uniform stress distribution Eq. (3.18) can be used, which when using the same approximations as in the one dimensional case yields

$$\tilde{k}_x^2 + \tilde{k}_y^2 = \pm \tilde{k}^2 \quad (3.22)$$

where in the high tensile stress regime k and k_e are approximated as

$$\tilde{k} = \begin{cases} \pm k \\ \pm i k_e \end{cases}, \quad k \approx \omega \sqrt{\frac{\rho}{\sigma}}, \quad k_e \approx \sqrt{\frac{12\sigma(1 - \nu^2)}{Eh^2}}. \quad (3.23)$$

and correspondingly for no tensile stress

$$k = k_e = \left(\omega^2 \frac{m''}{B'} \right)^{1/4} = \left(\omega^2 \frac{12\rho(1 - \nu_s^2)}{Eh^2} \right)^{1/4} \quad (3.24)$$

Notice the similarity to the one-dimensional case, where the only difference being the slightly added stiffness for the evanescent wavenumber. The general solution for a two-dimensional system is much more complicated, and it is not used in any context in this work. Instead, solutions are obtained by probing a proposed modeshape into Eq. (3.17).

The partial differential equations derived above give a good overview of the expected behavior of a resonator and is a good starting point for analyzing idealized resonators like strings and membranes under high tensile stress from which we can derive qualitative conclusions. Note for patterned membranes the stress distribution will not be uniform as assumed in Eq. (3.18). Consider a rectangular membrane initially fabricated with a completely uniform tensile stress distribution equal in both directions. Now etch some patterns into it. As soon as the membrane is released the whole structure will be in a state of force imbalances at the etched features. The whole membrane is then displaced until a new force equilibrium state is obtained. The membrane will now have a new spatially-dependent tensile stress distribution in both x and y directions which generally will be non-uniform. This makes any purely analytical solutions practically impossible except for the simplest membrane designs.

4 | Mechanical damping mechanisms

The main goal of the project is to design and fabricate mechanical resonators with the highest possible quality factors. This requires a deep understanding of all the relevant damping mechanisms one can expect in such resonators. This chapter outlines all the relevant damping mechanisms which may affect the resonator's performance. These can largely be divided into three types:

1. **Gas damping**, an external force of colliding gas molecules impeding the movement of the resonator.
2. **Intrinsic loss**, internal friction force resulting in internal damping.
3. **Phonon tunneling loss**, phonons of the resonator which couple and are lost to the surrounding substrate.

While most of the content will be a review of the existing literature, phonon tunneling losses for resonators operating at up to the low MHz range is largely unexplored. This is highly relevant for especially trampolines and other resonators operating in the sub-MHz range. A significant part of the chapter is dedicated to studying this loss mechanism in detail and develop applicable models for it.

Throughout the thesis damping will be represented by their respective quality factor contribution

$$Q_i = 2\pi \frac{W}{\Delta W_i} = \omega \frac{W}{\Delta P_i}, \quad (4.1)$$

where W is the resonator mode energy, ΔW_i the lost energy per cycle for the damping contribution i , ΔP_i is the corresponding lost power and ω the frequency in rad/s. The total quality factor of a resonator can then be computed by

$$Q^{-1} = \sum_i Q_i^{-1} \quad (4.2)$$

where it is evident the lowest quality factor contribution will dominate the quality factor of the resonator. A common feature is that the Qf product is constant. As the resonator size is increased this leads to lower frequencies, but often the quality factors is increased in an inverse proportional fashion leading to the same Qf product. Optimizing this product is therefore an important part of this work, and this section will highlight how to achieve it.

4.1 Gas damping

When the quality factor has been improved considerably one will eventually reach a point of being damped by the surrounding gas molecules. It may seem like a trivial damping mechanism. One can in principle simply create a vacuum good enough to disregard it, which one should in the quest for obtaining the best possible resonators. As this section will show, this can potentially put extreme requirements to the vacuum system.

Gas damping has two distinct regions depending on the pressure level [7]. At higher pressures the gas acts like a fluid and is known as the fluidic regime. At lower pressures the mean free path of the gas molecules become large and the phenomenon can then be modeled as a momentum transfer between the gas molecules and the resonator. This is known as the ballistic regime. Considering the extremely high quality factors obtainable with thin-film tensile stressed silicon nitride resonators these will always need to be

pumped down to high vacuum in order for them to operate unaffected. Therefore, the focus will be on the ballistic regime only.

In the ballistic regime gas molecules will hit randomly on both side of an oscillating membrane equally. When the membrane is moving with a velocity \dot{u} the molecules at the front will hit with the velocity $\dot{u} + v_g$ and the back with the velocity $\dot{u} - v_g$ where v is some stochastic variable for the gas molecule velocity. This creates a pressure difference which will impede the movement of the membrane. This pressure difference is given by [8]

$$\Delta p(x, y, t) = p \sqrt{\frac{32M}{\pi R_0 T}} \dot{u}(x, y, t) . \quad (4.3)$$

The distribution of the instantaneous power transferred to the gas molecules can then be defined by

$$\Delta w_g(x, y, t) = \Delta p(x, y, t) \dot{u}(x, y, t) . \quad (4.4)$$

Letting $u(x, y, t) \rightarrow u(x, y) \cos(\omega t)$ the total lost power per cycle can be obtained by integrating across the membrane surface and integrating temporally over a cycle

$$\Delta W_g = \int_0^{2\pi/\omega} \iint \Delta w_g(x, y, t) \, dx dy \, dt = p\omega \sqrt{\frac{32\pi M}{R_0 T}} \iint u^2(x, y) \, dx dy . \quad (4.5)$$

The energy of membrane can be obtained by considering its kinetic energy. The maximum kinetic energy density is given by

$$w_{k,\max}(x, y) = \frac{\rho h \omega^2}{2} u^2(x, y) . \quad (4.6)$$

Performing the same spatial integrations leads to

$$W_{k,\max} = \frac{\omega^2}{2} \iint \rho h u^2(x, y) \, dx dy . \quad (4.7)$$

Finally, the ballistic gas quality factor is

$$Q_g = \frac{\omega}{p} \sqrt{\frac{\pi R_0 T}{32M}} \frac{\iint \rho h u^2(x, y) \, dx dy}{\iint u^2(x, y) \, dx dy} . \quad (4.8)$$

Most membranes and strings are designed with a single thickness and density (but not all, see Part III). This reduces the above to the design independent solution

$$Q_g = \frac{\rho h \omega}{p} \sqrt{\frac{\pi R_0 T}{32M}} , \quad (4.9)$$

which is the expression used in various textbooks. A typical silicon nitride resonator operating at room temperature could have the specifications $h = 50 \text{ nm}$, $M = 28.9 \text{ g/mol}$ and $Q = 10^7$. This leads to a required vacuum with a pressure $p \ll 10^{-5} \text{ mbar}$. Thinner membranes pushes this requirement to even lower pressures. For ultra-high quality membranes, the thickness is typically down to 10 nm , and pressures below 10^{-7} mbar must be used to guarantee that the results are unaffected by gas damping. All this illustrates the importance and necessity of a high quality vacuum system, if the goal is to measure ultra coherent resonators. If this is difficult to fulfill, one option is then to design resonators at higher frequencies. This lessens the requirement. Often, it also leads to lower quality factors thereby reducing the vacuum requirement even further. Conversely, this highlights one of the difficulties working with low frequency high quality factor resonators.

4.2 Intrinsic damping

Intrinsic losses are all the losses which are a direct consequence of the oscillations of strains and stress inside the resonator itself. While it is tempting to describe it all as internal friction losses, there exists also fundamental loss mechanisms, which set a lower limit on the achievable intrinsic losses even for idealized materials. When designing resonators with ultra high quality factors one ultimately ends up with a device which is limited by intrinsic losses. A proper understanding of the mechanisms behind it is therefore crucial for engineering the best possible resonator.

A good reference which lists all the relevant intrinsic loss mechanisms is [7]. Intrinsic loss mechanisms can largely be divided into two types: Friction losses and fundamental losses. In the following these will be discussed based on the existing literature as well as how high static tensile stress can be used to push the intrinsic loss limited quality factors to ultra high values.

4.2.1 Friction losses

Consider an infinitesimal small element consisting of a spring and in parallel another spring connected via a dashpot as illustrated on Figure 4.1a. This is known as the Zener model and is used to describe the internal friction of anelastic materials [9]. By evaluating the force balances for a harmonic excitation one can derive the stress-strain relation of the form

$$\sigma = \varepsilon \mathbf{E} \approx \varepsilon E (1 + i\tilde{\phi}(\omega)) , \quad (4.10)$$

where the loss angle $\tilde{\phi}$ is given by

$$\tilde{\phi}(\omega) = \Delta_E \frac{\omega\tau}{1 + \omega^2\tau^2} , \quad (4.11)$$

and where $\tau = \eta/E_2$ and $\Delta_E = E_2/E_1$ are the relaxation time and relaxation strength, respectively. A frequency dependence can be observed with a characteristic peak at τ^{-1} plotted on Figure 4.1b. The above are also known as Debye equations, but in this case rewritten assuming small damping. Generally, materials can be expected to have multiple peaks. This can lead to a situation where the total sum of all the contributions may lead to an effectively frequency independent loss angle [10]. Note, the intrinsic quality factor of a material at low losses is related to the loss angle via $Q_{\text{int}} = \tilde{\phi}^{-1}$.

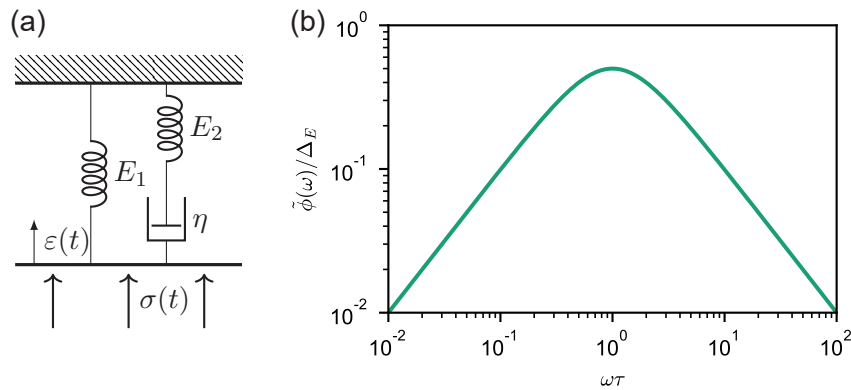


Figure 4.1: (a) Illustration of the Zener model used to describe the internal friction of anelastic materials. (b) Debye functions plotted.

4.2.1.1 Two-level-systems and temperature dependence

The underlying mechanism behind the intrinsic losses in silicon nitride and other amorphous materials have shown evidence for being dominated by two-level-systems [11, 12].

Generally these arise from various defects inside the material. Examples of this include dislocations in crystalline materials, grain boundary slipping and molecular chain movement. Defects are omnipresent in amorphous materials. The defects enable energy transfer from the resonator modes into the thermal bath via a three-particle scattering process illustrated on Figure 4.2. They can be described as a double-well potential separated by an energy barrier and possibly with an asymmetry between the two wells. At low temperatures these can be modelled as two-level-systems. These give rise to maxima in vibration absorption at specific temperatures T and frequencies ω .

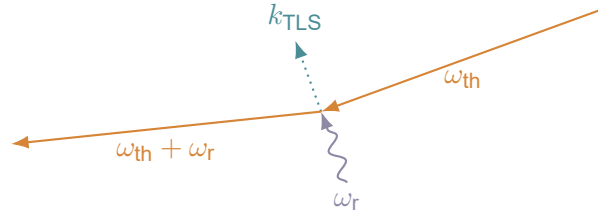


Figure 4.2: A depiction of how a two-level-system defect (dotted green) can introduce the momentum necessary for three-particle scattering. The high-frequency ω_{th} short-wavelength thermal phonons (solid red) can easily enter and exit the resonator. These can couple to the low frequency ω_{th} resonator phonons (wavy purple) via the defect, thereby creating a loss channel for the resonator phonons to dissipate out to the external environment.

What are the sources of these defects for silicon nitride? In [12] two sources were identified and their respective responses plotted on Figure 4.3. There is one occurring at 50 K which is similar to the observed value of another amorphous material, silica. The defects in this case are spread over a distribution of different energy barriers and well asymmetries. The total damping can be estimated by integrating over all these infinitesimal contributions leading to

$$\phi_{\text{amorph}}(\omega, T) = C\Phi\left(\frac{\sqrt{2}T}{\Delta_C}\right) \frac{1}{T} \int_0^\infty \left(\frac{V}{V_0}\right)^{-\zeta} e^{-\frac{V^2}{2V_0^2}} \frac{\omega\tau(T)}{1 + \omega^2\tau^2(T)} dV, \quad (4.12)$$

where $\Phi(\dots)$ is the error function, V is the energy barrier, $\zeta = 1/4$ is a distribution dependent parameter, V_0 and Δ_C are cutoff parameters for the energy barrier and well asymmetry, and $\tau(T) = \tau_0 e^{V_0/T}$ is the temperature dependent relaxation time. Note $\{V, V_0, \Delta_C\}$ are given in units of temperature.

The other peak is at 200 K and identified as an Arrhenius peak. It is believed this is caused by hydrogen defects incorporated into the silicon nitride film during deposition. This holds true even for the very clean low-pressure chemical vapor deposition approach. The Arrhenius peak can be modeled using Eq. (4.11) with the temperature dependent relaxation time $\tau \rightarrow \tau(T) = \tau_0 e^{V_0/T}$. The temperature dependence of both contributions are shown on Figure 4.3. It is obvious and illustrated on Figure 4.3 that two-level-system damping can be reduced by cooling the resonator down to low temperatures.

The discussed defects exist in bulk silicon nitride. Additionally, the surface has shown to have significant impurities consisting of oxygen and carbon [13]. Cleaning using hydrofluoric acid was demonstrated to be unable to remove these impurities, and it was concluded these impurities are ubiquitous for silicon nitride films. Furthermore, the same paper concluded cleaning using hydrofluoric acid also leaves fluorine impurities on the surface with some reports of the quality factor being generally lower as a result. On the other hand,

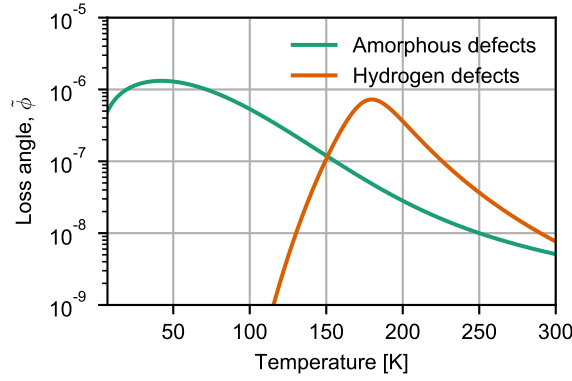


Figure 4.3: Temperature dependence of the amorphous and hydrogen defects in silicon nitride. Note, there will be other intrinsic damping contributions not shown here which sets a lower bound on the losses. The parameters used are given by [12].

there are evidence for a significant part of the surface losses is likely attributed to oxidation of the silicon nitride surface. This is formed naturally under atmospheric conditions [14] and can be further enhanced when exposed to oxygen plasma [15]. Comparisons of quality factors before and after oxygen stripping using hydrofluoric acid showed an improvement of 10 % for some time after the oxygen strip [16, 17], which hints at a significant amount of oxides on the surface. Although it seems the cited papers contradict each other when considering oxidized surface of silicon nitride and its damping contribution, it is speculated the studies of the former paper performed their measurements too long after the oxide strip, and therefore did not observe any quality factor improvement.

4.2.2 Thin-film loss model

As mentioned before, there are enhanced damping occurring at the surfaces of silicon nitride (and other materials, too). The loss angle of a material film with layer thickness h can be written as a sum of the volume $\tilde{\phi}_{\text{vol}}$ and surface $\tilde{\phi}_{\text{surf}}(h)$ contributions [13]

$$\tilde{\phi}(h) = \tilde{\phi}_{\text{surf}}(h) + \tilde{\phi}_{\text{vol}} \quad (4.13)$$

where

$$\tilde{\phi}_{\text{surf}}(h) = \frac{6\tilde{\phi}_{\text{surf},0}\delta_{\text{surf}}}{h} \quad (4.14)$$

and where $\tilde{\phi}_{\text{surf},0}$ is the loss angle of the lossy surface layer and δ_{surf} its layer thickness. Assuming its main contribution is oxidation the layer thickness will only be a few nanometers [14]. For experimental derived values it is beneficial to combine the two parameters into one, i.e.

$$\tilde{\phi}_{\text{surf}}(h) = \frac{1}{h\beta_{\phi}} \quad , \quad \text{where} \quad \beta_{\phi} \equiv \frac{1}{6\tilde{\phi}_{\text{surf},0}\delta_{\text{surf}}} \quad (4.15)$$

Eq. (4.13) is plotted on Figure 4.4 for experimentally derived values of silicon nitride. The majority of the work in this project is focused on resonators with a maximum thickness of 50 nm, which is well within the surface loss dominated regime. Therefore, the volume contribution will be ignored for the rest of the thesis unless otherwise stated.

4.2.3 Fundamental losses

There are two types of fundamental losses present in micromechanical resonators: Thermoelastic damping and Arkhiezer damping. They are fundamental as in they exist even

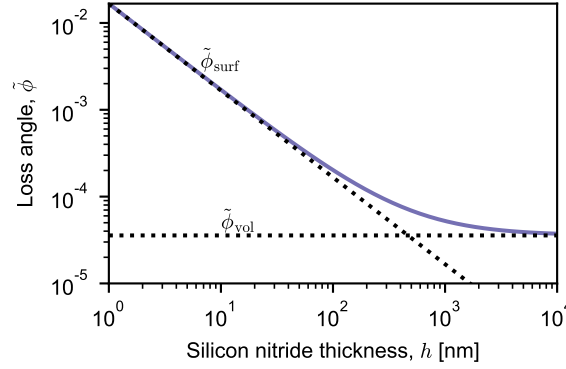


Figure 4.4: The effective loss angle vs thickness of a silicon nitride membrane when including the added intrinsic damping from surface impurities at room temperature. Plotted with $\beta_\phi = 6 \times 10^{10} \text{ m}^{-1}$ and $\tilde{\phi}_{\text{vol}} = 3.57 \times 10^{-5}$.

for the hypothetical case of pure defect-free materials. They are both irreversible heat flow processes and can be modeled using Eq. (4.11).

During transversal bending one side of the material will compress while the other side expands. Since the strain field is coupled to the temperature field via the thermal expansion coefficient the sides will experience heating and cooling, respectively. This will create a non-reversal heat flow and eventually lead to losses as illustrated on Figure 4.5a. Using the Debye equations the relaxation strength and time for thermoplastic damping for a beam given by [18]

$$\Delta_{\text{TED}} = \frac{E\alpha_{\text{th}}^2 T}{\rho c_p}, \quad \tau_{\text{TED}} = \frac{h^2}{\pi^2 \chi}, \quad (4.16)$$

where E , h , ρ , c_p are the beam's thickness, Young's modulus, density and specific heat capacity, respectively. $\chi = \kappa/(\rho c_p)$ is the thermal diffusivity, where κ the thermal conductivity.

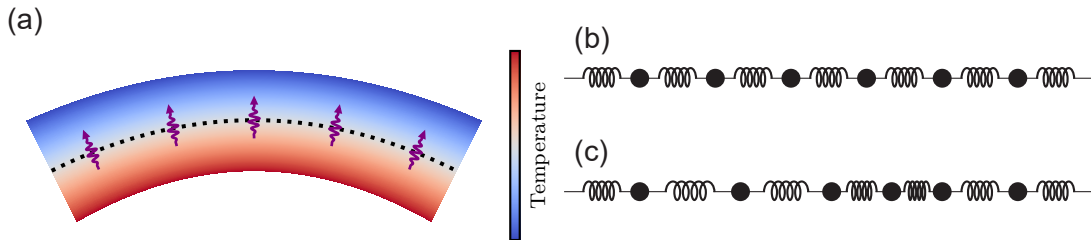


Figure 4.5: Illustration of the two fundamental loss mechanisms for micromechanical resonators. (a) Thermoelastic damping where bending creates temperature gradients due to the thermal expansion coefficient leading to irreversible heat flow. (b) An array of coupled atoms at rest. (c) An array of coupled atoms perturbed by a vibrational mode.

The Akhiezer damping, also known as the Akhiezer effect, is a quantum mechanical phenomenon [19]. It is often referred to as the quantum limit of the possible Qf -products obtainable in micromechanical oscillators. The mechanism is illustrated on Figure 4.5b and c. Consider an array of atoms. These have a discrete set of vibration modes of phonons, each defined by their wavelength λ , frequency ω and momentum $k = 2\pi/\lambda$. When the system is in equilibrium the modes are populated according to the Planck distribution. On the other hand, when the whole system is subject to longitudinal elastic vibration a

periodic distortion of the arrangement of atoms will occur. This changes the dispersion relation locally. Extension leads to a reduction of the slope in the dispersion relation while compression leads to an increase. The magnitude of this effect is characterized by the Grüneisen parameter γ . During the distortion the population of the phonon modes no longer follow the Planck distribution. This leads to inelastic phonon-phonon scattering processes to redistribute the population until a new thermal equilibrium is reached. It is therefore also known as phonon-phonon interaction loss. Using the Debye equations the relaxation strength and time for Akhiezer damping is given by

$$\Delta_{\text{AKE}} = \frac{\gamma^2 c_p \rho T}{E}, \quad \tau_{\text{AKE}} = \frac{3\kappa}{c_p E}. \quad (4.17)$$

For silicon nitride $\gamma = 1.2$ [20]. At low frequencies this leads to a maximum $Qf \approx 3 \times 10^{14}$ Hz for silicon nitride. Generally speaking, thermoelastic losses are only significant for thicker devices and are thus expected to be negligible. Therefore, Akhiezer damping can here be considered as the ultimate limit for obtainable quality factors.

4.2.4 Quality factor from intrinsic losses

Recall that for determining the quality factor of a resonator the mode energy and losses need to be defined. When the complex Young's modulus is known the losses can easily be derived by considering the energy stored in the time-varying part of the stress-strain fields [9]. In case of beams and plates this is simply the energy related to the bending. Starting from strains ε_{ij} and stress σ_{ij} and assuming harmonic vibrations, i.e. $\{\varepsilon_{ij}, \sigma_{ij}\} \rightarrow \{\varepsilon_{ij}, \sigma_{ij}\} e^{-i\omega t}$ the potential energy density w is given by

$$w = \sum_{i,j} \frac{1}{2} \varepsilon_{ij} \sigma_{ij} = E \sum_{i,j} \frac{1}{2} \varepsilon_{ij}^2 \quad (4.18)$$

and the total energy is then given by integrating across the whole resonator, i.e.

$$W_{\text{bend}} = \int_V w \, dV = \int_V \left(\sum_{i,j} \frac{1}{2} E \varepsilon_{ij}^2 \right) dV. \quad (4.19)$$

For a two-dimensional thin plate there are no significant strains in the z direction. Based on the results in section 3.2 the summation over strains be rewritten into

$$\begin{aligned} W_{\text{bend}} &= \iiint \frac{1}{2} \frac{E}{1-\nu^2} z^2 \left(\frac{\partial^2 u}{\partial x^2} + \frac{\partial^2 u}{\partial y^2} \right)^2 dx dy dz \\ &= \iint \frac{1}{24} \frac{E h^3}{1-\nu^2} \left(\frac{\partial^2 u}{\partial x^2} + \frac{\partial^2 u}{\partial y^2} \right)^2 dx dy, \end{aligned} \quad (4.20)$$

where $E \rightarrow E/(1-\nu^2)$ was used to include the enhanced stiffness in plates. The energy lost per oscillation can then be defined as

$$\Delta W_{\text{bend}} = 2\pi W_{\text{bend}} \tilde{\phi} = \iint \frac{\pi \tilde{\phi}}{12} \frac{E h^3}{1-\nu^2} \left(\frac{\partial^2 u}{\partial x^2} + \frac{\partial^2 u}{\partial y^2} \right)^2 dx dy. \quad (4.21)$$

Combined with the total resonator energy defined in Eq. (4.7) the quality factor for the intrinsic losses can be defined using Eq. (4.1). Note, for strings the $1-\nu^2$ denominator is removed.

4.2.5 Damping dilution using high tensile stress

Verbridge et al. discovered back in 2006 that the high tensile stress of low-pressure chemical vapor deposited silicon nitride had the property of boosting the quality factor of beams by orders of magnitude [5]. In the following years this phenomenon was investigated which culminated in 2011 by Schmid et al. with a satisfying description of the physics behind [21]. By considering the relevant energies in a high tensile stress string or membrane the quality factor can be defined as

$$Q = 2\pi \frac{W_{\text{bend}} + W_{\text{elon}} + W_{\text{tension}}}{\Delta W_{\text{bend}} + \Delta W_{\text{elon}}} , \quad (4.22)$$

where W_{tension} is the stored elastic energy required to deflect the string against the tensile force, and the 'elon' subscripts indicate the energy and losses related to the in-plane elongation of the string or membrane. It was already established in section 3.1 the coupling between the elongation and transversal movement is nonlinear and can be ignored for small displacements. It is therefore ignored in the following. At high tensile stress W_{bend} will be small compared to W_{tension} , thus the above can be reduced to

$$Q \approx 2\pi \frac{W_{\text{tension}}}{\Delta W_{\text{bend}}} = \left(1 + \frac{W_{\text{tension}}}{W_{\text{bend}}}\right) Q_{\text{bend}} , \quad (4.23)$$

where Q_{bend} is the quality factor in the absence of tensile stress. It is clear from the above the high tensile stress creates a large lossless energy contribution that dilutes the lossy bending part of the total energy. For this to work it is important that the tensile stress plays an active role in enhancing the energy of the mode. Just the mere presence of tensile stress is not enough [22]. For example, the stiffness of the twisting mode of a string is not significantly affected by tensile stress and thus no damping dilution is achieved.

4.2.6 Intrinsic losses on typical resonators

To further understand the effect of tensile stress in resonators some basic resonator types will be studied. The mode energy and intrinsic losses are based on the mode shapes defined in appendix B. The damping is defined from Eq. (4.21).

4.2.6.1 String

The string is a simple resonator, yet it still clearly illustrates the important physics valid for all tensile stress thin-film resonators. Consider a string of length L and width b . The bending loss distribution

$$\Delta w_{\text{bend}}(x) = \frac{\pi \tilde{\phi}}{12} E h^3 b \left(\frac{\partial u^2}{\partial x^2} \right)^2 \quad (4.24)$$

is plotted on Figure 4.6. Two distinct regions can be defined. At the outermost boundaries an extremely narrow but highly lossy region is found, which is a result of the evanescent part of the mode shape with the characteristic length $1/k_e$. The loss associated with the extreme bending along the boundary is known under a number of names: Clamping losses, anchoring losses and boundary losses. For this thesis a name is chosen to minimize confusion with other loss mechanisms and make its usage clear: *Boundary bending losses*.

Far away from the boundary, another type of mode shape dependent loss can be observed. The sinusoidal mode shape inherently includes bending which peaks at the anti-nodes. Higher mode indices will result in more tightly-squeezed sinusoidal bending thereby increasing the overall bending losses. The bending far away from the boundary will be named *distributed bending losses* largely inspired by [22]. This distinction between the two mode shape dependent bending loss types is important, as this will lead to different quality factor optimization strategies depending on which of the two is dominating.

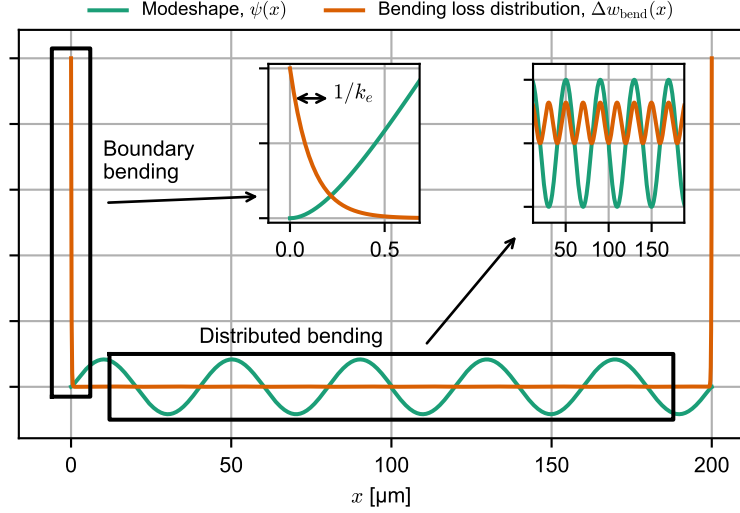


Figure 4.6: Mode shape and bending loss distribution of a string with high tensile stress. The insets zoom in on the marked bending losses. Plotted with $n = 10$, $L = 200 \mu\text{m}$, $\sigma = 1 \text{ GPa}$ and $h = 50 \text{ nm}$. Note the y-scales are arbitrarily scaled for the two functions in order highlight important aspects of bending losses.

Obtaining the total bending losses ΔW_{bend} by integrating Eq. (4.24) results in

$$\Delta W_{\text{bend}} = \Delta W_{\text{bound}} + \Delta W_{\text{dist}}, \quad (4.25)$$

where ΔW_{bound} and ΔW_{dist} are the boundary and distributed bending losses, respectively, defined as

$$\begin{aligned} \Delta W_{\text{dist}} &= \int_0^L \frac{\pi \tilde{\phi}}{12} E h^3 b \left(\frac{\partial^2}{\partial x^2} (u_n \sin kx) \right)^2 dx = \frac{\pi^5 n^4 E h^3 b \tilde{\phi}}{24 L^3} u_n^2 \\ \Delta W_{\text{bound}} &\approx 2 \int_0^\infty \frac{\pi \tilde{\phi}}{12} E h^3 b \left(\frac{\partial^2}{\partial x^2} \left(u_n \frac{k}{k_e} e^{-k_e x} \right) \right)^2 dx = \frac{\pi^3 n^2 h^2 b \tilde{\phi}}{L^2} \sqrt{\frac{\sigma E}{12}} u_n^2 \end{aligned} \quad (4.26)$$

When combined with the mode energy defined in Eq. (B.3) the quality factor takes the following form

$$Q_{\text{int}} = (Q_{\text{dist}}^{-1} + Q_{\text{bound}}^{-1})^{-1} \quad (4.27)$$

where the quality factor contributions of the boundary and distributed bending losses, respectively, are defined as

$$Q_{\text{dist}} = \frac{12}{(\pi n)^2} \frac{\sigma}{E} \left(\frac{L}{h} \right)^2 \frac{1}{\tilde{\phi}} \quad , \quad Q_{\text{bound}} = \sqrt{\frac{3\sigma}{E}} \frac{L}{h} \frac{1}{\tilde{\phi}}. \quad (4.28)$$

Looking at Q_{dist} it is observed enhancing the stress is a clear strategy for improving the quality factor, thereby confirming the expected damping dilution behavior. The same trends are observed for Q_{bound} although not as strong. This is due to the fact as the tensile stress is increased this increases k_e resulting in sharper bending at the boundary leading to higher losses. Furthermore, reducing the string thickness h results in lower bending stiffness at the boundary, which again leads to sharper bends and therefore less reduction in losses. Generally, the n dependence shows boundary bending losses are expected to dominate at low mode indices, whereas distributed bending losses dominate at high mode indices. The latter leads to more nodes in the mode shape, which reduces the curvature of the standing wave thus increases bending losses.

Now consider surface damping discussed in section 4.2.2, where $\tilde{\phi} \propto h^{-1}$. Substituting this into Eq. (4.28) leads to

$$Q_{\text{st,dist}} = \frac{12}{(\pi n)^2} \frac{\sigma}{E} \frac{L^2}{h} \beta_\phi, \quad Q_{\text{st,bound}} = \sqrt{\frac{3\sigma}{E}} L \beta_\phi. \quad (4.29)$$

In case of surface losses one can enhance the quality factor by fabricating thinner membranes if distributed bending losses dominate. On the other hand, when boundary bending losses dominate h cancels out and one therefore can no longer expect to see significant quality factor improvements by fabricating thinner membranes. This is an important result, which might not seem obvious at first.

Finally, the Qf product, where f is the frequency in Hz, is an important figure of merit for various applications including quantum optomechanics. For a string it is defined as

$$(Qf)_{\text{st,dist}} = \frac{24\sigma^{3/2}L}{nh^2E\sqrt{\rho}} \frac{1}{\tilde{\phi}}, \quad (Qf)_{\text{st,bound}} = \frac{2\pi^2 n\sigma}{h} \sqrt{\frac{3}{\rho E}} \frac{1}{\tilde{\phi}} \quad (4.30)$$

for each bending type, respectively. When limited by distributed bending losses, larger devices generally lead to higher Qf products. However, these also oscillate at a lower frequency, which leads to higher vacuum requirements (section 4.1). Furthermore, the noise from a laser light source can become an issue at very low frequencies and fabrication will become increasingly difficult. For practical reasons there will therefore be some upper limit for the size of the resonators. On the other hand, for boundary bending loss limited resonators there are no apparent size advantages in terms of Qf product.

Qualitatively, the same overall effects are present and the same conclusions can be made when deriving the intrinsic quality factor for other resonator types. Therefore, only the quality factor and Qf products will be shown and briefly discussed for the following. Due to this, the reader may skip directly to section 4.2.7 to move on to the next damping mechanism. It will be up to the reader to do the full derivation. Note, many of the underlying derivations are found in appendix B.

4.2.6.2 Trampoline

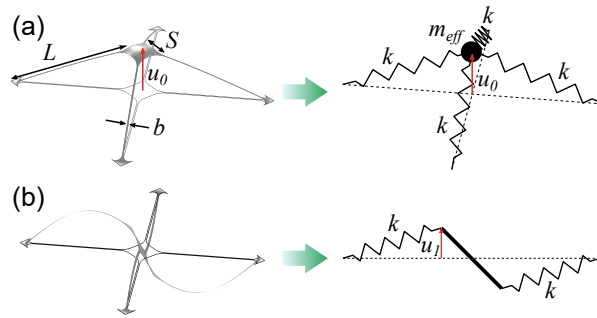


Figure 4.7: Trampoline resonator models. (a) and (b) show the fundamental and twisting modes, respectively, of a typical trampoline.

The modeshape for a trampoline cannot be solved for analytically. Instead, an approximate solution can be obtained by treating the trampoline as a mass-element connected with N tethers modeled as springs illustrated on Figure 4.7a. These springs are already prestressed which adds the crucial out-of-plane stiffness for tensile stress resonators. It is assumed the dominating contribution from intrinsic damping is the boundary bending

losses at the outer end of the tethers, i.e. the part connected to the surrounding substrate. The part connected to the central pad will not experience the same sharp bending, since that area can bend more softly. Based on this the quality factor and Qf product for the fundamental mode is given by

$$Q_{\text{tr},f} = \frac{4L}{h} \sqrt{\frac{3\sigma}{E}} \frac{1}{\tilde{\phi}} \quad , \quad (Qf)_{\text{tr},f} = \frac{24\pi\sigma}{h} \sqrt{\frac{NbL}{(NLb + 3S^2)\rho E}} \frac{1}{\tilde{\phi}} \quad , \quad (4.31)$$

which shows no thickness dependence when one assumes surface losses. While Q shows a result similar to the boundary bending loss limited string, Qf favors smaller pads or wide strings to minimize the drop in eigen-frequency due to the added mass from the pad. For completeness sake, the twisting mode of a trampoline is also shown when assuming $N = 4$ tethers. The twisting mode usually has a much higher eigen-frequency thus the assumption of a straight unbend tether starts to break down as seen on Figure 4.7b. Nevertheless, it provides a rough analytical solution. Q and Qf are given by

$$Q_{\text{tr},t} = Q_{\text{tr},f} \quad , \quad (Qf)_{\text{tr},t} = \frac{48\pi\sigma}{h} \sqrt{\frac{bL}{(4bL + S^2)\rho E}} \frac{1}{\tilde{\phi}} \quad , \quad (4.32)$$

which largely shows the same results.

4.2.6.3 Circular and rectangular membranes

Considering a circular membrane of radius a leads to the quality factors

$$Q_{\text{ci},\text{dist}} = \frac{12a^2\sigma(1-\nu^2)}{\Theta_{mn}bh^2E} \frac{\alpha_m}{\tilde{\phi}} \quad , \quad Q_{\text{ci},\text{bound}} = \frac{aJ_{m+1}^2(\Theta_{mn})}{hb} \sqrt{\frac{12\sigma(1-\nu^2)}{E}} \frac{\alpha_m}{\tilde{\phi}} \quad , \quad (4.33)$$

where

$$\alpha_m = \begin{cases} 2 & , \quad m = 0 \\ 1 & , \quad m > 0 \end{cases} \quad . \quad (4.34)$$

and where m and n are the angular and radial mode indices, respectively, and Θ_{mn} is the n 'th root of $J_m\Theta$. The Qf product is then defined as

$$\begin{aligned} (Qf)_{\text{ci},\text{dist}} &= \frac{24\pi\sigma^{3/2}a(1-\nu^2)}{\Theta_{mn}bh^2E\sqrt{\rho}} \frac{\alpha_m}{\tilde{\phi}} \\ (Qf)_{\text{ci},\text{bound}} &= \frac{4\pi\Theta_{mn}J_{m+1}^2(\Theta_{mn})\sigma}{hb} \sqrt{\frac{3(1-\nu^2)}{\rho E}} \frac{\alpha_m}{\tilde{\phi}} \end{aligned} \quad . \quad (4.35)$$

Likewise for a rectangular membrane with side lengths L_x and L_y in the x and y directions, respectively, the quality factors are given by

$$Q_{\text{re},\text{dist}} = \frac{12(1-\nu^2)\sigma}{\pi^2 \left(\frac{n_x^2}{L_x^2} + \frac{n_y^2}{L_y^2} \right) h^2E} \frac{1}{\tilde{\phi}} \quad , \quad Q_{\text{re},\text{bound}} = \frac{\left(\frac{n_x^2}{L_x^2} + \frac{n_y^2}{L_y^2} \right) (1-\nu^2)}{h \left(\frac{n_x^2}{L_x^3} + \frac{n_y^2}{L_y^3} \right)} \sqrt{\frac{3\sigma}{E}} \frac{1}{\tilde{\phi}} \quad (4.36)$$

and their Qf products

$$\begin{aligned} (Qf)_{\text{re},\text{dist}} &= \frac{24(1-\nu^2)}{Eh^2} \sqrt{\frac{\sigma^3}{\left(\frac{n_x^2}{L_x^2} + \frac{n_y^2}{L_y^2} \right) \rho}} \frac{1}{\tilde{\phi}} \\ (Qf)_{\text{re},\text{bound}} &= \frac{2\pi^2(1-\nu^2)\sigma}{\left(\frac{n_x^2}{L_x^3} + \frac{n_y^2}{L_y^3} \right) h} \sqrt{\frac{3 \left(\frac{n_x^2}{L_x^2} + \frac{n_y^2}{L_y^2} \right)^3}{\rho E}} \frac{1}{\tilde{\phi}} \end{aligned} \quad . \quad (4.37)$$

The results and the conclusions which can be drawn are similar to the string.

4.2.7 Concluding remarks on intrinsic losses

The use of Zener's model and the Debye equations derived from it provides a simple framework for describing the intrinsic losses occurring in various materials. While the fundamental losses, namely the Akhiezer damping, sets the ultimate limit on the quality factors obtainable in a resonator, there have been no reports of any resonators being limited by this mechanism for tensile stress thin-film resonators. The omnipresence of defects in amorphous materials, and especially the presence of surface impurities, seems to be the ultimate limiting factor when reducing the losses. While the focus here and in most of the field in general has been on silicon nitride, it could be worthwhile to look for other materials which do not observe the same degree of surface impurities. Silicon carbide has demonstrated intrinsic bulk quality factors above 10^5 in cantilevers [23] which is roughly an order of magnitude higher than for silicon nitride [13], although demonstrating this in trampolines have not yet resulted in high performing resonators [24] compared to similar silicon nitride based trampolines [25]. Obtaining a high quality silicon carbide layer for use in thin film tensile stress resonators seems nontrivial. Other materials showing high bulk quality factors above 10^5 include diamond, where cantilevers have been reported to preserve their high quality factors down the nm scale [26, 27] as well as calcium fluoride [28], although the latter has not been explored much yet.

One issue which I did not find a clear answer on is does the damping dilution effect dilute the fundamental loss mechanisms just as it clearly does for friction losses? Since the Akhiezer damping is presented as the quantum limit for obtainable Qf products it is tempting to conclude this is true regardless of the presence of tensile stress. However, recent results have shown silicon nitride resonators with $Qf = 1.1 \times 10^{15}$ [29], which is considerably above the limit predicted Akhiezer damping. Clearly, the limit can be broken, and it seems likely to believe it is due to the damping dilution effect. This has huge implications. For example, the Akhiezer damping for diamond defined at $Qf \approx 4 \times 10^{13}$ is nearly an order of magnitude lower than for silicon nitride. The knowledge that Akhiezer damping can be suppressed using damping dilution opens up the use of potentially a long list of alternative materials in ultra-coherent resonators.

Finally, studying the eigen-modes of a string under tensile stress reveals the damping dilution phenomenon, as well how the damping can be categorized into two mode-shape defined types: Distributed and boundary bending losses. Boundary bending losses are defined by their sharp bending along the resonator-substrate boundary and will dominate for resonators used in the fundamental or other low mode index. When surface damping is assumed, which is usually the case, boundary bending loss limited devices show no quality factor improvement when fabricating thinner resonators unlike their distributed bending loss limited counterpart. Similar conclusions can be drawn with other thin-film tensile stress resonator designs.

4.3 Phonon tunneling loss

Phonon tunneling losses are the phonons (or simply vibrations) which couple to the surrounding substrate and may lead to losses. Depending on how this mechanism is described, some of the vibrations can couple back into the resonator, or everything is lost to the external environment. This loss mechanism is in the field also known under a broad range of other names: Radiation losses, clamping losses, anchoring losses and external losses. The name phonon tunneling loss was inspired by [30] and chosen as it creates the least confusion of its meaning and applicability.

For membranes operating at few MHz and below this mechanism is poorly understood. Analytical studies have been conducted for resonators at multiple MHz and above [31,

32, 30]. In their work it is assumed the substrate vibrations primarily consist of longitudinal, transverse in-plane and surface waves. This is not a valid assumption at the lower frequencies, which are often seen for silicon nitride membranes, where transverse out-of-plane vibrations in the substrate are expected to dominate. As the stiffness of the latter is dependent on the substrate stiffness, a failure to include it will lead to incorrect results for especially thinner substrates. For example, a trampoline embedded with photonic crystals showed strong dependence on substrate thickness at ~ 100 kHz [25].

This section will derive phonon tunneling losses for two different cases: An infinite substrate and a finite substrate. The derivations will be based on Kirchhoff-Love plate theory to describe the transversal out-of-plane vibrations and is valid for wavelengths longer than six times the substrate thickness [6]. This corresponds to Eq. (3.17) without the tensile stress term. It is possible to extend this range when working with Mindlin plate theory [33] instead. The purpose of this derivation is to highlight important aspects for resonators used throughout the thesis. In that case, the simpler Kirchhoff-Love plate theory is sufficient. Most of the focus of the PhD has been on fundamental mode resonators and will therefore be the focus for the derived solutions. In general, both derivations can be extended for higher resonator modes. In fact, the infinite substrate case is an easy theoretical approach to work with, as will be obvious. It will therefore be extended to any arbitrary resonator modes. Finally, different approaches used by other groups for minimizing phonon tunneling losses will be briefly introduced and discussed.

4.3.1 Infinite sized substrates

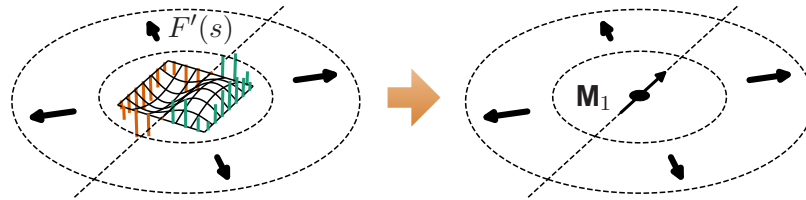


Figure 4.8: Illustration of the infinite substrate model. The boundary shear force distribution $F'(s)$ (shown as vertical lines) of a membrane placed on a substrate is integrated and an equivalent point-source excitation (in this example, a dipole with moment \mathbf{M}_1) is estimated. The dashed lines represent zero displacement lines for the radiating wave.

Consider a resonator with dimensions $700 \times 700 \mu\text{m}^2$ with a fundamental mode at 200 kHz placed on a $h_s = 500 \mu\text{m}$ thick silicon substrate with the parameters. Using Eq. (3.24) the wavelength in the substrate would then be $\lambda_s = 2\pi/k_s \approx 6.4$ mm. Since the wavelength is much longer than the membrane dimensions its shear force distribution along the resonator-substrate boundary can to a good approximation be considered as a point force on the substrate at point (x_F, y_F) . This is illustrated on Figure 4.8. The shear forces along the membrane-substrate boundary are treated as an external excitation on the substrate itself. In the following sections the possible solutions of an m -pole point source is explored and how the quality factor can be estimated is presented.

4.3.1.1 Solution of an m-pole point source

The general solution of a vibrating plate in polar coordinates is given by [34]

$$\begin{aligned}
 w_m(r, \theta) = & [A_{1m}J_m(k_s r) + A_{3m}Y_m(k_s r) \\
 & + B_{1m}I_m(k_s r) + B_{3m}K_m(k_s r)] \sin m\theta \\
 & + [A_{2m}J_m(k_s r) + A_{4m}Y_m(k_s r) \\
 & + B_{2m}I_m(k_s r) + B_{4m}K_m(k_s r)] \cos m\theta ,
 \end{aligned} \tag{4.38}$$

where r and θ are the radial and angular coordinates respectively and $\{A_{nm}, B_{nm}\}$ are constants to be determined. J_m , Y_m , I_m and K_m are Bessel functions of the first kind, second kind, modified first kind, and modified second kind, respectively. To solve for the constants the following conditions are given:

- For $m = 0$ the slope must be zero at the excitation point, e.g. $\partial w_0(0, \theta)/\partial r = 0$.
- For $m > 0$ the displacement must be zero at excitation point, e.g. $w_{m>0}(0, \theta) = 0$.
- Sommerfeld's radiation condition, i.e. the displacement must decay when $r \rightarrow \infty$.
- At the excitation point the of shear forces must equal the external drive force.

Applying all but the last condition yields a solution of the form

$$\begin{aligned}
 w_m(r, \theta) = & \left[J_m(k_s r) - iY_m(k_s r) - i\frac{2}{\pi}K_m(k_s r) \right] \\
 & \cdot (w_{mc} \cos m\theta + w_{ms} \sin m\theta) ,
 \end{aligned} \tag{4.39}$$

where w_{mn} are constants depending on the distribution of the external drive force. The shear force along the angular direction is given by

$$F'_m(r, \theta) = B'_s \frac{\partial}{\partial r} \nabla^2 w_m(r, \theta) . \tag{4.40}$$

Assuming the external drive force $F'_e(\theta)$ is applied on a circle at $r = r_e$, this can be related to the above solution using the superposition of solutions

$$F'_e(\theta) = \sum_{m=0}^{\infty} F'_m(r_e, \theta) . \tag{4.41}$$

The displacement amplitudes w_m can be estimated for each m by integrating along the the angular direction for any external drive force distribution at $r = r_e$. To evaluate w_{mn} it is advantageous to use the asymptotic limits of the Bessel functions valid for $r_e k_s \ll 1$:

$$\begin{aligned}
 J_m(x) & \approx \frac{1}{\Gamma(m+1)} \left(\frac{x}{2}\right)^m \\
 Y_m(x) & \approx -\frac{\Gamma(m)}{\pi} \left(\frac{2}{x}\right)^m , \quad K_m(x) \approx \frac{\Gamma(m)}{2} \left(\frac{2}{x}\right)^m
 \end{aligned}$$

By using the above approximations and substituting Eq. (4.39) into (4.41), multiply with $\sin m\theta$ or $\cos m\theta$, integrating with respect to $\theta \in [0, 2\pi]$ and utilizing the orthogonality of substrate modes one obtains

$$\begin{aligned}
 w_0 \equiv w_{0c} & = \frac{1}{i8B'k_s^2} M_0 , \quad w_{0s} = 0 , \quad m = 0 \\
 \begin{bmatrix} w_{mc} \\ w_{ms} \end{bmatrix} & = \frac{k_s^{m-2}}{i2^{m+1}\Gamma(m+1)B'} \begin{bmatrix} M_{mc} \\ M_{ms} \end{bmatrix} , \quad m > 0
 \end{aligned} \tag{4.42}$$

where M_{mi} are the force moments. The zeroth order corresponds to a monopole and is simply the summation of all the forces

$$M_0 \equiv \int_0^{2\pi} F'_e(\theta) r_e d\theta, \quad (4.43)$$

and for higher order moments its defined as

$$\begin{bmatrix} M_{mc} \\ M_{ms} \end{bmatrix} \equiv \int_0^{2\pi} F'_e(\theta) r_e^m \begin{bmatrix} \cos m\theta \\ \sin m\theta \end{bmatrix} r_e d\theta \quad (4.44)$$

It can be seen the moment definitions can be extended to any two dimensional driving force distribution $f_e(r, \theta)$:

$$M_0 \equiv \iint f_e(r, \theta) r dr d\theta, \quad m = 0 \quad (4.45)$$

$$\begin{bmatrix} M_{mc} \\ M_{ms} \end{bmatrix} \equiv \iint f_e(r, \theta) r^m \begin{bmatrix} \cos m\theta \\ \sin m\theta \end{bmatrix} r dr d\theta, \quad m > 0$$

Note it is increasingly difficult to excite substrate waves of higher order moments for small mechanical resonators due to the r^m dependence. Finally, it can be convenient to express the displacement field as

$$w_m(r, \theta) = \bar{w}_m \left[J_m(k_s r) - i Y_m(k_s r) - i \frac{2}{\pi} K_m(k_s r) \right] \cdot \cos(m\theta + \phi), \quad (4.46)$$

where $\bar{w}_m \equiv \sqrt{w_{mc}^2 + w_{ms}^2}$ and $\phi \equiv \tan^{-1} \frac{w_{ms}}{w_{mc}}$. The above form can be used to describe any radiated displacement field for any distribution of external driving force.

4.3.1.2 Radiated power and Q-factor estimation

With the radiative displacement field defined it is possible to quantify the total power that is coupled to the substrate and lost. When evaluating the displacement field $w_m(r, \theta)$ far away from the excitation point the wave can be treated as a plane wave. The total power transmitted a distance r away is given by

$$P_{PTL\infty} = 2 \frac{\omega}{k_s} \int_0^{2\pi} \epsilon_{\text{kin}}^{\text{max}}(r, \theta) r d\theta, \quad (4.47)$$

where $\epsilon_{\text{kin}}^{\text{max}}(r, \theta) = \frac{1}{2} \rho h_s \omega^2 |w(r, \theta)|^2$ is the energy distribution at r . Substituting $w(r, \theta) = \sum_{m=0}^{\infty} w_m(r, \theta)$ and noting the fact the $w_m(r, \theta)$ solutions are orthogonal yields

$$P_{PTL\infty} = \frac{\omega^3 \rho_s h_s}{k_s} r \int_0^{2\pi} \sum_{m=0}^{\infty} |w_m(r, \theta)|^2 d\theta. \quad (4.48)$$

Using the far-field asymptotic limit of the Bessel functions

$$J_m(x) \approx \sqrt{\frac{2}{\pi x}} \cos \left(x - \frac{m\pi}{2} - \frac{\pi}{4} \right) \quad (4.49)$$

$$Y_m(x) \approx \sqrt{\frac{2}{\pi x}} \sin \left(x - \frac{m\pi}{2} - \frac{\pi}{4} \right), \quad (4.50)$$

the resulting radiated power is then

$$P_{PTL\infty} = \sum_{m=0}^{\infty} P_{PTL\infty, m}, \quad P_{PTL\infty, m} = \begin{cases} \frac{4\omega^3 \rho_s h_s}{k_s^2} |\bar{w}_0|^2, & m = 0 \\ \frac{2\omega^3 \rho_s h_s}{k_s^2} |\bar{w}_m|^2, & m > 0 \end{cases} \quad (4.51)$$

When the radiated power is known the quality factor is then simply given by Eq. (4.1).

4.3.1.3 Solving for basic resonators

With the framework on which the phonon tunneling loss on an infinite substrate can be estimated defined, it can easily be applied on various mechanical resonators. In the following the quality factor of often used mechanical resonators are presented. For all calculations the following set of parameters are used, unless otherwise specified: $h = 50$ nm, $h_s = 500$ μ m, $\sigma = 100$ MPa, $b = 5$ μ m and $L = L_x = L_y = 2a = 700$ μ m. The derivations of the excited moments in the substrate and mode energies of the resonators are found in appendix B for each resonator type.

For a string only the zeroth and first order moments are excited. This yields the results

$$Q = \begin{cases} \frac{n\pi h_s^2}{bh} \sqrt{\frac{\rho_s E_s}{12\rho\sigma(1-\nu_s^2)}} & , n = \text{odd} \\ \frac{E_s h_s^3}{6bhL\sigma(1-\nu_s^2)} & , n = \text{even} \end{cases} \quad (4.52)$$

and plotted on Figure 4.9. Note the even modes' quality factor is independent on the mode index, and that it is independent of the string mass due to the lack of ρ . The latter can be seen on all resonators studied here which excite the first order moment. This result shows in general even modes are expected to couple worse into the substrate compared to the odd modes at low mode indices due to the vanishing zeroth order moment. This can also be seen as a result of constructive and destructive interference of the two anchor points of the string for odd and even modes, respectively.

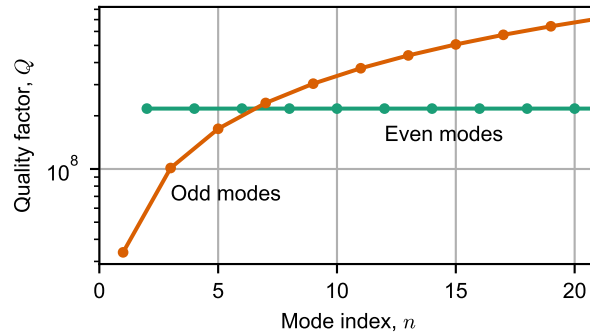


Figure 4.9: Quality factor of a phonon tunneling loss limited string vs mode index.

Following the same steps, the quality factor for the fundamental mode of a trampoline shown on Figure 4.7a is

$$Q_f = \sqrt{\frac{16h_s^4 \rho_s E_s}{3m_{\text{eff}} k_{\text{eff},f} (1 - \nu_s^2)}} \quad (4.53)$$

where ω_f , $k_{\text{eff},f}$, $m_{\text{eff},f}$ are the eigen-frequency, effective stiffness and effective mass of the trampoline's fundamental mode, respectively. For a twisting mode assuming $N = 4$ (see Figure 4.7b) the quality factor is

$$Q_t = \frac{2LE_s h_s^3}{3bh\sigma(\sqrt{2}S + 2L)^2(1 - \nu_s^2)} \quad (4.54)$$

For a trampoline with $N = 4$, $L = 425$ μ m and $S = 100$ μ m the resulting quality factors are $Q_f = 1.75 \times 10^7$ and $Q_t = 2.66 \times 10^8$. Comparing the fundamental model to the twisting mode it is again seen that the higher moment (twisting) excitation results in lower phonon tunneling losses.

For a circular membrane with radius a , and radial and angular mode index $\{n, m\}$ the quality factor is derived to be

$$Q_{mn} = \begin{cases} \frac{\Theta_{0n} h_s^2}{\pi a h} \sqrt{\frac{\rho_s E_s}{3\rho\sigma(1-\nu_s^2)}} & , m = 0 \\ \frac{2^m \Gamma^2(m+1)}{12 \cdot 3^{\frac{m}{2} - \frac{1}{2}} \pi \Theta_{mn}^{m-1}} \frac{h_s^{2+m}}{h a^{1+m}} \left(\frac{\rho_s}{\rho}\right)^{\frac{1-m}{2}} \left(\frac{E_s}{\sigma(1-\nu_s^2)}\right)^{\frac{1+m}{2}} & , m > 0 \end{cases} \quad (4.55)$$

and plotted on Figure 4.10. Θ_{mn} is the n 'th root of $J_m(\Theta)$. It can be observed that the general tendency of modes limited to exciting higher order moments increases the Q-factor of the resonator except for higher radial modes. A possible explanation for this could be the higher frequencies associated with these modes can more easily couple into the substrate as shown in equation (4.51).

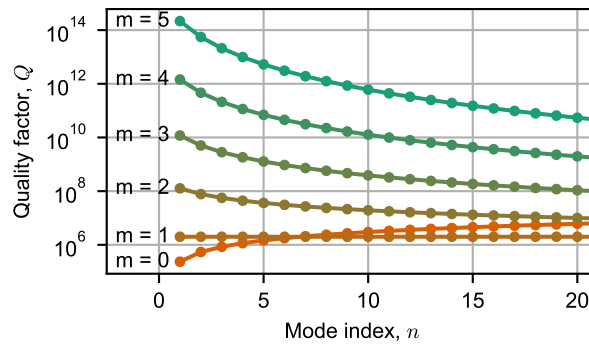


Figure 4.10: Quality factors of a circular membrane with radius $a = 350 \mu\text{m}$ for different radial n and angular m mode indices.

Next, for a rectangular membrane with the dimensions $\{L_x, L_y\}$ assuming $\frac{2}{3} \leq L_y/L_x \leq \frac{3}{2}$ the excited moment depends highly on the mode. For $n_x \cdot n_y = \text{odd}$, where n_i are the mode index in x and y directions, respectively, mainly the zeroth order moment is excited, which leads to

$$Q_0 \approx \frac{\pi^3 h_s^2 n_x^2 n_y^2}{48h} \sqrt{\frac{3\rho_s E_s}{(n_y^2 L_x^2 + n_x^2 L_y^2) \rho \sigma (1 - \nu_s^2)}} \quad (4.56)$$

For $n_x + n_y = \text{odd}$ mainly the first order moment is excited, which leads to

$$Q_1 \approx \frac{n_x^2 n_y^2 \pi^2 E_s h_s^3}{48(n_x^2 L_x^2 + n_y^2 L_y^2) \sigma h (1 - \nu_s^2)} \cdot \begin{cases} L_y/L_x & , n_x = \text{even} \\ L_x/L_y & , n_x = \text{odd} \end{cases} \quad (4.57)$$

Finally, for $n_x = \text{even}$ and $n_y = \text{even}$ mainly the second order moment is excited which leads to

$$Q_2 \approx \frac{n_x^2 n_y^2 \pi h_s^4}{18h} \sqrt{\frac{3\rho}{\rho_s}} \left(\frac{E_s}{(n_y^2 L_x^2 + n_x^2 L_y^2) \sigma (1 - \nu_s^2)} \right)^{\frac{3}{2}} \quad (4.58)$$

The results are plotted on Figure 4.12. Again, typically the modes that primarily excite the higher order moments will achieve higher Q-factors, in this case where both of the mode indices are even.

4.3.1.4 Solving for arbitrary designed resonators

Generally, there are two ways to calculate the quality factor for more complicated designs. First option is to use finite element simulations to obtain the mode shape and frequency

of the mode of interest using fixed boundary condition (i.e. no displacement and rotation). From the mode shape the shear force distribution $F'(s)$ along the boundary can be estimated. This works well for post processing an already existing result.

Another approach is to implement the infinite substrate model directly into the finite element model. When the substrate wavelength is much longer than the size of the resonator the response of the substrate can be described as a set of discretized degrees of freedom corresponding to each excitable substrate mode in Eq. (4.39). For example, the zeroth order moment can be implemented as a rigid non-bendable and non-rotatable frame around the resonator with only 1 degree of freedom in the z direction. This frame is coupled to a reference via a lossy spring with the spring constant $k_{\text{PTL}\infty,0}$ defined by Eq. (4.42), i.e.

$$k_{\text{PTL}\infty,0} = -i8B'k_s^2. \quad (4.59)$$

Note the frequency dependence of the spring will result in a nonlinear eigenvalue problem. It should be possible to extend this formulation to include higher order moments, but this was not investigated in this work.

4.3.1.5 Validation via finite element simulations

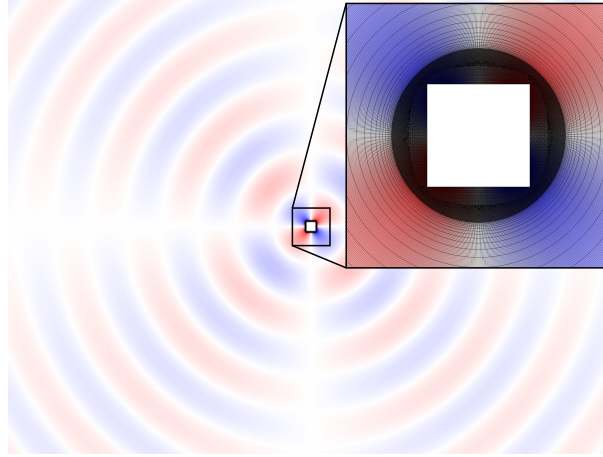


Figure 4.11: COMSOL simulation result of a radiating field for a $n_x = n_y = 2$ mode of a square membrane. The inset shows the mesh near membrane window.

The model for the infinite substrate is validated using finite elements simulations. A square membrane is investigated as this has the most rich range of possible results using the parameters defined earlier. The two dimensional plate module is used to model the substrate. Inspired by [35, 36] the outer boundary was designed to absorb all outgoing waves¹. The shear force along the boundaries of the square window are defined by Eq.(B.21) and (B.22). The results of one of the simulations can be seen on Figure 4.11. The simulated results are shown on Figure 4.12 together with the predicted analytical results.

The results for the $n_x = n_y = \text{odd}$ modes which primarily excite the zeroth order moment follow the analytical results quite well except for the highest plotted mode indices. The $n_y = n_x + 1$ modes which primarily excite the first order moment, as well as for the $n_x = n_y = \text{even}$ which primarily excite the second order moment, both have significant discrepancies at higher mode numbers. The frequency at $n_x = n_y = 10$ is ~ 2 MHz which

¹COMSOL Multiphysics as of version 5.5 has no perfectly matched layer implementation for physics described by fourth order partial differential equations. This necessitated an alternative absorbing boundary implementation.

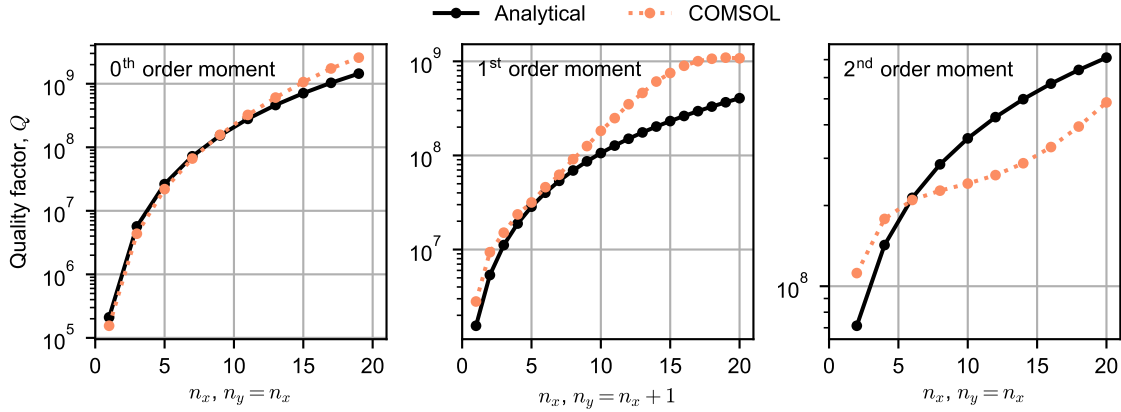


Figure 4.12: Quality factor comparisons of the analytical solution of a square membrane with COMSOL simulations. The results are divided into three plots corresponding to the dominating excited moment. The membrane has the size $L_x = L_y = 700 \mu\text{m}$.

corresponds to a substrate wavelength of 2 mm. This is only 1/4 of the substrate thickness thus the Kirchhoff-Love plate theory is expected to diverge from the true result. With a window dimension of $700 \mu\text{m}$ the point source assumption is also expected to fail. The discrepancies shown for the higher mode indices are therefore expected to be a result of breaking the two assumptions required for the analytical model.

It has been shown by obtaining the shear force distribution along membrane-substrate boundary one can derive good analytical predictions for the phonon tunneling losses for resonators placed on an infinite substrate. As long as the Kirchhoff-Love plate theory conditions are satisfied, as well as the window size is much smaller than the substrate wavelength, the analytical results are expected to give good results. The results predict that engineering modes to create destructive interference on the substrate thereby limiting the coupling to higher order moments only, can be used to enhance the phonon tunneling loss quality factor contribution by up to multiple orders of magnitude. Furthermore, the predictions clearly show a dependence on substrate thickness. This fact has to the author's knowledge not been properly discussed anywhere before, but it is essential for maximizing quality factors, especially for resonators not employing phononic crystals or other shielding designs.

The main problem with this approach is the core assumption of an infinite substrate: Resonators are often placed on small chips or finite sized wafers. These finite substrates have discrete sets of modes which can be coupled to resonantly or not at all. As will be shown in the next section this difference drastically changes the expected behavior for phonon tunneling losses.

4.3.2 Finite sized substrates

In substrates of a finite size only discrete modes can be excited. The energy transferred to the substrate then depends on the spatial and temporal overlap between the resonator mode and substrate modes. These are in turn dependent on the substrate dimensions, position on the substrates, material parameters etc.. When the resonator has a mode frequency corresponding to a high mode number of the substrate all these mentioned properties needs to be known to very high precision to ensure correct results. This is practically very difficult. Factor in each resonator that have gone through the exact same fabrication processes will not have completely identical properties, but will have frequen-

cies and mass spread around some mean values, this can lead to very different results for each resonator which is very difficult to predict. To be able to treat this problem in a systematic way a stochastic model will be developed for large, but finite substrates.

4.3.2.1 Substrate response function by eigen-function development

The coupling between the resonator and substrate can be described by treating the shear forces induced by the resonator along the resonator-substrate boundary as an external force distribution on the substrate just as for the infinite substrate case. For simplicity, the resonator-defined window in the substrate is ignored in the following derivations. The resulting response in the substrate can be determined via eigen-function development. Starting out with the Eq. (3.17) assuming no tensile stress the PDE for an eigen-function $\psi_n(x, y)$ has the form

$$B'(1 + i/Q_s)\nabla^4\psi_n(x, y) - \omega^2 m''\psi_n(x, y) = 0, \quad (4.60)$$

where the hysteric damping is added defined by the substrate's intrinsic quality factor Q_s . The total solution can be described as a superposition of eigen-modes

$$u(x, y) = \sum_n^\infty w_n \psi_n(x, y), \quad (4.61)$$

where w_n are weighting constants. For purely harmonic excitation $p_e(x, y, t) \rightarrow p_e(x, y)e^{-i\omega t}$. Substituting Eq. (4.61) into (3.17) and ignoring tensile stress yields

$$\sum_n^\infty w_n (B'\nabla^4\psi_n(x, y) - \omega^2 m''\psi_n(x, y)) = p_e(x, y). \quad (4.62)$$

Now multiply both sides with another eigen-function $\psi_m(x, y)$ and integrate over the whole domain. Making use of the orthogonality between eigen-functions and Eq. (4.60) yields

$$w_n = \frac{\iint p_e(x, y)\psi_m(x, y) \, dx dy}{m''S\Lambda_n(\omega_n^2(1 + i/Q_s) - \omega^2)} \quad (4.63)$$

where $\Lambda_s = \iint \psi_n^2(x, y) \, dx dy / S$ and S is the substrate's total surface area. Substituting Eq. (4.63) into (4.61) finally results in the response function

$$u(x, y) = \sum_n^\infty \psi_n(x, y) \frac{\iint p_e(x, y)\psi_m(x, y) \, dx dy}{m''S\Lambda_n(\omega_n^2(1 + i/Q_s) - \omega^2)}, \quad (4.64)$$

Just as for the infinite substrate case, the shear force distribution can to a good approximation be considered as a point force on the substrate at point (x_F, y_F) . This simplifies the above to

$$u(x, y) = \frac{M_0}{m''S} \sum_n^\infty \psi_n(x, y) \frac{\psi_n(x_F, y_F)}{\Lambda_n(\omega_n^2(1 + i/Q_s) - \omega^2)}, \quad (4.65)$$

where $M_0 = \int F' \, ds$ is the total shear force summed along the resonator-substrate boundary. An effective spring constant k_{PTL} can then be defined, which resembles the substrate by setting $u(x, y) \rightarrow u(x_F, y_F)$

$$M_0 = -k_{\text{PTL}}(x_F, y_F)u(x_F, y_F) \quad (4.66)$$

where

$$k_{\text{PTL}}(x_F, y_F) \equiv \frac{m''S}{\sum_n^\infty \frac{\psi_n^2(x_F, y_F)}{\Lambda_n(\omega_n^2 - \omega_n^2(1 + i/Q_s))}}. \quad (4.67)$$

Note the above is only valid when the zeroth order moment dominates the coupling between the resonator and the substrate. This is true for the fundamental mode and some higher modes for typical resonators (see appendix B). To simplify calculations it is convenient to substitute ω_n with the distance $\Delta\omega$ to each respective substrate mode, i.e. $\omega_n = \omega + \Delta\omega$. Additionally, assuming the spectral width of the substrate modes are much narrower than the inverse modal density only the closest substrate mode will contribute with any significant coupling. The spring constant can then be simplified to

$$k_{\text{PTL}}(x_F, y_F) \approx -m'' S \omega \frac{\Lambda_n}{\psi_n^2(x_F, y_F)} \left(2\Delta\omega + i \frac{\omega}{Q_s} \right). \quad (4.68)$$

4.3.2.2 Power dissipation in substrate

Now a choice has to be made. At which position should one assume the resonator is on the substrate? This will affect the power that eventually will be dissipated. As stated earlier, at very high substrate mode number it is very difficult to predict exactly how the spatial overlap between substrate modes and excitation will be. One solution is instead to work with an effective spring constant. This is obtained by the substitution $\psi_n^2(x_F, y_F) \rightarrow \Lambda_n$ leading to

$$k_{\text{PTL}}(x_F, y_F) \rightarrow k_{\text{PTL}} = m'' S \omega \left(2\Delta\omega + i \frac{\omega}{Q_s} \right). \quad (4.69)$$

The power transferred and lost to the substrate can be derived by considering a force $F(t) = M_0 \exp(i\omega t)$ driving the spring k_{PTL} . This results in a velocity response $v(t) = i\omega F(t)/k_{\text{PTL}}$. The dissipated power over one cycle is then given by

$$\Delta W_{\text{PTL}} = \int_0^{2\pi/\omega} \Re\{F(t)\} \Re\{v(t)\} dt, \quad (4.70)$$

where $\Re\{\dots\}$ is the real part of a complex number. When the resonator mode's energy W is known its quality factor is then given by

$$Q_{\text{PTL}} = 2\pi \frac{W}{\Delta W_{\text{PTL}}} = \frac{2\rho_s h_s S}{Q_s} (4\Delta\omega^2 Q_s^2 + \omega^2) \frac{W}{M_0^2} \quad (4.71)$$

where W , M_0 and ω depends on the resonator to be studied. For often used resonators see appendix B for how these can be defined. A rough approximation can be applied where the resonator is described as a simple 1 degree of freedom (1DOF) system with an effective mass m_{eff} and stiffness k_{eff} . The induced force is then defined as $M_0 = -k_{\text{eff}}u = -\omega^2 m_{\text{eff}}u$ and energy $W \equiv \max(W_{\text{kin}}) = \omega^2 m_{\text{eff}} u^2 / 2$ where u is its amplitude leading to

$$\frac{W}{M_0^2} \approx \frac{1}{2\omega^2 m_{\text{eff}}} \quad (4.72)$$

which clearly shows the influence of the resonator's characteristics on the phonon tunneling losses, where lower mass and frequency is preferred for enhancing the quality factor. Note the 1DOF description is only approximate and will lead to deviations for some resonator types and modes.

4.3.2.3 Defining the stochastic variables

So far, the phonon tunneling losses have been treated purely deterministic. This is not feasible for any practical use as the spectral distance $\Delta\omega$ is difficult to predict for large substrates. Consider the resonator's frequency. Assuming it is equally likely to be situated anywhere between two substrate resonances one may write

$$\Delta\omega \equiv \frac{XY}{2} \quad (4.73)$$

where X is a uniform distribution in the range $[0, 1]$, Y is a distribution describing the spectral distance between two substrate resonances and the denominator implies only half the distance between two resonances is considered. The modal density at high mode numbers is given by [37]

$$n_\omega = \frac{S}{\pi} \sqrt{\frac{3\rho_s(1-\nu_s^2)}{4E_sh_s^2}}. \quad (4.74)$$

The distance between two modes follows an exponential distribution with the mean $1/n_\omega$. This is used to model Y . The resulting expression for the distribution of Q_{PTL} is then given by

$$Q_{\text{PTL}}(X, Y) = \frac{2\rho_sh_sS}{Q_s} [(XY)^2Q_s^2 + \omega^2] \frac{W}{M_0^2} \quad (4.75)$$

and its distribution for a typical resonator on a wafer shown on Figure 4.13. The mean value is derived to

$$\begin{aligned} E[Q_{\text{PTL}}] &= \frac{2\rho_sh_sS}{Q_s} \left[\frac{2Q_s^2}{3n_\omega^2} + \omega^2 \right] \frac{W}{M_0^2} \\ &= \frac{2\rho_sh_sS}{Q_s} \left[\frac{8\pi^2E_sh_s^2Q_s^2}{9\rho_sS^2(1-\nu_s^2)} + \omega^2 \right] \frac{W}{M_0^2}. \end{aligned} \quad (4.76)$$

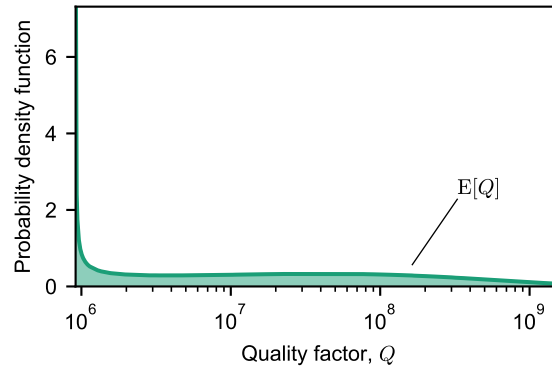


Figure 4.13: Probability density function for phonon tunneling losses of a substrate with finite size. Plotted with a silicon substrate with a diameter of 100 mm, $Q_s = 10^5$ and assuming a resonator at 200 kHz with an effective mass of 1 ng. Note there is no upper bound on this distribution.

Generally, it can be expected that Q_s is relatively high thus the last term can be omitted. The above result highlights a $Q_{\text{PTL}}(X, Y) \propto h_s^3$ dependence which has been observed in other studies [25]. Moreover, it differs from the $Q_{\text{PTL}\infty} \propto h_s^2$ seen for fundamental modes embedded in infinite substrate. Another interesting feature is this description predicts a potentially large spread in the resulting quality factor of the resonator. The lowest quality factor predicted by Eq. (4.75) is

$$\min[Q_{\text{PTL}}] = \frac{2\rho_sh_sS\omega^2}{Q_s} \cdot \frac{W}{M_0^2}. \quad (4.77)$$

The largest value is due to the exponential distribution of Y unbounded. However, at high quality factors the device will be limited by other mechanisms, presumably intrinsic losses or ballistic gas damping. Comparing the minimum value with the mean value it is evident for small and thick substrates the spread can be made extremely large as illustrated on

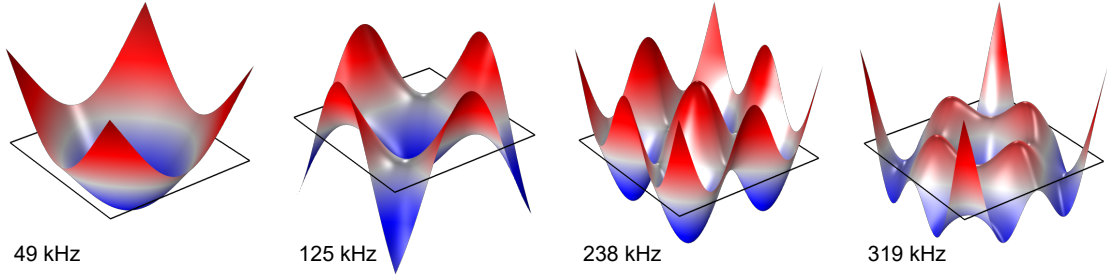


Figure 4.14: First four modes of a $1 \times 1 \text{ cm}^2$ silicon chip with the parameters: $h_s = 500 \text{ }\mu\text{m}$, $E_s = 170 \text{ GPa}$, $\rho_s = 2329 \text{ kg/m}^3$, $\nu_s = 0.28$.

Figure 4.13. This large spread is comparable to observed values in conducted experiments throughout the PhD (see Figure 11.1). It should be stated that the above does not explain all the spread one might encounter when characterizing resonators. Fabricational imperfections as well as the cleanliness of the environment (dust and particles) will also contribute to the spread.

It is speculated if fabricating small chips instead of leaving the resonators on large wafers may be a good strategy to obtain stable and high quality factors. Small chips lead to low density of modes making it easier to predict the relevant resonances of the chip itself. This should enable one to engineer the chips to impede any spatial and temporal overlap between the resonator and chip modes. For a fundamental mode resonator placed in the center of a $1 \times 1 \text{ cm}^2$ silicon chip the first few spatially overlapping modes are at 49, 125, 238 and 319 kHz, which are illustrated on Figure 4.14. These frequencies can be scaled up by fabricating even smaller chips making it easier to impede modal overlap. This was briefly tested and presented on Figure 11.4 which confirms this could be a valid strategy.

4.3.2.4 Finite element simulation implementation

Finally, for finite element simulations of arbitrary designs it can be convenient to adapt the current model to be directly implementable just as in section 4.3.1.4 for the infinite substrate case. For the mean estimate of the quality factor, substitute $\Delta\omega$ with its root-mean-square value in Eq. (4.69). This leads to

$$k_{\text{PTL}} = -m''S\omega \left(\frac{\sqrt{6}}{3n_\omega} + i\frac{\omega}{Q_s} \right). \quad (4.78)$$

The minimum obtainable quality factor is given by

$$k_{\text{PTL,min}} = -i\frac{m''S\omega^2}{Q_s}. \quad (4.79)$$

4.3.3 Substrates with phononic shields

When discussing phonon tunneling losses and how to mitigate them, one obvious and tested method is to engineer the surrounding substrate with some kind of mechanical shield. They have not been used in this work. Nonetheless, their ability to isolate any resonator independent of the design of the resonator itself has great value, although it will complicate fabrication considerably. Broadly speaking, there exists two approaches which will be presented and discussed briefly.

4.3.3.1 Multi-frame approach

One approach to isolate the resonator is by engineering the surrounding substrate to contain solid rings loosely coupled via small springs in the form of tethers [38, 39, 40, 41].

The idea is sketched in Figure 4.15. Each layer reduces the vibrations by some factor depending on the mass of the ring and the stiffness of the tethers. By describing it as a system of masses m_i and springs k_i an approximate analytical model can be build which is able to give a good prediction on the attenuation of the vibrations. Consider position i on the array where the vibration is attenuated by a factor α_i . Assuming $\alpha_i \ll 1$ the mass and spring at that position is then approximately related via

$$\alpha_i \approx \frac{k_{i-1}}{\omega^2 m_i}. \quad (4.80)$$

It is clear from Eq. (4.80) a weak spring connection and high mass is preferred for maximum attenuation and therefore resonator isolation.

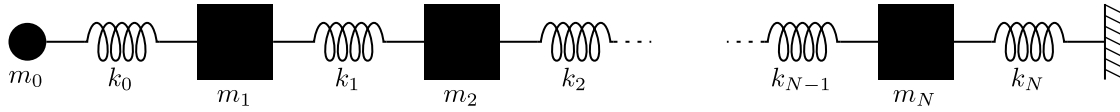


Figure 4.15: An illustration of the multi-frame approach to resonator isolation. m_0 and k_0 are the resonator's effective mass and an effective coupling spring from the resonator to the first mass element, respectively. m_i and k_i for $i > 0$ are the substrate mass and spring elements, respectively.

The approach is simple and has demonstrated the ability to effectively decouple the resonator. A design was developed to test this concept shown on Figure 4.16, which clearly demonstrate the effective attenuation of the coupled vibrations. However, this approach has some pitfalls. For resonators operating at higher frequencies the wavelength in the substrate is small enough for there to exist modes within the rings themselves. This poses the risk of the resonator coupling to these ring modes thereby enhancing the coupling and possibly damping. Of course, one can limit this effect by using thicker substrate thicknesses to stiffen them, which blueshifts the rings' eigen-frequencies. However, this is ultimately limited by the wafer thickness. Alternatively, one can engineer the rings and the resonator modes to ensure there will be no temporal overlap thus removing the risk of exciting the rings' eigen-modes.

A notable variation of this is patterning a string or the strings of a trampoline resonator [42] with blocks of mass elements connected by strings. Each block consists of some mass m_i and each string segment has a stiffness $k_i = A\sigma/L$ defined by their cross-sectional area A , length L and tensile stress σ . From these definitions Eq. (4.80) can be used to estimate the attenuation at each block. This design prevents the vibrations from propagating further along the string. Note in the cited work the mass blocks have been designed in a herringbone pattern in order to reduce the bending losses which would otherwise occur at the blocks.

4.3.3.2 Phononic crystal approach

Another approach is embedding the substrate in a phononic pattern shown on Figure 4.17 [44, 45, 43, 46]. In a sense it is similar to the approach described earlier, but in this case it is applied as a one or two-dimensional periodic pattern of masses connected via small springs. The concept will be explored more thoroughly for resonators in chapter 6. In short, the tether-mass configuration creates a propagation velocity contrast. This creates a band-gap, where vibrations at certain frequencies cannot exist. Anything that is embedded inside such a pattern and exciting with a frequency inside the band-gap will have the vibrations reflected back, i.e. it is perfectly isolated. In practice, the pattern only has a finite size thus the vibrations will experience an attenuation per phononic cell. It

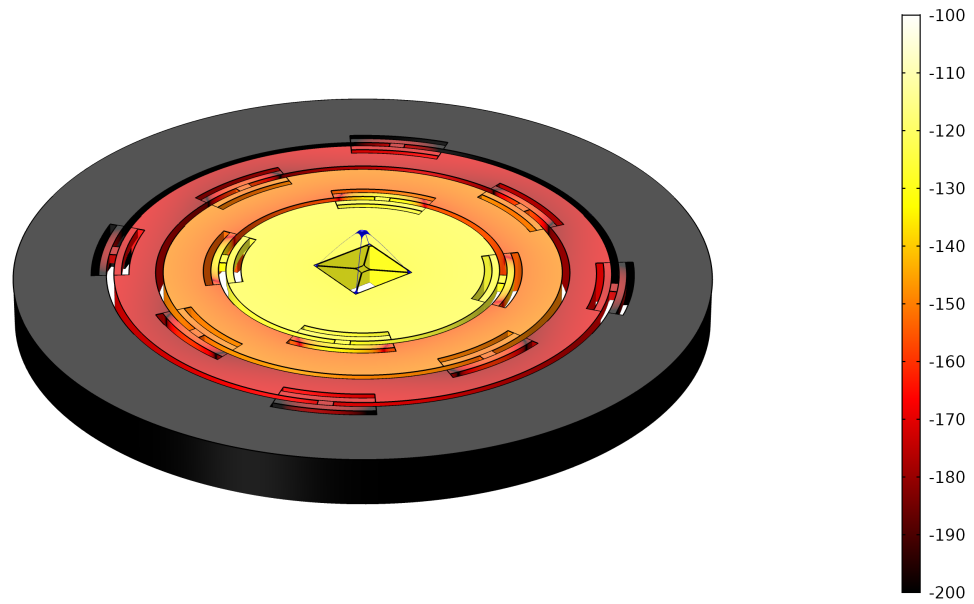


Figure 4.16: COMSOL simulation output of a proposed design of a $700 \times 700 \mu\text{m}^2$ sized trampoline with mechanical shield defined on a $500 \mu\text{m}$ thick wafer. The color bar shows the displacement in the substrate in terms of dB. The design was never realized as it was decided it would complicate fabrication too much.

has the obvious advantage compared to the previous approach that one does not have to worry about exciting some eigen-modes inside the embedded structure, since they are all forbidden inside the band-gap. The drawback is it only works for vibrations at frequencies *within* the band-gap. Vibrations at frequencies outside the band-gap are free to propagate.

4.3.4 Concluding remarks on phonon tunneling losses

Two different analytical approaches for predicting the phonon tunneling losses have been proposed and developed. The infinite substrate case can easily be solved analytically for a large array of mode configurations. Unfortunately, it does not reflect typical real world applications. Since the results for a finite substrate more closely resembles real world cases, this should be used for predicting the phonon tunneling losses.

The destructive interference effect predicted using the infinite substrate model is expected to hold true for the finite substrate model. It could be interesting to extend the latter to account for all mode configurations and not only modes primarily exciting the zeroth order moment. If it can be shown that modes confined to higher order moment excitations can have their minimum predicted quality factor improved by multiple orders of magnitude, this could lead to interesting design optimization strategies. In that case, it might be possible to engineer high-Q modes with highly suppressed phonon tunneling losses, which do not need phononic shields embedded in the substrate.

Finally, when resonators are placed on large substrates, like wafers, a large distribution of the phonon tunneling loss quality factors is expected due to the probability of resonant coupling to substrate modes. For stable reproducible result on a resonator-to-resonator case some kind of phononic shielding is needed. This requirement might be omitted by intelligent engineering of resonator mode and chip dimensions, although this might make

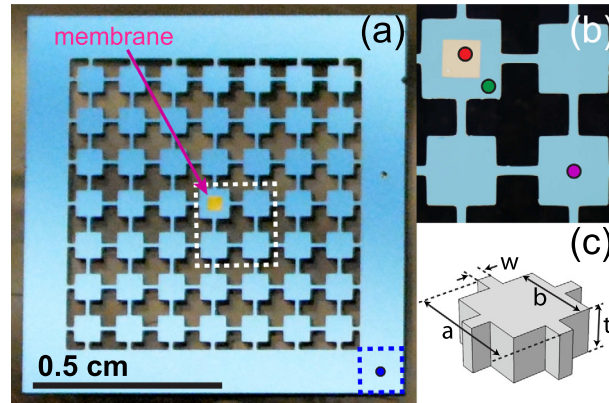


Figure 4.17: An example of how phononic patterns can be realized to isolate a resonator embedded within. (a) Microscope image of the device. (b) Expanded view near the isolated resonator. (c) Schematic of a single phononic cell. Figure adapted from [43].

the losses sensitive to the chip mounting technique used.

4.4 Conclusion on damping mechanisms

It has been shown having a well designed high-vacuum system is crucial when probing the quality factor of ultra-coherent resonators. Pressures below 10^{-7} mBar is typically used for the best performing resonators. In this regime the mean free length of the gas molecules is extremely long and therefore the damping is well described using the ballistic gas model. Since this is in principal an easy controllable external damping mechanism, this can be considered trivial and typically ignored when discussing high quality resonators.

The intrinsic losses can from the Zener model be described by the Debye equations. The damping mechanisms considered are the friction losses, which are a result of defects modeled as two-level systems, as well as fundamental losses thermoelastic damping and Akhiezer damping. The latter is often referred to as the quantum limit. The damping can be diluted using a high tensile stress and evidence indicate this can even dilute Akhiezer damping. Ultimately, the best performing devices will be limited by friction losses which typically is dominated by surface impurities, possibly surface oxidization.

To ensure the device can reach the limit set by intrinsic damping the supporting substrate has to impede vibrations coupling from the resonator into the substrate and potentially further out in the external environment. Existing literature on the topic only considers in-plane and surface waves. This does not include the quality factor enhancements which have been observed when using thicker substrates. Simulations conducted for resonators up to the low MHz range show the vibrations in the substrate are mainly out-of-plane transversal waves. From this, two new models were developed. The infinite substrate model predicts a substrate thickness dependence of the order h_s^2 . Furthermore, it clearly shows that often one can impede the phonon tunneling loss by going for modes which create destructive interference in the substrate thereby reducing the coupling. This corresponds to modes exciting only higher order moments in the substrate, i.e. dipoles, quadrupoles etc..

The finite substrate model predicts a large spread of quality factors, since the quality factor is dependent on how well it couples to one of the substrate modes. For large substrates, this is seemingly random which potentially allows for a spread in quality factors above

an order of magnitude. The mean value of the distribution shows a substrate thickness dependence of the order h_s^3 , again highlighting that substrate thickness is an important parameter for impeding phonon tunneling losses. It is believed smaller chips can allow engineering of the substrate modes and can thereby be used to limit this loss mechanism.

Furthermore, the substrate can be engineered with mass-spring or phononic crystal arrays to further isolate the resonator. This can be especially important when one adds structures on to the resonator like photonic crystals, which will add mass and therefore enhance the coupling to the substrate resulting in higher phonon tunneling losses. One has to be aware of these mechanical shields will complicate fabrication.

5 | Nonlinear analysis

In quantum optomechanics the application of micromechanical resonators is usually limited to cooling the mode of interest down to low phonon numbers followed by performing quantum mechanical experiments like transferring single photons and phonons. The resonator is not subject to large displacement and can (in the classical regime) easily be described using linear theory. However, in other applications, which includes ringdown experiments, the displacement of the resonator can become large enough to alter the behavior of the device. It enters a nonlinear regime where its characteristics is now dependent on the amplitude of the resonator itself.

This chapter investigates the dominating source of nonlinearity and develops a model to predict the behavior. Multiple scales analysis [47] is an often used method to study nonlinear systems with finite (but not large) perturbations. The string will form the basis of the analysis due to its simple description, but the approach used here can easily be applied to any resonator design. Furthermore, the conclusions derived from the string are quite general. A recent study was found obtaining similar results [48].

5.1 Source of nonlinearity: String elongation

The source of the studied nonlinearity is a geometric nonlinearity where the string is elongated from an original length L to an elongated length S illustrated on Figure 5.1a. Other nonlinearities possibly (in fact, surely) exists, but this has been identified as the dominant mechanism at finite displacement amplitudes, which also matches the description given in literature [7]. As the string is excited with some displacement amplitude, it is elongated as a result of the fixed boundary conditions. This increases the strain, which in turn leads to a higher effective tensile stress and therefore higher frequencies.

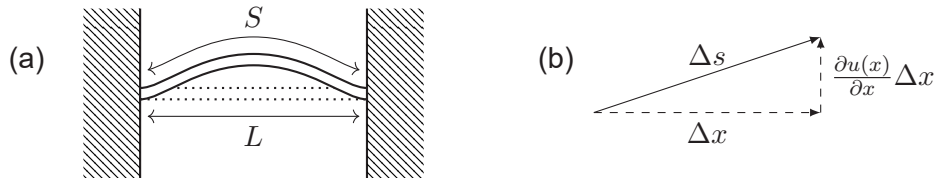


Figure 5.1: (a) Illustration of the string elongation at large displacement amplitudes where $S \geq L$. (b) Small string segment relating the local elongation of a string with its slope.

By analyzing the small string segment shown on Figure 5.1b one can derive the change in tensile stress as a function of displacement amplitude. Any perturbation of the string will result in a slope which will force an elongation of the string locally. Let s be a spatial coordinate along the string related to the x coordinate via the differential equation using Pythagoras's theorem

$$\Delta s \equiv s(x + \Delta x) - s(x) = \sqrt{\Delta x^2 + \left(\frac{\partial u(x)}{\partial x} \Delta x \right)^2} \quad (5.1)$$

Letting $\Delta x \rightarrow 0$ and assuming finite displacements yields

$$\frac{ds}{dx} \approx 1 + \frac{1}{2} \left(\frac{\partial u(x)}{\partial x} \right)^2. \quad (5.2)$$

Since the propagation velocity of in-plane vibrations $\sqrt{E/\rho}$ is much faster than out-of-plane vibrations $\sqrt{\sigma/\rho}$ it can be assumed the in-plane forces equalize along the elongated beam. When it is also assumed the beam is uniform, i.e. constant width b and thickness h as well as constant material parameters E and ρ the change in strain is uniform along the string. This change is given as a function the displacement

$$\varepsilon_u \equiv \frac{\int_0^L \frac{ds}{dx} dx - L}{L} = \frac{1}{2L} \int_0^L \left(\frac{\partial u(x)}{\partial x} \right)^2 dx, \quad (5.3)$$

where the change in tensile stress is related via $\sigma_u = E\varepsilon_u$. Adding the nonlinear tensile stress contribution into Eq.(3.2) leads to the now displacement-dependent tensile force

$$T(x) \rightarrow T = \sigma A + \frac{EA}{2L} \int_0^L \left(\frac{\partial u(x)}{\partial x} \right)^2 dx, \quad (5.4)$$

where σ is the prestress in the absence of transversal displacement. The partial differential equation then becomes

$$\frac{EI}{\rho A} \frac{\partial^4 u}{\partial x^4} - \left[\sigma_0 A + \frac{EA}{2L} \int_0^L \left(\frac{\partial u(x)}{\partial x} \right)^2 dx \right] \frac{\partial^2 u}{\partial x^2} + \rho A \frac{\partial^2 u}{\partial t^2} = F'_e. \quad (5.5)$$

where it is obvious the problem has become nonlinear. To proceed the above has to be converted into an ordinary differential equation by applying the Galerkin method where it is assumed the eigen-modes are given by Eq.(B.1). Using modeshape expansion, let $u(x, t) = \sum_n u_n(t) \psi_n(x)$, substitute it into Eq.(5.5), multiply by another modeshape $\psi_m(x)$ and finally integrate along the string. This leads to

$$m_{\text{eff}} \frac{d^2 u_m(t)}{dt^2} + \left[k_{\text{eff}} + \frac{AE}{2L} \int_0^L \frac{d^2 \psi_m(x)}{dx^2} \psi_m(x) dx \int_0^L \left(\sum_n u_n(t) \frac{d\psi_n(x)}{dx} \right)^2 dx \right] u_m(t) = p_e(t) \quad (5.6)$$

where m_{eff} , k_{eff} , p_e are the effective mass, stiffness and external force for the linear part, respectively, defined by

$$\begin{aligned} m_{\text{eff}} &= \rho A \int_0^L \psi_m^2(x) dx \\ k_{\text{eff}} &= k_{\text{bend}} + k_{\text{tens}} \\ k_{\text{bend}} &= EI \int_0^L \left(\frac{d^2 \psi_m(x)}{dx^2} \right)^2 dx \\ k_{\text{tens}} &= -\sigma A \int_0^L \frac{d^2 \psi_m(x)}{dx^2} \psi_m(x) dx \\ p_e(t) &= \int_0^L F_e(x, t) \psi_m(x) dx \end{aligned} \quad (5.7)$$

where it is assumed $\psi_m(x)$ is normalized to an amplitude of 1. The sum in the nonlinear term includes the nonlinear tensile stress contributions from *all* excited modes. Normally only a single mode m is excited during experiments. Therefore, all terms in the nonlinear sum can be dropped except for mode m . This leads to

$$\frac{d^2 u_m(t)}{dt^2} + (\omega_m^2 + u_m^2(t) \alpha_{\text{eff}}) u_m(t) = p_e(t) \quad (5.8)$$

where

$$\begin{aligned}\omega_m &= \sqrt{k_{\text{eff}}/m_{\text{eff}}} \\ \alpha_{\text{eff}} &= \frac{AE}{2Lm_{\text{eff}}} \int_0^L \frac{d^2\psi_m(x)}{dx^2} \psi_m(x) dx \int_0^L \left(\frac{d\psi_m(x)}{dx} \right)^2 dx\end{aligned}\quad (5.9)$$

Eq.(5.8) shows how a significant displacement can increase the effective stiffness thereby pushing the resonance frequency upwards.

5.2 Modeling damping

So far, damping has been omitted. Nonlinear equations of motion can have complicated behaviors which cannot be included by assuming a harmonic solution at a single frequency. It has to be solved in the time domain. Therefore, it is not possible to include the damping by simply adding the imaginary part of the Young's modulus to Eq.(5.8) as for the linear case. However, by observing it, it is already possible to deduce some expected behavior. For the linear case, the damping is diluted by the increase of tensile stress. This can be seen for k_{eff} where the first term containing the lossy stiffness defined by E is diluted by increasing σ in the second term. In the nonlinear case, the parameter α_{eff} also contains E , but there is no second term to dilute it. As the nonlinear stiffness contribution increases with displacement amplitude u_m , a larger part of the total stiffness will come from the nonlinear term. Recall the nonlinear term is a result of elongation of the string length, and this type of vibration does not benefit from tensile stress induced damping dilution [22]. Therefore, at larger amplitudes the damping is expected to increase.

How can the hysteretic damping be modeled in a nonlinear system? Hysteretic losses can be directly modeled using the Bouc-Wen model [49], which is also nonlinear. The implementation and solution using this approach is not clear for the current problem. A simpler approach is proposed inspired by [7]. The damping is modeled as viscous damping, i.e. by including a $\Gamma(u_m)du_m/dt$, where $\Gamma(u_m)$ is the displacement-dependent damping rate. This description can be exactly equivalent to hysteretic damping *at resonance*, but will diverge outside [50]. For the purpose of studying the nonlinear effects of the resonator this is deemed as an acceptable compromise, especially when considering the multiple scales approach is well suited for studying the effects at resonance.

At resonance, it can be shown the damping rate can be related to the lossy part of the total stiffness by

$$\Gamma(u_m) = \frac{\Im\{k_{\text{tot}}(u_m)\}}{\omega_m} \quad (5.10)$$

where $k_{\text{tot}}(u_m)$ is the displacement-dependent complex total stiffness of the resonator mode, and $\Im\{\dots\}$ takes the imaginary part. When including hysteretic damping, the total stiffness is given by

$$k_{\text{tot}}(u_m) = (1 + i\tilde{\phi})k_{\text{bend}} + k_{\text{tens}} + (1 + i\tilde{\phi})k_{\text{nlin}}(u_m) \quad (5.11)$$

where $k_{\text{nlin}}(u_m) = \alpha_{\text{eff}}u_m^2$. Recall $\tilde{\phi}$ is the undiluted loss angle of the resonator. This leads to the damping rate

$$\Gamma(u_m) = \tilde{\phi} \frac{k_{\text{bend}} + \alpha_{\text{eff}}u_m^2}{\omega_m} = \Gamma_{\text{lin}} + \Gamma_{\text{nlin}}u_m^2 \quad (5.12)$$

where $\Gamma_{\text{lin}} = \tilde{\phi}k_{\text{bend}}/\omega_m$ and $\Gamma_{\text{nlin}} = \tilde{\phi}\alpha_{\text{eff}}/\omega_m$. The nonlinear equation of motion then takes the form

$$\frac{d^2u_m(t)}{dt^2} + (\Gamma_{\text{lin}} + \Gamma_{\text{nlin}}u_m^2) \frac{du_m}{dt} + [\omega_m^2 + u_m^2(t)\alpha_{\text{eff}}] u_m(t) = p_e(t) \quad (5.13)$$

5.2.1 Nondimensionalization

Before proceeding with the analysis it is convenient to convert the above equation to dimensionless quantities. This simplifies later derivations while at the same time generalizing it to include other problems, which can be cast into the same form. First, define the dimensionless displacement $\theta \equiv u_m/L$ and time $\tau \equiv \omega_m t$. Substituting those into Eq. (5.13) leads to

$$\ddot{\theta} + \gamma_0 \dot{\theta} + \gamma_1 \theta^2 \dot{\theta} + \theta + \beta \theta^3 = q \quad (5.14)$$

where the dots indicate derivatives with respect to τ and

$$\gamma_0 = \frac{\Gamma_{\text{lin}}}{\omega_m m_{\text{eff}}} \quad , \quad \gamma_1 = \frac{\Gamma_{\text{lin}} L^2}{\omega_m m_{\text{eff}}} \quad , \quad \beta = \frac{\alpha_{\text{eff}} L^2}{\omega_m^2 m_{\text{eff}}} \quad , \quad q(\tau) = \frac{p_e(t)}{m_{\text{eff}} L \omega_m^2} \Big|_{t=\frac{\tau}{\omega_m}} \quad . \quad (5.15)$$

The equation takes the form of a Duffing oscillator with nonlinear damping added.

5.3 Multiple scales analysis

Multiple scales analysis can be used when the nonlinear effects are small. The solution is then a small nonlinear perturbation to a linearized solution. The displacement is expanded to

$$\theta(\tau) = \sum_{n=0}^{\infty} \theta_n(T_0, T_1, \dots) \quad (5.16)$$

where $T_n = \varepsilon^n \tau$ and $\varepsilon \ll 1$ is some small coefficient. For this analysis using only the first two terms is expected to yield satisfactory results, i.e.

$$\theta(\tau) \approx \theta_0(T_0, T_1) + \varepsilon \theta_1(T_0, T_1) \quad , \quad (5.17)$$

and parameters dependent on T_1 are slowly varying perturbations of the linearized solution. ε is used as a placeholder to highlight terms that are expected to be weak. Assuming a weak harmonic excitation, weak damping and weak nonlinear effects leads to

$$\ddot{\theta} + \varepsilon \gamma_0 \dot{\theta} + \varepsilon \gamma_1 \theta^2 \dot{\theta} + \theta + \varepsilon \beta \theta^3 = \varepsilon q_0 \cos \Omega \tau \quad (5.18)$$

where Ω is the normalized excitation frequency. Inserting the expansion and discarding terms containing ε at higher orders than one, the terms can be collected depending on the order of ε . Solving for terms containing $\varepsilon^0 \theta_0$ leads to

$$\frac{d^2 \theta_0}{dT_0^2} + \theta_0 = 0 \quad \rightarrow \quad \theta_0(T_0, T_1) = A(T_1) e^{iT_0} + \text{cc} \quad (5.19)$$

where cc is a placeholder for the complex conjugate of the whole expression, and $A(T_1)$ is a complex amplitude yet to be determined. Solving for terms containing ε^1 and using the above solution of θ_0 leads to

$$\frac{d^2 \theta_1}{dT_0^2} + \theta_1 = \left(-2iA' - i\gamma_0 A - i3\gamma_1 A^2 \bar{A} - 3\beta A^2 \bar{A} + \frac{q}{2} e^{i\delta T_1} \right) e^{iT_0} + (-i\gamma_1 A^3 - \beta A^3) e^{3iT_0} + \text{cc} \quad (5.20)$$

where the substitution $\Omega = 1 + \varepsilon \delta$ was used and where δ is a small detuning from resonance. The bar is the complex conjugate and the apostrophe is the derivative with respect to T_1 . Any valid solution require the secular terms to equal zero, i.e. the sum of terms containing the factor e^{iT_0} . This is known as the solvability condition here defined as

$$-2iA' - i\gamma_0 A - i3\gamma_1 A^2 \bar{A} - 3\beta A^2 \bar{A} + \frac{q}{2} e^{i\delta T_1} = 0 \quad . \quad (5.21)$$

When the solvability is fulfilled θ_1 is solved to

$$\theta_1(T_0, T_1) = \frac{A^3(T_1)}{8} (i\gamma_1 + \beta) e^{i3T_0} + \text{cc} , \quad (5.22)$$

leading to the total solution

$$\theta(\tau) \approx A e^{i\tau} + \frac{A^3}{8} (i\gamma_1 + \beta) e^{i3\tau} + \text{cc} , \quad (5.23)$$

where A is determined by solving the solvability condition.

Now, assume $A(T_1) = \tilde{a}(T_1) e^{i\phi(T_1)}$, where $\{\tilde{a}, \phi\}$ are real slowly varying coefficients and substitute Eq. (5.21). Separate the equation into two new equations for the real and imaginary terms, respectively. Finally, introduce the phase $\zeta(T_1) \equiv \delta T_1 - \phi(T_1)$. This leads to the two modulation equations

$$\begin{aligned} \zeta' &= \frac{q}{2\tilde{a}} \cos(\zeta) + \delta - \frac{3}{2}\beta\tilde{a}^2 \\ \tilde{a}' &= \frac{q}{2} \sin(\zeta) - \frac{1}{2}\gamma_0\tilde{a} + \frac{3}{2}\gamma_1\tilde{a}^3 \end{aligned} \quad (5.24)$$

The steady-state solution is obtained by letting $\tilde{a}' = \zeta' = 0$ leading to the frequency response equation

$$\left(\frac{q}{2}\right)^2 = \left[\left(\frac{3}{2}\beta\tilde{a}^2 - \delta \right)^2 + \left(\frac{1}{2}\gamma_0 + \frac{3}{2}\gamma_1\tilde{a}^2 \right)^2 \right] \tilde{a}^2 \quad (5.25)$$

and phase response equation

$$\tan \zeta = \frac{\frac{1}{2}\gamma_0 + \frac{3}{2}\gamma_1\tilde{a}^2}{\frac{3}{2}\beta\tilde{a}^2 - \delta} . \quad (5.26)$$

Eq. (5.25) can be used to calculate the valid steady-state solutions of the resonator, but it does not predict whether these solutions are stable. A stability analysis is needed for each valid solution. The stability can be determined by evaluating the eigen-values of the Jacobian matrix of the modulation equations Eq. (5.24) at each singular point (\tilde{a}, ζ) . The Jacobian is defined as

$$\mathcal{J}(\tilde{a}, \zeta) = \begin{bmatrix} \frac{\partial \tilde{a}'}{\partial \tilde{a}} & \frac{\partial \tilde{a}'}{\partial \zeta} \\ \frac{\partial \zeta'}{\partial \tilde{a}} & \frac{\partial \zeta'}{\partial \zeta} \end{bmatrix} , \quad (5.27)$$

where the eigen-values λ are given by $|\mathcal{J}(\tilde{a}, \zeta) - \lambda \mathbf{I}|$. If any of the eigen-values have positive real parts, the system will diverge away from the solution and is therefore unstable.

The frequency response Eq. (5.25) is plotted on Figure 5.2a for a simple string. At low force excitation the resonator shows a typical response for linear systems. However, at higher forces the amplitude response goes up and starts to skew towards higher frequencies. At sufficiently high excitation forces bifurcation occurs and the system becomes bi-stable. This is a common response for mechanical systems at high amplitudes. As the amplitude increases the resonance shifts. This is simply a result of the nonlinear stiffness contribution coming from the elongation of the beam length.

It was argued the onset of nonlinearity also leads to additional loss contributions not affected by damping dilution, thereby increasing overall losses at sufficiently high amplitudes. Figure 5.2b plots the quality factor as the resonator is excited to increasingly higher amplitudes. When the resonator is well into the nonlinear regime the quality factor starts to be severely affected.

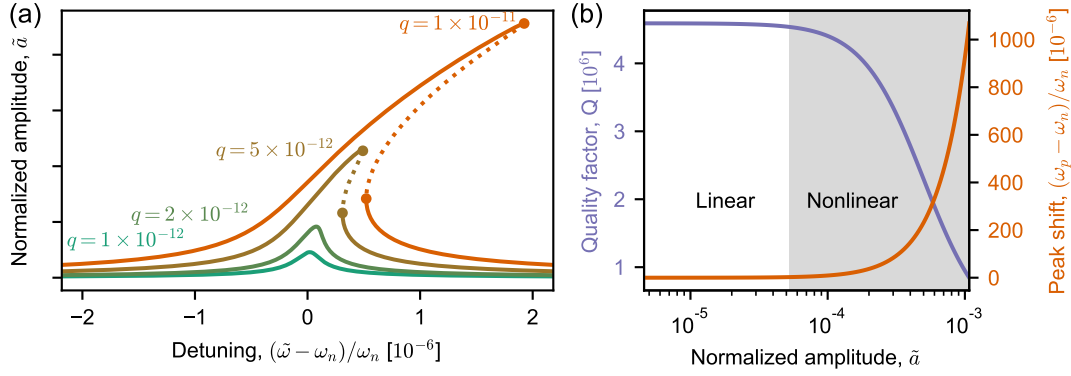


Figure 5.2: (a) Amplitude response of string plotted against the detuning of an external excitation at different force amplitudes. Dashed lines are unstable solutions. (b) Quality factor (purple) and resonance peak shift ω_p (red) vs resonator amplitude. The quality factor is determined by numerically evaluating the full-width-half-maximum of the peak. Plotted for $n = 1$, $\gamma_0 = 2.18 \times 10^{-7}$, $\gamma_1 = 0.205$ and $\beta = 616$. This corresponds to a silicon nitride string with the parameters $\sigma = 1$ GPa, $h = 50$ nm, $b = 1$ μ m, $L = 700$ μ m and $\beta_{\text{surf}} = 6 \times 10^{10}$ m^{-1} . With these parameters, optical forces in (b) correspond to the interval $F_e = [0.3, 300]$ fN or incident optical power modulation amplitude $[0.6, 600]$ μ W assuming a reflectance of 0.07.

5.4 Conclusion on nonlinear analysis

At significantly large displacement amplitudes a string will experience an elongation of its total length. The strain induced by this induces an extra displacement-dependent tensile stress contribution for the resonator. The multiple scales analysis showed as soon as the amplitude crosses a certain threshold the frequency will shift to higher frequencies as a function of amplitude. Furthermore, since in-plane vibrations generally do not experience any damping dilution, any stiffness contribution arising from this nonlinear effect is lossy. This leads to a significant drop in quality factor if the resonator is driven hard enough. Even though the derivation was performed for a string the results and conclusions are quite general and is applicable for *any* thin film tensile stress resonator.

6 | Phononic crystal patterned membranes and soft-clamping

One type of membrane design which have not been discussed yet are resonators embedded in a repetitive pattern. These are phononic crystals and their extraordinary properties deserve their own chapter. Current state-of-the-art resonators are all based on this and has in recent years enabled new gains for ultra-coherent devices. The chapter first explores the one-dimensional phononic crystal strings and establishes all the relevant effects and concepts. From there more complicated implementations used by by different groups will be presented and discussed.

6.1 Phononic crystal theory

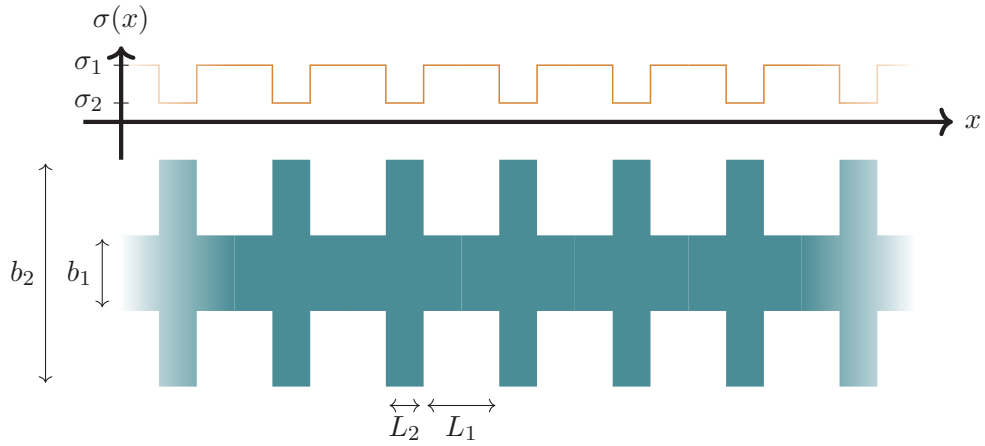


Figure 6.1: Top-view sketch of string with periodic width modulation. The resulting tensile stress is shown above.

The important aspects is, as for other phenomena, best illustrated on a simple one-dimensional case. Consider a string where its width is modulated as shown on Figure 6.1. From Newton's second law when the string is at rest the tensile forces must balance each other. This creates an equilibrium stress distribution. For the sketched string the equilibrium stresses are derived to

$$\sigma_i = \frac{\sigma_0}{b_i} \frac{L_1 + L_2}{L_1/b_1 + L_2/b_2}, \quad (6.1)$$

where σ_0 is the tensile stress *before* the string is released and will henceforth be known as the prestress. The resulting periodic stress will for some frequencies result in a fraction of the vibrations getting reflected at each cell and therefore impede propagation. How can this be modelled? From the study of electrons moving through a one-dimensional lattice of potentials a complete analog procedure can be employed to study the propagation of vibrations, or phonons, through periodic tensile stress distributions. Since the stress in this simple example is described by a rectangular function the Kronig-Penney model can aptly be used here.

From Eq.(3.15) and by assuming a tensile stress dominated string the wave-function traveling at any section of the string is given by

$$\psi_1(0 \leq x < L_1) = a_1 e^{k_1 x} + b_1 e^{-k_1 x}, \quad \psi_2(-L_2 \leq x < 0) = a_2 e^{k_2 x} + b_2 e^{-k_2 x}, \quad (6.2)$$

where the subscript $j = \{1, 2\}$ corresponds to the narrow and wide section, respectively. The wavenumbers are defined as $k_i = \omega \sqrt{\rho/\sigma_i}$. Using Bloch's theorem, one only has to consider a single cell of the periodic structure. The resulting periodic function $u(x)$ is given by $\psi_i(x) = e^{ikx} u_i(x)$, where the wavenumber k is the crystal momentum vector. By applying the appropriate boundary conditions and solving the resulting eigenvalue problem, one obtains the following expression

$$\cos kL = \cos k_1 L_1 \cos k_2 L_2 - \frac{k_1^2 + k_2^2}{2k_1 k_2} \sin k_1 L_1 \sin k_2 L_2 . \quad (6.3)$$

For any valid solution the right-hand-side must be confined within ± 1 . This opens up the possibility, that for some specific range of frequencies there exists no valid solution. These modes cannot exist on the string. These regions are known as band-gaps and are highlighted on Figure 6.2.

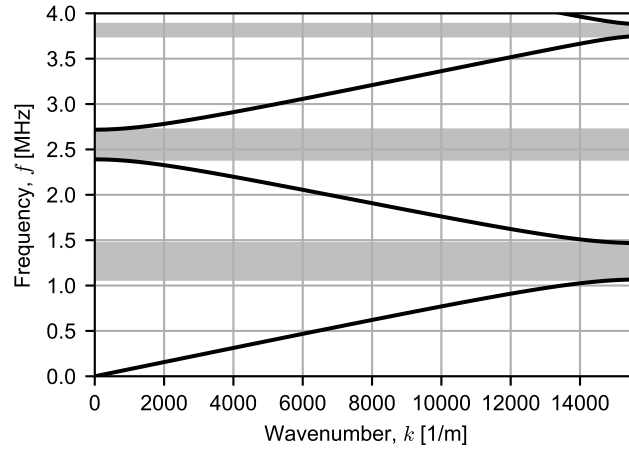


Figure 6.2: Dispersion relation based on the Kronig-Penney model for the transversal bending modes of a string. Shaded area are band-gaps. Generated for $w_1 = 3w_2$, $L_1 = L_2 = L/2 = 100 \mu\text{m}$ and $\sigma_0 = 1 \text{ GPa}$.

Eq.(6.3) also highlights other interesting details. The width of the band-gap is largely determined by the fraction. Considering $k_i \propto \omega \sqrt{\rho/\sigma_0}$ the band-gap width is only determined by the geometry, i.e. the relative widths and lengths of the two string sections. Changing σ_0 shifts the band-gap but preserves the same relative width. Moreover, when $w_2 \gg w_1$ the fraction equals $\alpha^{3/2}\beta$ where $\beta = w_2/w_1$ and $\alpha = L_1/(L_1 + L_2)$, which clearly shows the relative band-gap width can be enhanced by maximizing the width contrast in the pattern. One should note in that case the tensile stress in the wide segment will become very low and susceptible to high bending losses due to lack of the tensile stress induced damping dilution. Thus, there exists a trade-off between wide band-gap and low bending losses.

Another feature of Eq.(6.3) can be seen when considering the band-gap region, i.e. when the right-hand-sign is outside the ± 1 interval. The only way the equality can hold is when $k \rightarrow ik$. Such a wave will couple evanescently into the crystal and decay by some amount per cell as shown on Figure 6.3b. When placing a defect inside such a crystal the vibrations of the defect can be completely isolated when enough cells are used. This isolation is what other groups have utilized to push the performance of both strings and membranes. The defect can take many forms. Its main characteristic is it locally disturbs the periodic pattern which enables mode inside the band-gap to exists in the defect. For strings, it is usually just a narrow segment with a different length than used in the crystal (see Figure 6.3a).

The isolation achieves two things. Firstly, the isolation ensures the phonons confined to the defect are unable to couple to the external environment. This practically eliminates phonon tunneling losses. Secondly, the evanescent coupling to the phononic crystals is soft and does not induce the high boundary bending losses which other resonators are prone to. With sufficiently high number of isolating phononic cells the defect-confined mode cannot "see" the hard substrate boundary. In practice, the boundary bending loss term discussed in section 4.2.6 vanishes and only distributed bending losses remain. This effect is known as soft-clamping [51]. Furthermore, this evanescent wave can be used to engineer the coupling between the modes of two defects [48]. As will be seen, the use of phononic crystals can enable one to push the quality factor to extreme heights.

In the following some key implementations of phononic crystals will be presented and discussed for both one-dimensional and two-dimensional resonators.

6.2 Implementations of one & two dimensional crystals

A proof-of-principle was demonstrated in [52] using a string shown on Figure 6.3a. They confirmed the quality factor is improved considerably at higher frequencies when the string was isolated using phononic crystals to confine the mode. Based on their models they successfully managed to completely remove phonon tunneling losses. A simulation of their implementation is shown on Figure 6.3b, which shows a factor of ~ 0.2 drop in amplitude per phononic cell.

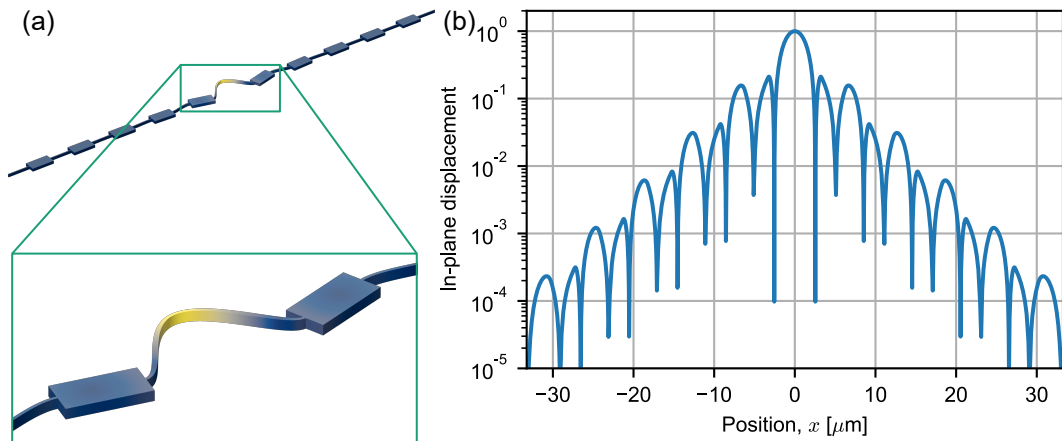


Figure 6.3: Simulation of the one-dimensional phononic crystal implement in [52] where the defect string is $6.5 \mu\text{m}$ long. Assuming a prestress of 1 GPa.

In their work they implement the phononic pattern a bit differently than discussed before. Firstly, the wide string section is 15 times wider than the narrow part. Secondly, they use the in-plane vibrational modes instead of out-of-plane. Since the in-plane bending stiffness is much higher for the wide string section it is practically unbendable. This creates huge bending losses at junctions between wide and narrow string sections evident on Figure 6.3a. Recall from section 4.2.6, when surface losses are present the quality factor is independent on membrane thickness when boundary bending losses dominate. In their case with in-plane modes, they observe only very weak dependence on the narrow beam width and quality factor. It can be concluded they are likely limited by boundary bending losses occurring at each narrow-wide boundary. This also means they were unable to utilize the full potential of phononic crystals. Nevertheless, they managed to obtain $Qf \approx 10^{12}$ at 100 MHz. At these high frequencies phonon tunneling losses would otherwise have decimated the quality factor.

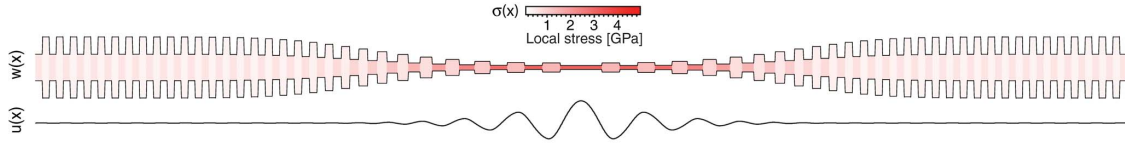


Figure 6.4: Illustration of strain engineering implemented on a string. The width and tensile stress distribution are shown. Combining soft-clamping from phononic crystals with co-localization of the confined mode-shape and enhanced tensile stress region creates a device with extremely high coherence. Adapted from [29].

Later on they have improved on their design [29] with three key differences. Firstly, they use out-of-plane vibrations now. Secondly, the width contrast (and thereby stress contrast) is much lower with $w_2/w_1 \approx 2$. Finally, the string is tapered such that it is at its thinnest at the defect. This co-localizes the confined mode with a region of enhanced tensile stress leading to more damping dilution and therefore higher quality factors. An illustration of their design is shown on Figure 6.4. The low width contrast results in a poorer band-gap. Nevertheless, when combined with out-of-plane vibrational modes the induced bending losses will be much lower than before. Their best result was a string with $Qf = 1.1 \times 10^{15}$ Hz at 1.3 MHz. To the author's knowledge no higher results have ever been published at room temperature for thin film tensile stress resonators.

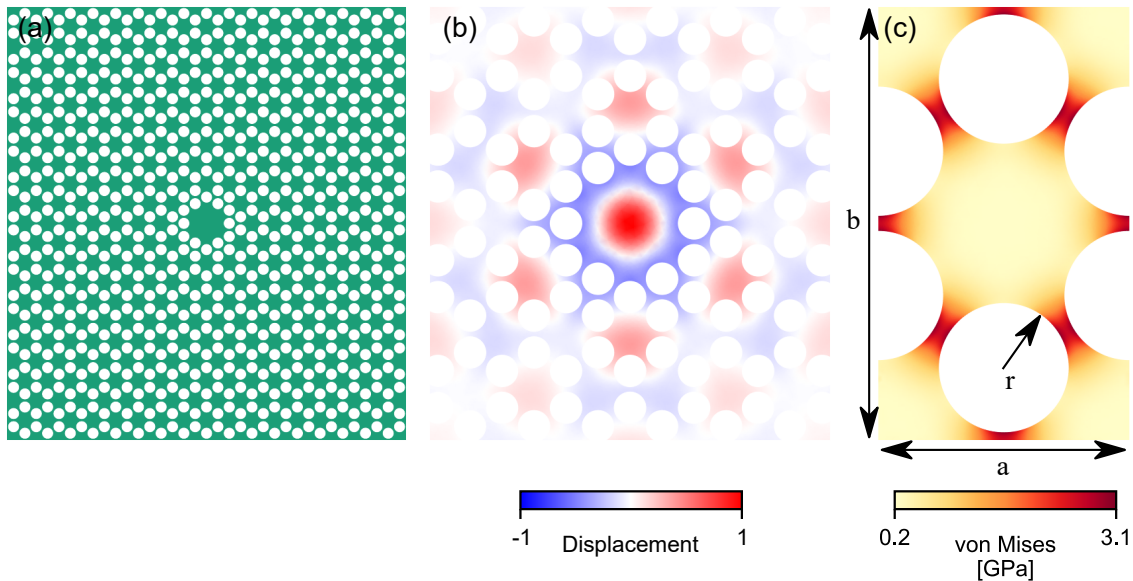


Figure 6.5: Drawing and simulations of a two dimensional phononic crystal. (a) shows a roughly 3-by-3 mm large phononic crystal patterned membrane with a defect placed in the middle. (b) Zoom-in on the defect with the symmetric defect-confined mode overlaid on top. (c) Static von Mises stress distribution of a phononic cell. Assumes a prestress of 1.27 GPa. Plotted with $a = 160 \mu\text{m}$ and $r = 0.26a$.

For the two dimensional counterpart, similar effect can be achieved by etching holes in a hexagonal pattern shown on Figure 6.5. The holes effectively creates a pattern of high-stress tethers connected via small low-stress pads. This omnidirectional stress pattern creates a band-gap in all directions and can be used to confine a two-dimensional inside a defect [51]. The band-gap of Figure 6.5c is shown on Figure 6.6. Notice the dispersion with sharp slopes. These are fast moving in-plane modes. As discussed before, for small

displacements the coupling between the in-plane and out-of-plane modes is negligible. One can therefore safely ignore these fast-moving modes. We then obtain a pseudo band-gap for the out-of-plane vibrations. The best results published based on these designs have $Qf = 5.6 \times 10^{14}$ at 1.48 MHz [53].

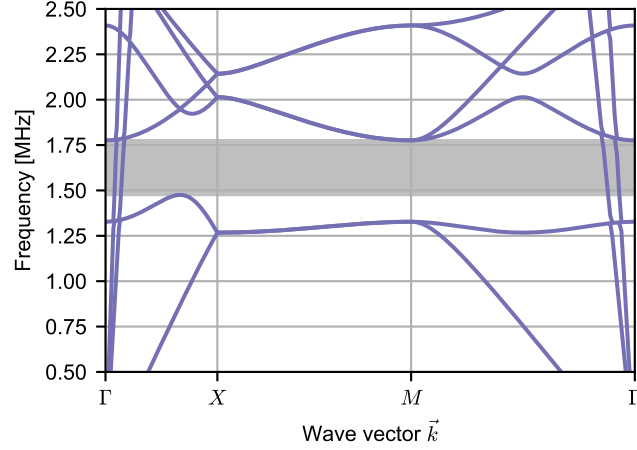


Figure 6.6: Dispersion relation of the device in Figure 6.5. The pseudo band-gap is highlighted.

A variation of the design has the band-gap enhanced by fabricating increasingly thinner tethers connecting the pads shown on Figure 6.7 [54]. As was argued for the one-dimensional case, thinner string segments can enhance to stress contrast, thereby widening the band-gap. The cost is the wider segments, or in this case larger pads, will have increasingly lower stress resulting in higher bending losses overall. They too concluded there exists the same compromise between a strong band-gap and low bending loss for two-dimensional phononic crystals. However, the benefit of this approach is it allows one to more effectively kill phonon tunneling losses which could start to dominate the quality factor significantly at cryogenic temperatures where intrinsic losses are observed to be much lower [55, 56].

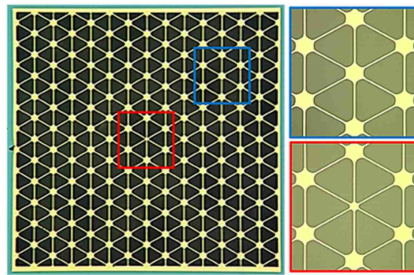


Figure 6.7: Microscope images of a membrane with band-gap enhanced phononic crystals by thinning the connecting tethers. Adapted from [54].

6.3 Soft-clamping of the fundamental mode: Fractals

For all the phononic crystal implementations studied so far they are all designed to confine the vibrations of some higher mode in a membrane. Due to this fact alone one can conclude this approach is incompatible with the fundamental mode of a resonator. Fortunately, a recent paper lays out an alternative design approach which can be applied on the fundamental mode of a string [57]: Self-similar structure using fractals. The approach

is shown on Figure 6.8a. At a given frequency f and tensile stress σ the mode vibrates at a specific wavelength $\lambda = 2\pi/k = \sqrt{\sigma/\rho}/f$. For a string with fixed boundary conditions, the eigen-frequency and its corresponding half-wavelength is obviously determined by its length. Now, at each end of the string replace the boundary condition with a new shorter string perpendicular to the original string. Since its length is much shorter than the original string, the mode cannot exist here. Furthermore, by removing the fixed boundary condition the original string can now freely rotate at each ends. This effectively removes the boundary bending losses which limits the performance of normal strings. Put in another way, it mimics the similar soft-clamping effect observed for phononic membranes.

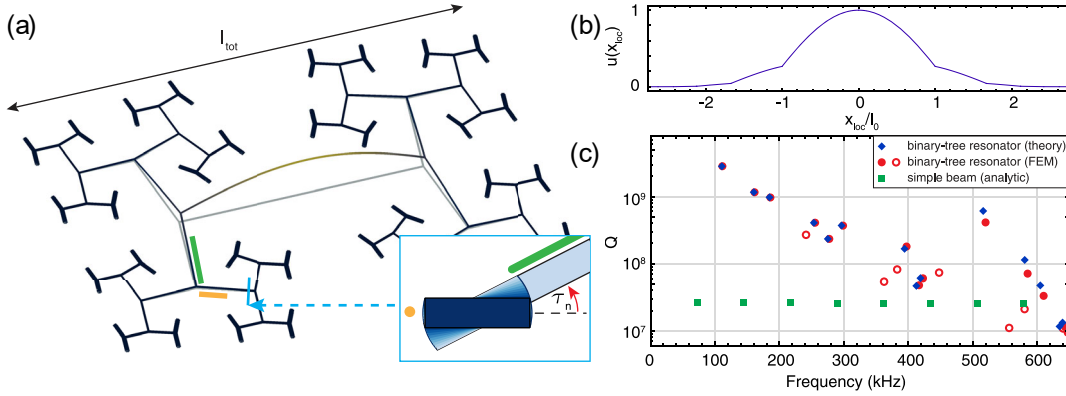


Figure 6.8: (a) Fractal designed resonator. (b) Displacement from the center going from tether to tether in the fractal design. (c) Predicted quality factors and frequencies. Adapted from [57].

For this implementation to work properly more than one branch is needed as shown on figure 6.8b to ensure proper soft clamping. Furthermore, each new branch needs to have their tethers slightly angled as well as increased tether width to preserve the high stress of the original string. In fact, by choosing the right angles and increasing the tethers widths more one can use this to enhance the stress above the prestress level. While they have only based their work on a string it should be possible to adapt this design to a trampoline, since a trampoline is essentially a pad connected by strings. Unfortunately, the design is just a proposal for now. To the author's knowledge no publications of any experimental realization exists yet. This could hint at this is difficult to fabricate. In-fact all the tethers at the outermost branches needs to be clamped at small points inside the design domain. Typically, one simply clamps the strings/membranes along an outer window, but this is incompatible with the fractal design.

6.4 Conclusion on soft-clamped resonators

Soft-clamping through the use of phononic crystals was reviewed. For tensile stress dominated resonators a phononic crystal can be defined by create a phase speed contrast defined by $c = \sqrt{\sigma/\rho}$, where σ can be modulated simply by modulating the width of a string or by creating pad-tether structures in a hexagonal pattern in two-dimensional membranes. The band-gap created by these crystals can be used to confine a vibrational mode inside the defect thereby isolating it when sufficient number of phononic crystal cells are used. Firstly, this eliminates phonon tunneling losses as this decouples it from the substrate. Secondly, due to the evanescent nature of this decoupling it effectively removes boundary bending losses. Combined, these two effects can be used to push the quality factor up to new heights compared to their fundamental mode counterpart.

For the fundamental mode, an alternative approach to soft-clamping can be applied through

the use of fractal layout of strings. Models show these can achieve high quality factor results comparable with their phononic crystal counterpart. Furthermore, it should be possible to adapt this approach for trampolines as well. Unfortunately, no experimental verification of this approach yet exists. This hints at these structures are a challenge to fabricate.

7 | Ringdown experiment

So far the focus has been on the physics behind resonators, what affects their quality factors and which designs have so far been developed to enhance this. A crucial element still missing is: How can the quality factor of a resonator be quantified? The best devices roughly have quality factors of $Q = 10^8$ at frequencies of $f = 1$ MHz. Based on the quality factor definition $Q = f/\Delta f$ the width of these modes are in the order of $\Delta f = 10$ mHz. Trying to resolve the spectrum of such a narrow mode is fraught with seemingly insurmountable challenges. The solution? Excite the mode and observe its amplitude decay over time. This is the mechanical ringdown experiment and for high quality factor modes this is an often used non-invasive method for quantifying the quality factor.

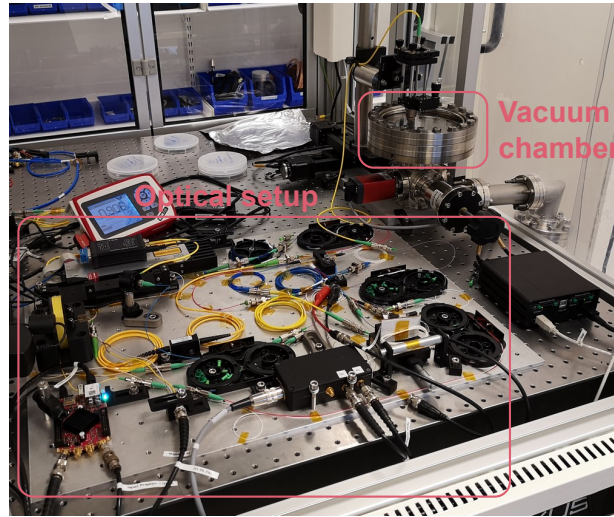


Figure 7.1: Photograph of the ringdown setup. All the fiber-optics is mounted on a bread-board with a fiber cable going out to the stage above the vacuum chamber.

This chapter first describes the experimental setup shown in Figure 7.1 used to measure the quality factor of *all* mechanical resonators studied during this work. The setup consists of an optical setup used for exciting and reading out the displacement of the resonators, as well as a high-vacuum system needed to remove gas damping losses. This is followed by considering some of the relevant physical effects affecting the experiment in the form of noise and perturbations.

7.1 Displacement measurement using homodyne detection

To successfully perform a ringdown experiment a sensitive and non-invasive method for probing the displacement of the resonator is needed. An obvious candidate is to probe the displacement with a light field and measure the reflected signal, since this can achieve high sensitivity with negligible perturbation and degradation of the probed sample when properly setup. An illustration of the measurement probing scheme is shown on Figure 7.2a.

A resonator oscillating with a frequency ω and displacement amplitude of $u(t)$ is probed by an incident plane light field $\alpha_i(x, t)$ which results in a reflected light field $\alpha_r(x, t)$. $\alpha_{\{i,r\}}(x, t)$

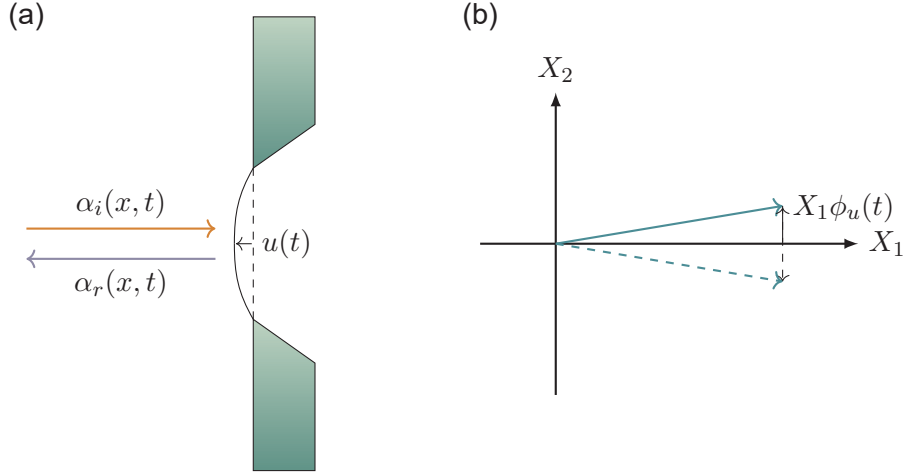


Figure 7.2: (a) Illustration of displacement measurement of micromechanical resonator embedded on a chip. (b) Phasor diagram showing the effects of the mechanical resonator on the phase quadrature of the reflected light.

is a complex dimensionless amplitude which is related to the electric field $\vec{E}(x, t)$ via [58]

$$\vec{E}(x, t) = E_0 \left[\alpha(x, t) e^{i\omega_E t} + \alpha^*(x, t) e^{-i\omega_E t} \right] \vec{p}(x, t), \quad (7.1)$$

where ω_E is the field's oscillating frequency and $\vec{p}(x, t)$ its polarization. The reflected amplitude is given by $\alpha_r(x, t) = \alpha_0 e^{i(kx + \phi_u(t))}$ where $\phi_u(t) = 2ku(t)$ is the phase change induced by the displacement of the resonator. The factor 2 arise from the fact the phase change has to take into account the path difference both before and after reflection. It is convenient to describe the reflected light field in terms of the amplitude $X1$ and phase $X2$ quadratures defined as

$$X1(x, t) \equiv \alpha_r(x, t) + \alpha_r^*(x, t) \quad , \quad X2(x, t) \equiv i[\alpha_r(x, t) - \alpha_r^*(x, t)] . \quad (7.2)$$

Substituting $\alpha_r(x, t)$ and assuming small displacements results in quadrature amplitudes

$$X1(t) \approx 2\alpha_0 \quad , \quad X2(t) \approx \delta X2(t) = 2\alpha_0 \cdot 2ku(t) , \quad (7.3)$$

where it is evident the displacement imprints linearly on the phase quadrature.

Homodyne detection is suitable for detecting weak signals in a specific quadrature. It consists of two beams, one containing the signal and one is the local oscillator, each defined by the amplitudes α_{in} and α_{lo} respectively. For the given system the amplitude of the beams are much larger than the fluctuations. Therefore, a linearized description is used $\alpha(t) \approx \alpha_0 + \sum_i \delta X_i(t)$. For each beam the following fluctuations are then defined

$$\begin{aligned} \alpha(t) &= \alpha_0 + \delta n1(t) + i[\delta X2(t) + \delta n2(t)] \\ \alpha_{lo}(t) &= \alpha_{lo,0} + [\delta n1_{lo}(t) + i\delta n2_{lo}(t)] e^{i\phi_{lo}} \end{aligned} \quad (7.4)$$

where $\delta n_i(t)$ are noise terms in the respective quadratures and ϕ_{lo} is the relative phase of the local oscillator. These two beams are then mixed through a beamsplitter and detected using a photo diode at each mixed beam. One of the beams will incur a π phase shift. When subtracting the two photo-currents, letting $\phi_{lo} = \pi/2$ and using the fact $\alpha_{lo,0} \gg \alpha_0$ leads to the result

$$i_{\Delta}(t) \propto 2\alpha_{lo,0}[\delta X2(t) + \delta N2(t)] , \quad (7.5)$$

where it is evident, that all noise from the local oscillator cancels out leaving only the signal from the phase quadrature. Furthermore, the local oscillator amplitude can be used to amplify any weak signal in the phase quadrature. Finally, the only optical noise left is the from the phase quadrature of the signal.

Assuming a measurement limited by shot noise, based on the above derivation this must come from the shot noise in the signal beam. The variance of the shot noise is given by

$$\text{Var}\{P_{\text{sn}}\} = 2P_{\text{in}}hfB \quad (7.6)$$

where P is the signal power, h the Planck constant, f the optical frequency in Hz and B the detector bandwidth. The amplitudes α_i can be defined relative to the local oscillator power, i.e. $\alpha_i = \sqrt{P_i/P_{\text{lo}}}$ or $P_i = P_{\text{lo}}\alpha_i^2$. This leads to the signal power fluctuation definition

$$\langle \delta P \rangle = P_{\text{lo}} \langle \delta X^2(t) \rangle = 16P_{\text{lo}} \frac{P}{P_{\text{lo}}} \frac{(2\pi f)^2}{c_0^2} \langle u^2(t) \rangle = 64\pi^2 P \frac{f^2}{c_0^2} \langle u^2(t) \rangle, \quad (7.7)$$

where $\langle \dots \rangle$ is the time averaged value and c_0 is the speed of light. The signal-to-noise ratio (SNR) is then

$$\text{SNR} = \frac{\langle \delta P \rangle}{\sqrt{\text{Var}\{P_{\text{sn}}\}}} = \langle u^2(t) \rangle \frac{32\pi^2}{c_0^2} \sqrt{\frac{2Pf^3}{hB}}. \quad (7.8)$$

It can be seen even though the local oscillator is able to amplify the signal coming into the homodyne, the shot noise poses a fundamental limit which can only be pushed by increasing the signal power. Furthermore, using a beam of shorter wavelengths (higher frequencies) increases the induced phase shift of the reflected signal thereby enhancing the embedded signal further. The minimum detectable amplitude can be defined by setting $\text{SNR} = 1$ leading to

$$u_{\text{rms,min}} \equiv \frac{c_0}{8\pi} \left(\frac{2hB}{Pf^3} \right)^{1/4}. \quad (7.9)$$

Based on the setup described in the following section, $P = 4 \mu\text{W}$ and $f = c_0/(1550 \text{ nm})$. Using a narrow band of $B = 1 \text{ Hz}$ then leads to the minimum detectable amplitude of 30 pm. As a comparison, the thermal motion amplitude is given via the equipartition theorem

$$m_{\text{eff}}\omega^2 \langle u^2(t) \rangle = k_B T, \quad (7.10)$$

where k_B and T is the Boltzmann constant and temperature, respectively. For a resonator at room temperature with $m_{\text{eff}} = 1 \text{ ng}$ and $m_{\text{eff}} = 2\pi \cdot 100 \text{ kHz}$ this leads to an effective thermal amplitude of 100 pm. The homodyne detection system is thus expected to easily be able to detect the thermal motion of a typical resonator.

7.2 The optical setup and measurement

The optical setup is sketched on Figure 7.3. A 1550 nm laser source is used for the ringdown setup, since commercial components at this wavelength are easily available. The first beamsplitter creates two arms. The top arm is the local oscillator where the phase modulator is used to lock the phase quadrature of the signal based on the DC part of the homodyne signal. The attenuator is used to control the phase quadrature signal amplification for the homodyne detection. The bottom arm contains the light send to the probed sample via the circulator and sends the reflected signal further towards the homodyne. The fiber polarization controller tunes the polarization to ensure proper

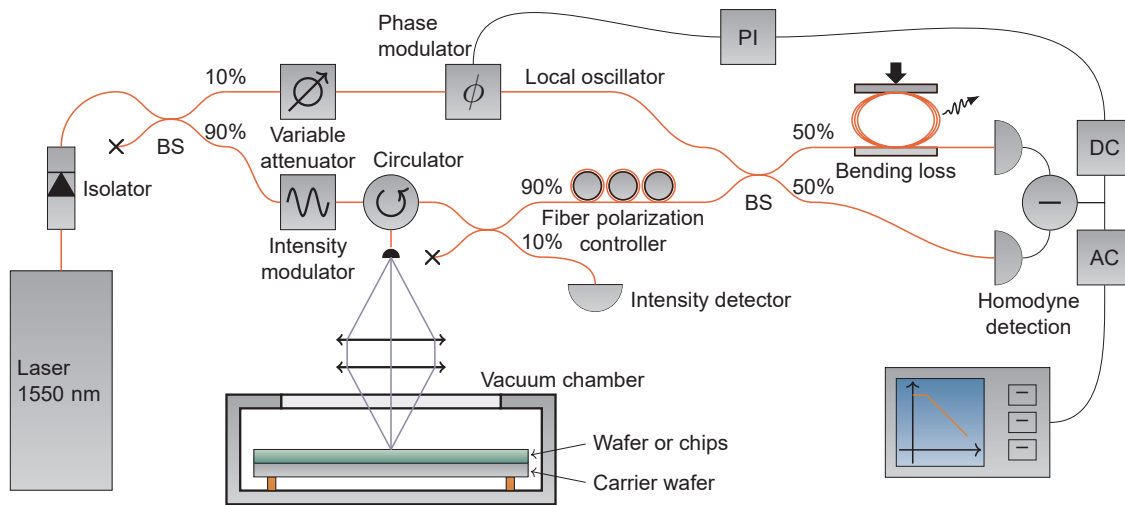


Figure 7.3: Sketch of the mechanical ringdown experiment setup used for characterizing all the samples.

overlap between the probed signal and local oscillator. The bending loss device is used to fine tune the balance between the two photo-detectors.

When the resonator to be analyzed is in focus the phase quadrature is locked using the PI-regulator of a Red Pitaya board. The sensitivity is high enough to detect the thermal motion of the mechanical modes at room temperature. The spectrum analyzer is now set to zero-span at the mechanical mode to be probed. Typically, a bandwidth of 30 or 100 Hz is used. Narrower bandwidths is possible and will create better signal-to-noise ratio, but it can make measurements difficult (see section 7.3.1). The intensity modulator is now switched on to modulate at the mechanical frequency. It requires some tuning of the intensity modulator's excitation frequency to hit the resonance due to the extremely narrow linewidth of the mechanical mode. When it is in resonance a large increase of the reflected signal will be detected. In fact, this signal is usually much greater than what is returned by the intensity modulator itself, thus it can be seen even when the modulation is on. When everything looks fine the modulation is switched off and the ringdown decay is recorded and saved.

7.2.1 Vacuum system

As mentioned previously, a proper high-vacuum system is needed to ensure the high-Q resonators won't be affected by gas damping. The pressure must be below 10^{-7} mbar to effectively remove gas damping. A turbomolecular pump (Edwards T-Station 85) is used together with a diaphragm vacuum pump (Edwards XDD1) as the backing pump to achieve the required vacuum. Pressures down to 3.5×10^{-9} mbar have been measured using this setup. Pressure measurement is done with a cold cathode ionization vacuum gauge (Pfeiffer Vacuum D-35614 Asslar).

To achieve such low pressures the chamber needs to be clean. Any contamination might outgas and therefore act as a lower limit on the obtainable pressures. To prevent this, every part must be cleaned using acetone followed by ethanol or isopropanol. This includes all vacuum parts. Moreover, all joints are sealed with copper gaskets. If the system has been vented for longer amounts of time water will get adsorbed to the chamber walls. When pumping out these will outgas again preventing one to obtain high vacuum. When this is the case there are two solutions: Let it pump until all the water is outgassed. No

proper estimation of this was done on this project, but from experience this will take at least a week. To accelerate it one may instead bake it for a day at 120-130 °C. Ideally, the chamber should never be vented for a long enough time for this to become an issue. By always having it pumped down and only venting it for short durations for changing the wafer/chips this problem can be prevented.

When inserting the wafer/chips the system is typically pumped overnight resulting in a pressure below 10^{-7} mbar. When left for a few days the pressure drops to below 10^{-8} mbar. No data indicates the latter is needed. This enables one to characterize a wafer full of resonators per day.

7.2.2 Quality factor estimation

After a mechanical ringdown is performed the quality factor needs to be estimated. Consider a resonator mode with an initial amplitude u_0 and decay rate α_Δ . The time evolution of its amplitude has the form $u(t) = u_0 e^{-\alpha_\Delta t}$. The decay rate is related to the mode's eigen-frequency f and quality factor Q via $\alpha_\Delta = \pi f / Q$. For exponential decays it is convenient to use decibel-based units instead. By defining $u_{\text{dB}}(t) = 20 \log_{10}(u(t))$ the slope is then given by

$$\frac{du_{\text{dB}}(t)}{dt} = \frac{20\pi}{\ln 10} \frac{f}{Q} \approx 27.288 \frac{f}{Q}. \quad (7.11)$$

The quality factor is then simply defined by the slope of the decay of the oscillation amplitude on the dB scale

$$Q = \frac{20\pi}{\ln 10} \frac{f}{du_{\text{dB}}/dt} \approx 27.288 \frac{f}{du_{\text{dB}}/dt}. \quad (7.12)$$

An implementation of this on a select ringdown is shown on Figure 7.5.

7.3 Noise and perturbation during measurement

The setup is highly sensitive, both in terms of resolvable displacements as well as resolvable frequencies. Unfortunately, it also makes it susceptible to various sources of noise and perturbations which may affect the ringdown experiment. This section provides an overview of these problems encountered during this work.

7.3.1 Thermal drift

Ultra-coherent resonators are remarkable sensors. Their low thermal mass and high quality factors mean they are very sensitive thermal sensor and potentially an attractive candidate for broadband photo-detection [59]. When performing the ringdown experiment the absorption of the incident infrared light will heat up the resonators. Due to thermal expansion the resonator will expand slightly leading to lower stresses and a small offset of the resonance frequency.

Simulations show the characteristic time constant for reaching a new thermal equilibrium is typically measured in milliseconds as shown on Figure 7.4. Curiously, the frequency shifts has in some samples been observed shifting 100s of Hz over the time span of minutes upwards towards *higher* frequencies, which contradicts the previous reasoning. It is therefore difficult to argue if this is really due to thermal effects or some other effects are acting on the resonator. If the presence of an incident beam changes the absorptivity of the resonator over time, this could create slow frequency drifts related to thermal effects. Indeed, it was observed bad samples with inherently low quality factors often showed more aggressive frequency drifts compared to good samples. Consider this case: If the bad quality factor is a result of residual material or particles on the resonator, a focused high intensity beam might burn off some of these contaminants slowly over time.

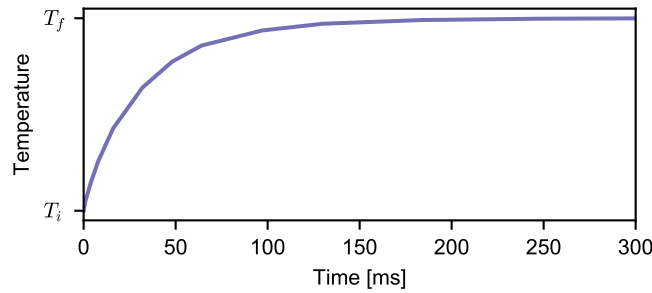


Figure 7.4: Simulation of heating of the central pad of the reference trampoline design in Part II. The time constant is estimated to 29 ms. T_i and T_f are the initial and equilibrium temperatures, respectively.

This slowly leads to lower absorption, and as a consequence, less heating and therefore slightly higher frequencies over time.

Similar experiments performed in a cryostat showed no drift for resonator modes below 1 K. The low temperature requires low power of the incident beam which combined with the already low temperature likely prevents any burning of contaminants. It is believed the above explanation for the observed frequency drift is plausible.

In general, when it is known resonance drifts are possible, one cannot use the narrowest bandwidth of the spectrum analyzer even though it would lead to higher signal-to-noise ratio. For example, if the bandwidth is set to 1 Hz, but the resonance drifts 10 Hz during the course of a ringdown experiment, what the user will observe is a gradual steepening of the slope of the decay as the resonance leaves the bandwidth of the spectrum analyzer. This gives the illusion of the damping increasing as the amplitude goes down. Such a measurement is useless. Normally, a bandwidth of 100 Hz is more than sufficient for these measurements, which guarantees the resonance is kept within the bandwidth of the spectrum analyzer. In case of cryostat experiments, the signal will be low due to the requirement of low laser power. Since no significant drifts have been observed in these conditions, using the narrowest bandwidth of the spectrum analyzer is appropriate in order to maximize the signal-to-noise ratio.

7.3.2 Nonlinear mechanical effects

For the purpose of this work restricting oneself to the linear regime valid for small displacement is fine when attempting to maximize the quality factor. However, the low mass and high quality factor of ultra-coherent resonators make them very easy to excite into the nonlinear regime as discussed in chapter 5. Both the predicted stiffening and increased damping at larger amplitudes have been observed during measurements.

There are no data available clearly demonstrating the stiffening effect, thus a description of the observation will instead be given illustrated on Figure 7.5a. When the frequency of the external force modulation is swept from the left of the resonance, one will observe an increasingly higher amplitude signal. At some point, due to the nonlinear stiffness, the threshold of maximum possible displacement amplitude is reached and the amplitude will quickly jump down again. To get back into resonance again one cannot simply return back to last excitation frequency, where the resonance was last observed. The nonlinear skewed amplitude response means one has the sweep back by a considerable amount before sweeping from left again. In general, the nonlinear response implies excitation is easiest when sweeping from the left side of the resonance.

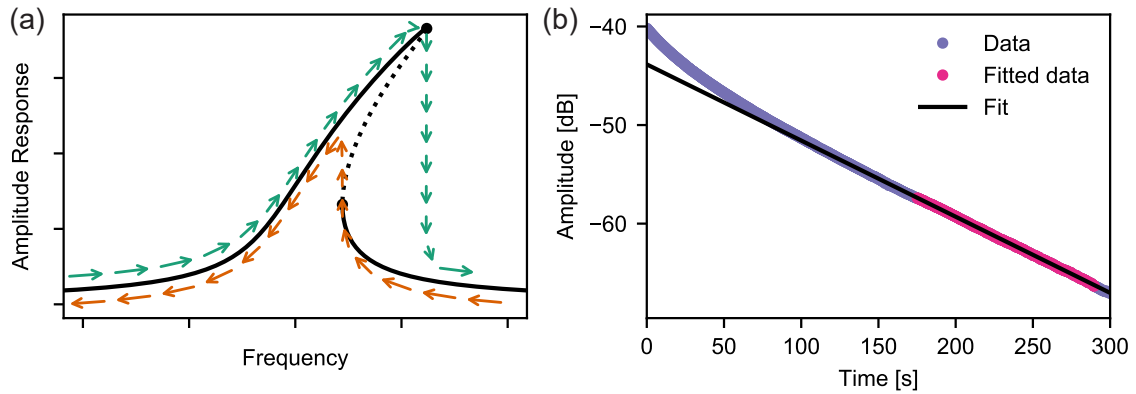


Figure 7.5: (a) An illustration of how the nonlinear amplitude response of a resonator affects excitation of the mode. The maximum achievable response amplitude depends on the direction of the external excitation frequency sweep. (b) An example of a ringdown, where a steeper decay was observed in the first 100 seconds. This is evidence for nonlinear induced damping.

An example of the observed nonlinear induced damping at higher amplitudes is shown on Figure 7.5b. This has only been observed in a subset of data and only on high quality factor resonators, which is expected. It is evident on Figure 5.2 this effect can only be observed deep in the nonlinear regime.

7.3.3 External vibrations



Figure 7.6: Photograph of the setup showing the turbomolecular pump and how it is connected to the vacuum chamber.

When performing measurements with a sensitivity down to the picometer scale obviously any external source of vibrations can pose problems. Seen on Figure 7.6 the combination of optical table and isolation of the turbomolecular pump should impede the majority of vibrations coupling into and interfering with the measurements. While the resonator itself appears unaffected by anything going on outside (other people working on the optical table, turbo-pump, walking, etc.) the measurement does register these external disturbances. The largest challenge however is the vibrations induced by the diaphragm

vacuum pump. These have large low-Hz frequency components which require a large dynamical range of the phase-locking scheme to keep it locked. This leads to a more unstable lock. Often, the lock is lost more than once during a single ringdown. Tests were performed turning the pump off for short amounts of time. This removed the noise completely. It is worth noting these artifacts in the measurements can easily be filtered away in post-processing, and is therefore not a major problem. A solution to this problem is to use a passive pumping system like an ion pump when performing ringdowns.

7.3.4 Other effects

It is speculated there are nonlinear effects within the ringdown setup affecting the measurements. There are many examples of ringdown decays where the slope is small at high amplitudes and then converging to a steeper slope mid-way during the ringdown. Since large amplitudes also correlate to large optical and electrical signals there might be a component somewhere getting saturated. No deeper investigation on this was ever performed. The prime suspect for this effect is the home-build homodyne detector.

7.4 Conclusion

A description of the homodyne detection system used to detect the small resonator displacements was given. The setup is able to measure the thermal motion. This is enabled by the homodyne's inherent ability to amplify weak signals. Since this also amplifies the noise embedded in the signal, there is a fundamental limit of how large an SNR that can be obtained, which is ultimately defined by the shot noise. The only way to improve the SNR is thus reducing losses of the signal beam between the resonator and homodyne, and by using a shorter wavelength for the optical system.

The optical system is fiber-based and build for 1550 nm wavelength. A high vacuum is needed to ensure gas damping does not affect the results. This is obtained through the use of a turbomolecular pump and sealing vacuum components using copper gaskets. Proper cleaning and subsequent baking ensures all humidity is baked off the surfaces thereby preventing prolonged out-gassing, which would limit the obtainable vacuum of the system.

Multiple noise sources and other perturbing effects were identified. Firstly, the low mass and high quality factors of the resonators make them easy to excite well into the nonlinear regime. This perturbs their behavior when exciting them for the ringdown experiments. Secondly, a fraction of the incident beam will be absorbed by the resonator, which will shift the frequency over time. The slow drift compared to the time-constant derived from simulation provides evidence for slow changes happening on the resonator. It is not clear if this is a result of particles getting burned off or if it might be something else either related or not related to the incident beam at all. Thirdly, the diaphragm vacuum pump induces strong low-frequency mechanical vibrations making the phase-lock in the homodyne detection unstable. While this is not a critical problem, it is an annoyance during measurements. Finally, there are signs of nonlinear effects from the measurements themselves at large signals. This might be a result of a component somewhere saturating.

This concludes the fundamentals which is the foundation on which the rest of this work is build upon. With the important theory and mechanical effects defined as well as the relevant experiments described it is time to move on. The rest of the thesis will focus on the new designs developed with the aim of pushing the performance of already existing designs using different approaches.

Part II

Topology Optimized Trampolines

8 | Overview

When generating a new mechanical design to solve a given problem how can one obtain the best possible design? There are a multitude of options. One could study an array of existing designs trying to solve similar problems and systematically adapt or improve on them to solve the current problem in the best possible way. For example, when optimizing the Qf -product of the fundamental mode of a trampoline one could make use of the expressions for the quality factors in Eq. (4.31) and (4.53) for intrinsic and phonon tunneling losses, respectively, to perform this analytically or by sweeping relevant parameters using finite element simulations. The disadvantage of using an approach like this is its inherent uncreativity. It is naive to believe the trampoline as previously presented is the best type of design possible. How does one then escape this box of traditional designs and instead create something truly novel and exotic?

A major part of this work is to achieve exactly that by using topology optimization [60]. Starting out from some initial feature-less design it can generate new designs based on the given objective, conditions and constraints. This approach has for the last decades created impressive optimized designs in countless macro- and micromechanical problems as well as other fields like photonics [61, 62, 63, 64, 65]. From this track record, it is believed that topology optimization can enhance the coherence of micromechanical resonators.

To limit the scope of this project, the focus is the fundamental mode of a thin-film tensile stress resonator. The figure of merit for a resonator's coherence is the Qf product, which is chosen as the objective function to be maximized. The actual implementation of the topology optimized was done by Wenjun Gao under the supervision of Ole Sigmund and Fengwen Wang. Chapter 9 describes the implementation and conditions of the topology optimization. Since the implementation itself is outside the scope of this work, the reader is referred to [66] for a more detailed description.

The novel designs obtained using topology optimization are put through a rigorous analytical analysis in chapter 9, where important aspects of these designs will be discussed. The fabrication of the designs is treated in chapter 10 followed by a presentation and discussion of the record-breaking ringdown experimental results in chapter 11.

9 | Topology optimization

Topology optimization is a mathematical method for optimizing a layout within a given design domain for a given set of conditions and constraints [67]. When a model is defined and meshed, topology optimization can be used to generate designs solving the problem in the best possible way. The designs may converge to familiar solutions or generate completely new and exotic structures which highlight new approaches otherwise difficult for a designer to anticipate.

As with other algorithmic methods, the designs are only as good as the model. Any weakness which may exist in the model are at risk to be exploited which may lead to nonsense results. Furthermore, convergence towards to global minimum is never guaranteed. Even though topology optimization is an incredible tool for solving various problems, there can be serious physical, mathematical and algorithmical challenges which needs to be dealt with to ensure good and meaningful results.

In the first section some basic theory of topology optimization will be presented. Even though the implementation of topology optimization is outside the scope of this work, having some basic knowledge of the approach is valuable for understanding the results. This is followed by a presentation of the physical model used for the optimization. In section 9.2 the generated designs are presented.

9.1 Basic theory and implementation

In topology optimization a spatial-dependent *design parameter* $\tilde{\rho}(x, y) \in [0, 1]$ is defined and is a measure of the density of the material within the domain $\tilde{\Omega}$ to be optimized. When performing topology optimization one tries to iteratively update the distribution of $\tilde{\rho}(x, y)$ which maximizes/minimizes the objective function. It is up to the user to determine how to relate $\tilde{\rho}(x, y)$ to some physical parameters. For the current case of optimizing a resonator, the design parameter scales the material density $\rho \rightarrow \rho(x, u) = \rho_0 \tilde{\rho}(x, y)$ and element volume $V_e \rightarrow V_e(x, u) = V_0 \tilde{\rho}(x, y)$. The Young's modulus E is also related to $\tilde{\rho}(x, y)$, using the *rational approximation of material properties* model [68]

$$E \rightarrow E(x, y) = E_{\min} + \frac{\tilde{\rho}(x, y)}{1 + q(1 - \tilde{\rho}(x, y))} (E_0 - E_{\min}) , \quad (9.1)$$

where $q \geq 0$ is a penalization parameter which penalizes intermediate values of $\tilde{\rho}(x, y)$. E_{\min} and E_0 are the minimum and maximum allowed values of E . Setting $E_{\min} > 0$ prevents numerical singularities. The above is a simple description of topology optimization, where important concepts like projected and filtered design parameters have been left out for the sake of brevity.

With the basics of topology optimization presented, it is time to focus on the physical model of the system sketched on Figure 9.1. The optimization is performed on a $700 \times 700 \mu\text{m}^2$ large domain. To save computational costs only a quarter of the membrane is modeled. The purpose of the resonator is to be used in opto-mechanical systems. Therefore, a pad in the center is needed for to effectively couple the vibrations to an incident light field. This is modeled as a fixed material, i.e. $\tilde{\rho}(x, y) = 1$ at the pad. Likewise, to ease fabrication a narrow overhang is defined along the outer boundary by setting $\tilde{\rho}(x, y) = 1$. The rest of the quarter domain is free to evolve.

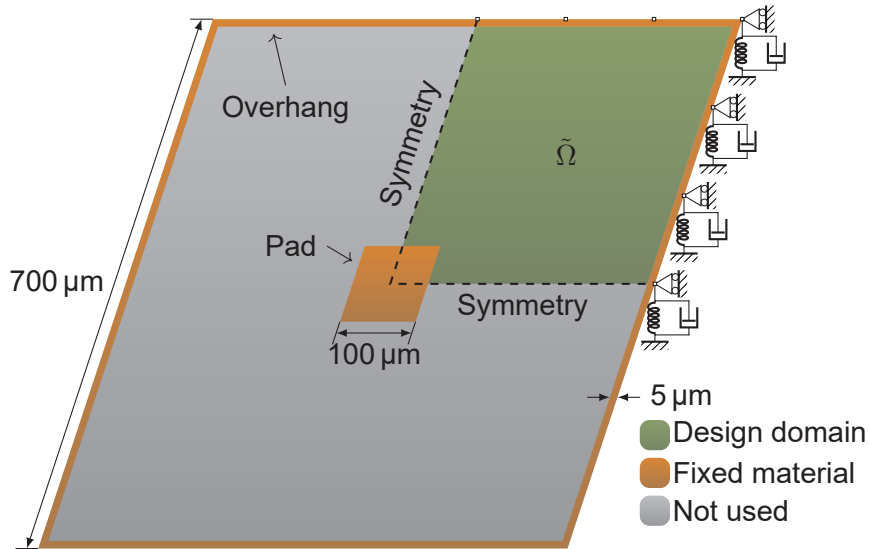


Figure 9.1: An illustration of the model used for topology optimization. Only one quarter is modeled. Note the overhang is not drawn to scale.

The mechanical system is modeled using the Mindlin plate theory assuming 50 nm silicon nitride. Recall, for a membrane under high tensile stress whenever some segment is removed or added this changes the equilibrium state of the membrane leading to a new tensile stress distribution for the whole membrane. To account for this the evaluation of the membrane design has to be done in two steps:

1. Static step: Estimate the equilibrium state to obtain the strain, and thereby tensile stress distribution for the current design.
2. Dynamic step: Solve the eigen-value problem to obtain the modeshapes and eigen-frequencies of the resonator.

So far, damping has been ignored. Two damping mechanisms were included: Intrinsic and phonon tunneling losses. The intrinsic losses were modeled as hysteretic damping, i.e. a lossy Young's modulus is used as described in section 4.2. The phonon tunneling losses however were implemented differently than discussed in section 4.3. This was due to the lack of proper understanding of the damping mechanism early on during this work and the literature was lacking. For this model, a continuous distribution of independent lossy springs was used as a boundary conditions for the out-of-plane displacements while keeping all other degrees of freedom fixed as illustrated on Figure 9.1. From this, five different damping cases were defined:

- D1: Only limited by intrinsic losses.
- D2: Mostly limited by intrinsic losses.
- D3: Equally limited by intrinsic and phonon tunneling losses.
- D4: Mostly limited by phonon tunneling losses.
- D5: Only limited by phonon tunneling losses.

For exact details on how this was defined and implemented the reader is directed to [66].

Finally, how should the objective function be chosen? The figure-of-merit for optomechanical systems is the Qf product making it an obvious candidate. By optimizing only for the

quality factor one, will obtain a design with a high quality factor, although there is a risk the generated design could have a low tensile stress distribution leading low frequencies and therefore low Qf -products. Recall from chapter 4 lower frequencies generally lead to higher quality factors. However, it should be noted for the current cases when optimizing only for the quality factor the difference compared to using the Qf -product was in fact shown to be very small.

The phonon tunneling loss model used here is strictly speaking not optimal. Recall from section 4.3 when only the fundamental mode is considered the phonon tunneling loss should be modeled assuming a single spring attached to a rigid frame defined along the resonator-substrate boundary. By instead defining a distribution of independent springs the expected damping will be different. Consider the case of the reference trampoline where all the forces are focused on the corners of the domain only. The springs at the corners will feel the full force of the trampoline whereas the springs along the sides won't be activated at all. Effectively, only a fraction of the springs are actuated which reduces the overall coupling stiffness to the substrate. This leads to easier coupling to the substrate and therefore higher losses. This is a clear weakness of the model and as will be seen it is suspected the topology optimization takes advantage of it in the cases where phonon tunneling losses are included.

Another problem comes from the use of simple springs. Again, from section 4.3 when a lossy spring is used to model phonon tunneling losses it is frequency dependent, unlike the normal spring. This is another weakness of the model which the topology optimization might take advantage of. To illustrate the problem, consider a resonator with mass m and stiffness k connected in series with a lossy spring ik_ϕ to some reference frame. The complex spring represents the coupling to the substrate. Assuming $k \ll k_\phi$ the quality factor is given by

$$Q \approx \frac{k_\phi}{m\omega^2}, \quad (9.2)$$

where $\omega = \sqrt{k/m}$ is the resonance frequency of the resonator. For the phonon tunneling loss implementation used for topology optimization this leads to the scaling $Qf \propto \omega^{-1}$. The results will be biased towards lower frequencies using this approach. Compared to the proposed models in section 4.3 where $k_\phi \rightarrow k_\phi(\omega) \propto \omega$ leading to the scaling $Qf \propto \omega^0$ and thus no bias with respect to the frequency.

Finally, the chosen mesh resolution is fine enough to resolve features which can be reasonably fabricated. However, it is too coarse to resolve the sub- μm high boundary bending losses. This will lead to an underestimation of the boundary bending losses which could lead to improper designs for the fundamental mode when intrinsic losses dominate. However, simply refining the mesh to resolve this would lead to extreme computational demands. One could transform the meshed grid to a finer resolution only near the boundary. This is left for future work.

9.2 Topology optimized designs

Based on the optimization and physical model described above a set of topology optimized designs were generated presented on Figure 9.2. The original designs are directly translated from a two-dimensional binary image. The processed designs have "overhanging" features filtered out followed by smoothing of sharp features to prevent local areas with extremely high tensile stresses, which could lead to breakage. The difference between the original and processed designs are highlighted in Figure 9.3. The reason for this design modification will be explained in section 10.7. As a comparison, a reference model was defined based on the nominal parameters of the trampoline Ref. [25].

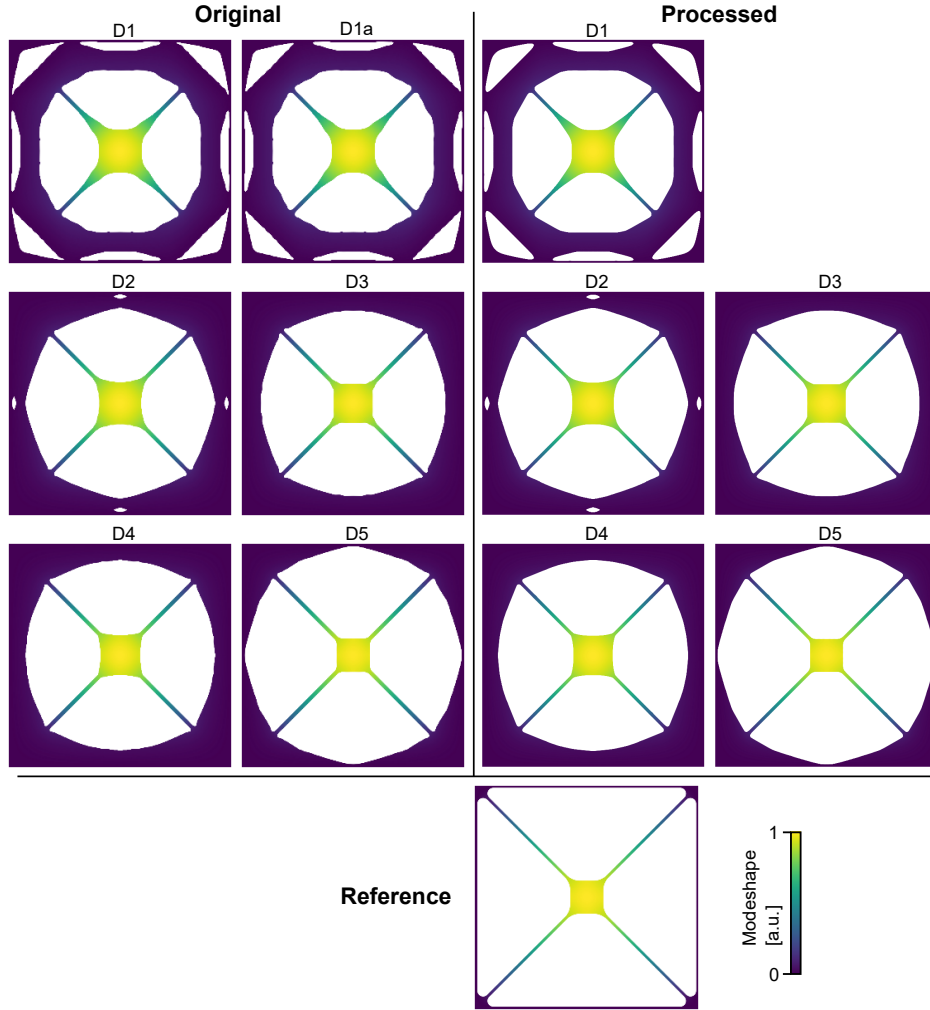


Figure 9.2: All the generated fundamental mode topology optimized designs used in this work shown together with their fundamental mode. The original designs are without post-processing. The processed designs have overhang features filtered away. The design labeling correspond to the damping cases. D1a is a modified version of the original D1 design with lower max tensile stress. The reference trampoline design is based on the nominal parameters given in [25].

9.2.1 Numerical evaluation of the designs

Before testing the designs experimentally a thorough numerical analysis should be performed on them to validate their performance as well as identify key design features explaining their advantages. COMSOL Multiphysics is a great tool for this and has been used throughout this work to develop and analyze various designs and structures.

COMSOL is used to estimate the eigen-frequency and modeshape of the fundamental mode of each design. COMSOL has build-in functionality to estimate the intrinsic quality factor when the material loss factor ($\approx \tilde{\phi}$) is given. However, under high tensile stress it leads to nonsense results. For now, there is no solution to this bug. Instead, one can easily estimate the intrinsic losses in post-processing by using Eq. (4.21).

Next, how to model the phonon tunneling losses? Ideally, one want to model the whole substrate-resonator system. This means modeling the resonator placed on a fully three-dimensional substrate. While COMSOL does support the combination of a two-dimensional

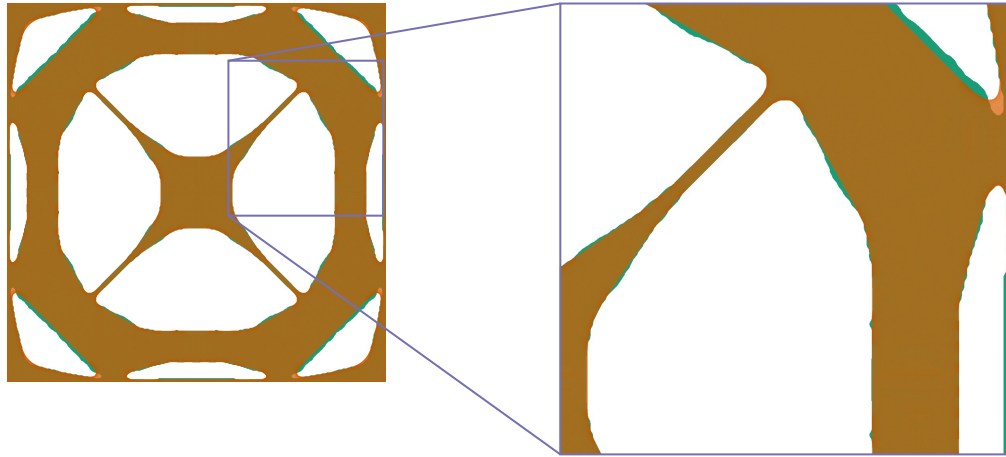


Figure 9.3: Comparison between the original D1 design (green) and the corresponding processed design overlaid on top (brown).

shell module with a three-dimensional structure, evaluations of such a system has shown to yield unstable numerical results. Moreover, modeling the whole system as a three-dimensional structure is unfeasible with the aspects ratio of a typical resonator. An alternative approach is needed. The phonon tunneling losses for the fundamental mode can be estimated by implementing a rigid frame around the resonator. This frame is then connected to some reference via a lossy spring. For most measurements the resonators will be embedded on a 100 mm diameter silicon wafer with thickness 500 μm . Under these conditions the spring constant defined for the expectation value of the finite substrate model is used, i.e. Eq. (4.78).

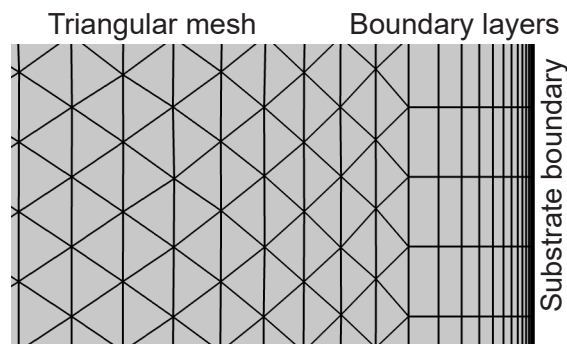


Figure 9.4: Boundary layer implementation used for modeling boundary bending losses for trampolines and other structures. The smallest element equals the membrane thickness h .

Using COMSOL a maximum mesh size of 2.5 μm is defined. To properly resolve boundary bending losses this is combined with boundary layers along the resonator-substrate edge, where the first elements have a size of h , i.e the membrane layer thickness. This is illustrated on Figure 9.4. This was found to be a suitable value and works well for multiple thicknesses. To estimate the different quality factors a four step simulation is performed:

1. **Static simulation, fixed boundaries:** Estimates the equilibrium state for obtaining the tensile stress distribution.
2. **Eigen-frequency simulation, fixed boundary:** Obtains the eigenfrequency to be

used for the nonlinear lossy spring for the phonon tunneling loss model. Furthermore, the total intrinsic loss quality factor Q_{int} is estimated via post-processing of the modeshape.

3. **Eigen-frequency simulation, simply supported boundary:** Removes the boundary bending loss contribution, thus enables estimation of the distributed loss quality factor Q_{dist} . The boundary bending loss quality factor can then be estimated via $Q_{\text{bound}}^{-1} = Q_{\text{int}}^{-1} - Q_{\text{dist}}^{-1}$.
4. **Eigen-frequency simulation, rigid frame boundary:** By coupling the rigid frame to a phonon tunneling loss model defined lossy spring the respective quality factor Q_{PTL} can be estimated. The frame cannot rotate and can only move in the out-of-plane direction. The membrane cannot rotate at the frame.

Note, by replacing the fixed boundary condition with a simply supported one, evanescent wave k_e at the boundary will disappear. Apart from removing boundary bending losses it will also increase the effective size of the modeshape at the order of $1/k_e$ thereby reducing the eigen-frequency. However, at high tensile stress $1/k_e \approx 200$ nm thus this effect is negligible. An overview of the quality factors, eigen-frequencies and effective masses can be seen on Figure 9.5 for all designs.

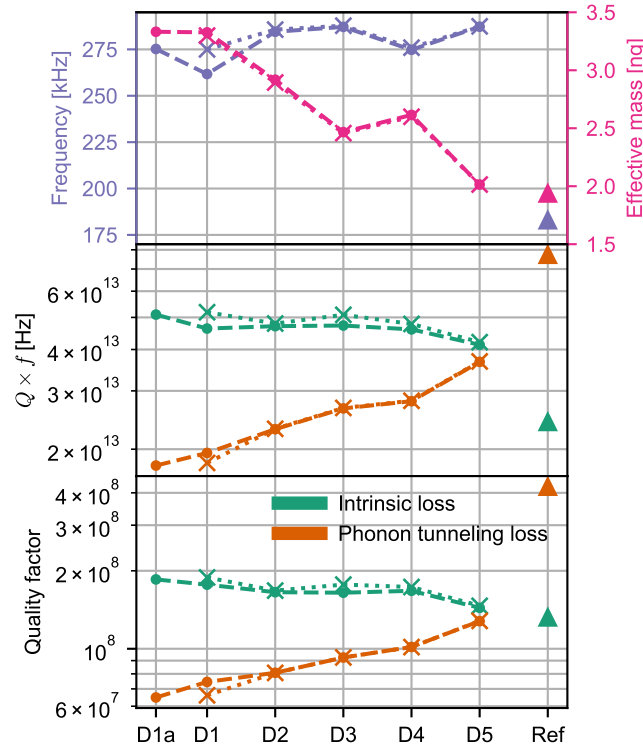


Figure 9.5: An overview of simulation results of all generated topology optimized designs based on 50 nm silicon nitride thickness. Circle-dashed lines are the original designs. Cross-dotted lines are processed designs. Note the phonon tunneling loss defined quality factor is the analytically derived expected value with a spread of orders of magnitude in both directions. Prestress is 1.14 GPa estimated via Eq. (10.1). The remaining values assumed: $\beta_{\text{surf}} = 4.74 \times 10^{11} \text{ m}^{-1}$ and $Q_s = 1.45 \times 10^5$.

9.2.2 Discussion on results

Firstly, there is practical no difference between the original and the processed results, thus for simplicity all later numerical estimates will be based on the processed designs,

only. Next, the resonance frequencies for all of the optimized designs are almost equal at ~ 285 kHz where the D1 and D4 designs show a somewhat lower frequency.

When looking at the intrinsic loss defined quality factors, one expects to see D1 designs to perform best, which is indeed the case. However, the difference between all the optimized designs is less than a factor of two. This is likely a consequence of the surrounding circular-like frame, which they all have. With that in mind, the reference trampoline's quality factor is only a little worse compared to the rest, but when combined with the significantly lower resonance frequency, the optimized D1 designs have Qf products at more than a factor of two compared to the reference.

How is the Qf -product enhancement obtained in terms of intrinsic losses? Figure 9.2 clearly shows the mode is well confined inside the circular frame. How does this affect bending losses? The bending losses for D1 is shown on Figure 9.6a. Firstly, as expected there is a large amount boundary bending losses highlighted by the inset. There is also a lot of bending at the central pad which is due to the low stress inside the pad. This lowers the stiffness locally leading to sharper bending and consequently higher losses. Moreover, there is also a significant amount of bending at the outer end of the central tethers. On Figure 9.6b a large stress component on the circular frame perpendicular to the tethers is observed. The wavelength predicted by the stress and frequency is ~ 2 mm, which is much larger than the dimensions of the resonator. The mode cannot exist on the circular frame which naturally leads to the mode confinement seen on all the designs. It is believed this mode confinement partially dilutes the boundary bending losses which overall leads to a higher intrinsic loss limited quality factor. The distributed and boundary bending quality factors for the designs are shown on Figure 9.6c. Here it is seen the quality factor is clearly limited by boundary bending losses, and that D1 is better optimized in reducing this loss mechanism compared to the rest. It is worth noting the mode confinement strategy for D1 is similar to the fractal designs discussed in section 6.3, when considering only one level of branches.

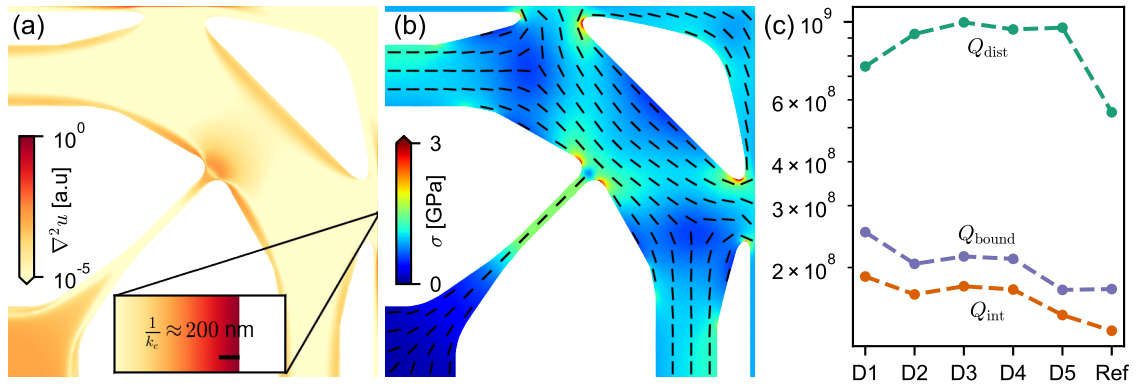


Figure 9.6: (a) Bending loss distribution of D1. The inset demonstrates the high bending boundary losses expected for fundamental mode resonators. (b) Von Mises stress distribution of D1. The bars are oriented with respect to the dominant stress component. (c) The intrinsic loss quality factor (Q_{int}) for the different designs together with the distributed (Q_{dist}) and boundary (Q_{bound}) bending loss quality factor contributions.

For the phonon tunneling loss quality factors in Figure 9.5 there is a clear trend from the bad performing D1 designs up to the optimized D5 designs. This seems to neatly follow their effective masses, where lower mass is generally better at limiting phonon tunneling losses. However, when compared to the reference trampoline the optimized

D5 performs bad even when taking the higher resonance frequency into account. Why is that? As highlighted in section 9.1 it is likely evidence of the topology optimization exploiting a weakness of the model. To better discuss this the shear boundary force for the optimized design D5 is shown on Figure 9.7. When phonon tunneling losses is modeled as a distribution of independent lossy springs the maximum effective coupling spring stiffness, and thereby quality factor, is achieved when the force is evenly distributed across the boundary. From the plot it is evident this distribution for D5 is much more evenly distributed than the reference design. It is therefore reasonable to believe this weakness has affected the results considerably.

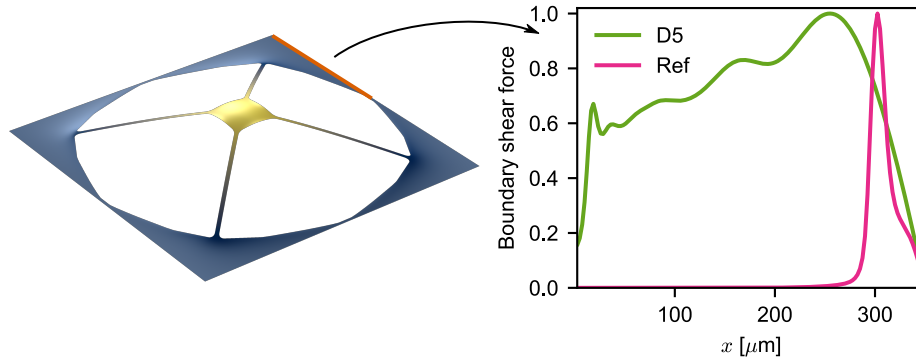


Figure 9.7: Boundary shear force of design D5 and the reference along a 1/8 section of the resonator. The amplitude of the shear force is normalized.

9.3 Conclusion on topology optimization

A simplified description of the theory behind topology optimization was given. The implemented model for the optimization was introduced and discussed. Five damping cases were defined ranging from a purely intrinsic loss limited case to a purely phonon tunneling loss limited case as well as mixtures of those two in between.

The use of a continuous distribution of independent springs along the boundary to model the phonon tunneling losses is problematic and could be a weakness of the model the optimization might utilize. In fact, numerical evaluation of the generated designs show there is reason to believe this has happened. Unfortunately, D5, which supposedly should be well optimized against phonon tunneling losses, shows considerably worse performance compared to the reference trampoline design. Since the theory for phonon tunneling losses became properly understood on a later stage of the work it was never implemented in the topology optimization model. This is left for future work

In terms of intrinsic losses the quality factor shows small improvements for the optimized design D1 compared to the reference. When combined with the higher frequency the Qf -product shows a factor 2.14 improvement. However, the poor resolution of $1.75\text{ }\mu\text{m}$ for the topology optimization model likely leads to an underestimate of the dominating boundary bending losses. It therefore cannot be guaranteed that D1 represents the best possible design for mitigating (boundary) bending losses.

10 | Fabrication

Fabrication of micromechanical resonators is a major part of this work. Fabricating resonators based on thicknesses with 10's of nm with window sizes just below 1 mm is not a trivial task. The high prestress of silicon nitride only complicates matter further. Countless days have been spend at the cleanroom facility at DTU Nanolab on testing and fine-tuning various processes and approaches to optimize for not only the survival rate, but also the quality of the resonators.

An overview of the fabrication steps are shown on Figure 10.1. A set of wafers are bought and then an initial set of of silicon nitride is deposited. This is followed by a front-side etch where the resonator designs are transferred from the design file to the nitride layer. An optional step is included where a protective layer is deposited on top. Then the back-side is etched to define the resonator window. Finally, the resonators are released in a ~ 7 hour long etch in potassium hydroxide (KOH) before being cleaned and dried. From this work two partially similar process flows have been developed which all have shown to produce satisfactory results. The main difference is in how the resonator is protected during the release in KOH. The two variants are:

- A. Protection via a protective coating.
- B. Extra thick silicon nitride layer instead of protection.

In this chapter each step in Figure 10.1 will be described in detail and include important considerations as well as calculations illustrating critical effects. For a detailed process flow see appendix C.

10.1 Initial wafer and low-pressure chemical vapor deposition

The arguably simplest part of fabrication is buying silicon wafers and deposit silicon nitride uniformly on both sides. However, there are still some important aspects to note. Firstly, in order to limit phonon tunneling losses as much as possible the previous studies show one should always use the thickest possible silicon wafers. If one wants to study the effects of phonon tunneling losses thinner wafers can be used. Since both sides will be processed, they must be double-side polished. For this work the majority have been fabricated using 500 μm thick double-side polished 100 mm diameter silicon wafers, which are the thickest wafers available at DTU Nanolab. Thicker wafers can be ordered via external suppliers, but this was not done.

Next step is to deposit stoichiometric silicon nitride using low-pressure chemical vapor deposition (LPCVD) at $\sim 800^\circ\text{C}$. Stoichiometric has shown to exhibit extremely high stresses which is vital for obtaining the damping dilution effect enabling ultra-coherent resonators. The origin of the stress is a result of two separate contributions [69]. One is the high deposition temperature combined with the thermal expansion coefficient mismatch between silicon and silicon nitride leading to a stress enhancement of about 650 MPa [70]. The second contribution is an intrinsic stress related to the deposition itself. The density of the reacting species (dichlorosilane and ammonia) is lower at the adsorbed phase (before reaction) than in the solid phase (after reaction). This leads to an elongation of the bonds. Moreover, micro-cavities may form which leads to van der Waals forces adding further to the tensile stress. When combined with the comparably large Young's modulus

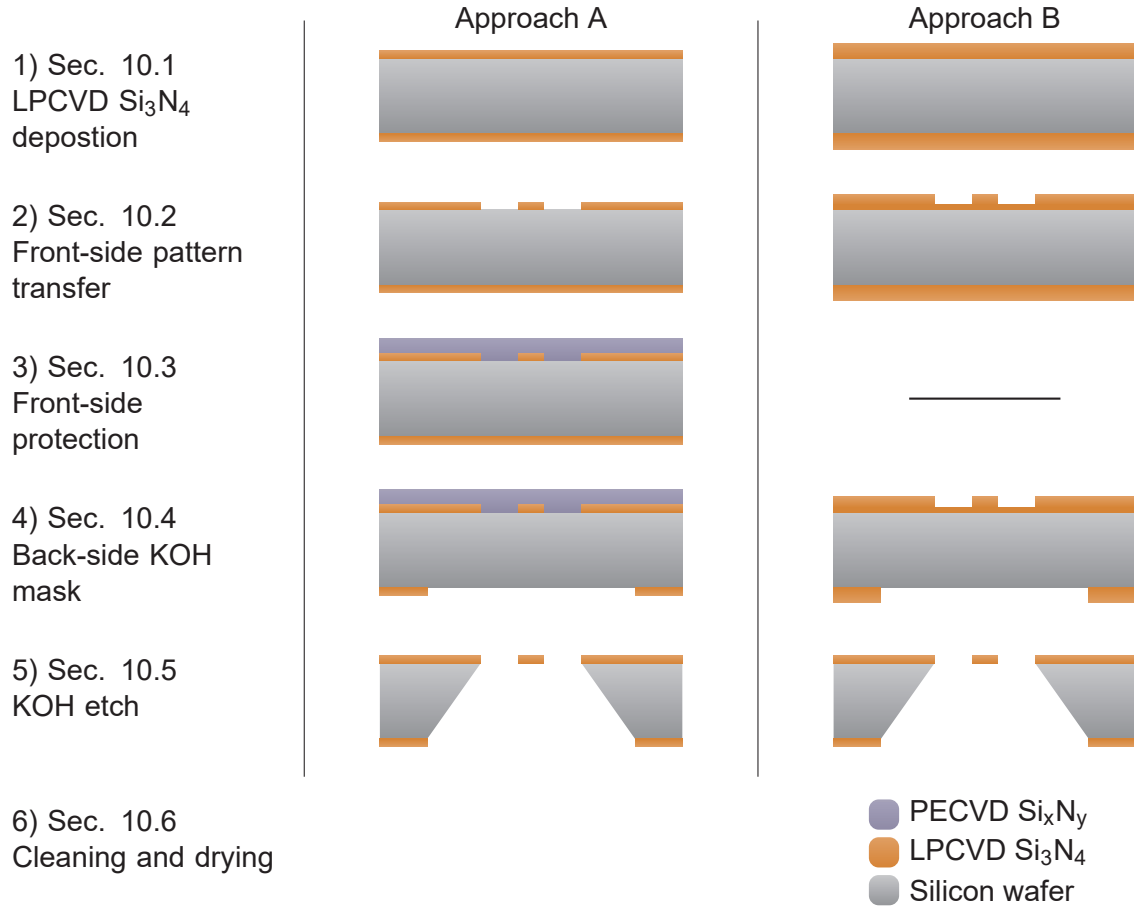


Figure 10.1: An overview of the fabrication steps used to fabricate topology optimized trampolines as well as other pure silicon nitride resonators. 1) LPCVD of stoichiometric silicon nitride. 2) Front-side spin-coating of photo resist, UV-lithography, pattern development, reactive ion etch and photo resist stripping in oxygen plasma. 3) PECVD of silicon nitride. 4) Back-side spin-coating of photo resist, UV-lithography, pattern development, reactive ion etch and photo resist stripping in oxygen plasma. 5) BHF and KOH etch. 6) HCl and "7-up" cleaning process and drying in ethanol. See the respective sections for more details.

of silicon nitride this leads to a large intrinsic stress contribution on top of the thermal effects. However, there are also surface effects, namely oxidization, which increases the density of the surface leading to material expansion and therefore a compressive stress contribution. The effective tensile stress thereby becomes thickness dependent.

No data has been found to properly predict this thickness dependence. During this work thousands of various membranes and trampolines have been characterized at different thicknesses. By comparing their eigen-frequencies with a numerically derived reference frequency defined at a reference prestress, it is possible to estimate the effective prestress of the resonator. From the dataset a simple model was developed relating the stoichiometric silicon nitride effective prestress to layer thickness. The model assumes a nitride layer with tensile stress σ_0 and thickness h and an oxide layer on both sides with compressive stress σ_1 and thickness δ . When $h \gg \delta$ the effective stress can be described as

$$\sigma(h) = \sigma_0 - \beta_\sigma/h, \quad (10.1)$$

where $\sigma_0 = 1.2350 \pm 0.002$ GPa and $\beta_\sigma = 4.518 \pm 0.059$ Pa m, where the \pm indicates the standard error of the estimation. The fit is shown on Figure 10.2. This approach for estimating the prestress is prone to fabrication related defects and uncertainties and will lead to a significant spread as seen on the figure. This uncertainty is offset by the large data set.

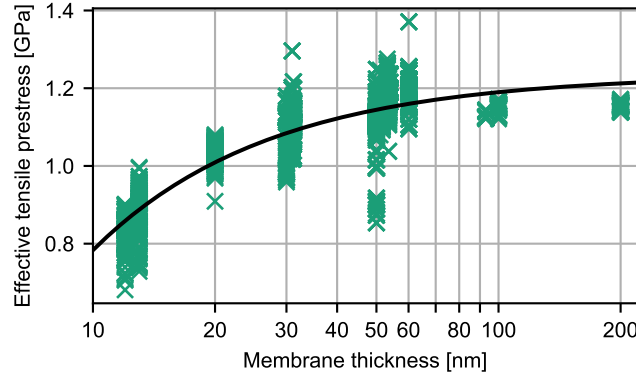


Figure 10.2: Extraction of the stress-thickness relation of stoichiometric silicon nitride measured across 2573 samples of various designs of membranes and trampolines with a fitted function superimposed (solid). The stress is derived from the measured frequency f and compared to a FEM derived reference frequency f_{ref} at a reference prestress σ_{ref} . The estimated stress is then obtained by $\sigma = (f/f_{\text{ref}})^2 \sigma_{\text{ref}}$. The spread is likely caused by fabrication defects and wafer-to-wafer variations.

Finally, LPCVD grown silicon nitride is a very clean process obtaining high quality films. Locally, there can be microscopic fractures. This problem is intrinsic to the deposition and cannot be avoided. The consequence of this is when a trampoline/membrane feature overlaps with a micro-fracture the structure will likely break as soon it is released. This problem increases as one tries to fabricate larger and larger resonators. To reduce the problem the cleanliness of the LPCVD process must be ensured and great care should be taken when handling the wafers, especially the side containing the resonators, to preserve the quality of the film. It is speculated that the film quality has been the limiting factor for obtaining high yield in some cases.

For approach A the deposited layer thickness ends up being the thickness for the resonator, i.e. thicknesses of 20-60 nm. For approach B the layer should be 2-3 times the desired thickness.

10.2 Resonator design transfer

Transferring the pattern from a design file into the silicon nitride layer is straight forward: A 5-inch mask is ordered containing the pattern, the wafers are spin coated with a UV-sensitive polymer, the pattern on the polymer is developed exposing the parts of silicon nitride to be etched using a reactive ion etch, and finally the remaining polymer is stripped in an oxygen plasma. When the mask-less aligner is used one can go directly from design file to UV-exposure.

Using UV-lithography the resolution limit is approximately at 1 μm which is sufficient for the generated designs. One should note the oxygen plasma will oxidize the surface of the nitride layer, although a short etch in hydrofluoric acid should remove any excess oxides [15].

For approach A the silicon nitride layer is etched all the way through. For approach B it is etched $\sim 75\%$ through. The reason for this is the remaining silicon nitride will be used to shield the front-side part of the silicon wafer from the KOH etch later.

10.3 Protective layer deposition

For approach A an extra step is added. In order to shield the resonator and the underlying silicon a protective layer is deposited on the front-side. This is done instead of using the PEEK wafer cap to shield the device during KOH etch, thus it has to survive 7 hours of KOH etching. Which materials are suitable for this? An obvious candidate is silicon nitride. For stoichiometric nitride the etch rate is zero for all practical purposes.

An immediate problem arises: Using the same material for the resonator as well as the protective layer makes it very difficult to selectively remove the latter. Fortunately, for silicon nitride deposited using plasma-enhanced physical vapor deposition (PECVD) the film quality is considerably worse. Using buffered hydrofluoric acid (BHF) the etch rate was found to be 0.75 nm/min and $25\text{--}200\text{ nm/min}$ for stoichiometric and PECVD silicon nitride, respectively. The latter depends on the recipe used. The PECVD layer is less dense and incorporates more hydrogen into the film making it more susceptible to BHF as well as KOH. With that said, the etch rate in KOH is only $10\text{--}35\text{ nm/h}$ making it a promising candidate for use as a protective layer. For later batches this has been combined with an initial $30\text{--}50\text{ nm}$ layer of silicon oxide to ensure proper detachment of the PECVD nitride layer when releasing in BHF after the silicon underneath has been removed in KOH.

This approach is not without its problems. Firstly, anything that is deposited on top of the resonator has to be removed again completely, otherwise the performance can be degraded due to the added mass and possibly added damping, too. No systematic tests have been conducted on this specific problem, but the results obtained using protective layers are similar to other approaches, so it is not considered to be a significant problem here.

Another problem becomes apparent when the structure is being released. A thick PECVD layer is deposited on top with a different prestress than the underlying LPCVD layer shown on Figure 10.3a. As soon as a feature is etched into one of the layers, force imbalances between the layers will result in bending. This has been studied on a phononic crystal patterned membrane similar to the one in Figure 6.5. The resulting bending is illustrated on Figure 10.3b. As the the PECVD layer is etched away in BHF the bending stiffness of the two-layer system is getting lower and lower. At a critical point ($h_p = 0.6 \cdot h_{\text{mem}}$) the stiffness is so low the stress mismatch between the layers induces significant bending shown on Figure 10.3c. The induced stresses from this effect can in the worst case lead to a total stress of 3.6 GPa up from 3.0 GPa in the narrow tethers. When already being this close to the yield strength of silicon nitride at $\sim 6\text{ GPa}$ [71], such an increase in stress can be enough to lead to breakage of the structure. This is true no matter how thick the stoichiometric nitride layer is, as this simply shifts the critical point. One can reduce this effect by depositing a PECVD layer with higher stresses. However, this also increases the total in-plane force which might create other problems. Early batches of the topology optimize designs showed low yield on structures when using the approach just described. In fact, due to this issue we were not able to fabricate D1 using that approach.

How can one mitigate this breakage? The protective layer must be removed *before* removing the silicon beneath the LPCVD layer. How this is done in practice will be described in section 10.5.

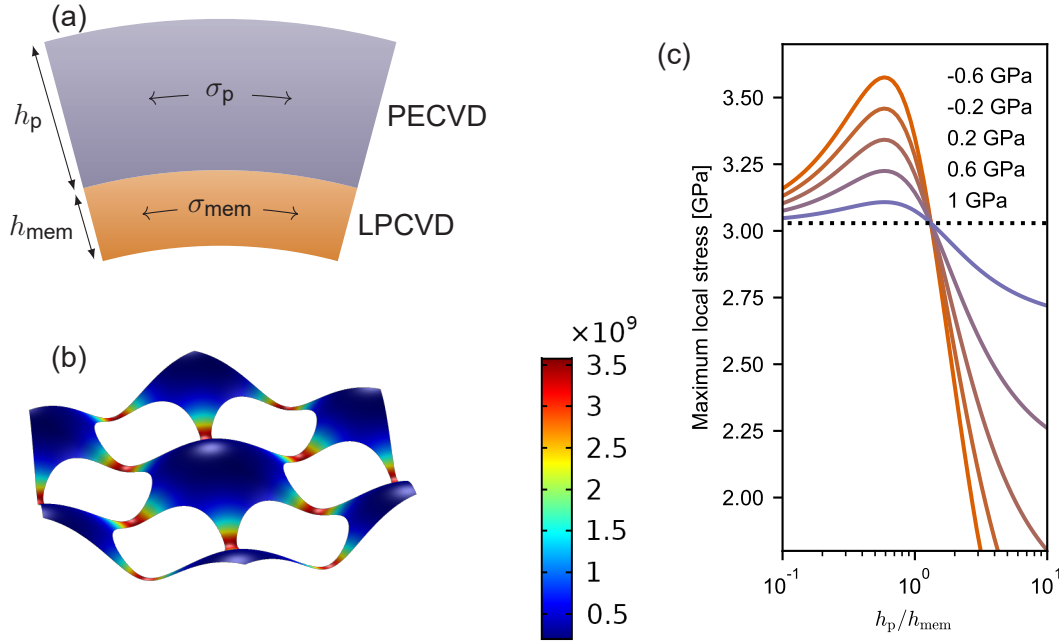


Figure 10.3: (a) Illustration of a bilayer system consisting of the LPCVD-deposited stoichiometric silicon nitride layer and PECVD-deposited protective silicon nitride layer each with their own stress σ_i . The stress-mismatch induces a bend. (b) A simulation of a phononic crystal cell shown in Figure 6.5. The colors represent maximum stress obtained on the surface of the LPCVD layer when $h_p = 0.6 \cdot h_{mem}$ and PECVD prestress is -0.6 GPa. (c) A sweep of simulation results using different PECVD thicknesses relative to the membrane layer for different PECVD prestresses. The plot shows the maximum stress obtained on the surface of the LPCVD layer in units of Pa. The dotted line correspond to no stress-mismatch between the layers. The prestress of the membrane layer is 1.27 GPa.

10.4 KOH etch window design transfer

In order to release the resonator an opening needs to be defined in the silicon nitride on the back-side of the wafer. The opening exposes the underlying silicon which can afterwards be etched using KOH. The fabrication steps and some of the considerations from section 10.2 also apply here. The etch is anisotropic where the etch rate depends on the crystal plane being etched. In the $\langle 111 \rangle$ direction the etch rate is negligible compared to the $\langle 100 \rangle$ direction and can therefore for practical purposes be assumed to be zero. By taking the etch angle into account the back-side window can easily be sized to obtain the desired front-side window after etching through with KOH. However, this makes the front-side window dependent on the thickness of the wafer. The spread of the wafer-to-wafer thickness is $\pm 15 \mu\text{m}$, which directly translates to an spread of the resonator window size. This spreads the resonance frequency of the trampolines by a few kHz according to simulations.

One word of caution during this step. One cannot perform UV-lithography and reactive ion etch on the back-side without handling the front-side. Approach A has the advantage of the protection layer, but the other approach is exposed. Extra care has to be taken to minimize potential damage to the front-side during these steps, as these will otherwise

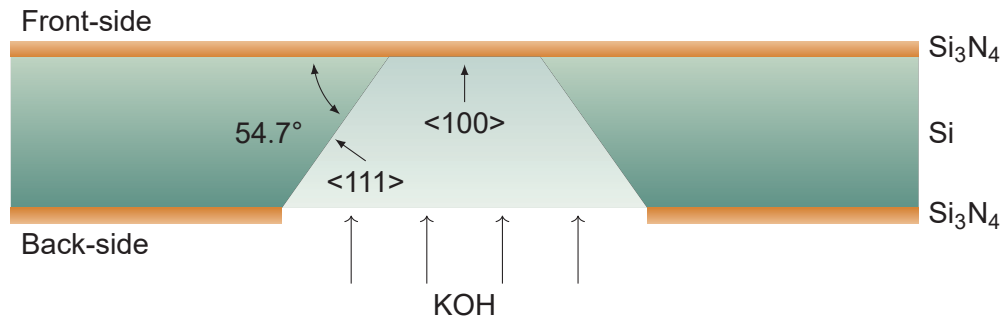


Figure 10.4: Illustration of a typical chip being anisotropically etched by potassium hydroxide (KOH) from the back-side.

degrade the film quality and possibly lead to lower yields.

10.5 Membrane release

The most critical part of the whole fabrication process is the release of the resonators. As soon as they are released they are directly exposed to the elements without any protection or support. Even the smallest mistake or misstep from this point on can have catastrophic effect on the obtained yield. Any handling must be done with the utmost of care and the number of steps must be kept at an absolute minimum.

Other groups typically use some kind of front-side cap to cover and protect the front-side. The downside of using this type of protection is this limits the number of wafers which can be fabricated significantly. When fabricating 100s of resonators this becomes a huge time-factor. Furthermore, the yield obtained using this type of protection was not satisfactory. Early on, a test run was made on $700 \times 700 \mu\text{m}^2$ square membranes. The yields of the different approaches is shown on Table 10.1. It does not seem the PEEK wafer cap has any benefits, except it prevents the front-side from being expose to KOH until the very last few minutes of the etch. However, the PECVD based protection layer resulted in high yields. From this, two approaches for releasing the fragile trampolines were developed. This will be described in the following.

Table 10.1: Overview of release using different front-side protection techniques performed on $700 \times 700 \mu\text{m}^2$ square membranes grouped in batches of 49 membranes. The PECVD layers are removed in BHF after the KOH etch.

	No protection	PEEK wafer holder	500 nm PECVD Si_3N_4	400 nm PECVD Si_3N_4 100 nm PECVD SiO_2
Survivors	8	9	33	27
Yield [%]	16	18	67	55

Release of membrane using protective layer

KOH etch is a wet chemistry process. The flow of liquid may induce force on the wafer, and more importantly, on the resonator. When these are released the large window size act as a large area which can "catch" this flow like a sail. When combined with the extremely small thickness the resonators have very little strength to withstand these forces. They risk breaking. To limit the forces which can be induced by the liquid normal to wafer surface the wafers should be packed as closely as possible. This is illustrated Figure 10.5. This constraints the flow of liquid to be only parallel to the wafer surface. Early tests showed this can improve the yield considerably. For the reference trampoline the yield improved

from $\sim 30\%$ to just below 100% on 50 nm silicon nitride. Note the dummies should be coated in silicon nitride to ensure they too survive the whole KOH etch process.

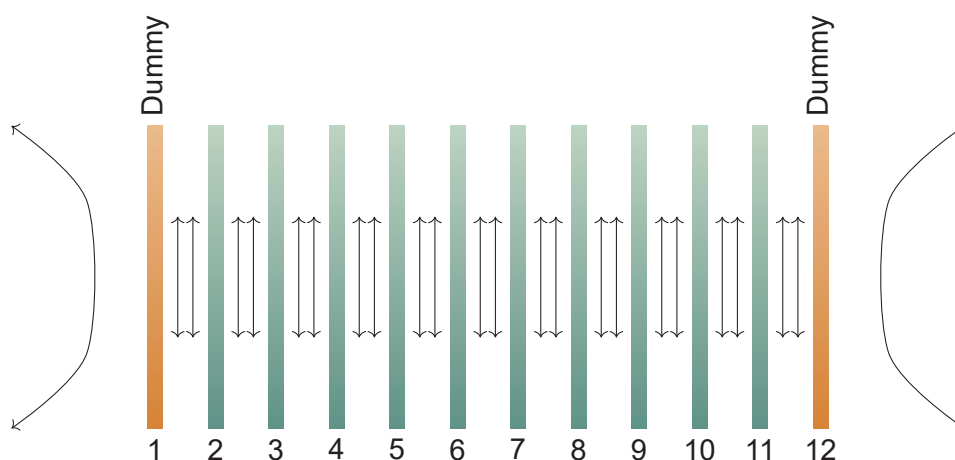


Figure 10.5: Closely packed wafers for wet chemistry processes. This constraints the direction of flow to being parallel to the wafer surface.

Next they are etched in KOH. At DTU Nanolab available baths are fixed at a concentration of 28% . At 80°C this leads to an etch rate of $\sim 1.3\ \mu\text{m}/\text{min}$ leading to a total etch time of approximately six and a half hours. Moreover, there is constant mixing flow to ensure uniform etch and temperature distribution. Beware, if the full silicon etch is done in one continuous etch followed by removing the protective layer in BHF, one ends up in the situation described in section 10.3 and some of the structures will likely break. Instead, the wafers are etched until there is $\sim 40\ \mu\text{m}$ of silicon left (or 30 min before release). The wafers are then removed and exposed to a short BHF etch to remove the protective layer. Since the structures are supported now, they will survive easily.

For some structures, the PECVD layers seems to be difficult to remove. Examples of this is shown on Figure 10.6. Residuals are observed as small particles at some samples or as a distribution along edges on other samples. Prolonged etch in BHF does not always help. Note, etching for too long in BHF also significantly etches the resonator itself, thus one has to be careful when overetching the protective layer. Predepositing silicon oxide below the protective layer helps, but it does not completely eliminate this effect. It might be possible to optimize the removal of the protective layer by testing out different silicon oxide thicknesses or deposition techniques. For example, silicon oxide deposited via an LPCVD furnace with tetraethyl orthosilicate (TEOS) as the reactive gas is a cleaner process with really good coverage. This ensures none of the dirtier PECVD deposited materials get into direct contact with the LPCVD silicon nitride layer.

To remove the remaining silicon the wafers are put back into the KOH bath. Now the flow and heating is turned off to reduce the risk of the flow ripping the structures apart. Turning off the flow in this way has lead to significant improvements in yield for a large number of structures fabricated throughout the PhD. One should note the etch rate will slow down since the temperature will be dropping albeit slowly. Moreover, the etch rate and uniformity will likely change when turning off the flow. When the etch is finished the wafers are carefully rinsed in a 80°C bath to avoid temperature shocks, although it has not been found using the heated bath improves the yield significantly.

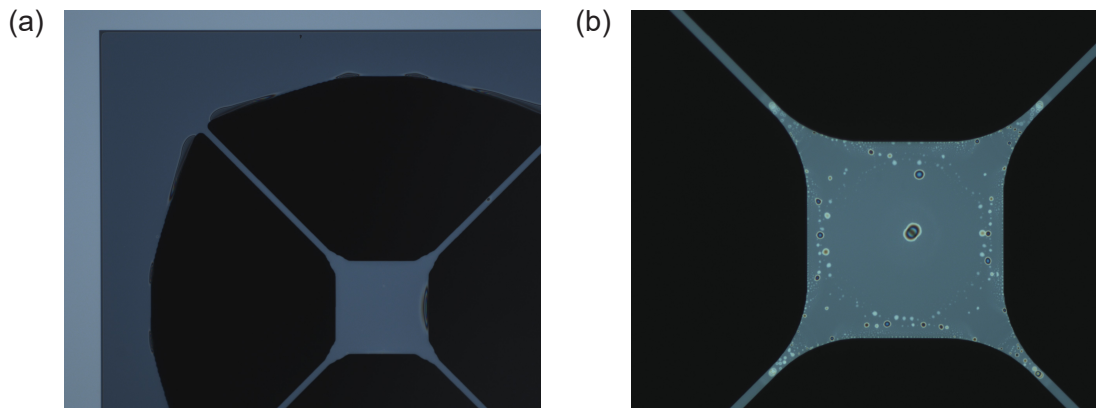


Figure 10.6: Select microscope images of trampolines possibly containing residual PECVD material from the protective layer. (a) and (b) are the designs D3 and Ref, respectively.

Release of membrane using thick LPCVD layer

When using the approach B based on a thick LPCVD layer, the steps for releasing the membrane is the same as when a protective layer is used. In fact, the LPCVD layer doubles as the protective layer in this case. The difference lies in the BHF step. The resonators are etched in BHF until the desired thickness of silicon nitride is obtained. The only requirement is the pre-etched parts of the LPCVD layer must be completely etched through during the BHF etch step. Since the etch rate is slow an etch time of the order of 1 h is expected. The final yield is comparable to using the protective PECVD layer. The results generally look cleaner in comparison, but it can be challenging to obtain the exact final thickness of silicon nitride layer. The cleanliness is possibly a result of the long BHF step as it can etch a wide range of materials although some of them only slowly. Not depositing any material on top is also an advantage when comparing to the approach A.

10.6 Post process cleaning, drying and dicing

The finale part of the fabrication is cleaning for residual contamination and drying the resonators. The number of steps needs to be kept at a minimum in order to prevent damaging (too many) resonators on the wafers. KOH etching is known to leave potassium ions on the surface. Furthermore, contaminants from the KOH bottles may lead to iron oxide particle contamination on the surface [72]. To remove these as well as other possible contaminants like organic materials a two-step cleaning process is devised.

First step is to clean the wafers in a 5 % hydrochloric acid. This completely removes the iron oxide contamination. This is followed by a "7-up" cleaning step consisting of a sulfuric acid solution heated up to 80 °C followed by a spoon of ammoniumpersulfate added into it. This cleans for organic and alkali ion contamination including the potassium ions from the KOH etch.

Next step is to dry the wafers. Water is known to have significant surface tension. It is feared these will rip the fragile structures apart as they dry up. The wafers are dried by heating up an ethanol bath. By placing the wafers above the bath the ethanol fumes will drive out the moisture. After some time the wafers can be removed and gently evaporate the residual ethanol.

In general, dicing the membranes into chips is avoided. This is another step in the most fragile part of fabrication which could lead to lower yields. The dicing is done by etch-

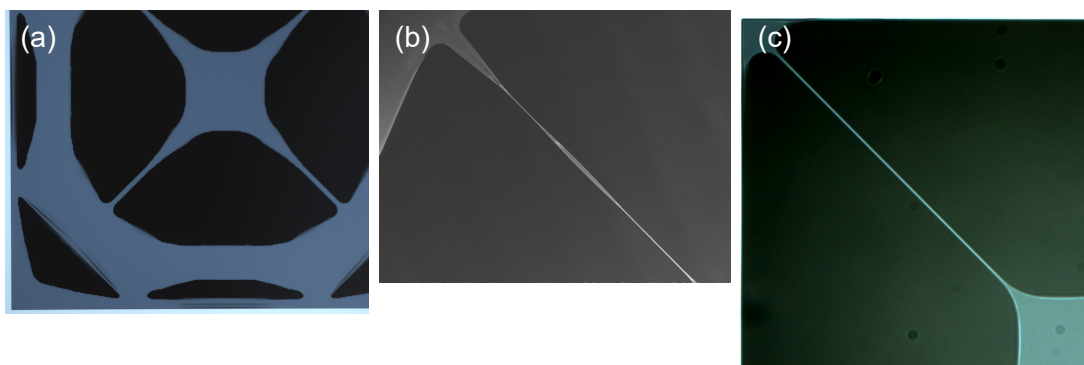


Figure 10.7: Select images of trampolines with collapsed and buckling features. (a) Microscope image of original design D1 at 20 nm resonator thickness. The effect is especially pronounced at edge along the hole at the border. (b) Scanning electron microscopy (SEM) image of a tether of design D3 at 13 nm resonator thickness. The tether is clearly buckled. The slightly wider section is a result of the SEM charging the tether which lead it to widen slightly from the repelling electrostatic forces. (c) Microscope image of a reference trampoline at 13 nm resonator thickness. The blurred edges is a result of buckling along all the edges.

ing grooves into the silicon during the KOH etch on the back-side. Afterwards, the chips can easily be split by hand. This was found to be the most gentle approach to dicing. However, it has been observed a few resonators did break. Moreover, while dicing some particles will be created which fly in all directions. Some of them landed on the resonator themselves. These particles add mass and possibly damping thus ruining their performance. It is speculated many of these particles are from silicon nitride on the front-side. Since this layer is amorphous it will not dice as cleanly as silicon. Newer mask designs have the silicon nitride on the front-side etched away along the chip boundary to remove this source of contamination when dicing. It has never been thoroughly investigated if this has indeed helped on the dicing-related contamination.

10.7 Collapsing and buckling structures

The generated designs were fabricated over a large number of batches. Initially, in order to fine-tune the fabrication process flow and individual steps all batches were based on the original designs using 50 nm silicon nitride. After this was accomplished thinner samples were fabricated in an effort to push the quality factors further using the original designs. Unfortunately, this highlighted a fundamental problem of the original designs shown on Figure 10.7a. The parts of the structure which are "sticking out" without any support simply collapse. The bending stiffness at these extreme low thicknesses is not enough to support it. The performance of these structure were quite poor. It is believed the collapsed structures create additional damping.

The above problem highlighted the need to update the designs. An algorithm was developed to filter away any features which were "sticking out" and were therefore at high risk of buckling. This lead to the *processed* designs. These new designs performed much better at 20 nm. When pushing down further to ~ 13 nm the problem reappeared. There are plenty examples of tethers and other features buckling. This is the main limiting factor on the yield since otherwise most structures survive just fine despite the low thickness. It is believed *any* part not supported by the tensile stress stiffness contribution is at high risk of collapsing since the bending stiffness at this thickness is practically zero. This includes

the tethers, where there is no tensile stress component perpendicular to the tether. This effect is clearly visible on Figure 10.7b. Other features containing long straight lines with no curvature contain no stress component perpendicular to the line at the vicinity of the edge. They are therefore also at risk of buckling/collapsing. The reference design shown on Figure 10.7c with its long straight tethers was especially difficult to fabricate due to this effect.

To avoid this the designs need fundamental changes. All hole-like features must contain at least some minimum curvature to enable the high tensile stress to support the structures along the edges. Phononic crystal based membranes (Figure 6.5) are designed like this, and they do not exhibit this problem at any thickness. One could imagine a smart design-processing algorithm which could adapt the topology optimized designs to accomplish this. However, this might change the designs so much they no longer resemble the original optimized designs. They could lose some critical design features, which enable their optimized performance.

Microscope images of samples representing each fabricated design is shown on Figure 10.8. It can be seen the design of all designs have been properly transferred to the silicon nitride layer. This even includes the overhanging features of the original designs, where the bending stiffness of 50 nm silicon nitride seems to be enough to support them. The yield obtained based on the latest batch of both approaches is shown on Table 10.2. The thick LPCVD based approach was supposed to end up with 20 nm, but was etched for too long in BHF. Both approaches work well for fabricating the structures across all designs. Note, the difficulty in fabricating ~ 13 nm reference trampolines is clearly visible here leading to a much lower yield compared to the rest.

Table 10.2: Yield of each design type based on the latest batch from each approach. Each batch contains 8 wafers each containing 60 resonators. Yield was determined by visual inspection and does not reflect their performance.

Batch	D1	D2	D3	D4	D5	Ref	Total
20 nm using protective layer	53 %	71 %	52 %	55 %	57 %	45 %	55 %
~ 13 nm using thick LPCVD	38 %	29 %	30 %	33 %	39 %	16 %	31 %

10.8 Concluding on fabrication

The fabrication of the topology optimized trampolines have been presented with an emphasis on important effects and considerations. Two successful approaches were developed. The first approach is based on the use of a protective layer deposited on top of the resonator to shield against handling and KOH. The protective layer consists of PECVD silicon nitride combined with a pre-deposition of PECVD silicon oxide to ease removal of the layer using BHF. The second approach instead used an extra thick layer of LPCVD silicon nitride which then doubles as the protective layer and resonator layer. The excess material is then removed in a long slow etch in BHF.

A relation between the effective tensile stress of LPCVD silicon nitride tensile stress and its thickness was experimentally obtained, which showed a decreasing tensile stress below 20 nm. Moreover, the use of a protective layer may lead to a significant stress mismatch between the two layers. The induced bending stress can result in a local stress enhancement of 0.6 GPa which could break already highly stressed features. In order to optimize the yield some of the tricks used include packing the wafers closely together during wet chemistry processes to minimize flows and forces acting normal to the wafer surface, as

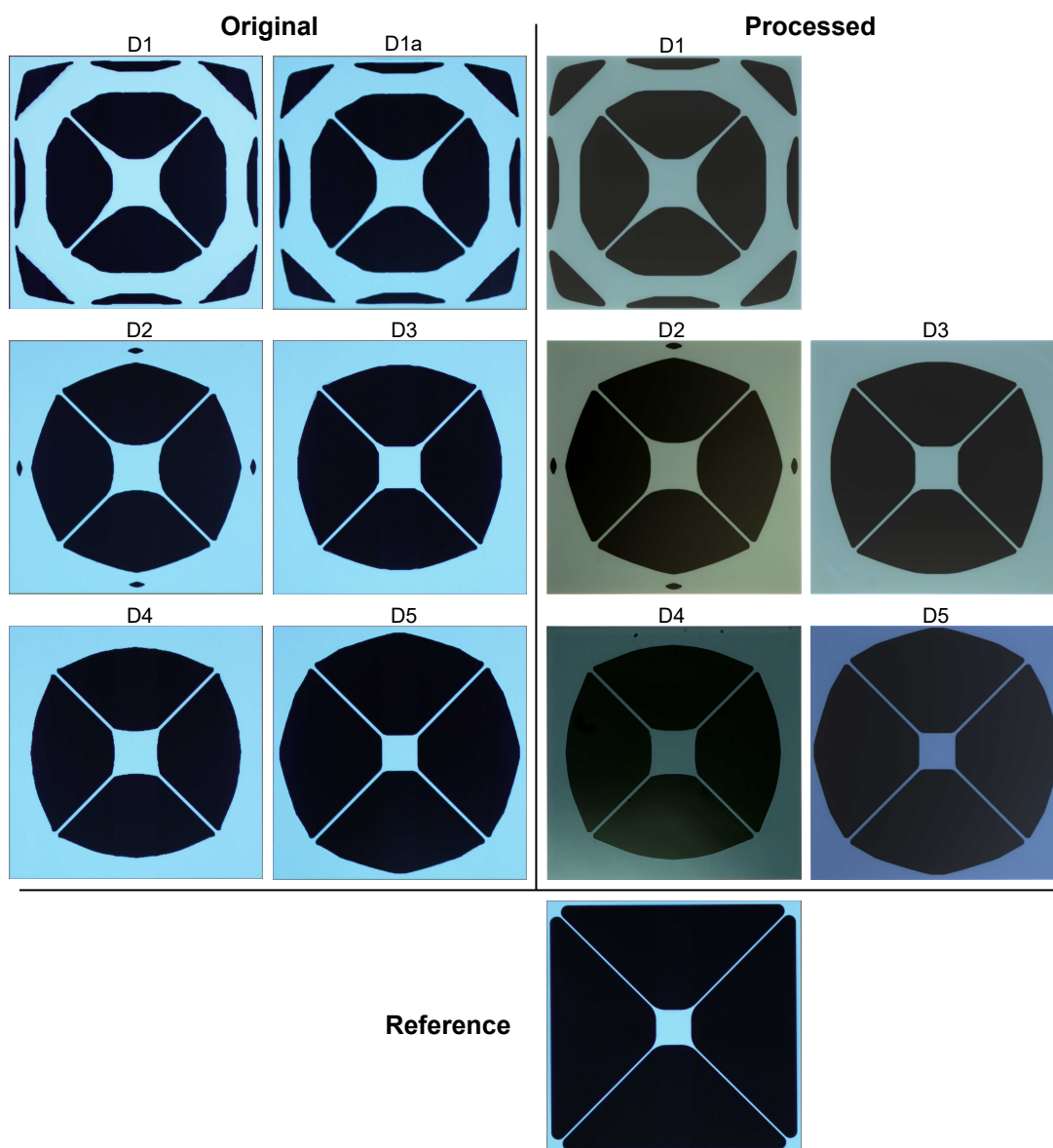


Figure 10.8: Microscope images of select samples consisting of one from each fabricated design. The original designs as well as the reference are shown for 50 nm thicknesses. The rest are shown for 12-20 nm. The particle-like features observed here are imperfections or dirt from the microscope.

well as turning off the ventilation flow in the final and most critical stage of KOH etching. Drying using ethanol fumes to drive out the liquid is believed help to improving the yield, however this was not thoroughly investigated.

Finally, problems with collapsing and buckling structures were identified. This seems to be a problem with features not supported by the tensile stress. For thin structures the bending stiffness is too weak to support them leading to collapse or buckling. The problem was reduced by updating the designs to remove unsupported features from the original designs, however it still persists at 13 nm resonator thicknesses.

11 | Experimental results and discussion

From all the fabricated designs, the resonators to be characterized by mechanical ring-down were chosen based on quick optical evaluation using an optical microscope. Resonators containing dirt, buckling/collapsed features or otherwise deviated were discarded. In order to minimize the risk of dicing related contamination and damage, initially none are diced. The rest are characterized using the mechanical ringdown setup described in section 7. The results of all these resonators are shown on Figure 11.1. The ringdown of the best sample is shown on Figure 11.2.

Firstly, the frequency show a clear dependence to the resonator thickness where the frequencies start to drop sharply below 20 nm. This is a clear consequence of the thickness dependence of the effective tensile stress of stoichiometric silicon nitride discussed in section 10.1. Based on the derived stress-thickness relationship the measured eigen-frequency follows the predicted values well with a minor discrepancy for the thin reference trampolines.

Looking at the obtained quality factors it is obvious the spread is quite large and in the order of two orders of magnitude. It is tempting to attribute this to the presence of phonon tunneling losses. The distribution plotted in Figure 4.13 is generated with values which closely correspond to the topology optimized resonators and both the spread and the lower bound match quite well. Initially, a model was build assuming a fixed value for the intrinsic losses and letting the phonon tunneling losses be described by the finite substrate model in section 4.3.2. The result of this fit was inconclusive and did not pass the chi-squared test to quantify the goodness of the fit. The assumption that only phonon tunneling losses creates the spread is likely incorrect and probably naive. Some samples may have other factors influencing the damping including microscopic contamination or damages not detected in the initial optical characterization. Moreover, the characterized wafer containing the resonators are loosely stacked on top a carrier wafer inside the vacuum chamber. How does this affects the modes of the resonator-containing-wafer? Is the coupling between the two wafers strong enough to significantly affect the eigen-modes of them? In that case the derived phonon tunneling loss model is no longer a valid description.

One way to test the effects of phonon tunneling losses is by dicing the wafers into chips. According to Figure 4.14 the relevant resonances of a $1 \times 1 \text{ cm}^2$ chip are 125, 238 and 319 kHz, which are far away from any of the measured resonances when ignoring the thinnest samples. This guarantees an extremely low coupling to the chip. By ensuring these chips are loosely positioned, i.e. not clamped or fixed in any way, the phonons that do couple to them do not propagate further out of the system. By dicing, one should expect to see resonators that were previously limited by phonon tunneling losses should have their quality factors improved after dicing. This was done for a subset of samples. The mounting of the samples is shown on Figure 11.3 and the results on Figure 11.4.

A large part of the samples do see an improvement of their quality factor. More importantly, most of them converge towards roughly the same level at $\sim 4 \times 10^7$ which is a good indication on this is the intrinsic loss limit. This is a strong evidence for phonon tunneling losses heavily affecting the measured quality factors as well as the spread. However, many of the samples showed a dramatic decrease of their quality factor as well post dicing and the rest only saw minor changes. It is believed this is a result of contamination

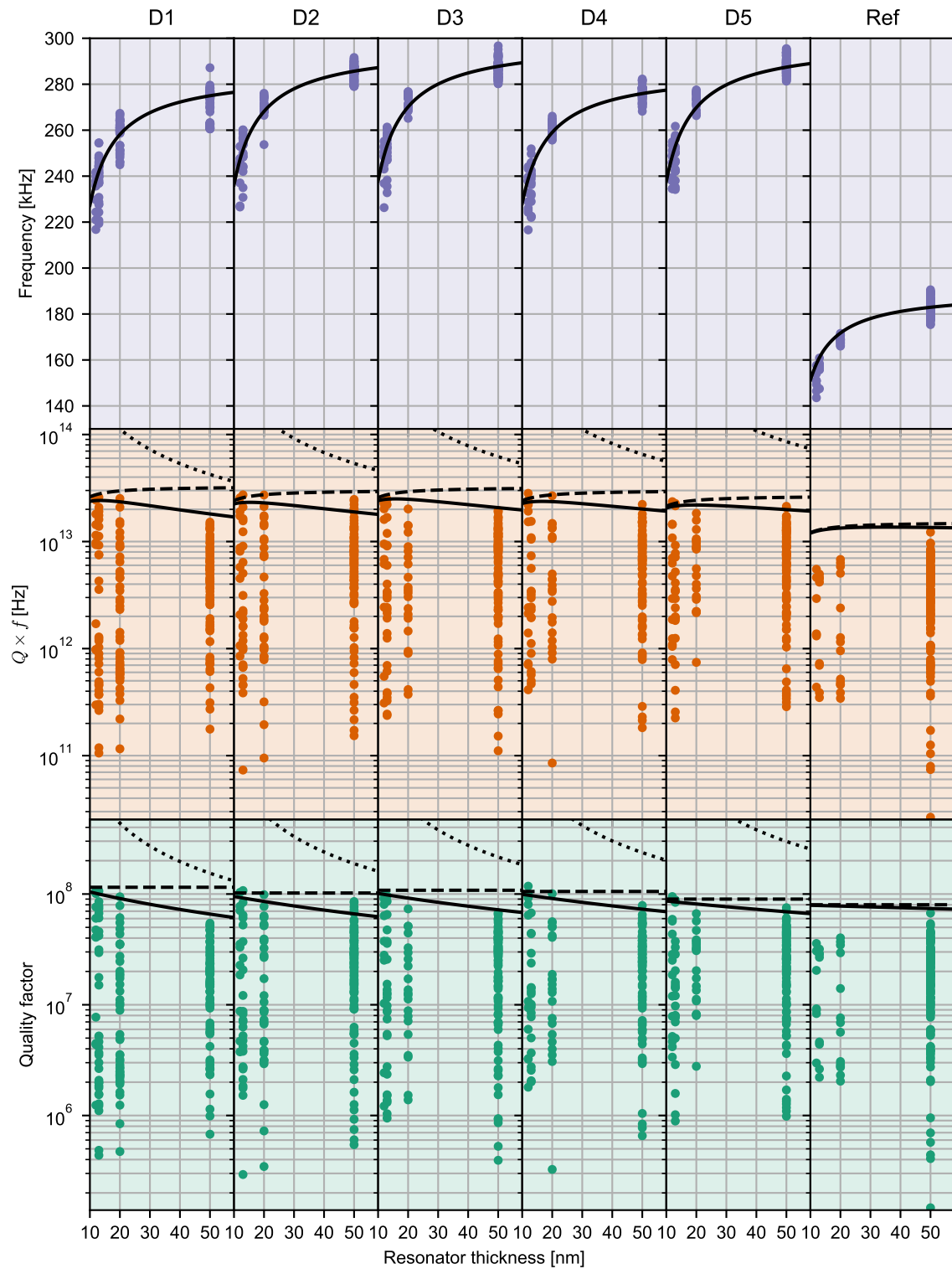


Figure 11.1: Mechanical ringdown results of all characterized topology optimized trampolines. The solid line for the frequency plots are predicted by Eq. (10.1). The solid, dashed and dotted lines for the other plots are the fitted models for the total, intrinsic loss and phonon tunneling loss quality factors, respectively. The fit is performed on the best sample for each thickness group at each design. The plots include 914 samples in total.

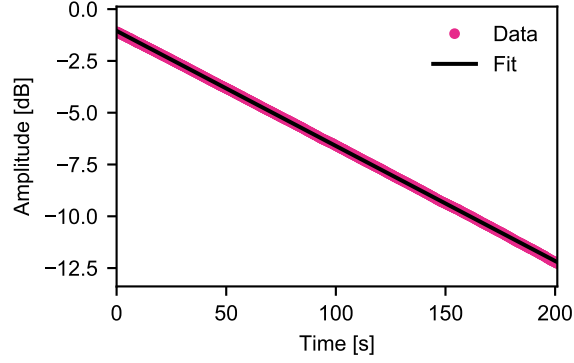


Figure 11.2: Ringdown of the best topology optimized sample. 12 nm thick design D4 at 240 kHz with $Q = 1.18 \times 10^8$.

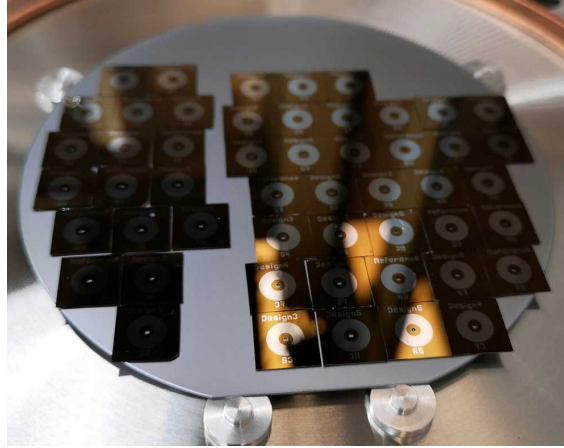


Figure 11.3: Loosely placed diced samples placed for ringdown measurements.

or microscopic damage related to the dicing of the trampolines. No thorough inspection was ever performed on these after dicing. The result from this experiment show the spread is likely a combination of phonon tunneling losses as well as other factors.

With no analytical model available to completely describe the spread in Figure 11.1 how can one perform a meaningful fit of the data? The best performing samples are most likely clean samples limited by intrinsic losses. However, these experience some thickness dependence not described by the purely intrinsic loss model. For the purpose of extracting meaningful data a simple approach was opted for. The best samples for each design at each thickness group are included in a fit consisting of a combination of intrinsic losses and using the expectation value of the finite substrate phonon tunneling loss model. This leads to a model with only two unknowns: The surface loss coefficient β_{surf} and intrinsic quality factor of the substrate Q_s . The estimated values are $\beta_{\text{surf}} = (2.93 \pm 0.19) \times 10^{11} \text{ m}^{-1}$ and $Q_s = (1.27 \pm 0.31) \times 10^5$. The β_{surf} estimate is somewhat higher than the $(6 \pm 4) \times 10^{10} \text{ m}^{-1}$ given by [13]. It could be a result of the ongoing optimization of fabrication combined with selectively choosing only the best samples. Combining phonon tunneling losses into the model might also inflate the predicted intrinsic loss quality factor. The Q_s estimate is comparable to other reported values for silicon structures with dimensions relatively close to the wafer thickness [73, 74]. More rigorous and systematic experiments are needed to confirm phonon tunneling losses are successfully described by the derived model, but the results obtained here indicate this is

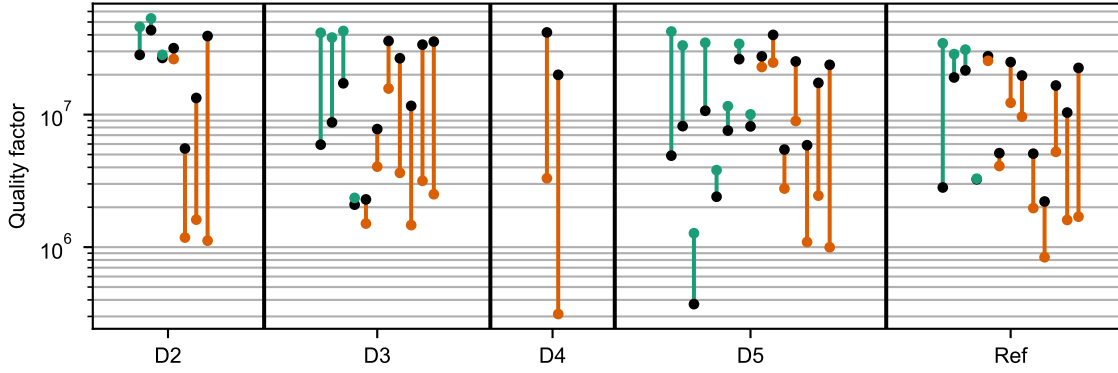


Figure 11.4: Quality factor measurements of topology optimized trampolines before and after dicing. Black points are the pre-dicing quality factors. Green and red points are the improved or deteriorated post-dicing quality factors, respectively. The samples are among the earliest batches where the fabrication process was not properly optimized yet, hence the relatively lower quality factors and missing design D1. All samples are based on 50 nm stoichiometric silicon nitride.

plausible.

While the above fitting procedure is approximate at best, it does highlight some new features of the data. Based on the fit it is clear the thinner reference trampolines perform significantly worse than predicted. It is not clear why this is the case. Based on the fabrication difficulties this design had at these thicknesses in terms of buckling edges and collapsing tethers, it is possible the ones which passed visual inspection still had some related fabrication imperfections significantly affecting the losses. In that case, it highlights the importance of concave hole-like features where the tensile stress can be used to support the structure and its edges. The long straight lines of the reference trampoline design lacks this property. Apart from this problem, it is clear the best reference trampolines are entirely limited by intrinsic damping only.

At the other end design D1 with its relatively high mass and poorly optimized design in terms of phonon tunneling losses is clearly affected by phonon tunneling losses. This holds true even for the best resonators. Only the thinnest samples approach the limit set by the intrinsic losses. This highlights a benefit for thin resonators. For fundamental mode resonators as discussed in section 4.2.6 the intrinsic losses will not improve by fabricating increasingly thinner resonators. However, it still reduces the effective mass thereby lowering the loss contribution from phonon tunneling losses, which in turn might enable one to reach the limit set by intrinsic losses. However, in terms of Qf product there is a lower limit to how thin a resonator should be. The thickness dependence of the effective tensile stress will result in a significant drop in frequency, which will affect the quality factor and especially the Qf product. For these resonators, this limit is set at ~ 14 nm thick stoichiometric silicon nitride. Fundamental mode resonators which are thinner than this are predicted to have worse performance especially when going below 10 nm.

An overview of the best samples is shown on Table 11.1. When comparing the best topology optimized trampoline with the best reference trampoline regardless of thickness an improvement of a factor of 2.3 is seen. This goes up to a factor of 5.1 when only looking at the thinnest structures. This improvement is quite consistent across all designs except for D5. Considering all of them make use of the circular frame design feature and

Table 11.1: An overview of the best sample for each design at each thickness h determined by their Qf product.

h	Quality factor \times frequency [10^{12} Hz]					
	D1	D2	D3	D4	D5	Ref
12 nm	25.1	25.6	24.5	28.2	23.6	5.51
13 nm	25.9	27.3	24.8	15.5	22.7	4.96
20 nm	25.3	27.2	20.2	26.8	18.4	6.80
50 nm	15.2	24.7	19.2	22.3	21.3	12.2

that the best samples are likely limited by intrinsic losses this is not surprising. However, what is surprising is, when assuming they are all limited by intrinsic losses, design D1 is not among the very best even though it has been designed purely for intrinsic losses. It is possible even for the thinnest structures there are still significant phonon tunneling losses, thus any of the other designs will in the end perform better simply because they are optimized for both mechanisms as a compromise. For applications where embedding the resonators in a phononic shield to eliminate phonon tunneling losses is not an option, designs optimized for both losses could be the best choice.

12 | Conclusion and outlook

The use of topology optimization was used to optimize the Qf product of the fundamental mode of a thin-film tensile stressed resonator with $700 \times 700 \mu\text{m}^2$ window using stoichiometric silicon nitride. While the topology optimization did succeed in generating designs optimized with respect to different damping cases the implementation itself had a few problematic issues. The resolution of the grid defining the design space is far from fine enough to resolve boundary bending losses. Moreover, the implementation of the phonon tunneling losses based on using a distribution of strings along the boundary instead of the more physically correct rigid frame description has an inherent weakness. Analysis of these show there is reason to believe the optimizer has utilized this weakness leading to structures badly optimized against phonon tunneling losses.

Fabrication was challenging due to a combination of high tensile stress and small thicknesses. Two successful variants of fabrication approaches were developed. Although fabrication was eventually optimized, difficulties with buckling and collapsing features heavily affected yield of structures below 20 nm. This was especially an issue for the reference structure.

Numerical analysis of the generated designs showed the optimized designs were predicted to perform approximately twice as good compared to the reference trampoline determined by their Qf product, when considering intrinsic losses. The same was seen for the experimental results. The same analysis showed phonon tunneling losses were badly optimized even for design D5, which was only optimized against this loss mechanism and still performed worse than the reference. Experimental results showed the designs were heavily influenced by phonon tunneling losses, which was especially affecting design D1. In general, designs which were optimized for both mechanisms performed the best. By dicing a subset of the resonators, many of them improved their quality factor dramatically which indicates some of the resonators were indeed limited by phonon tunneling losses. The same experiment also highlighted that there were likely other mechanisms, too, leading to badly performing resonators resulting in a large spread of the characterized quality factors. When looking at the best samples, the Qf product was improved by a factor of 2.3 compared to the reference trampoline.

Topology optimization has proven its ability to generate well performing abstract new designs based on the given model. The proposed design for the trampoline successfully mimics the important features of the fractal design briefly presented in section 6.3 when considering only a single branch. The above factor of two improvement is a considerably improvement for a fundamental mode resonator. Based on the fact that boundary bending losses clearly dominate, there is still much room for improvement. An interesting approach to improve on these result would be to change the underlying model. Inspired by the fractal design, one could include regions *inside* the window that are fixed (clamped). This could lead to exotic structures where soft clamping can more easily be engineered. Extending the model used for topology optimization to freely define these regions would be highly interesting. Such structures will be challenging to fabricate. The proposed model is likely not trivial to develop for topology optimization. The question then has to be asked if time is better spend on adapting the fractal design for trampolines "by hand" or other numerical techniques.

The problematic implementation of phonon tunneling losses leaves a lot to be desired.

Future work includes updating this implementation to match the model described in section 4.3.2. It is expected such a change will lead to vastly different structures optimized against phonon tunneling losses. Furthermore, the designs have all been focused on one size of the window, i.e. $700 \times 700 \mu\text{m}^2$. While one can easily scale the frequencies by scaling the whole design, this changes the size of the central pad, too. When the $100 \times 100 \mu\text{m}^2$ central pad constraint is kept there is potential for new designs depending on the window size. Therefrom, a size and frequency dependence can be obtained which could highlight a favorable scaling/optimization route. Larger devices could open the possibility for extremely high Qf product devices at lower frequencies, if and only if the optimization is able to reduce boundary bending losses.

When looking outside the scope of fundamental mode resonators there are key areas which has seen no recent improvements, but still holds potential for performance gains purely by optimizing the geometry. Two-dimensional resonators based on phononic crystals has one major design problem: Most of the bending of the defect-confined modes overlap with low stress regions. This leads to high bending and therefore high losses limiting their performance. So far, no proposals have been seen into how this can be prevented. Topology optimization can possibly be used to create new phononic membranes designs. In-fact, assuming it has to generate a repetitive pattern of identical phononic cells is an unnecessary constraint. It is entirely possible it can be used to generate completely new abstract designs with phononic band-gap-like behavior which enable soft-clamping, but with improved performance. Recent work conducted by one of Ole Sigmund's undergraduates hint at this possibility [75].

All in all, topology optimization has shown it can improve the performance of mechanical resonators. This provides the motivation to extend this work to not only improve fundamental mode resonators further, but also apply this to other resonator types with the ultimate goal of creating the best possible ultra-coherent mechanical resonators.

Part III

Density Phononic Membranes

13 | Overview

Other groups have already demonstrated impressive results using membranes embedded with a phononic crystal pattern [51]. The efficient mode isolation removes phonon tunneling losses. Moreover, soft-clamping removes boundary bending losses. The result is a resonator only limited by distributed bending losses, which is the ideal scenario for any thin film resonator. All of this is already covered in chapter 6.

From a design point of view, it is difficult to see how these can be improved upon. However, by studying the design it can be shown there is definitely room for improvement. As mentioned previously, the defect-confined modeshape co-overlaps poorly with the high tensile stress regions. This is shown for a typical variant of the design on Figure 13.1. This means that the damping dilution effect, which has otherwise helped push these devices to the extreme coherence seen today, is not utilized properly. One could try and tweak the phononic pattern. By making the tethers wider will result in higher stress in the pads, but this comes at the cost of a poorer band-gap due to the reduced tensile stress contrast. This in turn leads to poorer mode confinement. One then has to compensate by adding more phononic cells to preserve proper mode isolation. This design problem is a promising candidate for topology optimization, which could highlight alternative approaches to mode confinement allowing good overlap between the mode-shape and tensile stress. However, this is outside the scope of the thesis.

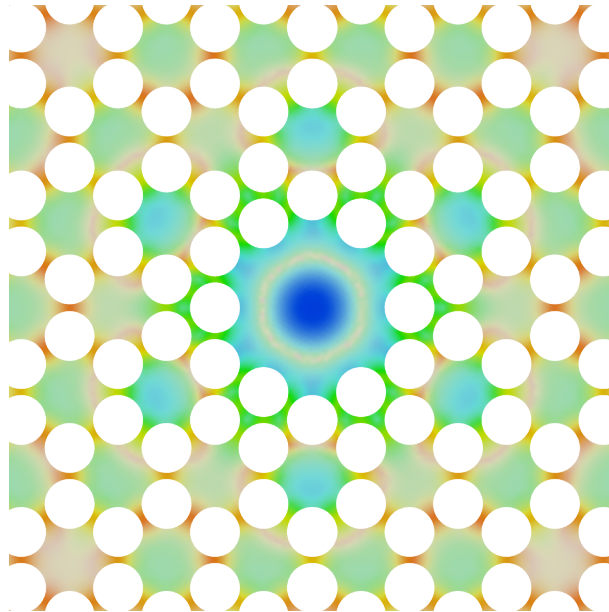


Figure 13.1: The displacement of a typical stress phononic membrane (blue) overlaid on the static von Mises stress distribution (red). Co-overlap of the displacement and tensile stress is defined as mixing of the two colors (i.e. green for perfect overlap).

What else can be done to circumvent this issue? Here, a novel approach for designing phononic crystals is presented and experimentally validated. Whereas the former is based on a tensile stress contrast to create the band-gap in the phononic crystals, the new approach instead make use of modulating the *effective material density* to achieve the same effect. This approach enables one to preserve the tensile stress uniformly which

guarantees perfect overlap between the tensile stress and mode-shape. To differentiate between the two types of phononic crystal designs the former will from this point on be referred to as *stress* phononic membranes/crystals, whereas the novel design is named *density* phononic membranes/crystals.

The theoretical background and design development for these novel structures are presented and discussed in chapter 14. The fabrication of these structures are significantly different compared to anything else fabricated during this work and is discussed in chapter 15. The preliminary results so far obtained are presented in chapter 16 which include new world record breaking results.

14 | Theory and design development

The key to creating a phononic band-gap is by introducing a significant contrast in the phase speed c_σ of the out-of-plane vibration in the membrane. In chapter 3 this was defined as

$$c_\sigma = \sqrt{\frac{\sigma}{\rho}}. \quad (14.1)$$

valid for the high tensile stress regime. σ and ρ are tensile stress and material density, respectively. For stress phononic membranes, this is achieved by creating a stress contrast, i.e. creating regions of high and low tensile stress. Hypothetically, the exact same effect can be achieved by modulating the material density. This is the effect which will now be explored in detail.

14.1 One-dimensional density enhanced string

To illustrate how the material density ρ can be increased we will once again use the simple one-dimensional string as an example. ρ is simply a measure of the amount of mass per unit of length. An obvious way to increase the mass is by fabricating thicker strings. However, this also increases the total tensile force ($\propto \sigma h$) thus the phase velocity will be unchanged. It also increases the bending stiffness which again leads to other problems like enhanced losses. What is needed is a design allowing an increase of mass while leaving the tensile force and bending stiffness unchanged. One design which approximates this behavior is a string embedded with pillars. An illustration of the concept is shown in Figure 14.1.

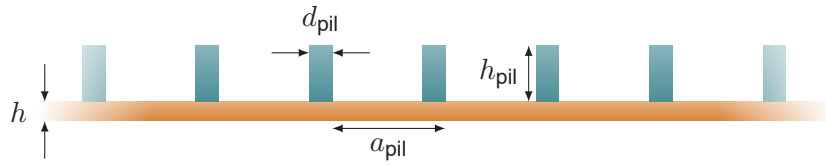


Figure 14.1: Illustration of the core design concept for density phononic. A string is embedded with small pillars.

The pillars add the mass required for the concept to work. Between the pillars the original string thickness is preserved, which allows the string to freely bend and thus the bending stiffness is unchanged. The tensile force is also preserved. From this description an effective material density can be defined as

$$\rho_{\text{eff}} = \rho + \rho_{\text{pil}} \frac{h_{\text{pil}}}{h} \frac{d_{\text{pil}}}{a_{\text{pil}}} \quad (14.2)$$

where ρ and ρ_{pil} are the material densities of the string and pillars, respectively. This is derived by considering the mass contribution of a pillar and comparing to the mass of a string segment. Numerical validation of this description is presented on Figure 14.2a where it can be seen the resulting eigen-frequencies are indistinguishable from a normal string with $\rho = \rho_{\text{eff}}$, even when only a relative few number of large pillars are used. For the given example this region is defined at $d_{\text{pil}} = a_{\text{pil}}/2 \leq 80 \mu\text{m}$.

It is important to note that the introduction of pillars on the string *will* introduce extra damping in the form of an evanescent wave at each pillar similar to boundary bending losses.

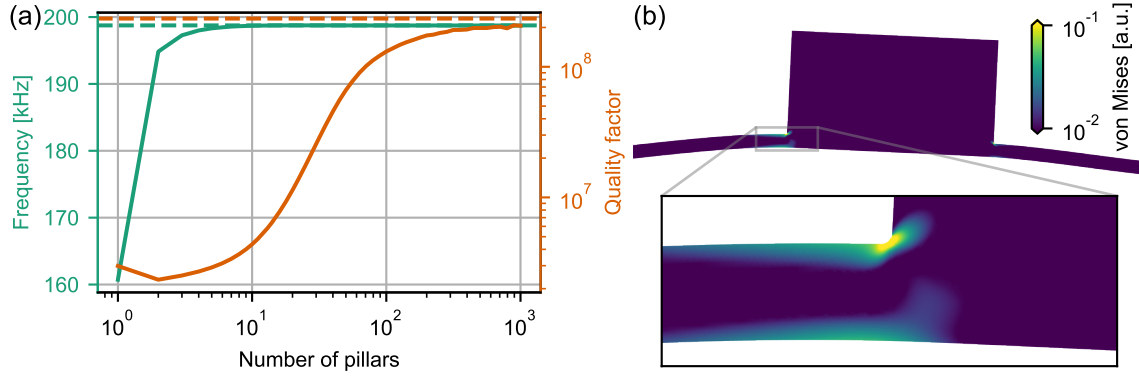


Figure 14.2: Numerical evaluation of the one-dimensional density enhanced string. (a) Eigen-frequency and quality factor of a simply supported silicon nitride string vs. number of pillars uniformly spread along the string. The dashed lines are the solution for a normal string where $\rho \rightarrow \rho_{\text{eff}}$. Plotted for $L = 700 \mu\text{m}$, $h = 50 \text{ nm}$, $\sigma = 1.2 \text{ GPa}$, $d_{\text{pil}} = a_{\text{pil}}/2$ and $\rho_{\text{eff}} = 5\rho$. Loss angle taken from Eq. 4.13. (b) Highlight of the added bending losses introduced by pillars.

This is highlighted on Figure 14.2b. On Figure 14.2a it can be seen that the pillar-induced damping contribution can be reduced by using an increasingly finer mesh of pillars, where a resolution of $d_{\text{pil}} = a_{\text{pil}}/2 \leq 1 \mu\text{m}$ is sufficient to effectively negate it. Such a structure can easily be realized fabrication-wise. The current understanding is that a fine distribution of pillars dilutes the resulting added bending losses into many and overall negligible contributions compared to a coarse distribution. In order to use this approach to design ultra-coherent resonators, one of the main challenges will be to fabricate pillars with as fine resolution as possible. One should note the pillar mesh requirement is dependent on the wavelength and hence the frequency of the device. Numerical evaluations show doubling the frequency changes the required pillar mesh periodicity to half the distance to negate the added damping. Finally, when damping is of no concern the pillar mesh requirement can be relaxed considerably.

With the relevant fundamental properties established, how can this be used for creating one-dimensional phononic crystals? Using the exact same procedure as for the stress-based case described in section 6.1 the band-gap can be created by modulating the effective material density. One could make a binary distribution, i.e. have regions with high pillar density and regions with no pillars. It is also possible to create any other completely arbitrary distributions. This approach can even be combined with one-dimensional strain engineering to create ultra-coherent strings where the mode-shape is co-overlapped with a tensile stress enhanced region to push the Qf product further upwards [29].

In this work strings were not fabricated. Compared to its stress-based counterpart it has only limited advantage as both approaches can easily create high performing resonators with optimal co-overlap between tensile stress and modes-shape [29]. For strings, the density phononic implementation is an alternative approach for 1-dimensional phononic crystals suitable for situations where the stress-based counter-part cannot be used (see chapter 20 for an example on this).

14.2 Two-dimensional density enhanced membrane

Two-dimensional membranes is where density phononics has a clear advantage. As discussed before, a stress contrast in membranes can only be created by etching holes.

This will result in low-stress regions which do not take full advantage if stress dilution effect thus leading to non-optimal performance. Furthermore, the high stress tethers will already be stressed close to the breaking point. This prohibits any attempt to increase the quality factor by applying strain engineering to increase the overall stress. In contrast, membranes embedded with density phononic crystals do not suffer from any of these limitations. This offers a huge opportunity to create novel membranes with the potential to completely outperform existing ultra-coherent membranes based on stress phononics.

For optimal performance the pillars should be patterned as tightly as possible. Naturally, a hexagonal pattern consisting of circular pillars is a good candidate for this, as this allows the pillars to be placed with a high density and the circular shape is among the easiest structures to fabricate. From Figure 14.3a the effective material density is then given by

$$\rho_{\text{eff}} = \rho + \rho_{\text{pil}} \frac{\pi\sqrt{3}}{6} \frac{h_{\text{pil}}}{h} \frac{d_{\text{pil}}^2}{a_{\text{pil}}^2}. \quad (14.3)$$

The above is derived considering the mass contribution from a single pillar and then comparing to the mass contribution from the membrane in a single hexagonal cell.

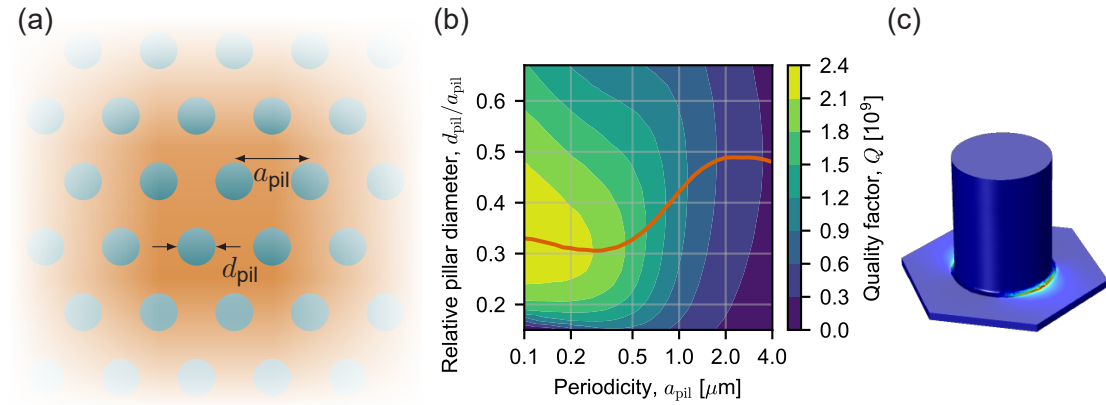


Figure 14.3: (a) A membrane section embedded with pillars in a hexagonal grid. (b) COMSOL simulation results. A parametric sweep of the pillar periodicity and relative diameter where the intrinsic quality factor is estimated for each combination. The red line is the optimal pillar diameter for a given periodicity. (c) A select configuration from the sweep of simulations illustrating the three-dimensional model plotted for bending losses. Simulated for silicon nitride with $h = 20$ nm, $\sigma = 1.1$ GPa, $\rho_{\text{eff}}/\rho = 5$ and $\dot{\phi} = 8.69 \times 10^{-4}$ performed for a single pillar with Floquet periodic boundaries for wave-number $k = 33\,020$ m $^{-1}$ (~ 1.4 MHz). Larger periodicities were too computationally intensive to model in 3D. For the ideal membrane $Q = 2.8 \times 10^9$.

A more detailed study was performed for the two-dimensional case to determine the optimal pillar design. Figure 14.3b shows how the intrinsic quality factor of a membrane section deposited with pillars varies with the periodic distance and relative width of the pillars. For the two-dimensional case it is again clear that a finer mesh will minimize the damping contribution from the bending occurring at base of the pillars illustrated on Figure 14.3c. A feature not discussed for the 1-dimensional case is the relative width of the pillars. It is observed there is an optimum represented by the red line where the damping contribution is at a minimum. This is another route for optimizing the pillars. In general, for a rough pillar mesh the ideal width of the pillars is $d_{\text{pil}} \approx a_{\text{pil}}/2$ whereas for a fine mesh

it is closer to $d_{\text{pil}} \approx 0.3a_{\text{pil}}$. However, for the rough mesh the quality factor dependence on the relative width is weak, hence it is not an important factor in that case. For the studied structure the periodicity must be $a_{\text{pil}} \leq 200 \text{ nm}$ to effectively remove the added damping from the pillars. This is in principle possible, but will certainly pose a challenge fabrication-wise.

Which type of density distribution is suitable for phononic crystals? If one assumes a membrane with no holes or features etched into it, the stress will be completely uniform. Far away from any boundaries the physics will then be completely described by a simple isotropic wave equation of the form

$$T' \nabla^2 u(x, y) + m'' \frac{\partial^2 u}{\partial t^2} = p_e. \quad (14.4)$$

which from a mathematical point of view is very similar to optical waves. It is then intuitive to generate direct mechanical analogues based on common photonic crystal designs. An often seen pattern with good band-gap properties is a binary distribution of circular shaped air domains placed on a hexagonal pattern in a dielectric material [76]. The circles represent high phase-velocity domains whereas the surrounding domain are slow phase-velocity. To limit the amount of mass getting added to the membrane an inverted adaptation of this distribution was studied as well as a softer sine-like distribution to demonstrate the flexibility of this scheme and compare the effects. Both of these are shown in Figure 14.4. The binary distribution is defined as

$$\begin{aligned} g_{\text{bin},0}(x, y) &= \begin{cases} g_{\text{max}} - 1 & , \quad \sqrt{x^2 + y^2} \leq \frac{\alpha_w}{2} a_{\text{ph}} \\ 0 & , \quad \text{otherwise} \end{cases} \\ g_{\text{bin}}(x, y) &= 1 + g_{\text{bin},0}(x, y) + g_{\text{bin},0}\left(x - \frac{a_{\text{ph}}}{2}, y - \frac{\sqrt{3}a_{\text{ph}}}{2}\right) \\ &\quad + g_{\text{bin},0}\left(x + \frac{a_{\text{ph}}}{2}, y - \frac{\sqrt{3}a_{\text{ph}}}{2}\right) + g_{\text{bin},0}\left(x - \frac{a_{\text{ph}}}{2}, y + \frac{\sqrt{3}a_{\text{ph}}}{2}\right) \\ &\quad + g_{\text{bin},0}\left(x + \frac{a_{\text{ph}}}{2}, y + \frac{\sqrt{3}a_{\text{ph}}}{2}\right), \\ &\quad \text{for } -\frac{a_{\text{ph}}}{2} \leq x \leq \frac{a_{\text{ph}}}{2} \text{ and } -\frac{\sqrt{3}a_{\text{ph}}}{2} \leq y \leq \frac{\sqrt{3}a_{\text{ph}}}{2} \\ g_{\text{bin}}(x, y) &= g_{\text{bin}}(x - na_{\text{ph}}, y - m\sqrt{3}a_{\text{ph}}) \quad , \quad \{n, m\} = 0, \pm 1, \pm 2, \dots \end{aligned} \quad (14.5)$$

and similarly for the sine-like distribution

$$g_{\text{sine},0}(x, y) = \begin{cases} \frac{g_{\text{max}} - 1}{2} \left[1 + \cos\left(2\pi \frac{\sqrt{x^2 + y^2}}{\alpha_w a_{\text{ph}}}\right) \right] & , \quad \sqrt{x^2 + y^2} \leq \frac{\alpha_w}{2} a_{\text{ph}} \\ 0 & , \quad \text{otherwise} \end{cases} \quad (14.6)$$

with $g_{\text{sine}}(x, y)$ defined in the same manner as $g_{\text{bin}}(x, y)$. The effective density is then given by $\rho_{\text{eff}}(x, y) = \rho \cdot g_i(x, y)$ where $i = \{\text{bin}, \text{sine}\}$.

Both of these distributions have a few degrees of freedom. When ignoring the pillars these are: The maximum relative effective density g_{max} , relative distribution width α_w and the phononic crystal periodicity a_{ph} . These will be explored in the next section.

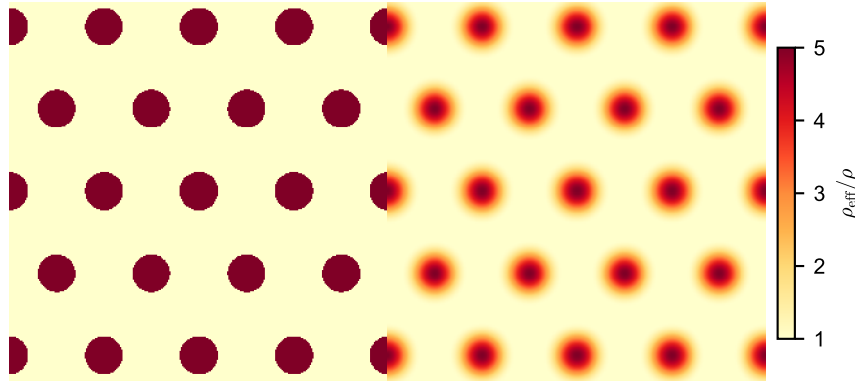


Figure 14.4: The two effective density distributions studied for use a phononic crystals.

14.3 Optimizing the density phononic crystal

How one eventually chooses to design the density phononic crystal has a huge effect on how well any modes confined to a defect will end up performing. A wide band-gap ensures an efficient isolation of the mode. However, the distribution must also be designed to prevent additional design-induced losses. Finally, while a large effective density contrast will generate a correspondingly wide band-gap, it is also increasingly difficult to fabricate, thus the lowest possible contrast should be used. All these factors were studied for the two proposed distributions presented in the previous section.

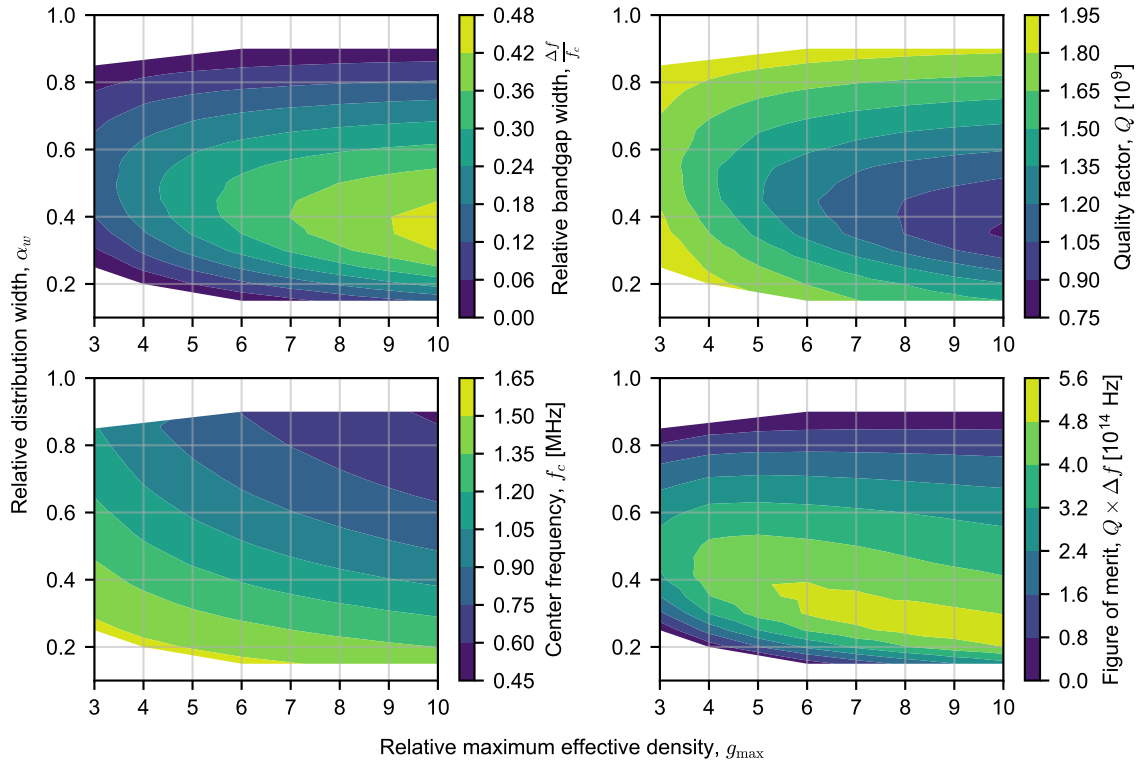


Figure 14.5: Study of the binary effective density distribution based phononic crystal. White areas have no band-gap defined. Quality factor estimated by taking the mean of the estimated quality factors of the mode just above and just below the band-gap. Simulated for $h = 20$ nm, $\sigma = 1.1$ GPa, $\beta_{\text{surf}} = 2.93 \times 10^{11}$ and $a_{\text{ph}} = 253$ μm .

On Figure 14.5 a range of parametric sweeps were conducted for the binary effective density distribution. The phononic periodicity a_{ph} was kept constant as this simply scales the whole solution with respect to frequency. The remaining parameters are the relative distribution width α_w and relative effective density maximum g_{max} , which were swept across a meaningful range. For the band-gap width it is clear as the density contrast is increased the band-gap becomes wider just as one would expect. There is also clearly an optimum distribution width defined at $\alpha_w \approx 0.4$. However, at the same time the quality factor of a mode passing through a region of increasingly higher densities is reduced. This is a direct consequence of the phase velocity definition. Higher densities lead to slower velocities and therefore shorter wavelength. This in turn leads to sharper bending of the mode-shape and therefore higher losses. This compromise between band-gap and losses is also seen for stress phononic devices [54]. Moreover, the center frequency of the band-gap is red-shifted as the mass of the phononic cell increases, which is intuitively expected.

How does one then pick the optimal set of parameters for a given density phononic distribution? For ultra-coherent resonators the important figure of merit is the $Q \times f_c$ product where f_c is the center frequency. Since a wide bandwidth is desirable, a proposed figure of merit for choosing the optimum band-gap design is $Q \times f_c \times \frac{\Delta f}{f_c} = Q \times \Delta f$. This is also shown on Figure 14.5, where a line of optimum solutions can be seen. In fact, based on this definition no improvement of the device can be seen for $g_{\text{max}} \geq 5$. Above this range, the added mass will reduce the quality factor and frequency at the same rate as the band-gap is enhanced. Going above $g_{\text{max}} = 5$ is then a compromise between strong mode isolation versus high quality factor.

The same study was performed for the sine-like distribution and presented in Figure 14.6. Overall, the same conclusions can be drawn. The only significant difference can be seen when comparing the $Q \times \Delta f$ products of the two distributions. They converge to about the same maximum value, but the sine-like distribution reaches this plateau for a broader range of parameters, and it is obtained for a slightly higher g_{max} just below 6. In general, the sine-like distribution obtains slightly lower losses at the cost of slightly worse band-gap widths. The higher g requirement also makes it slightly more difficult to fabricate.

14.4 Phononic membrane designs

Next step in the design process is to use the knowledge obtained from the phononic crystal analysis to design full-scale membranes. This section presents the membrane designs developed and discusses how the defects can be engineered to properly confine a mode interest. Two main designs were developed:

DP1: Binary density distribution with $\alpha_w = 0.4$, $a_{\text{ph}} = 198.8 \mu\text{m}$, $g_{\text{max}} = 5$ and $g_{\text{cmax}} = 3.9$.

DP2: Sine-like density distribution with $\alpha_w = 0.7$, $a_{\text{ph}} = 204.3 \mu\text{m}$, $g_{\text{max}} = 5$ and $g_{\text{cmax}} = 3.6$.

The g_{cmax} parameter will become apparent later. Both of the designs were engineered to have a defect-confined mode at exactly 1.4 MHz at the center of the band-gap. The designs and characteristics are shown on Figure 14.7 and 14.8 for design DP1 and DP2, respectively.

The density distribution for DP1 at Figure 14.7a illustrates how the defect can be implemented. The enhanced density is removed at one of the cells. This disturbance in the lattice is enough to confine an eigen-mode to the defect. However the resonance frequency of such a mode won't be well centered within the band-gap, but instead be

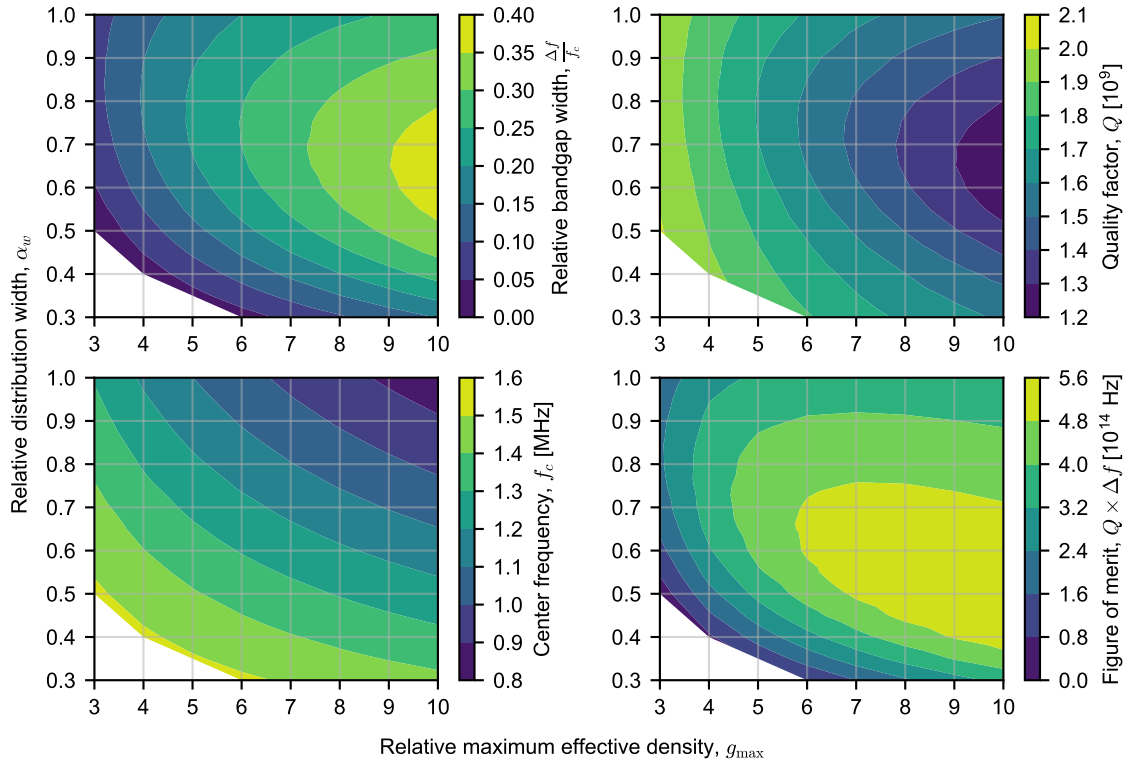


Figure 14.6: Study of the sine-like effective density distribution based phononic crystal. White areas have no band-gap defined. Quality factor estimated by taking the mean of the estimated quality factors of the mode just above and just below the band-gap. Simulated for $h = 20$ nm, $\sigma = 1.1$ GPa, $\beta_{\text{surf}} = 2.93 \times 10^{11}$ and $a_{\text{ph}} = 260$ μm .

near the lower end. In order to guarantee maximum mode confinement, the resonance frequency must be shifted to the center of the band-gap. This is easily achieved by manipulating the phononic cells right next to the defect. By lowering their effective density to g_{cmax} the effective mass of the defect confined mode is reduced which results in a higher resonance frequency.

Simulations of the defect confined mode is shown Figure 14.7b confirming the mode-confining behavior. The band-gap for this specific configuration was estimated and shown in Figure 14.7c. An interesting difference between this and what is typically seen for stress phononic band-gaps is the absence of fast-traveling in-plane modes within the band-gap. Stress phononic membranes only exhibit pseudo band-gaps (see Figure 6.6), whereas the density phononic membranes exhibit a full band-gap. No deeper study was performed into this. It is known the in-plane modes's stiffness are unaffected by in-plane tensile stress and therefore stress-modulating a membrane or string cannot ever create a band-gap for all types of vibrations simultaneously [22]. Conversely, mass contrast works equally well on all types of vibrations and is likely the reason for the full band-gap.

The density distribution for DP2 at Figure 14.8a was designed and manipulated in the exactly same manner as DP1. The dispersion diagram in 14.8c shows a somewhat narrower width of the band-gap. By comparing the defect-confined mode-shape in 14.8b with DP1 one can (with a sharp eye) barely see the mode is slightly less confined for DP2 as a result.

One important parameter so far omitted is how many phononic crystal cells (i.e. number

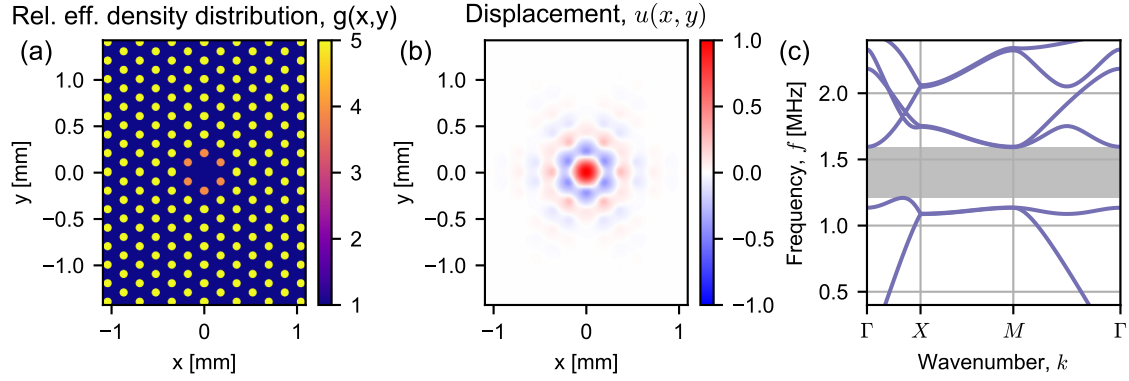


Figure 14.7: A study of density phononic membrane design DP1. (a) Relative effective density distribution near the defect of an infinite membrane. (b) Mode-shape of the defect confined mode at 1.4 MHz. (c) Dispersion relation of the chosen phononic crystal design. The band-gap is marked by a shaded region and has a width of $\Delta f = 383$ kHz.

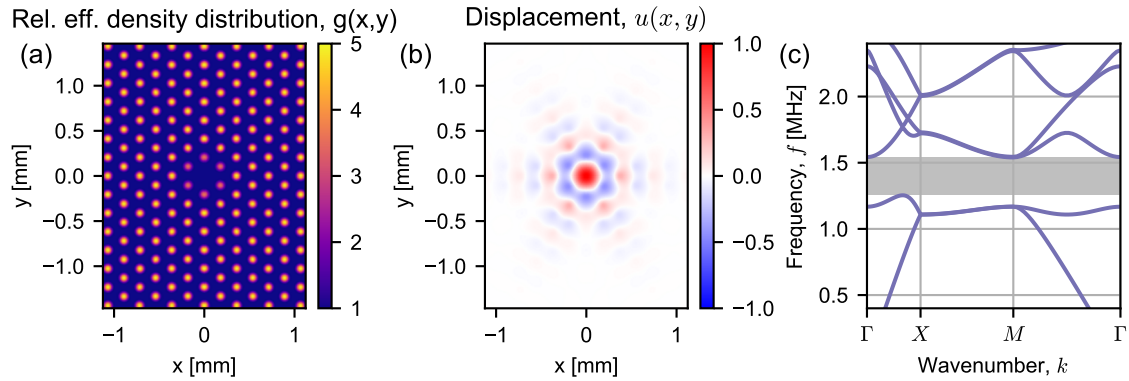


Figure 14.8: A study of density phononic membrane design DP2. (a) Relative effective density distribution near the defect of an infinite membrane. (b) Mode-shape of the defect confined mode at 1.4 MHz. (c) Dispersion relation of the chosen phononic crystal design. The band-gap is marked by a shaded region and has a width of $\Delta f = 286$ kHz.

of repetitions of the pattern) are needed for proper mode confinement, N_{ph} . This number depends on the damping mechanism. For intrinsic losses one needs to keep adding more crystals until the boundary bending losses become insignificantly small. For phonon tunneling losses one needs to reduce the coupling to the substrate until only the intrinsic losses dominate. The risk of resonant coupling to a substrate mode might lead to a large mode isolation requirement, but this has so far not been investigated. One may choose to be on the safe side and simply fabricate huge membranes with many cells. However, huge membranes, especially thin highly stressed membranes, are increasingly difficult to fabricate as the size goes up. A study was performed to numerically estimate the required number of cells. For simplicity, only the intrinsic losses were considered. Moreover, a hexagonal window was assumed as this fits naturally with the lattice as shown on Figure 14.9a. The results for both resonators are presented on Figure 14.9b using the extracted surface loss parameter from the topology optimized trampolines.

From the simulations it is clear how even the small difference in band-gap width affects the required number of phononic crystal cells. For DP1 the minimum number of cells needed is approximately $N_{\text{ph}} = 7$ and for DP2 it is around $N_{\text{ph}} = 9$. This small difference can lead to a significant difference in yield during fabrication, since this directly corre-

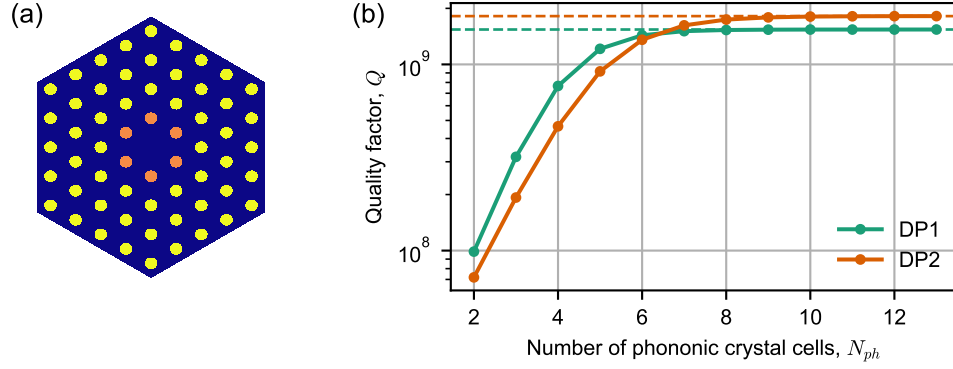


Figure 14.9: A study to illustrate the effect of the number of phononic crystal cells N_{ph} has on the intrinsic quality factor. (a) An example model for DP1 with $N_{ph} = 4$. (b) The estimated quality factors. Assumes $h = 20$ nm, $\sigma = 1.1$ GPa and $\beta_{surf} = 2.93 \times 10^{11}$ m⁻¹. Both designs operate at 1.4 MHz. Added losses from the pillars have been ignored here.

lates to larger membranes, which are more difficult to fabricate. However, above this limit DP2 is predicted to have a slightly higher quality factor, which is expected based on the prior phononic crystal analysis. The presented results represent the upper predicted limit obtainable when the pillars are fabricated at a sufficiently fine mesh resolution. For comparison, the highest reported room-temperature resonator with similar frequency based on stress phononics is 380 million [53]. From this analysis, it is clear that the method of using a modulated material density shows great promise in pushing the current record by a significant amount. With these promising predictions in mind we can now highly motivated move forward to the implementation of these designs.

14.5 Density distribution to pillar layout conversion

A convenient feature of using pillars to alter the effective density of the material, is that *any* density distribution can be used and approximated by a sufficiently fine mesh of pillars. A script was written in MATLAB and used on the layout editor CleWin to convert any effective density distribution. This section won't go into depth of the script itself. The approximated converted layouts for both designs will be presented and discussed.

To simplify fabrication and the mask layout, all pillars will be fabricated with the same diameter, height and resolution on a hexagonal grid. The pillar diameter is set to half the periodicity. With these parameters fixed the only way to modulate the effective density is by omitting pillars at certain hexagonal coordinates depending on the density defined. This discretization scheme will only be approximate, but experiments have so far shown this is good enough. Of course, finer pillar mesh resolutions will result in a better approximation of the effective density distribution being converted. In all cases, the total added mass matches the original distribution $g(x, y)$ as close as possible.

The simplest distribution to convert is the binary distribution which is shown for design DP1 on Figure 14.10 for pillar periodicities used in fabrication. Finer resolutions are of course possible, but for normal UV lithography 1 μ m features are about the smallest structures which can be fabricated reliably. Note the bottom row has a relatively lower effective density defined by g_{cmax} resulting in some pillars being skipped on the hexagonal pattern. The corresponding layout for the more complicated sine-like distribution is shown on Figure 14.11 for DP2. The continuous density distribution is approximated by a high density of pillars in the center which gradually become less dense away from the center. Here it is

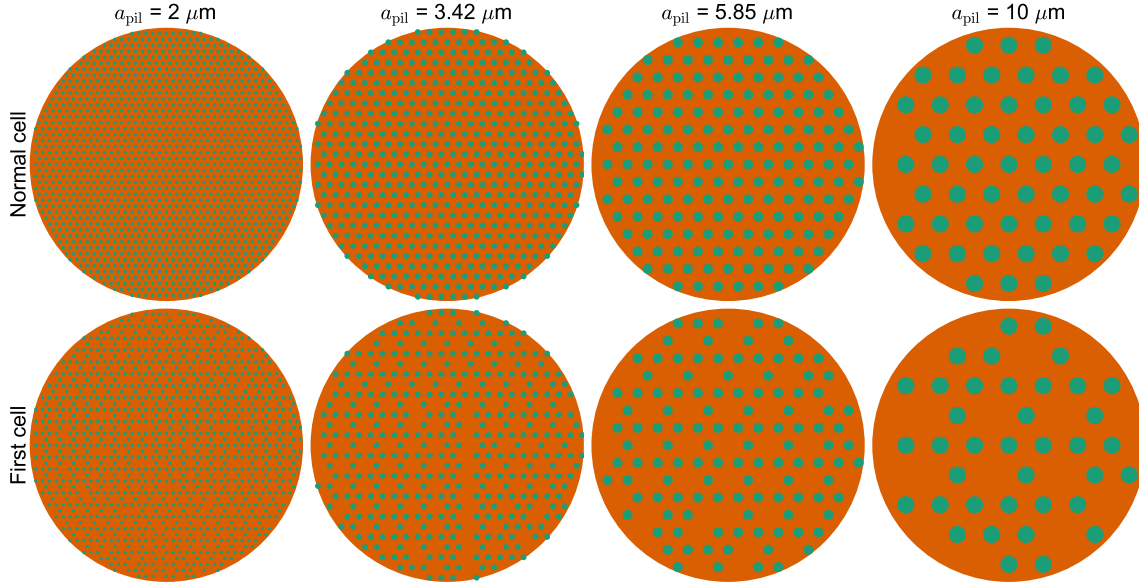


Figure 14.10: Effective density distribution (red background) to pillar layout (green circles) conversions for DP1 for different pillar periodicities a_{pil} . The bottom row are phononic cell layouts with reduced effective density which are placed next to the defect.

clear the finer mesh resolution does a significantly better job at replicating the sine-like distribution compared to the rough resolution of $a_{\text{pil}} = 10 \mu\text{m}$ which fails at it completely.

The above presented designs were all fabricated initially. However, in order to optimize the fabrication in the limited time left DP2 was discarded, since DP1 with its lower requirement for number of phononic crystal cells was expected to have higher yields. Therefore, the majority of fabricated membranes and mechanical ring-downs were based on DP1, which will be the focus for the rest of the chapters in Part III.

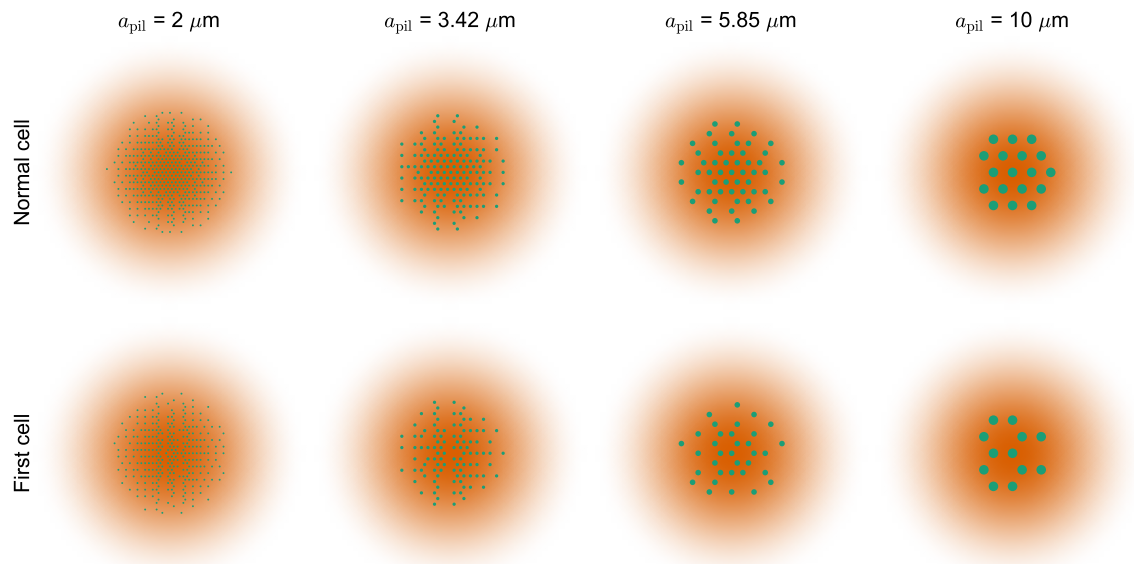


Figure 14.11: Effective density distribution (red background) to pillar layout (green circles) conversions for DP2 for different pillar periodicities a_{pil} . The bottom row are phononic cell layouts with reduced effective density which are placed next to the defect.

15 | Fabrication

Fabrication of the novel density phononic membranes were not trivial at first. A few factors were identified, which have a huge impact on the yield and sets the limits of fabrication. These are ongoing challenges which needs to be resolved in order for these membranes to reach their full potential. This chapter goes through some of the key elements in fabrication and suggestions on how to improve on them. For a detailed process flow the reader is referred to appendix C.

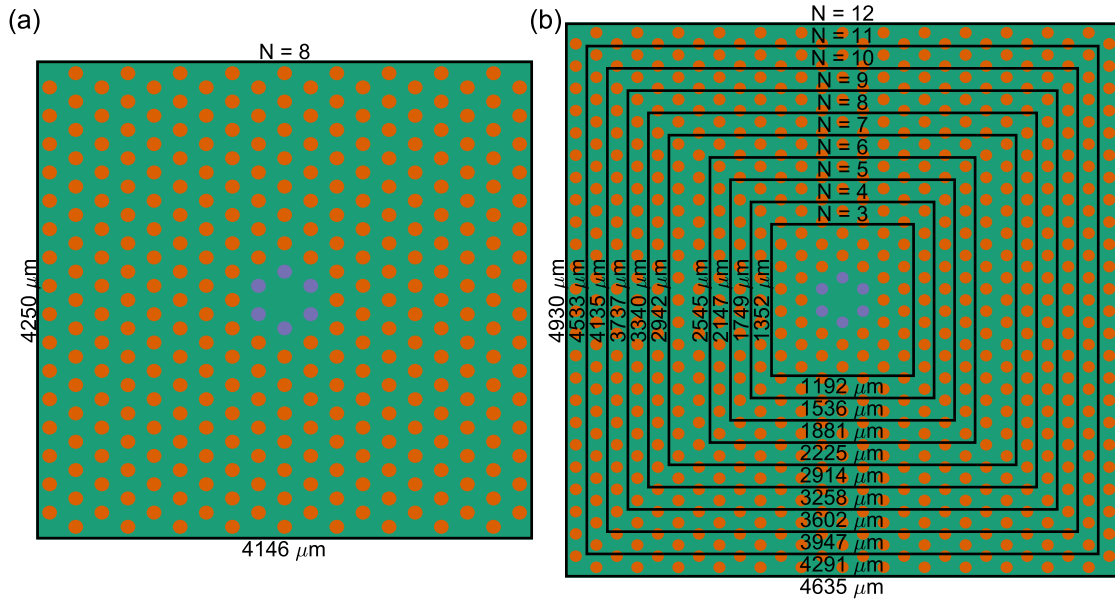


Figure 15.1: An overview of the fabricated membranes of design DP1 for the two successful batches. Green is pure stoichiometric silicon nitride. Red are the high effective density regions defined by g_{max} . Purple are the slightly lower effective density regions defined by g_{cmax} . (a) A variant of DP1 with $a_{\text{ph}} = 253 \mu\text{m}$. (b) DP1 fabricated with different number of phononic crystal cells. Note, cells overlapping with a membrane border are ignored in the mask in order to prevent spurious discontinuities. Moreover, N corresponds to N_{ph} used in the rest of the text.

Two successful batches were fabricated each with their own purpose. The first batch (Figure 15.1a) was designed for different pillar diameters to study how it affects the quality factor. The second batch (Figure 15.1b) was designed for different number of phononic crystal cells to verify the behavior seen on Figure 14.9. The latter is designed for $d_{\text{pil}} = a_{\text{pil}}/2 = 1 \mu\text{m}$ for all membranes. It should be noted that the first batch was first and foremost a test of fabrication and the design parameters do not exactly match DP1. Moreover, the batch size was also much smaller and the yield poor hence most of the focus will be on the second batch. The fabrication steps on both batches are the same with minor tweaks to optimize the yield and quality of the membranes. An overview of the different fabrication steps can be seen on Figure 15.2. Many of the same fabrication problems and solutions overlap with the topology optimized trampolines described in chapter 10, thus there will be no detailed step-by-step description here. The focus will be on the most critical aspects of fabrication.

Three main challenges were identified during fabrication:

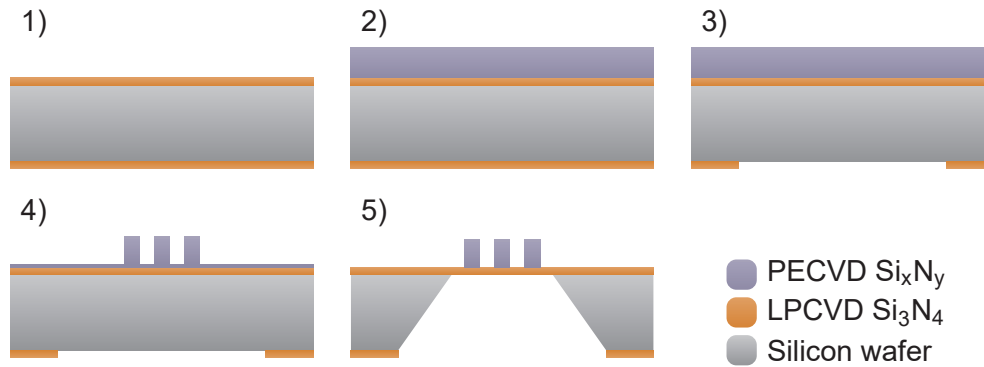


Figure 15.2: Illustration of the density phononic membranes between steps of micro-fabrication. Note, it is not drawn to scale. 1) LPCVD of stoichiometric silicon nitride. 2) PECVD of silicon nitride. 3) Back-side spin-coating of photo resist, UV-lithography, pattern development, reactive ion etch and photo resist stripping in oxygen plasma. 4) Front-side spin-coating of photo resist, UV-lithography, pattern development, reactive ion etch and photo resist stripping in oxygen plasma. Only ~ 40 nm of PECVD material remain on exposed areas. 5) BHF and KOH etch (see section 15.1 for more details).

1. Stoichiometric silicon nitride film quality and membrane size.
2. Lithography of pillars.
3. Etch and release of pillars.

As mentioned for the trampolines, the film quality of the stoichiometric silicon nitride layer has an influence on the yield. From Figure 15.1 it is evident that the membranes can easily become quite large. The nominal membrane size ($N_{ph} = 8$) is approximately $3 \times 3 \text{ mm}^2$ with the largest membranes being just below $5 \times 5 \text{ mm}^2$. When considering that the total area of the membrane scales with the side-length squared, the probability of the membrane overlapping with a region of the silicon nitride layer containing microscopic damages scales quickly with size. This effectively sets an upper limit on how large a membrane one can reasonably hope to fabricate in large quantities. An overview of the yield with respect to different number of phononic crystal cells is shown on Figure 15.3, which confirms the trend of lower yield for larger membranes. What seems to work well is to deposit the PECVD layer as soon as possible on the front-side to protect the LPCVD layer. Apart from that, handling the front-side with a maximum of care is important to prevent any further degradation of the LPCVD layer.

The second challenge is the lithography of the pillar pattern. A mask-less aligner (MLA150 WMI maskless aligner from Heidelberg Instruments GmbH) was used with great success to define pillars with diameters down to $1 \mu\text{m}$. Tests showed this can be pushed down to diameters of 500 nm , but no further. However, in order to properly minimize the added damping from the pillars the diameter should be as low as 100 nm . Deep-UV lithography could be used to define smaller pillars. The technicians at DTU Nanolab report features down to $\sim 200 \text{ nm}$ is possible. Evidently, this is not enough. Alternative approaches are nano-imprint lithography and e-beam lithography. Both are available at the facility and are reported to have a resolution limit of $\sim 20 \text{ nm}$. The use of these two approaches have not been thoroughly investigated, hence the viability of these cannot be commented on any further.

The third and finale challenge is the etch and release of pillars. This step will be described

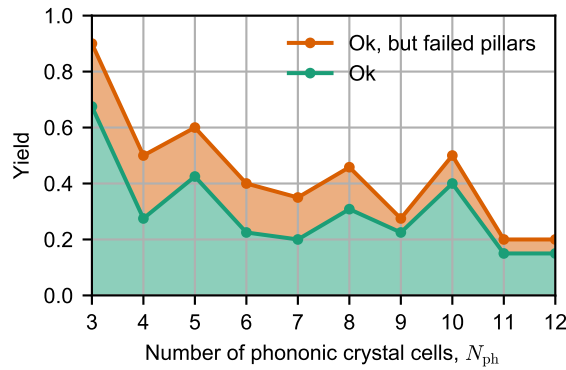


Figure 15.3: Yield for the batch where the number of phononic crystal cells were swept. Yield determined by inspection via microscope. Ok samples had no visual damages or contamination. Red include membranes where the pillars were not fully released, but still had residual material in between.

in more detail below.

15.1 Etch and release of pillars and membrane

How the pillars are fabricated is crucial. There are a number of factors determining the survivability of pillars. First, the choice of material matters. Similar to the trampolines the membrane is released via a long KOH etch, which is known to etch a range of other materials, too [77]. Even when a protective cap is placed on the front-side one must expect some of the membranes will break as soon as the KOH has etched all the way through. This allows KOH to diffuse into the front-side and start etching any vulnerable materials exposed. This means for an unprotected front-side the pillars must survive ~ 7 hours of KOH, or when the protective cap is used it has to survive for at least some minutes (probably at the order of ~ 10 minutes to allow for some over etch). PECVD silicon nitride naturally satisfies this requirement. When this is combined with the experience already obtained with using this material in other projects, it became the material of choice. Chromium offers some resistance against both KOH and BHF and is an interesting metallic alternative.

As the process is described in 15.2 the pillars are defined using a top-down approach via reactive ion etch. Since the underlying LPCVD layer is extremely thin and the quality of the layer is not allowed to be comprised, the PECVD layer cannot be completely removed during this etch alone. There is no significant selectivity between the two nitride depositions. Therefore, a residual layer is kept at the order of 40 nm. This is achieved by etching 2-3 times and measure the thickness in between etches using an ellipsometer (M2000XI-210 ellipsometer from J.A. Woollam Co., Inc.). One should be aware of the combined non-uniformity of the PECVD process and following reactive ion etch. This leads to a spread of the residual PECVD layer thickness by tens of nm across a wafer.

The next step is a tricky one. How to remove the residual layer while still preserving the pillars? For the successful batches, what worked was the simplest (and riskiest) approach tried. When the wafers are directly exposed to 80 °C KOH the etch rate of the used PECVD layer is ~ 10 nm/h which decreases the diameter by 120-140 nm over the course of the KOH etch. To ensure that in-fact all of the residual material is removed this is combined with pre-etching the pillars in BHF for a short amount of time (typically 40 s). With an etch rate of ~ 30 nm/min this removes an additional 40 nm from the diameter. When fabricating

large pillars this works perfectly well since the selectivity between the two silicon nitride layers is high. However, with these two isotropic etches up to 180 nm of the diameter is removed, which is a significant amount for pillars defined with a diameter of 1 μm . Moreover, it will be impossible to fabricate pillars with the required diameter of 100 nm. The loss of mass can be compensated by simply fabricating the pillars proportionally taller, which was done for the 1 μm pillars.

Another problem observed using the approach described is the perceived non-uniformity of one or several of the etch processes when fabricating small pillars. Figure 15.4f-j shows some of numerous samples where the residual material between pillars was not properly removed. This happened for a significant fraction of the membranes as shown on Figure 15.3. The etch rate is slower than expected in those regions for at least one of the wet or dry processes. This is a common feature when etching structures with large aspect ratio, where the etchant has a harder time getting into small gaps and react with the exposed material. The downside of this effect is that an even longer isotropic etch time is needed than already described, to guarantee the removal of the residual layer for all samples on a wafer.

The above is right now the main limiting factor for pushing the pillar mesh resolution. As long as this part of the fabrication cannot be optimized it will not be possible to push the performance of these membranes considerably. What can be done to improve on this process? The problem is the isotropic etches. These steps cannot be included for any solutions. I propose an alternative process for fabricating the pillars. Through the use of lift-off technique it is possible to deposit material only where it is needed. The rest is easily removed via lift-off. This eliminates the need for isotropic wet etches. The approach has not been thoroughly investigate yet, but nm scale pillars have been demonstrated before in other groups (see for example [78]), hence it is believed this is a viable approach here, too. A recurring question is then which material to use? Chromium is an obvious candidate as this can be easily sputtered. Silicon nitride can also be sputtered [79] and is likely the preferred non-metallic alternative. Depending on the chosen material's resistance to KOH a protective PEEK cap on the front-side might be needed to minimize the KOH related etch on the pillars.

15.2 Resulting membranes

A subset of the fabricated membranes are presented on Figure 15.4. Most of the pillars are reasonably defined. The dense and less dense patterns of the two types of phononic cells are well transferred as evident on Figure 15.4a, 15.4b and 15.4c. However, they do exhibit a rounded base as shown on Figure 15.4d and 15.4e. It is likely a combination of the isotropic etches and the difficulty of etching between narrow regions.

The resulting pillar heights and diameters were estimated to be 446 ± 14 nm and 602 ± 97 nm, respectively, based on probing a few select samples of the second batch. The diameter is smaller than the 1 μm aimed for as evident on Figure 15.4, which is a direct consequence of the isotropic wet etch processes. However, as long as the total mass added is near the expected amount the performance of these devices are expected to be fine as predicted in Figure 14.3b.

Generally, as a proof of concept, the fabrication detailed here show these membranes can be fabricated with pillars deposited on top to significantly enhance their effective densities. Doing this on membranes with sizes up to 5×5 mm² which are only 20 nm thick is a feat, which to my knowledge, has not been demonstrated anywhere before. Fortunately, the faults described above have not prevented the membranes to achieve remarkable results,

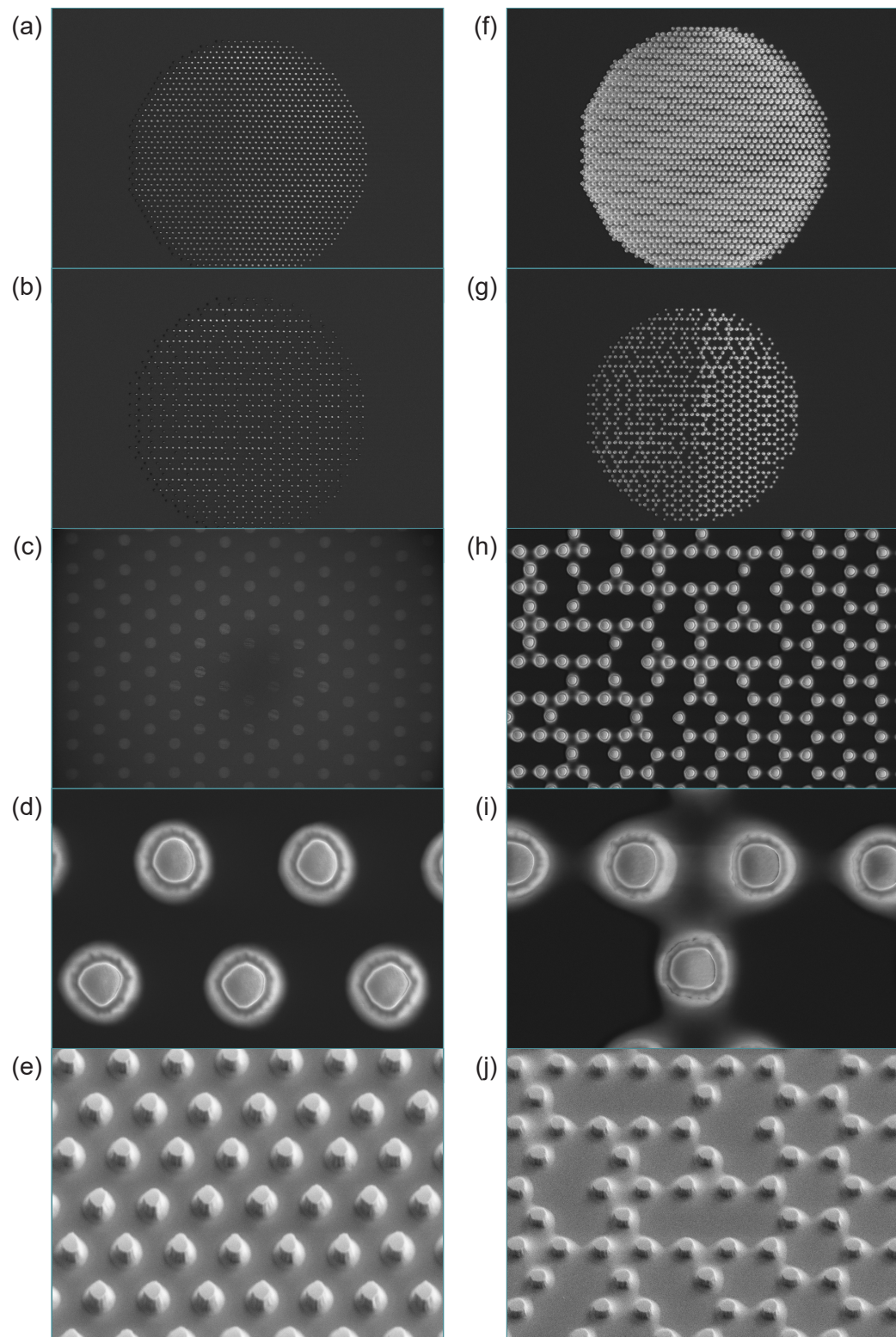


Figure 15.4: Scanning electron microscopy images from fabricated density phononic membranes. Images (a)-(e) are membranes which passed visual inspection. Images (f)-(j) are membranes with failed pillar release.

which will be shown in the following chapter. This hints at these membranes might be fabricated with high tolerances.

16 | Experimental results and discussion

The two batches presented in the previous chapter were characterized using the mechanical ringdown experimental setup presented in chapter 7. This chapter presents and discusses the results obtained, which includes a *new record* for ultra-coherent membranes.

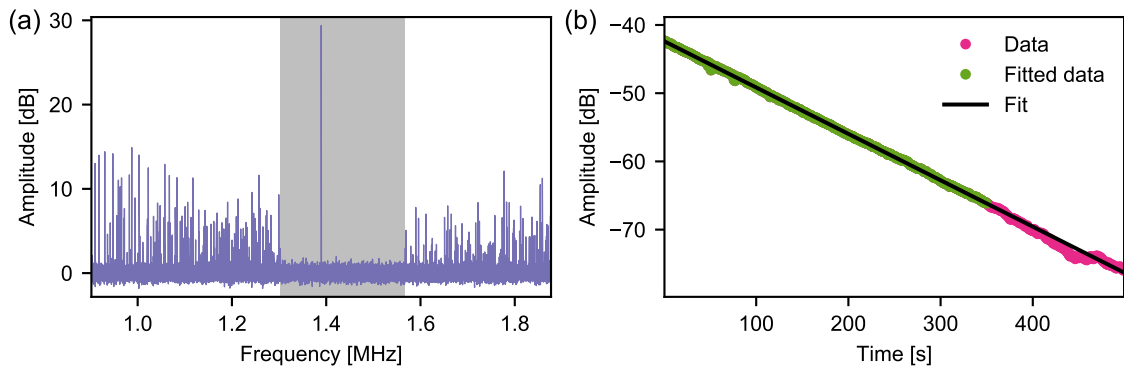


Figure 16.1: (a) Spectrum of a DP1 sample with $N_{\text{ph}} = 10$. The shaded area is the observed band-gap of the phononic crystal. (b) Ringdown of the best performing density phononic membrane at 1.41 MHz and $Q = 5.65 \times 10^8$.

As a first step, the existence of the band-gap must be verified as this is the cornerstone for this type of resonator. The spectrum near the engineered resonance frequency can be seen on Figure 16.1a. The defect-confined mode is near the expected 1.4 MHz. However, it does not lie perfectly within the center of the band-gap since the band-gap is blue-shifted a little. When comparing the position and width of the band-gap with the results in Figure 14.5 the maximum effective density extracted is $g_{\text{max}} \approx 3.75$ instead of the expected $g_{\text{max}} = 5$. This is a clear indication that the pillars were overexposed to isotropic etches, which consequently lead to smaller than expected pillars, and therefore smaller than expected mass contributions. The same is observed for many of the samples studied here.

The measured quality factors of the two successful batches are presented on Figure 16.2. The ringdown of best performing resonator is shown on Figure 16.1b. The first batch where the pillar mesh resolution a_{pil} was swept it is clearly seen it heavily affects the quality factor of the resonator as predicted from the pillar analysis. Judging from the slope it is reasonable to believe that these results can be improved quite considerably by fabricating the pillars smaller than what was done here. Quality factors above 10^9 is expected to be possible based on the predictions in Figure 14.9. Looking at the spread in quality factors the membranes with larger pillars have seemingly very reproducible results. However, the membranes based on the smallest pillars have quite a large spread in comparison. This is likely related to the difficulty in fabrication. The expected frequency of the resonators of the first batch was 1.1 MHz. The membranes containing large pillars match this prediction reasonably well. However, the membranes containing the smallest pillars have their frequency shifted upwards by ~ 0.1 MHz. This is another clear indication of the isotropic etches removing a significant amount of the pillars thereby reducing the overall mass of the membrane ultimately leading to higher frequencies.

In the second batch the number of phononic crystal cells embedded in the membrane

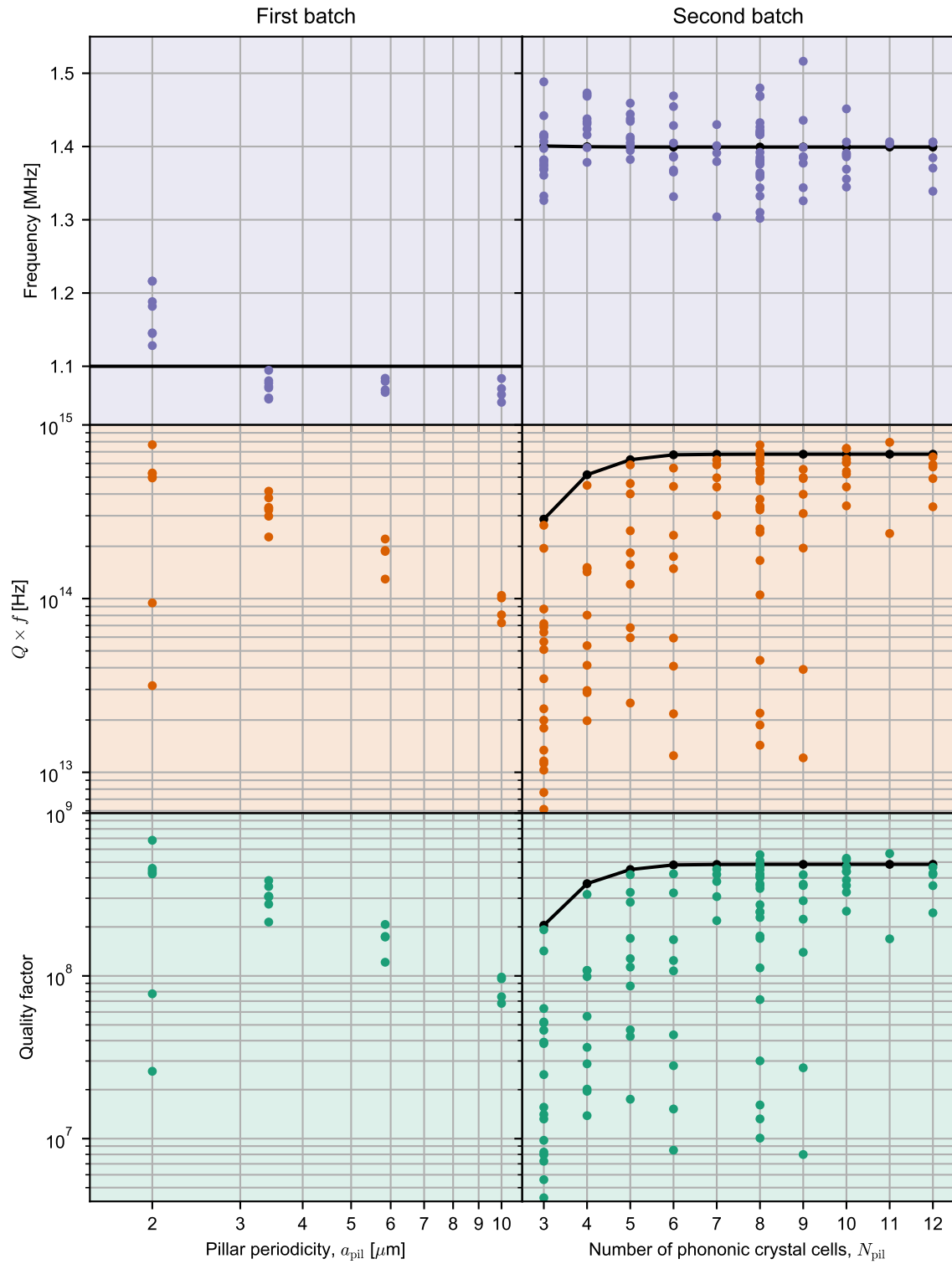


Figure 16.2: Overview of the measured quality factors for density phononic membranes. Black lines are predicted values. The first batch is a variant of design DP1 with $L_{ph} = 253 \mu\text{m}$. Thickness is $h = 20 \text{ nm}$ for both batches. From the fit on the second batch the surface loss coefficient is estimated to $\beta_{\text{surf}} = 9.23 \times 10^{10} \text{ m}^{-1}$.

was swept. When looking at the best samples, the quality factor's dependency on this parameter follows the prediction quite well, which confirms the assumption that these resonators will be limited by intrinsic losses. The model assumes $g_{\max} = 5$ which is higher than the estimated value based on Figure 16.1, but this discrepancy does not seem to affect the required number of phononic crystal cells much. Again, the spread is quite large. Furthermore, the spread in frequency is ~ 0.1 MHz. Since all samples here are based on the smallest fabricated pillar diameter, it is believed the underlying cause of the spread similar to the previous batch. To find an explanation, the samples quality factors are plotted vs their resonance frequencies and presented on Figure 16.3. It is seen samples significantly above 1.4 MHz exhibit a declining quality factor trend. The higher frequency is likely related to a lower mass of the pillars. This leads to a poorer band-gap. Samples with low quality factors are likely modes which are poorly confined as a result of the degrading band-gap. This effect is only visible for samples with $N_{\text{ph}} \leq 9$. The $N_{\text{ph}} = 10$ sample at 1.45 MHz does not exhibit the degradation. This can be explained by the extra phononic crystal cell layer providing the necessary mode isolation. Looking at the other end, the quality factor drops a little. These samples have relatively larger amounts of mass. According to the phononic crystal analysis in Figure 14.5, higher mass enhancement generally leads to higher losses in the cells. The results at the lower end of the frequency spectrum likely reflect this behavior.

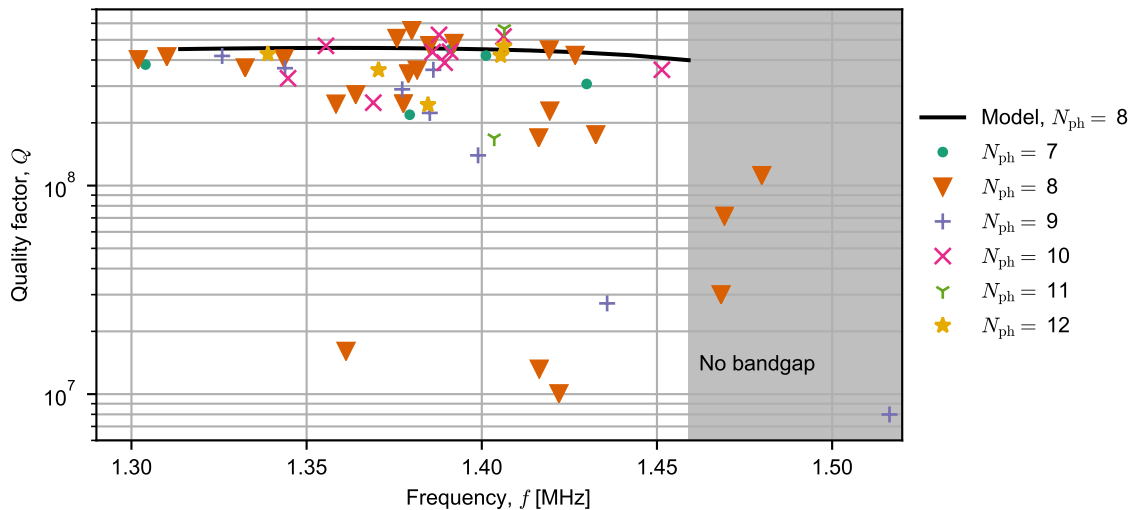


Figure 16.3: The quality factor plotted against the resonance frequency for the samples of the second batch with $N_{\text{ph}} \geq 7$. A set of simulations where the maximum density enhancement is swept is overlaid (black). No band-gap is predicted in the shaded area.

To test these hypotheses, the frequency and quality factors are simulated for different values of g_{\max} to mimic the over-etch of pillars. The observed spread in frequency is replicated seen by the black line in Figure 16.3. The quality factor changes very little, but it exhibits the behavior described above. When $g_{\max} < 2.8$ the band-gap disappears and the modes are no longer expected to be confined to the band-gap. This limit is crudely indicated on the figure. It can be observed samples above this limit have a heavily degraded quality factor, which fits the narrative of a disappearing band-gap.

All in all, the results look very promising. The best samples have Qf products of 8×10^{14} Hz, which is higher than reported anywhere else for thin film membranes [53] and only beaten by strain engineered phononic strings [29]. When considering the clear observed dependence on the pillar mesh density and the predictions from chapter 14 this approach

to designing and fabricating resonators has the potential to break the $Q = 10^9$ barrier at room temperature for MHz resonators as soon as the fabrication has been optimized further.

17 | Conclusion and outlook

In conclusion, the drawbacks of phononic crystal based membranes defined by modulating the tensile stress was highlighted and it was argued that another approach to realization of phononic membranes was needed to further enhance their performance. A novel approach was developed based on modulating the effective material density of the membrane. This can be realized by defining a fine mesh of pillars placed on top the membranes. Apart from locally shortening the wavelength, the pillars also add damping in the form of an evanescent wave at the base of each pillar. However, this added damping can be mitigated by diluting it over many smaller narrower pillars. For 20 nm thick resonators operating at 1.4 MHz the required periodicity of the pillar is 200 nm corresponding to a maximum feature size of 100 nm. This is a fabrication challenge and requires ongoing optimizations in fabrication to realize.

Studies of the obtainable band-gaps were performed confirming the validity of this approach. From this, two designs were created based on a binary and sine-like effective density distributions. While the latter showed slightly higher obtainable quality factors it also had a worse band-gap, which ultimately leads to the requirement of larger number of phononic crystal cells to properly confine the mode, thereby complicating the fabrication further. Both designs predicted quality factors above 10^9 at 1.4 MHz assuming a 20 nm thick membrane, which is unprecedented.

A process flow for fabrication was developed to realize the membranes. However, limitations related to UV lithography and the use of isotropic etch processes to define the pillars ultimately prevents fabrication of pillars much smaller than $1\ \mu\text{m}$. The use of KOH sets a limit on materials and processes which can be used for fabricating the pillars. It was proposed to define the pillars using lift-off technique and combine it with either sputtered chromium or silicon nitride. This could enable fabrication of narrower pillars. Furthermore, it was suggested UV-lithography could be replaced by either deep-UV, nano-imprint or e-beam lithography to enable pattern transfers of much smaller pillars. Moreover, the yield showed a dependence on the size of the resonator which effectively sets an upper limit on how large a membrane one can realistically fabricate. It is believed a critical factor for the yield is the quality of the stoichiometric silicon nitride layer used for the membrane itself.

Experimental results confirm the existence of a band-gap with a defect-confined mode slightly offset from the center. Characterization confirms the difficulty in obtaining the desired effective densities. Furthermore, the results clearly confirm the expected dependence of the quality factor to the resolution of the pillar mesh. Combined, this provides strong motivation for optimizing the fabrication process. To achieve proper mode isolation defined as the removal of boundary bending losses and phonon tunneling losses the required number of phononic crystal cells was predicted to be eight for design DP1, which was validated experimentally. Furthermore, the dominating loss mechanism was confirmed to be intrinsic losses. With the best samples having a Qf product of 8×10^{14} Hz these membranes already perform better than any similar resonators published. On top of this, there is a clear indication these resonators can be improved significantly simply by refining the fabrication process.

These already impressive results can also be improved further in other ways. The trick used in [53] to achieve their impressive resonator is to utilize the inverse proportional-

ity of the quality factor with respect the membrane thickness. Early batches did realize membranes with thicknesses measured down to ~ 10 nm, which directly corresponds to a factor of two improvement in the quality factor. However, the batch in question was never characterized due to contamination from processing. A defining feature of the density phononic membrane is the uniform tensile stress distribution fixed at the prestress level. This opens up the possibility to, among other approaches, make use of strain engineering to enhance the tensile stress leading to both higher quality factors and frequencies. It should be possible to enhance the Qf product by a factor of three by increasing the tensile stress to ~ 3 GPa, which is still a factor of two below the reported yield strength of stoichiometric silicon nitride [71]. Combining all these effects it should be possible to realize density phononic resonators with Qf products reaching 10^{16} Hz, which is more than an order of magnitude compared to any other membrane design. A key element to realize the above is strain engineering. This has to my knowledge never been demonstrated for two-dimensional structures. A proposal on how this could be done is presented in chapter 20.

If the above resonator can be realized to its fullest potential one ends up with a mechanical oscillator with truly quantum behavior even at room temperature. This makes it an interesting platform in possibly a range of applications. It is expected such a device can help push the field of quantum optomechanics where the Qf product is an important parameter [3]. Furthermore, it is believed such a device may find use in enhancing the sensitivities and performance in various quantum and classical sensing schemes where mechanical noise is a limiting factor.

Part IV

Two-dimensional strain engineering

18 | Overview

For some applications, the ability the engineer the tensile stress is useful for optimizing a resonator for a given task. In the context of maximizing the Qf product of a resonator a high tensile stress is beneficial as this drives up energy without adding any damping. However, there exists applications where higher tensile stress is not beneficial. In fact, some stress-sensing devices have their sensitivities improved by *lowering* the tensile stress. As part of this work designs were developed to achieve both using different strain engineering approaches on two-dimensional membranes.

During my external stay at Vienna University of Technology under Silvan Schmid's group I gained a lot of insight into using tensile stressed resonators for thermal sensing. For such devices the relative change in frequency scales as $\Delta f/f_0 \propto \sigma_0^{-1}$, where f_0 is the resonance frequency at the tensile stress σ_0 [59]. The highest sensitivity is hence obtained when the tensile stress is minimized. However, it should be noted the stress must still be high enough for it to dominate the overall stiffness of the device. There were discussions about how one may reduce the stress in the most controllable and reliable way. This lead to a proposed design for a geometric approach where the tensile stress can be reduced by orders of magnitude. This will be presented in chapter 19.

Strain engineering for the purpose of enhancing the tensile stress has already been demonstrated for strings [29]. However, for two-dimensional membranes no demonstrations or proposals exists. As this is vital for realizing the full potential for density phononic membranes a solution is needed. Strain engineering in two dimensions is not as straightforward as in the one-dimensional case since there are numerous issues to factor in. Combined with the fact there exists no other designs which can properly utilize the enhanced stress, it is not surprising this hasn't been explored yet. A way of achieving strain engineering for two-dimensional membranes is presented in chapter 20 compatible with density phononic membranes.

19 | Stress reduced design

Designing a membrane which ends up with a lower tensile stress than the prestress level can be achieved by including features which are allowed to relax by some controllable amount. By letting the stress be defined purely by the geometry, one obtains a device with easily reproducible relaxed stress levels, which is an advantage compared to more complicated alternatives. These include oxidizing the silicon nitride layer [15] and defining thin stress-less silicon-based membranes with a silicon nitride frame [80]. This section presents the developed design and suggests how such a device may be fabricated.

19.1 Design

The core principle behind the design is best illustrated using a string sketched in Figure 19.1. The string is connected via two perpendicular strings, where the latter is much shorter than the former. This length mismatch ensures the mode cannot exist in the perpendicular strings and therefore the mode will be confined to the central string. When considering the tensile stresses *before* relaxation, it is clear there is a force imbalance where the central string is connected to the perpendicular strings. The tensile stress of the central string cannot be sustained. When the string is released this will result in a new static equilibrium where the final tensile stress of the central string will now be much lower than before. The exact stress is dependent on the geometry and includes the relative lengths of the tethers as well as their widths. The effect can also be adjusted by introducing an angle different from 90 deg between the tethers. Unfortunately, the system has one crucial flaw. The string not only reduces the static tensile stress. It also reduces any changes of stress induced by, for example, thermal heating. This is because any changes in stress changes the stress in the whole string *uniformly*. Whenever a change in stress is induced, the same change occurs at the ends of the central string. This in turn changes the equilibrium configuration of the whole central-perpendicular-strings system. The end result is a partial negation of the induced stress leading to a very low sensitivity overall. It is therefore unfit for enhancing the sensitivity of sensors depending on changes in stress.

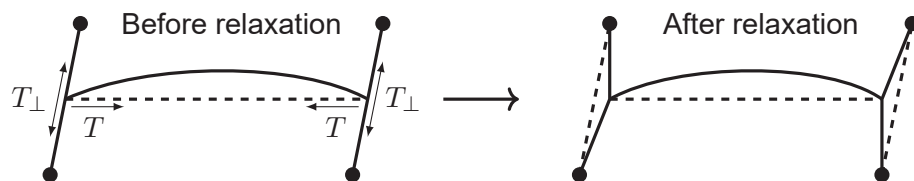


Figure 19.1: The core design principle in geometrically engineering membranes with reduced tensile stress. Solid circles are fixed points.

For two-dimensional membranes things are a little different. An example of a local change in stress in the center of a square membrane is shown on Figure 19.2. When the center of a membrane is heated the change in the equilibrium stress distribution is now confined to the center. This is a consequence of the now non-uniform stress distribution which confines the change in stress. Since the change in stress at the outer boundary is now negligible for a sufficiently large membrane, one can now use the stress reduction scheme described earlier to obtain a lower stress while still preserving the expected gain in sensitivity.

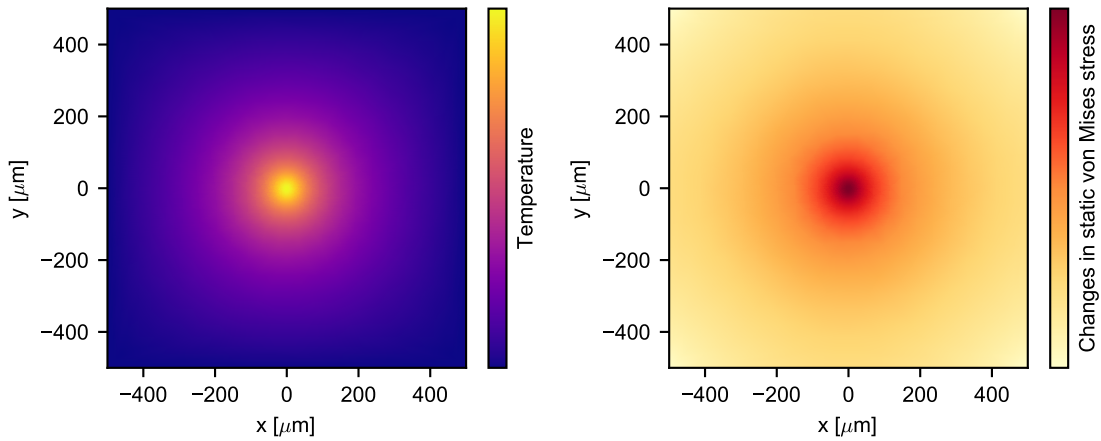


Figure 19.2: Thermo-mechanical simulation of a $1 \times 1 \text{ mm}^2$ square membrane heated in the center.

A two-dimensional adaptation of the initial sketch is shown on Figure 19.3. One of the motivation for the design was to combine it with a stress phononic membrane design. This requires a uniform stress distribution. The simplest way to guarantee this is by using a circular window with evenly spaced tethers connecting it to the substrate. The design of the tethers are designed with the same relaxation effect in mind as for the one-dimensional case.

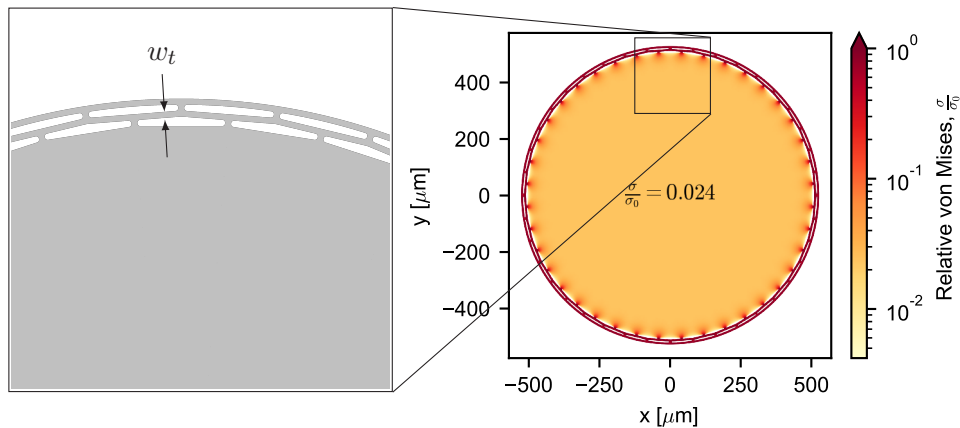


Figure 19.3: An implementation of two-dimensional strain engineering for reducing the tensile stress in the membrane.

As can be seen on Figure 19.4 one can easily obtain multiple orders of magnitude reduction of the tensile stress relative to the prestress level. One should be aware as the number of tethers is reduced, the uniformity of the stress within the membrane will start to degrade. This will be especially pronounced along the outer rim of the membrane. This can be a potential problem if one plan to place phononic crystals within the membrane as these are dependent on a well defined stress distribution.

19.2 Proposed fabrication

Circular frames are not trivial to fabricate, since they are incompatible with KOH etching otherwise used for releasing membranes. However, an interesting alternative have been demonstrated using hydrofluoric vapor etch illustrated on Figure 19.5a [32]. By defining

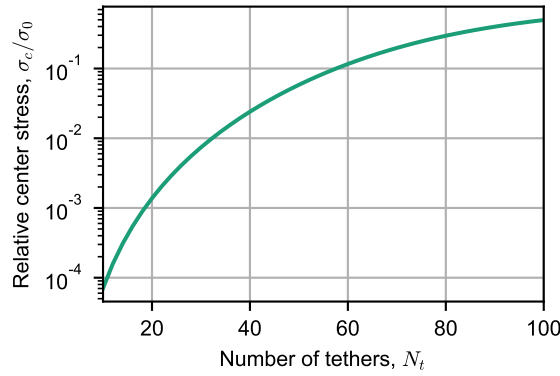


Figure 19.4: The relative tensile stress reduction for the membrane vs. number of tethers placed. Simulated for $w_t = 5 \mu\text{m}$ for a prestress of $\sigma_0 = 1 \text{ GPa}$ membrane radius of $500 \mu\text{m}$.

tiny holes evenly distributed across the membrane, the vapor can get access to a silicon oxide layer underneath. Using this technique any kind of window can in principle be fabricated. An example of a mask designed for this purpose is shown on Figure 19.5b. Silvan Schmid's group did try fabricating these devices based on my designs using the proposed technique. However they encountered problems. The stress reduction is so large the stiffness of the membrane is too low to properly support it. This results in the membranes collapsing to the silicon surface just below the silicon oxide layer and cannot be freed again.

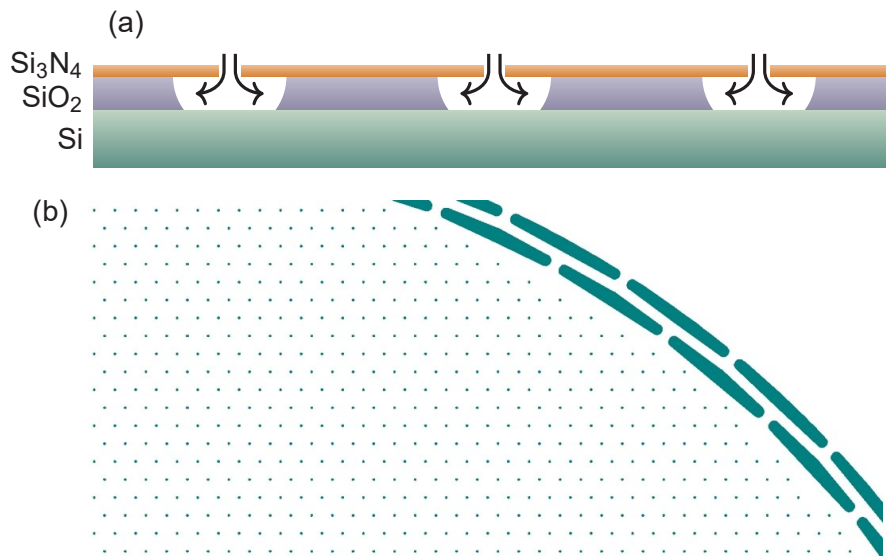


Figure 19.5: (a) Illustration of the proposed hydrofluoric vapor etch. (b) A segment of the mask designed for fabricating the proposed stress reduced membranes using hydrofluoric acid vapor. Colored parts are etched away. The shown mask is designed for membrane radius of $500 \mu\text{m}$, $N_t = 50$, $w_t = 5 \mu\text{m}$. The holes are $1 \mu\text{m}$ in diameter placed with a pitch of $10 \mu\text{m}$.

A solution to this problem could be to adapt the design to be compatible with a rectangular window. This will then allow KOH etching from the back-side and thereby eliminate the risk of the membrane touching any layer beneath. However, such a design change is not trivial if one intent to preserve the uniform stress distribution inside the membrane. It is in

principle possible, but every tether must be customized individually to ensure a uniform result. An example on how this can be done is demonstrated in the next chapter.

In conclusion, a design was proposed based on perpendicular tethers, which can displace and relax resulting in multiple orders of magnitude reduction of the equilibrium tensile stress inside a membrane. This is especially promising for thermal sensing and related applications. Its circular shape however makes fabrication problematic. An approach using hydrofluoric acid vapor was tried, but failed due to the extreme stress reduction obtained by the design. For any future fabrication attempt the design should be adapted to be compatible with a rectangular window, which will allow the use of back-side KOH etch.

20 | Stress enhanced design

The ability to enhance the stress of a membrane is an important tool for achieving the highest possible Qf products. This is exemplified by the similar implementation performed for strings [29], which to my knowledge is the only demonstration of a thin film tensile stress resonator with Qf products above 10^{15} Hz. This chapter details the development and optimization of a stress enhancing frame which can be used to enhance the tensile stress of a centrally placed membrane by a factor of three (and higher). This will be followed by a discussion of its use and applicability.

20.1 Design principle

The simplest approach for enhancing the tensile stress of a membrane which came to mind, is shown on Figure 20.1a. A circular membrane with a thickness h_1 is embedded inside a larger membrane with thickness $h_2 \gg h_1$. When such a structure is released the thicker part will pull with a much larger force than the thinner part. This forces the inner membrane to expand thereby increasing its tensile stress. It is simple and ensures a uniform stress distribution. However, there are two major problems with this approach. As one tries to push this to induce larger and larger stress the angular stress components of the thick layer will start to resist this relaxation. This ultimately sets an upper limit on how much the stress can be enhanced using this approach. To illustrate the problem, the central pad was simulated with different outer radii R_2 and presented on Figure 20.1b.

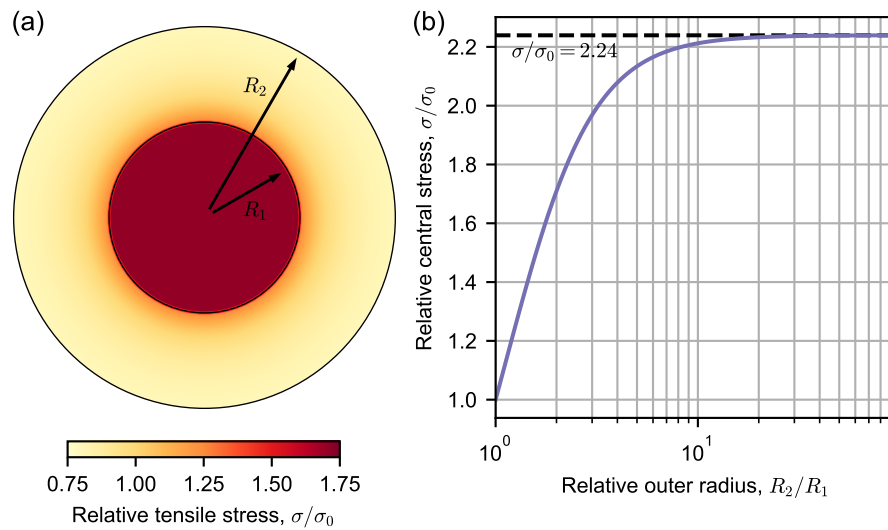


Figure 20.1: A study of the simplest two-dimensional stress-enhancement approach. (a) An excerpt of the performed simulations for $R_2 = 2R_1$. (b) A sweep where the outer thick radius R_2 is increased to enhance the tensile stress of the thinner inner membrane. Simulated for prestress $\sigma_0 = 1$ GPa and $h_2 = 10h_1$.

The second problem is such relaxations of the outer part will result in a non-uniform stress distribution in that area. When noting these structures are supposed to be used with vibrating membranes embedded in the center, one has to consider how to prevent these vibrations from coupling to the outside environment. Unless the outer layer has a thickness of at least multiple μm it simply isn't thick enough to prevent a significant portion of the vibrations to couple to this layer. This leads to bad mode confinement and possibly

increased losses. Such high thicknesses cannot be achieved by using stoichiometric silicon nitride. A solution would be to embed the outer part with a phononic crystal pattern to prevent this coupling. However, the non-uniform stress distribution will be non-trivial to pattern with a well defined band-gap.

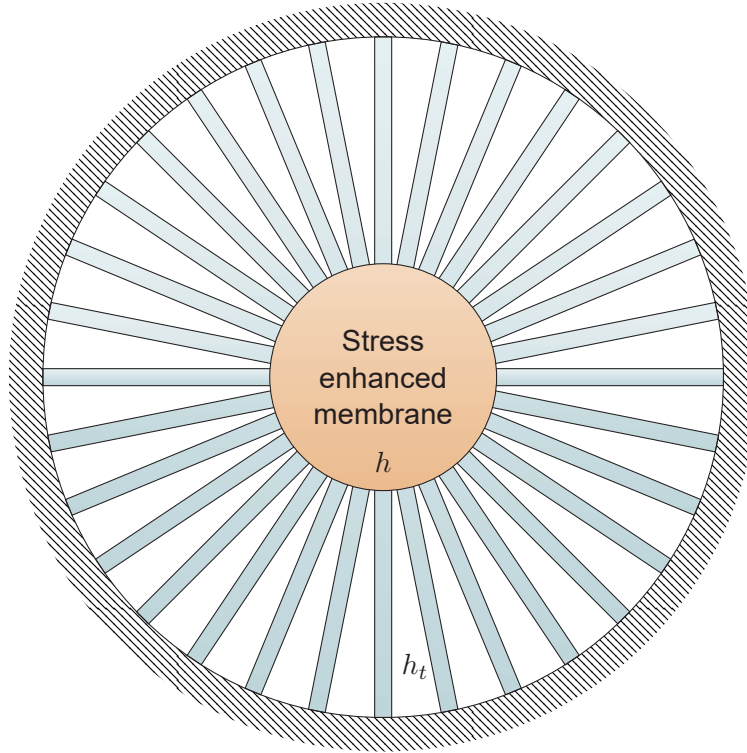


Figure 20.2: A sketch illustrating the idea for enhancing the tensile stress in the central pad. h and $h_t \gg h$ are the layer thickness of the central pad and tethers, respectively.

The above problems motivates one to search for alternative designs, which can pull on the central membrane to enhance the tensile stress with no upper limit, while at the same time enable some form of effective confinement of the vibrations. A proposal to how this can be done is sketched up in Figure 20.2. The membrane to be stress-enhanced is placed in the center. This is then connected to the substrate via tethers with a thickness h_t much larger than the membrane thickness h . The use of tethers eliminates the angular stress components which impeded the stress enhancement of the previous design. Furthermore, other groups have already demonstrated one-dimensional phononic patterns even on strings with non-constant tether widths. Similarly, one can embed the tethers with phononic crystals thereby preventing any modes from exciting the tethers and propagate any further. There are a number of pitfalls one need to consider. The geometry of the tethers not only affect the possible stress enhancement of the inner membrane. It also affects the maximum stress that might locally be induced. For example, sharp features typically have high stresses focused on to them which could lead to them tearing apart. One has to take extra care during the design phase to ensure the stresses all over the structure are kept below some safe threshold. How this can be done will be described in the following.

20.2 Design optimization

A base model was defined shown on Figure 20.3a for half a tether. The tethers should be designed to be able to pull with as large a force for as long a distance as possible without

locally inducing stress high enough for it to break. To optimize for all these, some degrees of freedom are needed which can be explored in an optimization routine. Looking at the three points P_1 , P_2 and P_3 their positions have an effect on the stress induced in that region. The fillet is defined by a quadratic Bezier line going from P_1 to P_2 using P_3 as a control point. This allows one to control the smoothness of the fillet-like feature. Having a more "flat" fillet spreads the local stress along the whole fillet instead of focusing it on a single point, as observed in the inset of Figure 20.3b. This design feature allows one to minimize the inner rim width of the tether domain without increasing the stress associated with the fillet. A narrower rim leads to less resistance to stress enhancement and ultimately higher stress gains. At the other end, the tethers should be as wide as possible to maximize the pulling force. Again, the same considerations apply for minimizing local stress.

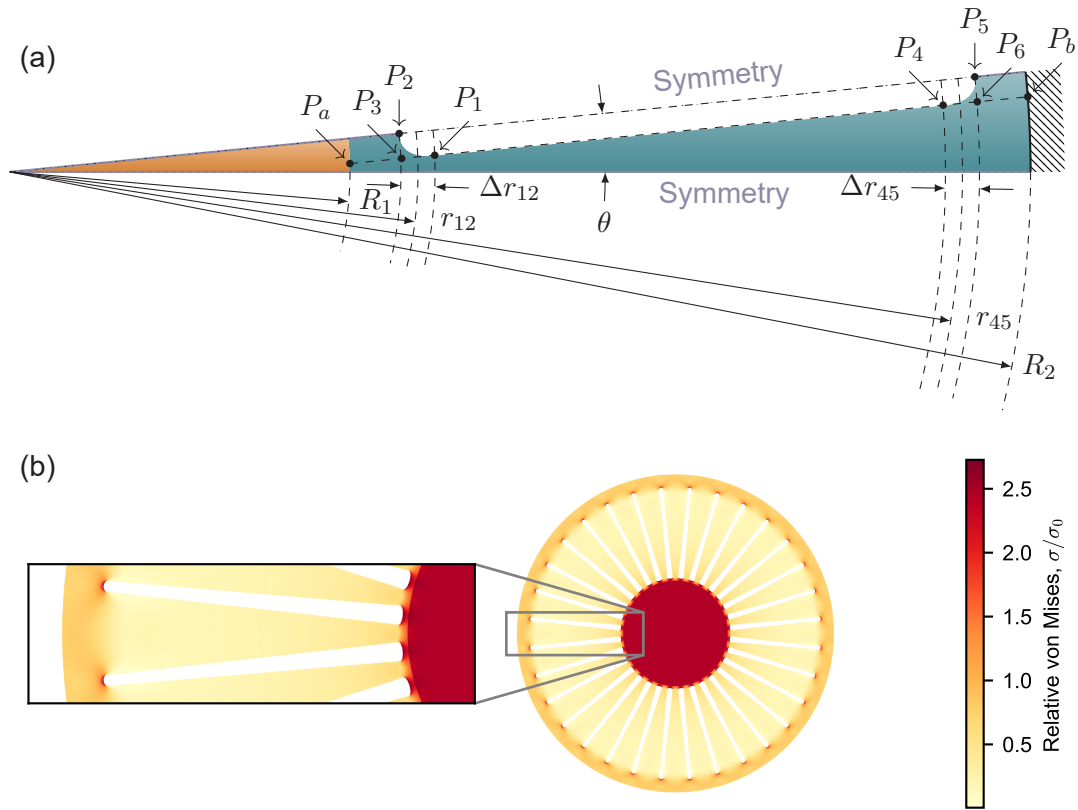


Figure 20.3: Strain enhanced membrane using thick tethers in a circular window. (a) Detailed drawing illustrating how the tethers are designed. Red is the central membrane. Green is the tether domain. (b) An excerpt of the performed simulations. Simulated and optimized for $N_t = 32$ tethers, $R_2 = 2R_1$, $h = 20$ nm, $h_t = 200$ nm and $\sigma_0 = 1.2$ GPa.

To optimize for these effects, an optimization model was build based on six variables: r_{12} , r_{45} , Δr_{12} , Δr_{45} as well as the angular coordinates of points P_a and P_b . To study the limits of what can be achieved with such a structure the number of tethers N_t and outer diameter R_2 are swept. A constraint was included: Locally, the stress is not allowed to exceed 3.3 GPa anywhere on the whole structure. The optimizations were performed using the Nelder-Mead method and simulated in COMSOL Multiphysics. Results are shown on Figure 20.4a. It is important to note convergence to the global minimum was not guaranteed. Choosing a bad initial guess lead to convergence towards a bad local minimum. This likely explains the noisy results for the long tethers. It is observed the

results only weakly depends on the number of tethers, where the maximum stress is obtained at $N_t \approx 30$. Figure 20.4b shows the pad stress follows a linear relationship to the length of the tethers, which levels off as the stress nears the maximum allowed stress defined by the constraint i.e. $\sigma \rightarrow 3\sigma_0$. In that regime the optimizer has very little room to find a good compromise between high stress enhancement and fulfilling the constraint. Stress enhancement of a factor of 2.7 can easily be obtained for $R_2 = 3.4 \cdot R_1$ and the maximum enhancement achieved was a factor of 2.9 at $R_2 = 5R_1$.

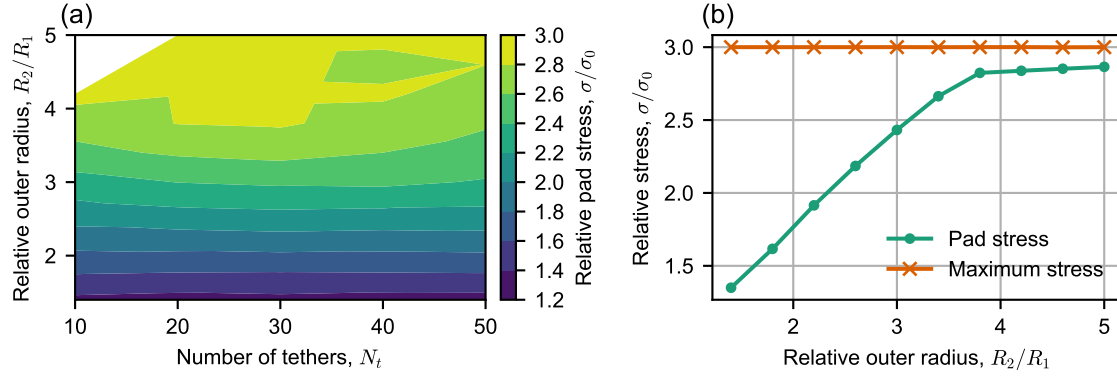


Figure 20.4: Optimization results of the circular stress enhancement design. (a) For each tether number and outer radius combination the parameters were optimized. The presented results are the maximized stress at the pad relative to prestress. White areas lead to nonsense results. (b) Pad stress and maximum stress in the whole structure plotted versus the relative outer radius for $N_t = 30$. Simulations performed with $h = 20$ nm, $h_t = 200$ nm and $\sigma_0 = 1.1$ GPa.

As was the case for the stress reduced design in chapter 19, a circular window is *not* ideal for fabrication. To address this issue an adaptation of the above was developed. Using a solution of the circular membrane as a starting point the tethers are then extended to all fit inside a square window. Now, if no other modifications are made the tethers attached at the corners will be able to pull harder and extend more compared to the tether attached to the sides. This will result in a non-uniform stress distribution inside the membrane in the middle. This cannot be accepted if they are to be used with phononic membranes.

To continue, each tether needs to be uniquely optimized. For each tether a separate model was build consisting of the corresponding slice of the inner membrane, and the tether itself connected from the inner membrane to the edge of the square window. One of these models is overlayed on Figure 20.5. Using the original estimated parameters from the circular optimization as initial values, the tether was optimized again to replicate the result obtained in the first optimization. By replicating the original results each tether can be optimized independently from each other which simplifies computation considerably. An example of this performed for a structure containing 32 tethers is shown on Figure 20.5. Here it can be seen how the optimizer reduced the width of the tethers at the corners to counteract the larger force and displacement, which they would otherwise induce. The resulting enhanced stress is identical to the circular version it is based on.

20.3 Discussion

While a large enhancement of the tensile stress can be obtained using the tether-based frame, there is a serious drawback not yet mentioned. The *size* of the whole device can become quite large. Recall the typical size of phononic membranes is $\sim 3 \times 3$ mm². Based on the above result the total size of the whole structure then needs to have a side

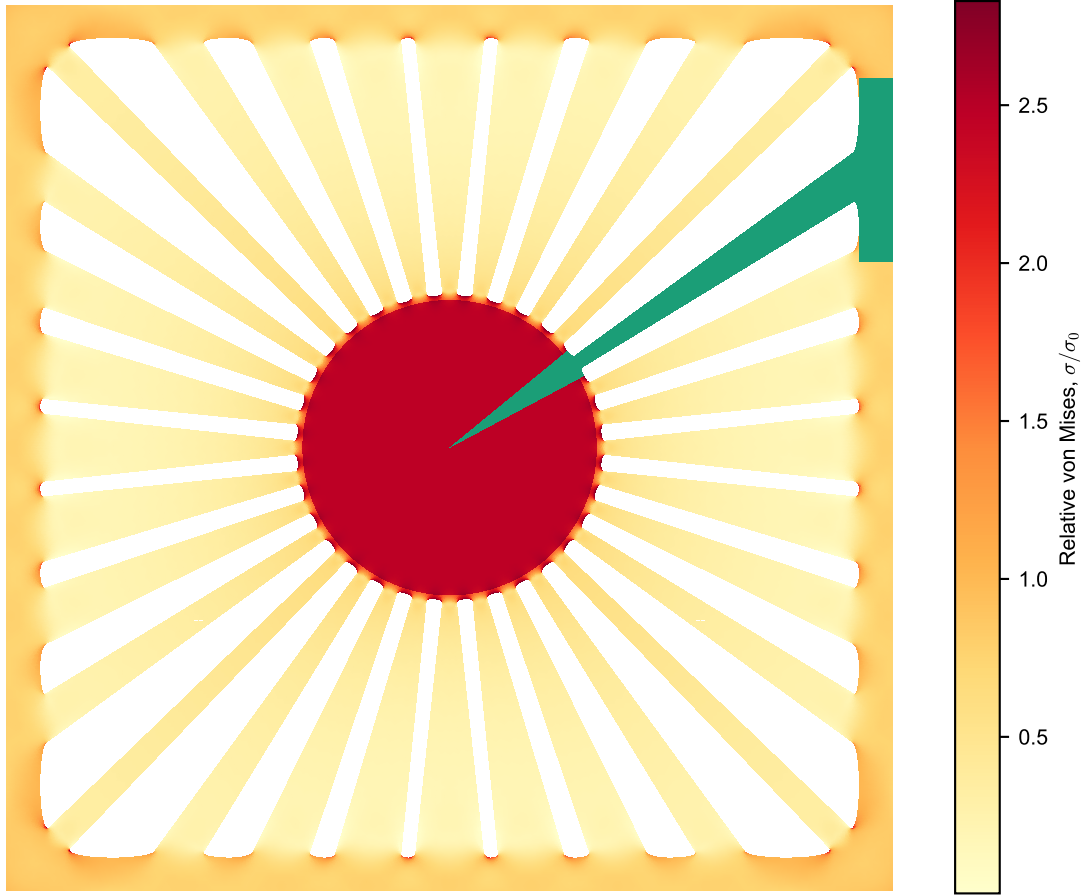


Figure 20.5: An adaptation of the a circular stress enhanced design to a square window. The overlaid green slice is the geometry of one of the separate models used to optimize each individual tether. Based on the results of Figure 20.3b.

length three times as large leading to a size of $\sim 9 \times 9 \text{ mm}^2$! However, there exists a real possibility the required size of the phononic pattern will be lower. The absence of a hard fixed boundary, which would otherwise induce large boundary bending losses, is believed to lower this requirement considerably. How much depends on how lossy the thick tether domain will be. This has not yet been investigated. Moreover, the required length of the outer diameter can be reduced by having a larger thickness difference between the h and h_t to amplify the enhancement. This amplification is even greater when taking into account that thicker layers also have higher effective prestresses compared to thinner layers (see section 10.1). This effect was not included in the above simulations.

A convenient feature of using tethers is that they can be embedded with a one-dimensional phononic crystal pattern to further isolate the mode. These also serve to prevent any modes of the tethers themselves to be excited. This two-stage phononic isolation is expected to effectively remove phonon tunneling losses. Looking at Figure 20.5 some of the tethers are so wide it is doubtful there is room for efficient stress phononic structures. For this to work one-dimensional density phononics should be used instead. If the mode-shape of the defect-confined mode located in the center is attenuated enough at the tethers, it might even be sufficient to simply fabricate "massive" blocks instead of tiny pillars, which would simplify fabrication considerably.

An interesting application of this structure not yet mentioned is the potential to use it for

inducing stress in membranes based on other materials. This even includes materials which would otherwise be stress-free. Examples of this includes silicon, silicon carbide and diamond. The latter two are expected to have high yield strength which opens up the potential for even larger damping dilution [81] and ultimately higher Qf -products compared to silicon nitride.

In conclusion, a design was developed enabling stress-enhanced membranes based in thick tethers with high tensile prestress. The design was optimized for maximizing the stress enhancement while limiting the maximum stress which may be induced locally. An approach for converting the circular membrane design to a square membrane was presented enabling easier fabrication. The design is compatible with density phononics and can be used to enhance the tensile stress of these structures, thereby enabling them to reach extraordinarily high Qf products via damping dilution. Moreover, this stress enhancement design can also be applied to induce or increase tensile stress in other materials, which could open up the possibility of using alternatives to silicon nitride.

21 | Overall conclusion and outlook

In this chapter the most important results of the thesis are highlighted and future work is discussed. In Part I the fundamental theory for describing thin-film micromechanical resonators was presented. This included a thorough study of sub-MHz phonon tunneling losses, which is poorly understood within the field. A generalized model was developed for the infinite substrate case. However, this rarely reflects real world conditions. This was then extended to a stochastic model for large, but finite substrates, for resonators operating at their fundamental mode and some higher modes. Proper experimental validation is still missing. With that said, it gives a good qualitative description of results seen in this and other work.

In Part II topology optimization was used to optimize the fundamental mode of a trampoline, which lead to the largest ever reported Qf product for a fundamental mode resonator. However, the model used for topology optimization was not properly made. Boundary bending losses were not well resolved in the used model and phonon tunneling loss model lead to misleading results. Despite these problems, good experimental results were obtained where intrinsic losses were significantly reduced. This also means improving on the topology optimization model could potentially lead to even greater gains.

In Part III the use of tiny pillars to modulate the effective density of a membranes has lead to impressive early results, where the best performing membranes already outperform state-of-the-art stress phononic membranes. Fabrication of the pillars was a major challenge and can still be improved upon a lot. A major obstacle is lithography. UV-lithography is not suited for defining structures down to 100 nm needed for fulfilling the full potential of this scheme. Another major obstacle is how to fabricate the pillars. The current approach of using plasma-enhanced chemical vapor deposited silicon nitride, followed by etching away excess material using dry and wet processes, can only barely fabricate pillars at $\sim 1 \mu\text{m}$. An alternative approach is needed. It was suggested lift-off techniques could be used, but this needs further investigations and tests. If the above challenges can be solved, room-temperature MHz resonators with $Q > 10^9$ should be possible.

In Part IV two proposals for strain engineering on two-dimensional membranes were presented. The first was focused on *reducing* the tensile stress in controllable way. This is especially interesting for thermal sensing, where the low stress directly translates into higher sensitivities. It is believed the design can be refined to ease fabrication. The second proposal was focused on *enhancing* the stress through the use of thick decoupled tethers. The approach shows it can enhance the stress of a centrally placed membrane by up to a factor of three. Such a device has interesting applications. It could be combined with density phononic membranes to enhance their coherence. In that case, the predicted Qf product exceeds 10^{16} , which would be an incredible result if realized. Moreover, the technique could be used for inducing or enhancing tensile stress in any material imaginable.

The thesis leaves several open-ended challenges. The use of topology optimization for the trampolines have already lead to great results. However, the original scope of its implementation was too limited. What happens if we change the size of the domain? It will surely change the resonance frequencies. Depending on how it attempts to reduce boundary bending losses, it might reveal an interesting route for design optimization in terms of the Qf product. Moreover, by extending the model to allow it to define clamped

points or regions *inside* the design domain, one might reveal compact yet high performing designs, where boundary bending losses are effectively removed, just as for the fractal designed string [57]. It could open the possibility of generating a design with negligible boundary bending losses and high co-overlap between the modeshape and tensile stress field. Such a device would outperform anything in existence and possibly even outperform the stress-enhanced density phononic membranes. It would be the best possible design imaginable based on the current theory. All of this is heavily dependent on being able to adapt the topology optimization model for this task, which is not straight forward.

In contrast, the path for extreme coherent devices is clearly outlined for density phononic membranes. With the theory well established and early results confirming the possibility of obtaining spectacular results, it all relies on developing fabrication steps and processes to enable fabrication of pillars down to the required 100 nm. An interesting addition would be combining density phononics with topology optimization to improve the confinement and quality factor of the mechanical mode. Similar optimization has already been demonstrated for photonic systems [62]. Considering the similarity between optical waves and mechanical waves on a uniformly stressed thin-film membrane, it should be possible to adapt it to the current case. The assumption of uniform stress also vastly simplifies the challenges encountered in [75]. Finally, when combining it all using the stress-enhanced frame design, it is clear there are plenty of routes for optimizing the current density phononic membrane results, where all these contributions can be combined cumulatively leading to an extremely coherent oscillator.

To answer the question back in the beginning of the introduction: Did we succeed in fabricating the most coherent mechanical resonator possible? No, but two clear paths have been identified in which both could lead to the ultimate silicon nitride based micromechanical resonator.

Bibliography

- [1] Niklas Luhmann et al. "Ultrathin 2 nm gold as impedance-matched absorber for infrared light". In: *Nature Communications* 11.1 (2020). ISSN: 20411723. DOI: 10.1038/s41467-020-15762-3. arXiv: 1911.13126.
- [2] Dennis Høj et al. "Ultra-coherent fundamental mode mechanical resonators designed using topology optimization". In: *The 3rd International Forum on Quantum Metrology and Sensing*. Kyoto, 2020.
- [3] Markus Aspelmeyer, Tobias J. Kippenberg, and Florian Marquardt. "Cavity optomechanics". In: *Reviews of Modern Physics* 86.4 (2014), pp. 1391–1452. ISSN: 15390756. DOI: 10.1103/RevModPhys.86.1391. arXiv: 1303.0733.
- [4] Kater W. Murch et al. "Observation of quantum-measurement backaction with an ultracold atomic gas". In: *Nature Physics* 4.7 (2008), pp. 561–564. ISSN: 17452481. DOI: 10.1038/nphys965. arXiv: 0706.1005.
- [5] Scott S. Verbridge et al. "High quality factor resonance at room temperature with nanostrings under high tensile stress". In: *Journal of Applied Physics* 99.12 (2006). ISSN: 00218979. DOI: 10.1063/1.2204829.
- [6] L. Cremer, M. Heckl, and B. A.T. Petersson. *Structure-borne sound: Structural vibrations and sound radiation at audio frequencies*. 2005, pp. 1–607. ISBN: 3540226966. DOI: 10.1007/b137728.
- [7] Silvan Schmid, Luis Guillermo Villanueva, and Michael Lee Roukes. *Fundamentals of nanomechanical resonators*. 2016, pp. 1–175. ISBN: 9783319286914. DOI: 10.1007/978-3-319-28691-4.
- [8] RG Christian. "The theory of oscillating-vane vacuum gauges". In: *Vacuum* 16.4 (1966), pp. 175–178. ISSN: 0042207X. DOI: 10.1016/0042-207X(66)91162-6.
- [9] M. Khochikar and N. Waterfall. "Simplified stapling technique for securing the dorsal vein complex [1]". In: *British Journal of Urology* 81.2 (1998), p. 342. ISSN: 00071331.
- [10] Quirin P. Unterreithmeier, Thomas Faust, and Jörg P. Kotthaus. "Damping of nanomechanical resonators". In: *Physical Review Letters* 105.2 (2010), pp. 1–4. ISSN: 00319007. DOI: 10.1103/PhysRevLett.105.027205. arXiv: 1003.1868.
- [11] René Vacher, Eric Courtens, and Marie Foret. "Anharmonic versus relaxational sound damping in glasses. II. Vitreous silica". In: *Physical Review B - Condensed Matter and Materials Physics* 72.21 (2005), pp. 1–11. ISSN: 10980121. DOI: 10.1103/PhysRevB.72.214205. arXiv: 0505560 [cond-mat].
- [12] Thomas Faust et al. "Signatures of two-level defects in the temperature-dependent damping of nanomechanical silicon nitride resonators". In: *Physical Review B - Condensed Matter and Materials Physics* 89.10 (2014), pp. 1–5. ISSN: 10980121. DOI: 10.1103/PhysRevB.89.100102. arXiv: 1310.3671.
- [13] L. G. Villanueva and S. Schmid. "Evidence of surface loss as ubiquitous limiting damping mechanism in SiN micro- and nanomechanical resonators". In: *Physical Review Letters* 113.22 (2014), pp. 1–6. ISSN: 10797114. DOI: 10.1103/PhysRevLett.113.227201. arXiv: 1405.6115.
- [14] S. I. Raider et al. "Surface Oxidation of Silicon Nitride Films". In: *Journal of The Electrochemical Society* 123.4 (1976), pp. 560–565. ISSN: 0013-4651. DOI: 10.1149/1.2132877.
- [15] Niklas Luhmann et al. "Effect of oxygen plasma on nanomechanical silicon nitride resonators". In: *Applied Physics Letters* 111.6 (2017). ISSN: 00036951. DOI: 10.1063/1.4989775. arXiv: 1706.02957.

- [16] Scott S. Verbridge et al. "Macroscopic tuning of nanomechanics: Substrate bending for Reversible control of frequency and quality factor of nanostring resonators". In: *Nano Letters* 7.6 (2007), pp. 1728–1735. ISSN: 15306984. DOI: 10.1021/nl070716t.
- [17] R. Zhang et al. "Integrated tuning fork nanocavity optomechanical transducers with high f M Q M product and stress-engineered frequency tuning". In: *Applied Physics Letters* 107.13 (2015), pp. 12–14. ISSN: 00036951. DOI: 10.1063/1.4932201.
- [18] Clarence Zener. "Internal friction in solids. I. Theory of internal friction in reeds". In: *Physical Review* 52.3 (1937), pp. 230–235. ISSN: 0031899X. DOI: 10.1103/PhysRev.52.230.
- [19] Shirin Ghaffari et al. "Quantum limit of quality factor in silicon micro and nano mechanical resonators". In: *Scientific Reports* 3 (2013), pp. 3–8. ISSN: 20452322. DOI: 10.1038/srep03244.
- [20] Surabhi Joshi, Sherman Hung, and Srikar Vengallatore. "Design strategies for controlling damping in micromechanical and nanomechanical resonators". In: *EPJ Techniques and Instrumentation* 1.1 (2014), pp. 1–14. DOI: 10.1186/epjti5.
- [21] S. Schmid et al. "Damping mechanisms in high-Q micro and nanomechanical string resonators". In: *Physical Review B - Condensed Matter and Materials Physics* 84.16 (2011), pp. 1–6. ISSN: 10980121. DOI: 10.1103/PhysRevB.84.165307.
- [22] S. A. Fedorov et al. "Generalized dissipation dilution in strained mechanical resonators". In: *Physical Review B* 99.5 (2019), pp. 1–16. ISSN: 24699969. DOI: 10.1103/PhysRevB.99.054107. arXiv: 1807.07086. URL: <http://arxiv.org/abs/1807.07086>.
- [23] Boyang Jiang et al. "SiC CANTILEVERS FOR GENERATING UNIAXIAL STRESS Boyang". In: *2019 20th International Conference on Solid-State Sensors, Actuators and Microsystems & Eurosensors XXXIII (TRANSDUCERS & EUROSENSORS XXXIII)* June (2019), pp. 1655–1658.
- [24] Erick Romero et al. "Engineering the Dissipation of Crystalline Micromechanical Resonators". In: *Physical Review Applied* 13.4 (2020), p. 1. ISSN: 23317019. DOI: 10.1103/PhysRevApplied.13.044007. arXiv: 1911.03835. URL: <https://doi.org/10.1103/PhysRevApplied.13.044007>.
- [25] R. A. Norte, J. P. Moura, and S. Gröblacher. "Mechanical Resonators for Quantum Optomechanics Experiments at Room Temperature". In: *Physical Review Letters* 116.14 (2016), pp. 1–6. ISSN: 10797114. DOI: 10.1103/PhysRevLett.116.147202. arXiv: 1511.06235.
- [26] Y. Tao et al. "Single-crystal diamond nanomechanical resonators with quality factors exceeding one million". In: *Nature Communications* 5 (2014), pp. 1–8. ISSN: 20411723. DOI: 10.1038/ncomms4638. arXiv: 1212.1347.
- [27] Hadi Najar et al. "High quality factor nanocrystalline diamond micromechanical resonators limited by thermoelastic damping". In: *Applied Physics Letters* 104.15 (2014). ISSN: 00036951. DOI: 10.1063/1.4871803. URL: <http://dx.doi.org/10.1063/1.4871803>.
- [28] J. Hofer, A. Schliesser, and T. J. Kippenberg. "Cavity optomechanics with ultrahigh-Q crystalline microresonators". In: *Physical Review A - Atomic, Molecular, and Optical Physics* 82.3 (2010), pp. 1–4. ISSN: 10502947. DOI: 10.1103/PhysRevA.82.031804. arXiv: 0911.1178.
- [29] Nils J. Engelsen et al. "Elastic Strain Engineering for Ultralow Mechanical Dissipation". In: *International Conference on Optical MEMS and Nanophotonics 2018-July.6390* (2018), pp. 764–768. ISSN: 21605041. DOI: 10.1109/OMN.2018.8454645.
- [30] I. Wilson-Rae. "Intrinsic dissipation in nanomechanical resonators due to phonon tunneling". In: *Physical Review B - Condensed Matter and Materials Physics* 77.24 (2008), pp. 1–31. ISSN: 10980121. DOI: 10.1103/PhysRevB.77.245418. arXiv: 0710.0200.

- [31] Garrett D. Cole et al. "Phonon-tunnelling dissipation in mechanical resonators". In: *Nature Communications* 2.1 (2011). ISSN: 20411723. DOI: 10.1038/ncomms1212.
- [32] I. Wilson-Rae et al. "High-Q nanomechanics via destructive interference of elastic waves". In: *Physical Review Letters* 106.4 (2011), pp. 1–4. ISSN: 00319007. DOI: 10.1103/PhysRevLett.106.047205. arXiv: 1010.2171.
- [33] R. D. Mindlin and Jiashi Yang. *An introduction to the mathematical theory of vibrations of elastic plates*. 2006, pp. 1–191. ISBN: 9789812772497. DOI: 10.1142/6309.
- [34] F.H. Jackson. *Analytical Methods in Vibrations*. 1st ed. Vol. 13. 12. Pearson, 1967, p. 480. ISBN: 9780023801402. DOI: 10.1049/ep.1967.0353.
- [35] M. Morvaridi and M. Brun. "Perfectly matched layers for flexural waves: An exact analytical model". In: *International Journal of Solids and Structures* 102-103 (2016), pp. 1–9. ISSN: 00207683. DOI: 10.1016/j.ijsolstr.2016.10.024. URL: <http://dx.doi.org/10.1016/j.ijsolstr.2016.10.024>.
- [36] Maryam Morvaridi and Michele Brun. "Perfectly matched layers for flexural waves in Kirchhof–Love plates". In: *International Journal of Solids and Structures* 134 (2018), pp. 293–303. ISSN: 00207683. DOI: 10.1016/j.ijsolstr.2017.11.009. URL: <https://doi.org/10.1016/j.ijsolstr.2017.11.009>.
- [37] G. Xie, D. J. Thompson, and C. J.C. Jones. "Mode count and modal density of structural systems: Relationships with boundary conditions". In: *Journal of Sound and Vibration* 274.3-5 (2004), pp. 621–651. ISSN: 0022460X. DOI: 10.1016/j.jsv.2003.05.008.
- [38] A. Borrielli et al. "Low-Loss Optomechanical Oscillator for Quantum-Optics Experiments". In: *Physical Review Applied* 3.5 (2015), pp. 1–12. ISSN: 23317019. DOI: 10.1103/PhysRevApplied.3.054009.
- [39] A. Borrielli et al. "Control of recoil losses in nanomechanical SiN membrane resonators". In: *Physical Review B* 94.12 (2016), pp. 3–7. ISSN: 24699969. DOI: 10.1103/PhysRevB.94.121403. arXiv: 1607.04485.
- [40] M. J. Weaver et al. "Nested trampoline resonators for optomechanics". In: *Applied Physics Letters* 108.3 (2016). ISSN: 00036951. DOI: 10.1063/1.4939828. arXiv: 1510.00206.
- [41] Matthew J. Weaver et al. "Coherent optomechanical state transfer between disparate mechanical resonators". In: *Nature Communications* 8.1 (2017). ISSN: 20411723. DOI: 10.1038/s41467-017-00968-9. arXiv: 1704.02394.
- [42] Jingkun Guo, Richard Norte, and Simon Gröblacher. "Feedback Cooling of a Room Temperature Mechanical Oscillator close to its Motional Ground State". In: *Physical Review Letters* 123.22 (2019), pp. 1–9. ISSN: 10797114. DOI: 10.1103/PhysRevLett.123.223602. arXiv: 1911.01586. URL: <http://arxiv.org/abs/1911.01586>.
- [43] P. L. Yu et al. "A phononic bandgap shield for high-Q membrane microresonators". In: *Applied Physics Letters* 104.2 (2014), pp. 2–6. ISSN: 00036951. DOI: 10.1063/1.4862031. arXiv: 1312.0962.
- [44] Gregory S. MacCabe et al. "Nano-acoustic resonator with ultralong phonon lifetime". In: *Science* 370.6518 (2020), pp. 840–843. ISSN: 10959203. DOI: 10.1126/science.abc7312.
- [45] Yeghishe Tsaturyan et al. "Demonstration of suppressed phonon tunneling losses in phononic bandgap shielded membrane resonators for high-Q optomechanics". In: *Optics Express* 22.6 (2014), p. 6810. ISSN: 1094-4087. DOI: 10.1364/oe.22.006810. arXiv: 1312.7776.
- [46] William Hvidtfelt Padkær Nielsen et al. "Multimode optomechanical system in the quantum regime". In: *Proceedings of the National Academy of Sciences of the*

- United States of America* 114.1 (2017), pp. 62–66. ISSN: 10916490. DOI: 10.1073/pnas.1608412114. arXiv: 1605.06541.
- [47] Jon Juel Thomsen. *Vibrations and Stability*. 2nd ed. New York: Springer-Verlag Berlin Heidelberg, 2003. ISBN: 978-3-662-10793-5. DOI: 10.1007/978-3-662-10793-5.
- [48] Letizia Catalini, Yeghishe Tsaturyan, and Albert Schliesser. “Soft-Clamped Phononic Dimers for Mechanical Sensing and Transduction”. In: *Physical Review Applied* 14.1 (2020), pp. 1–16. ISSN: 23317019. DOI: 10.1103/PhysRevApplied.14.014041. arXiv: 2003.04072. URL: <http://arxiv.org/abs/2003.04072>.
- [49] Yi Kwei Wen. “Method for Random Vibration of Hysteretic Systems”. In: *ASCE J Eng Mech Div* 102.2 (1976), pp. 249–263.
- [50] M. A. Tomlinson. *Noise and vibration analysis at Cranfield*. 1st ed. Vol. 11. 5. Chichester: JohnWiley & Sons, Ltd Registered, 1980, pp. 167–173. ISBN: 9780470746448.
- [51] Y. Tsaturyan et al. “Ultracoherent nanomechanical resonators via soft clamping and dissipation dilution”. In: *Nature Nanotechnology* 12.8 (2017), pp. 776–783. ISSN: 17483395. DOI: 10.1038/nnano.2017.101. arXiv: 1608.00937.
- [52] Amir Hossein Ghadimi, Dalziel Joseph Wilson, and Tobias J. Kippenberg. “Radiation and Internal Loss Engineering of High-Stress Silicon Nitride Nanobeams”. In: *Nano Letters* 17.6 (2017), pp. 3501–3505. ISSN: 15306992. DOI: 10.1021/acs.nanolett.7b00573.
- [53] I. Galinskiy et al. “Phonon counting thermometry of an ultracoherent membrane resonator near its motional ground state”. In: *Optica* 7.6 (June 2020), p. 718. ISSN: 23318422. DOI: 10.1364/optica.390939. arXiv: 2005.14173.
- [54] C. Reetz et al. “Analysis of Membrane Phononic Crystals with Wide Band Gaps and Low-Mass Defects”. In: *Physical Review Applied* 12.4 (2019), p. 1. ISSN: 23317019. DOI: 10.1103/PhysRevApplied.12.044027. arXiv: 1906.11273. URL: <https://doi.org/10.1103/PhysRevApplied.12.044027>.
- [55] Mingyun Yuan, Martijn A. Cohen, and Gary A. Steele. “Silicon nitride membrane resonators at millikelvin temperatures with quality factors exceeding 10⁸”. In: *Applied Physics Letters* 107.26 (2015). ISSN: 00036951. DOI: 10.1063/1.4938747. arXiv: 1510.07468. URL: <http://dx.doi.org/10.1063/1.4938747>.
- [56] Junxin Chen et al. “Entanglement of propagating optical modes via a mechanical interface”. In: *Nature Communications* 11.1 (2020). ISSN: 20411723. DOI: 10.1038/s41467-020-14768-1. URL: <http://dx.doi.org/10.1038/s41467-020-14768-1>.
- [57] S. A. Fedorov et al. “Fractal-like Mechanical Resonators with a Soft-Clamped Fundamental Mode”. In: *Physical Review Letters* 124.2 (2020), p. 25502. ISSN: 10797114. DOI: 10.1103/PhysRevLett.124.025502. arXiv: 1912.07439. URL: <https://doi.org/10.1103/PhysRevLett.124.025502>.
- [58] Hans A. Bachor and Timothy C. Ralph. *A Guide to Experiments in Quantum Optics*. 2019, p. 421. ISBN: 9783527403936. DOI: 10.1002/9783527695805.
- [59] Maksymilian Kurek et al. “Nanomechanical Infrared Spectroscopy with Vibrating Filters for Pharmaceutical Analysis”. In: *Angewandte Chemie* 129.14 (2017), pp. 3959–3963. ISSN: 1521-3773. DOI: 10.1002/ange.201700052.
- [60] Martin P. Bendsøe and Ole Sigmund. *Topology Optimization*. Second Edi. Berlin: Springer-Verlag Berlin Heidelberg, 2004, p. 381. ISBN: 9783642076985. URL: <https://link.springer.com/book/10.1007/978-3-662-05086-6%7B%5C#%7Dtoc>.
- [61] Mads Baandrup et al. “Closing the gap towards super-long suspension bridges using computational morphogenesis”. In: *Nature Communications* 11.1 (2020), pp. 1–7. ISSN: 20411723. DOI: 10.1038/s41467-020-16599-6. URL: <http://dx.doi.org/10.1038/s41467-020-16599-6>.

- [62] Fengwen Wang et al. "Maximizing the quality factor to mode volume ratio for ultra-small photonic crystal cavities". In: *Applied Physics Letters* 113.24 (2018), pp. 0–5. ISSN: 00036951. DOI: 10.1063/1.5064468. arXiv: 1810.02417.
- [63] Fengwen Wang. "Systematic design of 3D auxetic lattice materials with programmable Poisson's ratio for finite strains". In: *Journal of the Mechanics and Physics of Solids* 114 (2018), pp. 303–318. ISSN: 00225096. DOI: 10.1016/j.jmps.2018.01.013. URL: <https://doi.org/10.1016/j.jmps.2018.01.013>.
- [64] Erik Andreassen, Boyan S. Lazarov, and Ole Sigmund. "Design of manufacturable 3D extremal elastic microstructure". In: *Mechanics of Materials* 69.1 (2014), pp. 1–10. ISSN: 01676636. DOI: 10.1016/j.mechmat.2013.09.018. URL: <http://dx.doi.org/10.1016/j.mechmat.2013.09.018>.
- [65] Niels Aage et al. "Giga-voxel computational morphogenesis for structural design". In: *Nature* 550.7674 (2017), pp. 84–86. ISSN: 14764687. DOI: 10.1038/nature23911. URL: <http://dx.doi.org/10.1038/nature23911>.
- [66] Wenjun Gao, Fengwen Wang, and Ole Sigmund. "Systematic design of high-Q pre-stressed micro membrane resonators". In: *Computer Methods in Applied Mechanics and Engineering* 361 (2020), p. 112692. ISSN: 00457825. DOI: 10.1016/j.cma.2019.112692. URL: <https://doi.org/10.1016/j.cma.2019.112692>.
- [67] Ole Sigmund and Kurt Maute. "Topology optimization approaches: A comparative review". In: *Structural and Multidisciplinary Optimization* 48.6 (2013), pp. 1031–1055. ISSN: 1615147X. DOI: 10.1007/s00158-013-0978-6.
- [68] M. Stolpe and K. Svanberg. "An alternative interpolation scheme for minimum compliance topology optimization". In: *Structural and Multidisciplinary Optimization* 22.2 (2001), pp. 116–124. ISSN: 1615147X. DOI: 10.1007/s001580100129.
- [69] M. Stadtmüller. "Mechanical Stress of CVD □ Dielectrics". In: *Journal of The Electrochemical Society* 139.12 (1992), pp. 3669–3674. ISSN: 0013-4651. DOI: 10.1149/1.2069141.
- [70] S. T. Ahn et al. "Film stress-related vacancy supersaturation in silicon under low-pressure chemical vapor deposited silicon nitride films". In: *Journal of Applied Physics* 64.10 (1988), pp. 4914–4919. ISSN: 00218979. DOI: 10.1063/1.342441.
- [71] Amit Kaushik, Harold Kahn, and Arthur H. Heuer. "Wafer-level mechanical characterization of silicon nitride MEMS". In: *Journal of Microelectromechanical Systems* 14.2 (2005), pp. 359–367. ISSN: 10577157. DOI: 10.1109/JMEMS.2004.839315.
- [72] C. Bergenstorf Nielsen et al. "Particle Precipitation in Connection with KOH Etching of Silicon". In: *Journal of The Electrochemical Society* 151.5 (2004), G338. ISSN: 00134651. DOI: 10.1149/1.1688802.
- [73] S. Reid et al. "Mechanical dissipation in silicon flexures". In: *Physics Letters, Section A: General, Atomic and Solid State Physics* 351.4-5 (2006), pp. 205–211. ISSN: 03759601. DOI: 10.1016/j.physleta.2005.10.103.
- [74] R. Nawrodt et al. "Investigation of mechanical losses of thin silicon flexures at low temperatures". In: *Classical and Quantum Gravity* 30.11 (2013). ISSN: 02649381. DOI: 10.1088/0264-9381/30/11/115008. arXiv: 1003.2893.
- [75] Søren Kjær Larsen. "Design of Micro Resonators". Master's Thesis. Technical University of Denmark, 2020, pp. 450–456.
- [76] J. D. Joannopoulos, R. D. Meade, and J. N. Winn. *Photonic Crystals: Molding the Flow of Light*. Second Edi. Vol. 3. 6. Singapore: Princeton University Press, 1995, pp. 38–47. ISBN: 9780691124568. URL: <http://library1.nida.ac.th/termpaper6/sd/2554/19755.pdf>.

- [77] Andrew J. Nathan and Andrew Scobell. "How China sees America". In: *Foreign Affairs* 91.5 (2012), pp. 1689–1699. ISSN: 00157120. DOI: 10.1017/CBO9781107415324.004. arXiv: arXiv:1011.1669v3.
- [78] C. Vieu et al. "Electron beam lithography: Resolution limits and applications". In: *Applied Surface Science* 164.1-4 (2000), pp. 111–117. ISSN: 01694332. DOI: 10.1016/S0169-4332(00)00352-4.
- [79] N. Khemasiri et al. "Silicon nitride thin films deposited by reactive gas-timing magnetron sputtering for protective coating applications". In: *Advanced Materials Letters* 6.6 (2015), pp. 554–559. ISSN: 0976397X. DOI: 10.5185/amlett.2015.SMS5.
- [80] A. Shchepetov et al. "Ultra-thin free-standing single crystalline silicon membranes with strain control". In: *Applied Physics Letters* 102.19 (2013). ISSN: 00036951. DOI: 10.1063/1.4807130. arXiv: 1303.1658.
- [81] Kurt E. Petersen. "Silicon as a Mechanical Material". In: *Proceedings of the IEEE* 70.5 (1982), pp. 420–457. ISSN: 15582256. DOI: 10.1109/PROC.1982.12331.

A | Material parameters

Most of the thesis is based on the same materials for various calculations and simulations. In order to prevent cluttering the text with repeating the same material property values this appendix collects on the commonly used values in this work. These are listed on Table A.1.

Table A.1: List of all materials used in this work and their assumed material property values.

Material	ρ [kg/m ³]	E [GPa]	ν [1]
Silicon nitride (SiN)	3100	250	0.23
Silicon (Si)	2329	170	0.28

B | Derivation of basic properties for typical resonators

This appendix is written as a look-up for basic solutions and derived quantities for basic resonator types. The following resonators are treated: String and trampoline as well as circular and rectangular membrane. All of the derivations assume the presence of high tensile stress.

B.1 String

Consider a string of length L , width b , thickness h , density ρ , and high tensile stress σ along the string direction. Assuming fixed boundary conditions, i.e. no rotations or displacements at either ends, the solution using Eq. (3.16) assuming high tensile stress has the form

$$\psi_n(x) = \begin{cases} \tilde{\psi}_n(x) & , \quad 0 \leq x \leq L/2 \\ (-1)^{n+1} \tilde{\psi}_n(L-x) & , \quad L/2 < x \leq L \end{cases} \quad (\text{B.1})$$

where

$$\tilde{\psi}_n(x) \approx \sin k_n x - \frac{k}{k_e} (\cos k_n x - e^{-k_e x}) \quad (\text{B.2})$$

and $k_n \approx n\pi/L$. The energy of the mode is defined as

$$W_n = \int_0^L \frac{\omega_n^2}{2} \rho \psi_n^2(x) u_n^2 dx = \frac{\sigma b h (n\pi)^2}{4L} u_n^2 \quad (\text{B.3})$$

where u_n is the amplitude of the modeshape. For strings under high tensile stress the shear force at the boundary can be derived from taking the slope of the string a short distance away from the boundary, e.g. away from the evanescent wave at the boundaries. This corresponds to ignoring the evanescent term, i.e. $\psi_n(x) \approx \sin kx$ and evaluating the slope at $x = 0, L$. This yields

$$F_{n-} = bh\sigma u'(0) = \frac{n\pi b h \sigma}{L} \bar{u}_n \quad (\text{B.4})$$

$$F_{n+} = -bh\sigma u'(L) = -F_{n-}(-1)^n$$

It can clearly be seen that for a system of two point sources on the substrate mainly the zeroth or first order moments can be excited depending on their polarity. The resulting moments exciting the substrate are thus

$$M_0 = \frac{n\pi b h \sigma}{L} [1 - (-1)^n] \bar{u}_n \quad (\text{B.5})$$

$$M_1 = \frac{n\pi b h \sigma}{2} [1 + (-1)^n] \bar{u}_n \quad (\text{B.6})$$

B.2 Trampoline

The trampoline can to a great extent be described by a mass element in the center coupled to the outside boundary via N tethers of length L , width b and tensile stress σ as illustrated on Figure 4.7a. The modeshape for a tether can be approximated by treating it as a string with fixed boundary condition at the substrate end and "free" at the central pad. Note, it is

not free in the sense it can relax and lose its tensile stress. It is simply free to displace out-of-plane as well as rotate while still preserving the tensile stress. The wavelength for such a string is usually much longer than $1/4$ of a tether length. This is simply a consequence from the added mass of the central pad reducing the eigen-frequency significantly. An approximate mode-shape can then be obtained by taking Eq. (B.2) and substitute the sine and cosine to the second order of x and normalize it to 1 at $x = L$, i.e.

$$\psi_i(x) \approx \frac{x}{L} - \frac{1}{k_e L} \left(1 - e^{-k_e x}\right) \quad (\text{B.7})$$

Using the same set of parameters as for the string and letting the center pad be defined by a square of sidelength S and thickness h effective stiffness and mass can be defined. For the fundamental mode these are given by

$$k_{\text{eff},f} = N \frac{bh\sigma}{L}, \quad m_{\text{eff},f} = \rho h(S^2 + NLb/3), \quad (\text{B.8})$$

where the mass of the tethers are included and the eigen-frequency given by $\omega_f = \sqrt{k_{\text{eff},f}/m_{\text{eff},f}}$ and energy defined as $W_f = m_{\text{eff},f}\omega_f^2 u_f^2/2$. The forces on the boundary depend on the angle of the tethers defined as u_f/L using the small angle approximation, where u_f is the displacement amplitude of the fundamental mode. The total boundary force is thus

$$F = M_0 = N \frac{bh\sigma}{L} u_f = k_{\text{eff}} u_f. \quad (\text{B.9})$$

The fundamental mode can only excite the zeroth order moment. A similar approach is used for the twisting trampoline (see Figure 4.7b). Assuming $N = 4$ the effective mass and stiffness are determined as

$$m_{\text{eff},t} = \rho h \left(\frac{2bL}{3} + \frac{S^2}{6} \right), \quad k_{\text{eff},t} = 2 \frac{bh\sigma}{L}, \quad (\text{B.10})$$

with similar definitions of the energy and eigen-frequency. The force excited on the substrate is asymmetric and equals the first order moment derived as

$$M_1 = 2 \frac{bh\sigma}{L} \cdot \left(L + \frac{S}{\sqrt{2}} \right) u_t, \quad (\text{B.11})$$

where u_t is the displacement of the twisting mode.

B.3 Circular membrane

Obtaining an analytical solution of a circular membrane with fixed boundary conditions and with radius a with high tensile stress is difficult. Depending on where on the modeshape one want to investigate, an approximate solution can be used given by [34]

$$\psi_{mn}(r, \theta) \approx \left(J_m(k_{mn}r) - \tilde{\psi}_{mn}(r) \right) \cos(\theta m + \psi) \quad (\text{B.12})$$

where ψ is some angular shift and

$$\tilde{\psi}_{mn}(r) = \begin{cases} \frac{k_{mn}}{k_e} (1 - e^{-k_e(a-r)}) & , \quad 0 \leq \frac{a-r}{k_{mn}} \ll 1 \\ 0 & , \quad \text{otherwise} \end{cases}, \quad (\text{B.13})$$

and where $m = 0, 1, 2, \dots$, $n = 1, 2, 3, \dots$, and the wavenumber $k_{mn} \approx \Theta_{mn}/a$ where Θ_{mn} is the n 'th root of $J_m \Theta$. Eigen-frequencies are given by $\omega_{mn} = k_{mn} \sqrt{\sigma/\rho}$. The energy can be derived by only evaluating the non-evanescent part of the modeshape resulting in

$$W_{mn} = \int_0^{2\pi} \int_0^a \frac{\omega^2 \rho h}{2} u_{mn}^2(r, \theta) r \, dr d\theta = \frac{\pi}{\alpha_m} \Theta_{mn}^2 \sigma h u_{mn}^2 J_{m+1}^2(\Theta_{mn}), \quad (\text{B.14})$$

where

$$\alpha_m = \begin{cases} 2 & , \quad m = 0 \\ 4 & , \quad m > 0 \end{cases} . \quad (\text{B.15})$$

Similar to the string the boundary forces per unit length are estimated using the slope at the boundary

$$\begin{aligned} F'_{mn}(\theta) &= -\sigma h \left. \frac{\partial(u_{mn}\psi_{mn}(r, \theta))}{\partial r} \right|_{r=a} \\ &= \begin{cases} u_{0n} \frac{\Theta_{0n} h \sigma}{a} \mathbf{J}_1(\Theta_{0n}) & , \quad m = 0 \\ u_{mn} \frac{\Theta_{mn} h \sigma}{a} \mathbf{J}_{m+1}(\Theta_{mn}) \cos(m\theta + \psi) & , \quad m = 1 \end{cases} . \end{aligned} \quad (\text{B.16})$$

Finally, it can be shown only a single order moment is excited depending on the angular mode m and is derived to

$$\begin{aligned} M_0 &\rightarrow M_{0n} = 2\pi\Theta_{0n}h\sigma\mathbf{J}_1(\Theta_{0n})u_{0n} \\ M_m &\rightarrow M_{mn} = \pi\Theta_{mn}h\sigma a^m \mathbf{J}_{m+1}(\Theta_{mn})u_{0n} \end{aligned} \quad (\text{B.17})$$

B.4 Rectangular membrane

A rectangular membrane with fixed boundary conditions with sidelengths L_x and L_y is less trivial to solve analytically. At high tensile stress an approximate solution can be derived based on the solution of the string [7] of the form

$$\psi(x, y) = \psi_{n_x}(x)\psi_{n_y}(y) \quad (\text{B.18})$$

where $\psi_{n_i}(x_i)$ is defined by Eq. (B.1). The eigen-modes have the wavenumbers defined by $k_x \approx n_x\pi/L_x$ and $k_y \approx n_y\pi/L_y$ with eigen-frequencies given by $\omega_{n_x n_y} = \sqrt{\frac{\sigma}{\rho} (k_{n_x}^2 + k_{n_y}^2)}$. Following the same steps as before, the energy equals

$$W_{n_x n_y} = \int_0^{L_y} \int_0^{L_x} \frac{\omega^2 \rho h}{2} u_{n_x n_y}^2(x, y) \, dx dy = \frac{\omega_{n_x n_y}^2 \rho h L_x L_y}{8} \bar{u}_{n_x n_y}^2 , \quad (\text{B.19})$$

and the boundary force per unit length can be shown to equal

$$F'_{x=0}(y) = \frac{n_x \pi \sigma h}{L_x} \sin \frac{n_y \pi y}{L_y} u_{n_x n_y} \quad (\text{B.20})$$

$$F'_{x=L_x}(y) = -(-1)^{n_x} \frac{n_x \pi \sigma h}{L_x} \sin \frac{n_y \pi y}{L_y} u_{n_x n_y} \quad (\text{B.21})$$

$$F'_{y=0}(x) = \frac{n_y \pi \sigma h}{L_y} \sin \frac{n_x \pi x}{L_x} u_{n_x n_y} \quad (\text{B.22})$$

$$F'_{y=L_y}(x) = -(-1)^{n_y} \frac{n_y \pi \sigma h}{L_y} \sin \frac{n_x \pi x}{L_x} u_{n_x n_y} \quad (\text{B.23})$$

Numerical calculations have shown that for membranes with low aspect ratio ($\frac{2}{3} \leq L_y/L_x \leq \frac{3}{2}$) mainly the zeroth, first or second order moment is excited for any membrane mode and not at the same time. Based on this knowledge approximate analytical solutions are possible. Using the above boundary force distributions and shifting the coordinates so the

origo matches the center of the membrane, the three order moments are given by

$$\begin{aligned}
 M_0 &\approx \begin{cases} -4u_{n_x n_y} \sigma h (-1)^{\frac{n_x+n_y}{2}} \left(\frac{n_x L_y}{n_y L_x} + \frac{n_y L_x}{n_x L_y} \right) & , \quad n_x n_y = \text{odd} \\ 0 & , \quad \text{otherwise} \end{cases} \\
 M_1 &\approx 2u_{n_x n_y} \sigma h (-1)^{\frac{n_x+n_y+1}{2}} \cdot \begin{cases} \frac{n_x L_y}{n_y} + \frac{n_y L_x^2}{n_x L_y^2} & , \quad n_x = \text{even} \& n_y = \text{odd} \\ \frac{n_y L_x}{n_x} + \frac{n_x L_y^2}{n_y L_x} & , \quad n_x = \text{odd} \& n_y = \text{even} \\ 0 & , \quad \text{otherwise} \end{cases} \quad (\text{B.24}) \\
 M_2 &\approx \begin{cases} 2u_{n_x n_y} (-1)^{\frac{n_x+n_y}{2}} \sigma h \left(\frac{n_x}{n_y} L_y^2 + \frac{n_y}{n_x} L_x^2 \right) & , \quad n_x = \text{even} \& n_y = \text{even} \\ 0 & , \quad \text{otherwise} \end{cases}
 \end{aligned}$$

C | Process flows


Three process flows are attached in the following order:

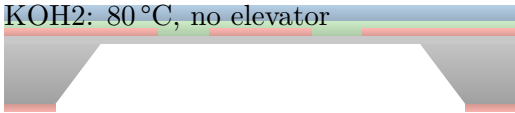
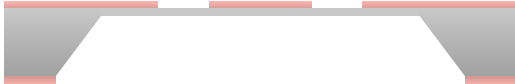
1. Fabricating topology optimized trampolines using a protective PECVD Si_xN_y layer.
2. Fabricating topology optimized trampoline using an extra thick LPCVD Si_3N_4 layer.
3. Fabricating density phononic membranes.


The process recipes and equipment are based on DTU Nanolab's cleanroom facility. The process flows can be found in the following pages.

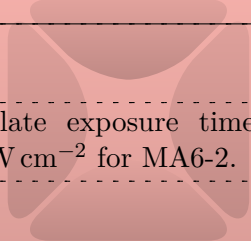
Process flow title			Reversion
Topology Optimized Trampoline - Protective PECVD layer			1.10
DTU Physics Department of Physics <hr style="border: 2px solid red; width: 100px; margin-top: 10px;"/>	Contact email	Contact person	Contact phone
	denho@fysik.dtu.dk	Dennis Høj	+45 26 14 93 66
	Labmanager group DTU Physics - QPIT	Batch name TOT	Creation date 6 th Mar, 2020
			Reversion date 24 th Jan, 2021


Step	Equipment and procedure	Purpose and comments
1 LPCVD nitride deposition		
1.1 Substrate	4", 500 µm double side polished silicon wafer.	Take directly to furnace without changing carrier. Remember to include a dummy wafer.
1.2 LPCVD Si ₃ N ₄	Furnace: LPCVD Nitride (4"). High stress. Deposition thickness 50 nm.	Check logbook to calculate deposition time.
1.3 Measure	Ellipsometer, Nanolab recipe for thin nitride.	Measure on dummy wafer and write in furnace log.
2 Frontside membrane lithography and etch		
2.1 front Spin coat	Spin Coater: Gamma UV: 1.5 µm AZ MIR 701 with HMDS.	Trampoline pattern exposure.
2.2 front Exposure	Aligner: MLA3: 200 mJ cm ⁻² .	
2.3 front Develop	Developer: TMAH UV-lithography: 3001, PEB60SP60.	
2.4 front Inspection	Inspect pattern in optical microscope.	If pattern is poorly defined, remove resist and redo lithography.
2.5 front SiN etch	AOE: sin_res, 00:00:15.	
2.6 Resist removal	Plasma asher 2: O ₂ : 400 sccm, N ₂ : 70 sccm, 1000 W, 30 min.	Verify all photoresist has been removed: Tilt wafer to check for any changes in color.
3 PECVD deposition		
3.1 front PECVD Si ₃ N ₄	PECVD4: Fysik/denho/MFSiN 50 MPa with Oxide, 200 nm, ~12 nm/min	Acts as a protective layer during handling and KOH etch. The 50 nm oxide layer below helps PECVD removal.
4 Backside window lithography and etch		
4.1 back Spin coat	Spin Coater: Gamma UV: 1.5 µm AZ MIR 701 with HMDS.	Calculate exposure time from intensity. 11 mW cm ⁻² for MA6-2.
4.2 back Exposure	Aligner: MA6 - 2: 220 mJ cm ⁻² .	
4.3 back Develop	Developer: TMAH UV-lithography: 3001, PEB60SP60.	
4.4 back Inspection	Inspect pattern in optical microscope.	If pattern is poorly defined, remove resist and redo lithography.
4.5 back SiN etch	AOE: sin_res, 00:00:15.	
4.6 Resist removal	Plasma asher 2: O ₂ : 400 sccm, N ₂ : 70 sccm, 1000 W, 30 min.	Verify all photoresist has been removed: Tilt wafer to check for any changes in color.

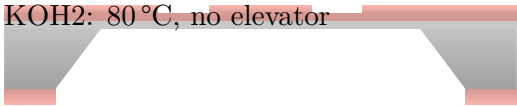
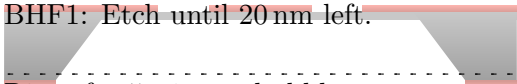
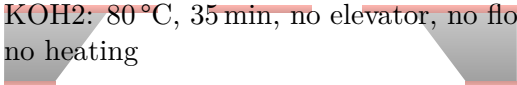
Process flow title			Reversion
Topology Optimized Trampoline - Protective PECVD layer			1.10
DTU Physics Department of Physics 	Contact email	Contact person	Contact phone
	denho@fysik.dtu.dk	Dennis Høj	+45 26 14 93 66
	Labmanager group DTU Physics - QPIT	Batch name TOT	Creation date 6 th Mar, 2020
			Reversion date 24 th Jan, 2021


Step	Equipment and procedure	Purpose and comments
5 Membrane release		
5.1 KOH	KOH2: 80 °C, no elevator 	Expect 50 min of preparation time. Place wafers closely packed. Place SiN coated dummy wafers at each end. Measure etch depth after 5 hour and estimated required total etch time for 515µm and add another 3 min. When there is 33 min left, take the wafers out.
5.2 Water rinse	Rinse for 5 min, no bubbles.	
5.3 BHF	BHF1: Over etch 300 nm 	Removes the remaining protective PECVD layer as well as oxides from oxygen plasma. The large over etch ensures no traces of the PECVD layer is left.
5.4 Water rinse	Rinse for 5 min, no bubbles.	
5.5 KOH	KOH2: 80 °C, 33 min, no elevator, no flow, no heating 	The lack of flow and heating will degrade the etch rate, but the etch will be more gentle on the fragile membranes, thereby increasing yield. Note: The membranes are very fragile from this point on.
5.6 Water rinse	Rinse for 5 min, 80 °C, no bubbles.	The bath takes 30 minutes to warm up.
5.7 HCl	5 % HCl for 10 min	Removes iron oxide contamination resulting from KOH etch.
5.8 Water rinse	Rinse for 5 min, no bubbles.	
5.9 Wafer cleaning	H ₂ SO ₄ (sulfuric acid) added with a spoon of (NH ₄) ₂ S ₂ O ₈ (ammoniumpersulfate)	Removes potassium ions resulting from KOH etch, as well as other possible alkali ions and organic contaminations.
5.10 Water rinse	Rinse for 5 min, no bubbles.	
5.11 Ethanol dry	Dry in ethanol bath. 70 °C, 10 min.	Alternatively: Rinse carefully in ethanol and let it evaporate in air.

Process flow title			Reversion
Topology Optimized Trampoline - Thick LPCVD layer			3.01
DTU Physics Department of Physics 	Contact email	Contact person	Contact phone
	denho@fysik.dtu.dk	Dennis Høj	+45 26 14 93 66
	Labmanager group DTU Physics - QPIT	Batch name TOT	Creation date 6 th Mar, 2020
			Reversion date 24 th Jan, 2021


Step	Equipment and procedure	Purpose and comments
1 LPCVD nitride deposition		
1.1 Substrate	4", 500µm double side polished silicon wafer.	Take directly to furnace without changing carrier. Remember to include a dummy wafer. Check logbook to calculate deposition time. Measure on dummy wafer and write in furnace log.
1.2 LPCVD Si ₃ N ₄	Furnace: LPCVD Nitride (4"). High stress. Deposition thickness 50 nm.	
1.3 Measure	Ellipsometer, Nanolab recipe for thin nitride.	
2 Frontside membrane lithography and etch		
2.1 front Spin coat	Spin Coater: Gamma UV: 1.5 µm AZ MIR 701 with HMDS.	Trampoline pattern exposure.
2.2 front Exposure	Aligner: MLA3: 200 mJ cm ⁻² .	
2.3 front Develop	Developer: TMAH UV-lithography: 3001, PEB60SP60.	
2.4 front Inspection	Inspect pattern in optical microscope.	If pattern is poorly defined, remove resist and redo lithography.
2.5 front Measure dummy	Ellipsometer, Nanolab recipe for thin nitride.	Measure on a Si ₃ N ₄ coated dummy wafer and save thickness result.
2.6 front AOE Etch dummy	AOE: SiO ₂ _res, etch 35 nm.	Expect etch rate of ~136 nm min ⁻¹ .
2.7 Measure dummy	Ellipsometer, Nanolab recipe for thin nitride.	Measure on dummy wafer and estimate etch rate.
2.8 front SiN etch	AOE: SiO ₂ _res, etch 35 nm.	Use previous calculated etch rate to obtain exact etch time.
2.9 Resist removal	Plasma asher 2: O ₂ : 400 sccm, N ₂ : 70 sccm, 1000 W, 30 min.	
3 Backside window lithography and etch		
3.1 back Spin coat	Spin Coater: Gamma UV: 1.5 µm AZ MIR 701 with HMDS.	
3.2 back Exposure	Aligner: MA6 - 2: 220 mJ cm ⁻² .	
3.3 back Develop	Developer: TMAH UV-lithography: 3001, PEB60SP60.	Calculate exposure time from intensity. 11 mW cm ⁻² for MA6-2.
3.4 back Inspection	Inspect pattern in optical microscope.	If pattern is poorly defined, remove resist and redo lithography.
3.5 back SiN etch	AOE: sin_res, 00:00:15.	
3.6 Resist removal	Plasma asher 2: O ₂ : 400 sccm, N ₂ : 70 sccm, 1000 W, 30 min.	


Process flow title			Reversion
Topology Optimized Trampoline - Thick LPCVD layer			3.01
DTU Physics Department of Physics 	Contact email	Contact person	Contact phone
	denho@fysik.dtu.dk	Dennis Høj	+45 26 14 93 66
	Labmanager group DTU Physics - QPIT	Batch name TOT	Creation date 6 th Mar, 2020
			Reversion date 24 th Jan, 2021

Step	Equipment and procedure	Purpose and comments
4 Membrane release		
4.1 KOH	KOH2: 80 °C, no elevator 	Expect 50 min of preparation time. Place wafers closely packed. Place SiN coated dummy wafers at each end. Measure etch depth after 5 hour and estimated required total etch time for 515 µm and add another 3 min. When there is 33 min left, take the wafers out.
4.2 Water rinse	Rinse for 5 min, no bubbles.	
4.3 front Measure dummy	Ellipsometer, Nanolab recipe for thin ni-tride.	During KOH etch, measure on a Si ₃ N ₄ coated dummy wafer and save thickness result.
4.4 front BHF Etch dummy	BHF1: Etch 30 nm.	Expect etch rate of ~0.7 nm min ⁻¹ .
4.5 Water rinse dummy	Rinse for 5 min, no bubbles.	
4.6 front Measure dummy	Ellipsometer, Nanolab recipe for thin ni-tride.	Measure on dummy wafer and save thickness result. Calculate etch rate.
4.7 front BHF Etch	BHF1: Etch until 20 nm left. 	Use previously calculated etch rate to obtain exact etch time.
4.8 Water rinse	Rinse for 5 min, no bubbles.	
4.9 KOH	KOH2: 80 °C, 35 min, no elevator, no flow, no heating 	The lack of flow and heating will degrade the etch rate, but the etch will be more gentle on the fragile membranes, thereby increasing yield. Note: The membranes are very fragile from this point on.
4.10 Water rinse	Rinse for 5 min, 80 °C, no bubbles.	The bath takes 30 minutes to warm up.
4.11 HCl	5 % HCl for 10 min	Removes iron oxide contamination resulting from KOH etch.
4.12 Water rinse	Rinse for 5 min, no bubbles.	
4.13 Wafer cleaning	H ₂ SO ₄ (sulfuric acid) added with a spoon of (NH ₄) ₂ S ₂ O ₈ (ammoniumpersulfate)	Removes potassium ions resulting from KOH etch, as well as other possible alkali ions and organic contaminations.
4.14 Water rinse	Rinse for 5 min, no bubbles.	
4.15 Ethanol dry	Dry in ethanol bath. 70 °C, 10 min.	Alternatively: Rinse carefully in ethanol and let it evaporate in air.

Process flow title			Reversion
Density phononic membranes			2.20
DTU Physics Department of Physics 	Contact email	Contact person	Contact phone
	denho@fysik.dtu.dk	Dennis Høj	+45 26 14 93 66
	Labmanager group DTU Physics - QPIT	Batch name	Creation date
		DP	5 th Mar, 2019
			Reversion date
			24 th Jan, 2021

Step	Equipment and procedure	Purpose and comments
1 Depositions		
1.1 Substrate	4", 500 μm double side polished silicon wafer.	Take directly to furnace without changing carrier. Remember to include a few dummy wafers.
1.2 LPCVD Si ₃ N ₄	Furnace: LPCVD Nitride (4"). Deposition thickness 20 nm.	Check logbook to calculate deposition time.
1.3 Measure	Ellipsometer, Nanolab recipe for thin nitride.	Measure on dummy wafer and write in furnace log.
1.4 front PECVD Si ₃ N ₄	PECVD4: Fysik/denho/MFSiN LS, ~1000 nm, ~12 nm/min	Exact thickness depends on the amount of isotropic etch.
1.5 Measure	Ellipsometer, PECVD on LPCVD	Set LPCVD parameters to the previous measurement.
2 Pillar Dry Etch		
2.1 front Spin coat	Spin Coater: Gamma UV: 1.5 μm AZ MIR 701 with HMDS	
2.2 front Exposure	Aligner: Maskless 02 (MLA2): 160 mJ/cm ² , Defocus = +1.	Parameters optimized for 1 μm pillars.
2.3 front Develop	Developer: TMAH UV-lithography: 3001, PEB60SP60.	
2.4 front Inspection	Inspect pattern in optical microscope or SEM.	If pattern is poorly defined, remove resist and redo lithography.
2.5 Measure	Ellipsometer, PECVD on LPCVD	Set LPCVD parameters to the previous measurement.
2.6 front SiN etch	AOE: nitr_res, etch down to ~100 nm PECVD SiN	Assume etch rate of 125 nm/min.
2.7 Measure	Ellipsometer, PECVD on LPCVD	Set LPCVD parameters to the previous measurement.
2.8 front SiN etch	AOE: nitr_res, etch down to ~50 nm PECVD SiN	Use estimated etch rate.
2.9 Measure	Ellipsometer, PECVD on LPCVD	Set LPCVD parameters to the previous measurement. Repeat AOE etch if still too thick.
2.10 Resist removal	Plasma asher 2: O ₂ : 400 sccm, N ₂ : 70 sccm, 1000 W, 30 min.	Verify all photoresist has been removed.

Process flow title			Reversion
Density phononic membranes			2.20
DTU Physics Department of Physics 	Contact email	Contact person	Contact phone
	denho@fysik.dtu.dk	Dennis Høj	+45 26 14 93 66
	Labmanager group DTU Physics - QPIT	Batch name DP	Creation date 5 th Mar, 2019
			Reversion date 24 th Jan, 2021

Step	Equipment and procedure	Purpose and comments
3 Backside window mask etch		
3.1 back Spin coat	Spin Coater: Gamma UV: 1.5 µm AZ MIR 701 with HMDS	
3.2 back Exposure	Aligner: Maskless 03 (MLA3): 200 mJ/cm ² , Defocus = 0.	
3.3 back Develop	Developer: TMAH UV-lithography: 3001, PEB60SP60.	
3.4 back Inspection	Inspect pattern in optical microscope.	If pattern is poorly defined, remove resist and redo lithography.
3.5 back Dry etch	AOE: Si_etch, 1:30	
3.6 Resist removal	Plasma asher 2: O ₂ : 400 sccm, N ₂ : 70 sccm, 1000 W, 30 min.	Verify all photoresist has been removed.
4 Membrane release		
4.1 BHF	BHF2 or BHF3: 20-60s, ~30 nm/min	Pre etch the residual PECVD layer.
4.2 Water rinse	Rinse for 5 min, no bubbles.	
4.3 back KOH	KOH2: 80 °C, ~7 h, no elevator 	Expect 50 min of preparation time. Measure etch depth after 5 hour via a dummy and estimate required total etch time for 515 µm. Add 5 minutes. When there is 35 min left turn off heating and pump.
4.4 Water rinse	Rinse for 5 min, 80 °C, no bubbles.	The bath takes 30 minutes to warm up.
4.5 HCl	5 % HCl for 10 min	Removes iron oxide contamination resulting from KOH etch.
4.6 Water rinse	Rinse for 5 min, no bubbles.	
4.7 Wafer cleaning	H ₂ SO ₄ (sulfuric acid) added with a spoon of (NH ₄) ₂ S ₂ O ₈ (ammoniumpersulfate)	Removes potassium ions resulting from KOH etch, as well as other alkali ions and organic contaminations.
4.8 Water rinse	Rinse for 5 min, no bubbles.	
4.9 Ethanol dry	Dry in ethanol bath. 70 °C, 10 min.	Alternatively: Rinse carefully in ethanol and let it evaporate in air.

Technical
University of
Denmark

Fysikvej, Building 307
2800 Kgs. Lyngby
Tlf. 4525 1700

www.fysik.dtu.dk